

FORECASTING URBAN AIR QUALITY

GUEST EDITORS: TAREQ HUSSEIN, CHRISTER JOHANSSON, AND Lidia MORAWSKA





Forecasting Urban Air Quality

Advances in Meteorology

Forecasting Urban Air Quality

Guest Editors: Tareq Hussein, Christer Johansson,
and Lidia Morawska



Copyright © 2012 Hindawi Publishing Corporation. All rights reserved.

This is a special issue published in “Advances in Meteorology.” All articles are open access articles distributed under the Creative Commons Attribution License, which permits unrestricted use, distribution, and reproduction in any medium, provided the original work is properly cited.

Editorial Board

Paulo Artaxo, Brazil
Rebecca Barthelmie, USA
Guy Brasseur, USA
Mladjen Ćurić, Serbia
Raymond Desjardins, Canada
Klaus Dethloff, Germany
Panuganti Devara, India
Ellsworth Dutton, USA
Shouting Gao, China
Luis Gimeno, Spain

Sven-Erik Gryning, Denmark
Ismail Gultepe, Canada
Hiroyuki Hashiguchi, Japan
Didier Hauglustaine, France
Qi Hu, USA
I. S. A. Isaksen, Norway
Yasunobu Iwasaka, Japan
Hann-Ming Henry Juang, USA
George Kallos, Greece
Harry D. Kambezidis, Greece

Markku Kulmala, Finland
Richard Leaitch, Canada
Monique Leclerc, USA
Barry Lefer, USA
Zhanqing Li, USA
Edward Llewellyn, Canada
Kyaw Tha Paw, USA
Sara C. Pryor, USA
Eugene Rozanov, Switzerland

Contents

Forecasting Urban Air Quality, Tareq Hussein, Christer Johansson, and Lidia Morawska
Volume 2012, Article ID 243603, 2 pages

Modeling the Short-Term Effect of Traffic and Meteorology on Air Pollution in Turin with Generalized Additive Models, Pancrazio Bertaccini, Vanja Dukic, and Rosaria Ignaccolo
Volume 2012, Article ID 609328, 16 pages

Temporal Forecasting with a Bayesian Spatial Predictor: Application to Ozone, Yiping Dou, Nhu D. Le, and James V. Zidek
Volume 2012, Article ID 191575, 13 pages

Application of Multiple Linear Regression Models and Artificial Neural Networks on the Surface Ozone Forecast in the Greater Athens Area, Greece, K. P. Moustris, P. T. Nastos, I. K. Larissi, and A. G. Paliatsos
Volume 2012, Article ID 894714, 8 pages

Examining the Impact of Nitrous Acid Chemistry on Ozone and PM over the Pearl River Delta Region, Rui Zhang, Golam Sarwar, Jimmy C. H. Fung, Alexis K. H. Lau, and Yuanhang Zhang
Volume 2012, Article ID 140932, 18 pages

Potential Impacts of the Introduction of Low-Sulfur Fuel on PM_{2.5} Concentrations at Breathing Level in a Subarctic City, Ketsiri Leelasakultum, Nicole Mölders, Huy N. Q. Tran, and Georg A. Grell
Volume 2012, Article ID 427078, 16 pages

An Air Quality Management System for Policy Support in Cyprus, Nicolas Moussiopoulos, Ioannis Douros, George Tsegas, Savvas Kleanthous, and Eleftherios Chourdakis
Volume 2012, Article ID 959280, 8 pages

Wood-Burning Device Changeout: Modeling the Impact on PM_{2.5} Concentrations in a Remote Subarctic Urban Nonattainment Area, Huy N. Q. Tran and Nicole Mölders
Volume 2012, Article ID 853405, 12 pages

Editorial

Forecasting Urban Air Quality

Tareq Hussein,^{1,2} Christer Johansson,^{3,4} and Lidia Morawska⁵

¹ Department of Physics, The University of Jordan, Amman 11942, Jordan

² Department of Physics, University of Helsinki, 00014 Helsinki, Finland

³ Department of Applied Environmental Science, Stockholm University, Stockholm, Sweden

⁴ Environment and Health Administration, Box 8136, SE-104 20 Stockholm, Sweden

⁵ International Laboratory for Air Quality and Health, Queensland University of Technology, Brisbane, QLD 4001, Australia

Correspondence should be addressed to Tareq Hussein, tareq.hussein@helsinki.fi

Received 12 September 2012; Accepted 12 September 2012

Copyright © 2012 Tareq Hussein et al. This is an open access article distributed under the Creative Commons Attribution License, which permits unrestricted use, distribution, and reproduction in any medium, provided the original work is properly cited.

Air pollution has significant impacts on both the environment and human health. Therefore, urban areas have received ever growing attention, because they not only have the highest concentrations of air pollutants, but they also have the highest human population. In modern societies, urban air quality (UAQ) is routinely evaluated and local authorities provide regular reports to the public about current UAQ levels. Both local and international authorities also recommended that some air pollutant concentrations remain below a certain level, with the aim of reducing emissions and improving the air quality, both in urban areas and on a more regional scale. In some countries, protocols aimed at reducing emissions have come in force as a result of international agreements.

While the routine assessment of UAQ is essential for analysing what has happened in the past, forecasting allows for the prediction of future trends and enables local authorities to plan new strategies aimed at reducing the risk of exposure to high levels of air pollution. For example, the EU directive (2008/50/EC) declared that Member States shall forecast air quality and inform the public if any alert thresholds are likely to be exceeded. However, whilst the forecasting of UAQ and its impact on the environment and human health is of great interest to both policy makers and the public, it is also extremely challenging. Forecasting UAQ requires long-term monitoring of the temporal-spatial variation of air pollutants, as well as data on weather patterns, anthropogenic, and biogenic emissions, and the local- and long-range transport of air pollution.

Three papers in this special issue present work on the development of statistical forecasting models that are superior in terms of their high productivity, but lacking in terms of the physical process. One paper illustrates how, in addition to vehicular traffic, meteorology also plays an important role in UAQ, and it can be used as one of the key predictors in air-quality forecasting models. The approach was based on a generalized additive model and it was applied for nitrogen dioxide (NO₂) and particulate matter (PM₁₀) in Turin-Italy during December 2003–April 2005. Another paper presents work in relation to the development of two empirical models: a Bayesian approach to forecast the next day ground-level ozone hourly concentrations and a state-space model approach. The predictions of these models were evaluated against many stations where the first approach was superior to the second. The third paper presents a forecast of daily maximum surface ozone concentration in the Athens area, based on multiple linear regression models. This paper also emphasized that basic meteorological parameters are of great importance in order to forecast ozone concentration levels. In addition, One paper presents data from an air quality management system installed at the Department of Labour Inspection in Cyprus. This system was applied for the measurement of NO₂, O₃, CO, Benzene, PM₁₀, and PM_{2.5}.

In principle, the statistical models presented in several papers, and the air quality management system presented in a paper, can be extended to other air quality parameters, with the aim of developing an integrated system to forecast UAQ. In general, statistical models are able to make highly accurate

short-term predictions, however they are unable to account for the many chemical and physical processes that impact on UAQ in the long-term.

The Community Multiscale Air Quality (CMAQ) modeling system and the CB05 mechanism were utilized in Paper IV to investigate the impact of nitrous acid (HONO) chemistry on regional ozone and particulate matter concentrations in the Pearl River Delta region. The results of the model simulations were in good agreement with the observed data for NO_x , SO_2 , PM_{10} , and sulfate.

In one paper, the Weather Research and Forecasting model was applied, in conjunction with chemistry packages that were modified for use in the subarctic region, to examine the effects of using low-sulfur fuel in oil-burning facilities on $\text{PM}_{2.5}$ concentrations at breathing level in an Alaska city. The simulation results suggested that introducing low-sulfur fuel would decrease the monthly mean 24 h-averaged concentrations during the winter. The results also suggested that $\text{PM}_{2.5}$ concentrations would further decrease on days with low atmospheric boundary layer heights, a low hydrometeor mixing ratio, low downward shortwave radiation, and low temperatures. Published in this issue, by the same research group and using the same modeling approach, another paper illustrates the effects of exchanging noncertified wood-burning devices with certified ones, on the 24 h-average $\text{PM}_{2.5}$ concentrations in winter. The results showed that changing out 2930 uncertified woodstoves and 90 outdoor wood boilers would reduce the 24 h average $\text{PM}_{2.5}$ concentrations by 6% and result in pollution falling below the alert threshold levels on 7 out of the 55 simulated exceedance days.

*Tareq Hussein
Christer Johansson
Lidia Morawska*

Research Article

Modeling the Short-Term Effect of Traffic and Meteorology on Air Pollution in Turin with Generalized Additive Models

Pancrazio Bertaccini,¹ Vanja Dukic,² and Rosaria Ignaccolo³

¹ Department of Biella, Environmental Protection Agency of Piemonte, 13900 Biella, Italy

² Department of Applied Mathematics, University of Colorado-Boulder, Boulder, CO 80309, USA

³ Department of Economics, University of Turin, 10123 Turin, Italy

Correspondence should be addressed to Rosaria Ignaccolo, rosaria.ignaccolo@unito.it

Received 15 February 2012; Revised 27 May 2012; Accepted 9 June 2012

Academic Editor: Tareq Hussein

Copyright © 2012 Pancrazio Bertaccini et al. This is an open access article distributed under the Creative Commons Attribution License, which permits unrestricted use, distribution, and reproduction in any medium, provided the original work is properly cited.

Vehicular traffic plays an important role in atmospheric pollution and can be used as one of the key predictors in air-quality forecasting models. The models that can account for the role of traffic are especially valuable in urban areas, where high pollutant concentrations are often observed during particular times of day (rush hour) and year (winter). In this paper, we develop a generalized additive models approach to analyze the behavior of concentrations of nitrogen dioxide (NO_2), and particulate matter (PM_{10}), collected at the environmental monitoring stations distributed throughout the city of Turin, Italy, from December 2003 to April 2005. We describe nonlinear relationships between predictors and pollutants, that are adjusted for unobserved time-varying confounders. We examine several functional forms for the traffic variable and find that a simple form can often provide adequate modeling power. Our analysis shows that there is a saturation effect of traffic on NO_2 , while such saturation is less evident in models linking traffic to PM_{10} behavior, having adjusted for meteorological covariates. Moreover, we consider the proposed models separately by seasons and highlight similarities and differences in the predictors' partial effects. Finally, we show how forecasting can help in evaluating traffic regulation policies.

1. Introduction

The impact of air pollution on human health and environment has been one of the central issues in environmental public policy and decision making [1–5]. For example, European Union mission mandates yearly improvement of environmental quality, lower emission standards, and support of environmental technology and scientific research and development [6–9] while the recent air quality directive [10] requires that information on air quality for current day with trend and forecast for the next days be publicly available. Similarly, the United States policy makers and industry leaders have recently begun instituting renewable energy and environmental protection research programs at universities and state agencies across the country.

Understanding the behavior of pollutants and understanding the components of variation in pollutant concentrations are arguably the most important goals of air quality

research for public policy purposes. For example, understanding how pollutant concentrations vary with respect to intensity and patterns of traffic would allow policy makers to assess the consequences of implementing certain traffic regulation measures. However, if an intervention such as traffic measure is being considered or evaluated, it is crucial to also account for those processes which covary with the outcome (pollutant) as well as with the regulatory (traffic) variable. In the studies of traffic and air pollution such confounding processes could include meteorological, health, social, and other societal-level processes that affect both pollution and traffic volume. Those confounders are unfortunately often unobserved, for example, asthma, flu, or other disease activity that makes people stay at home more and drive less and also happens to occur in winter when smog and air pollution are high, and thus the level of their covariation with traffic patterns and also with the pollution is difficult to ascertain. However, not accounting for those confounders at

all would hide the true effects of interest- and yield-biased estimates of the regulatory effects.

In the Turin metropolitan area, where air quality is a concern, previous analysis of pollution has examined carbon monoxide (CO) concentrations and traffic volume in the Turin metropolitan area, as in Bertaccini et al. [11] who used a seasonal linear regression model for each station monitoring CO. Subsequently, Fassó et al. [12] studied the same problem using a linear vectorial autoregressive model and carried out a sensitivity analysis to describe the relative roles of traffic and meteorology, by their respective principal components. Instead, Kim and Guldmann [13] evaluate the importance of wind direction in the air pollution concentration through land use regression models aided by geographical information systems. They analyze the pollution related to vehicular traffic (defined as vehicle-kilometers-traveled weighted by wind direction frequency) by fitting linear regression models for different sizes of the buffer zone.

However, sometimes in modeling city-level processes, (generalized) linear models are not the most adequate ones to use. Although chemical and physical dynamics of processes are deterministic, local behavior can be very difficult to understand and to model properly. Therefore, it would be advantageous to consider a statistical alternative to the deterministic differential-equation-based modeling of pollution. To that extent, generalized additive models, or GAM [14], offer an alternative which is capable of not only flexibly modeling relationship between pollution concentration and predictors but also relationships between predictors. This approach could flexibly approximate complex physical and chemical relationships between processes covarying with traffic and pollution. In addition, GAM can account for the smooth time-varying processes reflecting the confounders which vary slowly relative to the predictor of interest, by including “time” as a flexibly (but smoothly) modeled predictor. Thus, while there are many drivers of air pollution in Turin (some observed and measured and some not measured), the flexibility of the GAM approach allows us to capture and quantify the role of a single driver (traffic) without the confounding effects of the other drivers (confounders).

While generalized additive models have been widely used as a standard method in studies of pollution and health (see, e.g., the pioneering work [15]), they have only recently been introduced into the air pollution modeling of impact of traffic and meteorological covariates, as in the work of Carslaw et al. [16]. The authors find that one of the most important factor is the flexible interaction between wind speed and wind direction, due to the canyon effect of the nearby buildings. Their analysis has confirmed the important role of wind in pollutant dispersion and in describing the variation in pollutant concentration due to changes in meteorological conditions. Similarly, Aldrin and Hobæk Haff [17] use generalized additive models separately for several different pollutants in different locations over the Oslo urban area, using traffic- and meteorological-observed data. Then they apply GAM to evaluate the effect of salting the street with magnesium chloride (for ice condition in winter) on particulate matter concentrations [18], showing that it is a potentially useful measure to reduce PM in a road tunnel.

More recently, ultrafine particle concentration in Helsinki and Finland temporal trends were examined in the light of their relationship with rainfall and other meteorological variables in Clifford et al. [5] and Mlgaard et al. [4].

In this paper we focus specifically on quantifying the role of traffic on air pollution in Turin, Italy, in a way that could be useful to environmental policy makers. Air quality in Turin area is critical with respect to particulate matter, nitrogen dioxide, and ozone; in fact, air quality standards set by European directives are often exceeded for these three pollutants (in particular PM_{10}), whereas most other pollutant concentrations are below the limit values. We present a set of models that are able to realistically explain much of the variation in the pollutant concentration, while still yielding precise estimates of the effects of meteorology and traffic on pollution concentration. More specifically, building on the work in Bertaccini et al. [19, 20], we propose the use of generalized additive models to analyze the space-averaged air pollutant concentration over Turin metropolitan area as a function of vehicular traffic, while adjusting for potential meteorological and other possibly unobserved confounders. Our goal is to quantify the effect of traffic and evaluate potential interventions (traffic reductions) specifically for Turin. While we cannot generalize the estimated magnitude of the effects in Turin to other geographic areas, we hope that our analysis contributes to the urban air quality research in three ways: (1) the results for Turin present additional information for completing the pollution picture for European cities; (2) provides a good reference for environmental policy for cities with similar geographic surroundings; (3) methodologically, provides evidence that a simple form of the traffic variable can often describe the behavior of pollutants sufficiently well.

The paper is organized as follows. Section 2 is devoted to data description related to traffic, pollution, and meteorology. In Section 3 we describe the basic theory and some advantages of using the generalized additive models and then discuss the selection of the best model and the predictor subset for pollutant concentration, aiming to balance complexity and goodness of fit. Specific models are proposed and results analyzed for two critical pollutants, NO_2 and PM_{10} (Sections 3.1 and 3.2), both for the whole period December 2003–April 2005 and separately by season in a year. Moreover, we carry out a forecasting application of the proposed model for NO_2 in order to show how it can be used for traffic regulation policy assessment (Section 3.3). Conclusions are discussed in Section 4.

2. Data

2.1. Traffic. The traffic data are provided by 5T s.r.l., a company working in the Turin city area with a widely distributed set of 500 “inductive loop” sensors (i.e., flow counting points), embedded in the surface of the roads. Inductive loops work by a simple principle of sensing the change in inductance, when a car (or another large metal object) passes over a loop, the car’s presence changes the total inductance, and the loop sensor count goes up by one. Loop network is a part of the monitoring system UTOPIA/SPOT (Urban

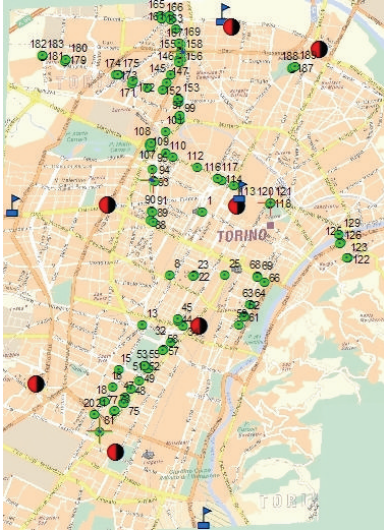


FIGURE 1: Turin vehicle traffic, air, and meteorology monitoring network: green disk are the 107 traffic counters, red and black disks are the pollution stations, and blue flags are the meteorological stations.

Traffic Optimization by Integrated Automation/System for Priority and Optimization of Traffic), designed to serve as an urban traffic control system as described in Kronborg and Davidsson [21] and Wood [22]. Such a system operates as a framework implemented to improve both private and public transportation efficiency in the Turin metropolitan area. The network of available sensors is set up to monitor the vehicular traffic at the main intersections of the city road graph (Figure 1).

This extensive network allows us to observe the behavior of traffic over time at multiple points throughout the city. However, having so many measuring devices also means that many of the individual time series will have a nontrivial fraction of missing data, sometimes over large continuous periods of time. These “gaps” in the measurement series are most often due to road maintenance or to the repair of the sensors themselves. In such cases, the missingness can be treated as missing at random (independent of the pollutant levels).

Our traffic data, the number of vehicles that pass over a certain monitor within 5-minute intervals have been aggregated into hourly counts. Specific subsets of all traffic time series have been chosen so that they all correspond to the outflow of traffic at any given crossroads (which also equal to the influx of traffic to the same crossroads), in order to avoid double counting of the vehicles. The availability of meteorological and chemical data constrains further our study period from December 19th, 2003, to April 27th, 2005, and the final dataset is thus composed of 107 hourly measurement time series.

In the analyses in this paper we use hourly city-wide averaged variables, focusing on the average traffic behavior of the city, as shown in Figure 2. The boxplots show typical features of the traffic trend at three different time scales: daily, weekly, and yearly. In the daily scale we can see the

TABLE 1: Available chemical sensors at the sites: Consolata (Con.), Rivoli (Riv.), Rebaudengo (Reb.), Cristina (Cri.), Gaidano (Gai.), Lingotto (Ling.), and Grassi (Gra.).

	Con	Riv	Reb	Cri	Gai	Lin	Gra
NO ₂	×	×	×	×	×	×	
PM ₁₀	×	×			×		×

strong difference in traffic magnitude between day time and night-time; as well as high traffic intensity due to the morning and evening rush hour. The weekly scale shows the differences between weekdays and weekends: Saturday and Sunday traffic differs both in the total number of vehicles and the timings of the peak volume hours. Observing the yearly representation we can see that traffic is almost constant during the year except for the month of August where a sharp reduction is due to the summer holidays.

2.2. Pollution. Pollution data have been provided by ARPA Piemonte and Regione Piemonte. In this paper we focus on NO₂ and PM₁₀, which are measured on an hourly and daily scales, respectively. The measurements were recorded at a subset of the total of seven environmental stations across Turin (*Grassi, Rebaudengo, Rivoli, Consolata, Cristina, Gaidano, and Lingotto* stations are located as shown in Figure 1), while NO₂ and PM₁₀ measurement sensors are distributed as in Table 1. All the measurement stations are traffic ones, except *Lingotto* that is a background site; in order to have an average representative of all Torino area, we consider *Lingotto* data too.

In order to provide an example of NO₂ behavior over time, we summarize the NO₂ concentration measured at the “Consolata” station (Figure 3). As can be seen in Figure 3(a), the lowest values happen during the middle of the month of August, while the highest are during the two winters (recall that the study period is December 2003 through April 2005). The hourly box plots of the concentration shown in Figure 3(b) allow us to see that the concentration decreases during the night and has two peaks: one in the morning and one in the evening, related to commuter behavior. Note that this shape is pretty similar to the one observed for vehicular traffic (Figure 2(a)), motivating the importance of using the hourly time scale. As can be seen from the boxplots by day of the week (Figure 3(c)) the concentration seems to increase in the first few weekdays and decrease during the weekend. The box plots by month (Figure 3(c)) confirm that the lowest values happen in August, while the highest happen in the winter.

Also for PM₁₀ we show, as an example, the concentration measured at the “Consolata” station in Figure 4. The weekly representation in Figure 4(b) shows, as usual with other pollutants, an increase in concentration during the first days of the week, followed by a decrease till the Sunday’s lowest values. The whole period time series (Figure 4(a)) and the box plots by month (Figure 4(c)) point out the large difference of concentration observed over the seasons of the year (cold and warm ones), despite the relative constancy of traffic. For further explorative analysis on pollution features see [20, Chapter 1].

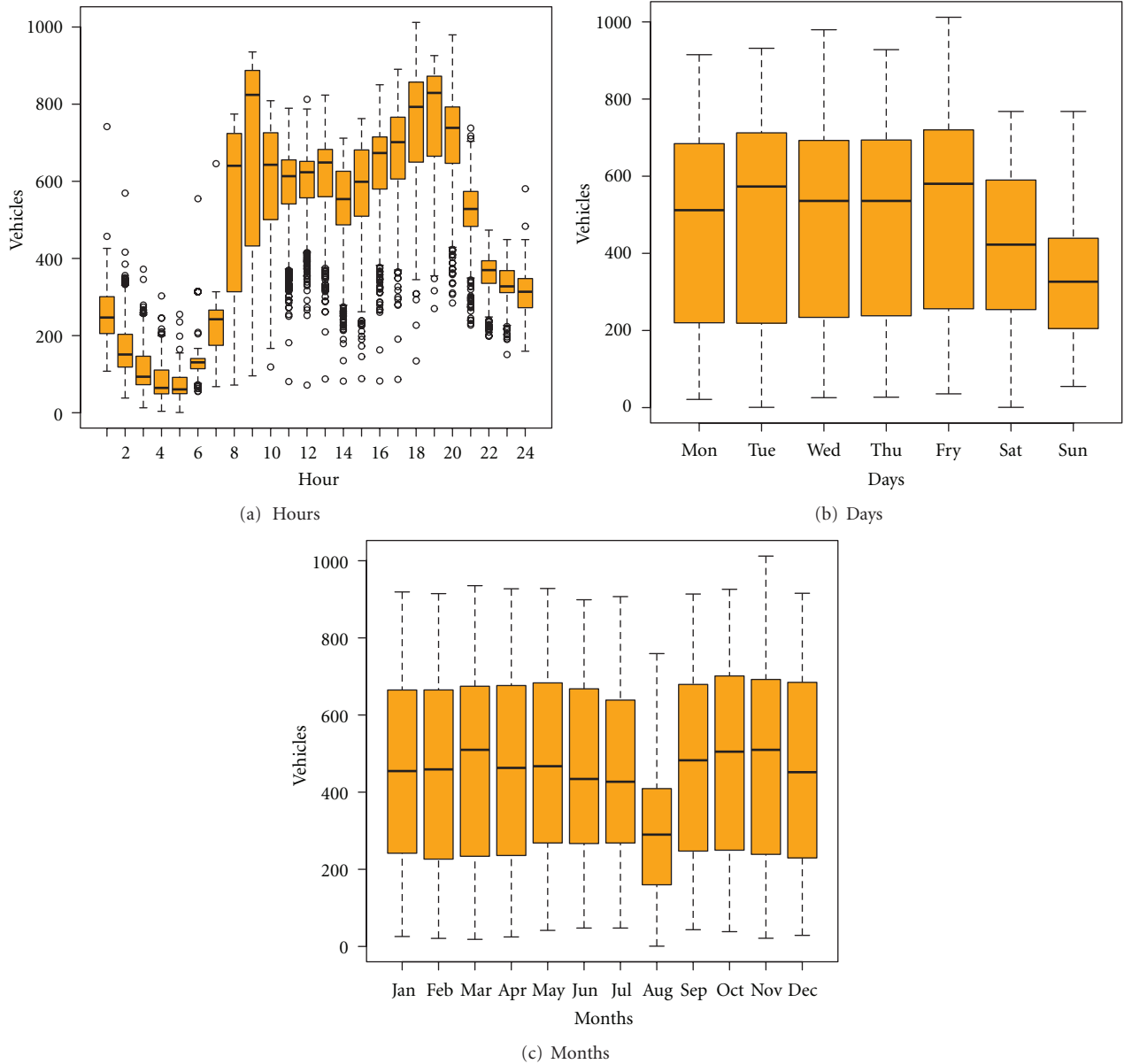


FIGURE 2: Box plots of the city-wide average traffic volume for different time scale.

2.3. Meteorology. Meteorological data are collected by four different stations by *ARPA Piemonte* and *Regione Piemonte*, shown in Table 2. The locations of the meteorological stations are shown in Figure 1, marked with the blue flags. For each variable we generally have at least three locations providing data at any given time. Hence, we have a rather reliable description of the meteorological conditions around the city. In addition, pressure generally differs very little across the entire Turin metropolitan area, so we can basically use the value measured by a single (*ReissRomoli (CSELT)*) station as representative of the city-wide pressure level.

Meteorology is reduced to the city-wide vector (ME) containing wind speed (*wsp*, in m/s), solar radiation (*sun*, in W/m^2), relative humidity (*rh*, in percentage), temperature (*tmp*, in degree Celsius), and pressure (*press*, in hPa).

TABLE 2: Available meteorological variables.

	RRom (North)	Cons (Center)	Alenia (West)	Vall (South)
Press.	×			
Temp.	×	×	×	×
Rel. Hum.	×	×		×
Wind Sp.	×	×	×	
Wind Dir.	×	×	×	
Solar Rad.	×	×	×	
Rain	×	×	×	

Precipitation has not been included due to being composed of relatively rare and localized events and to having a rather

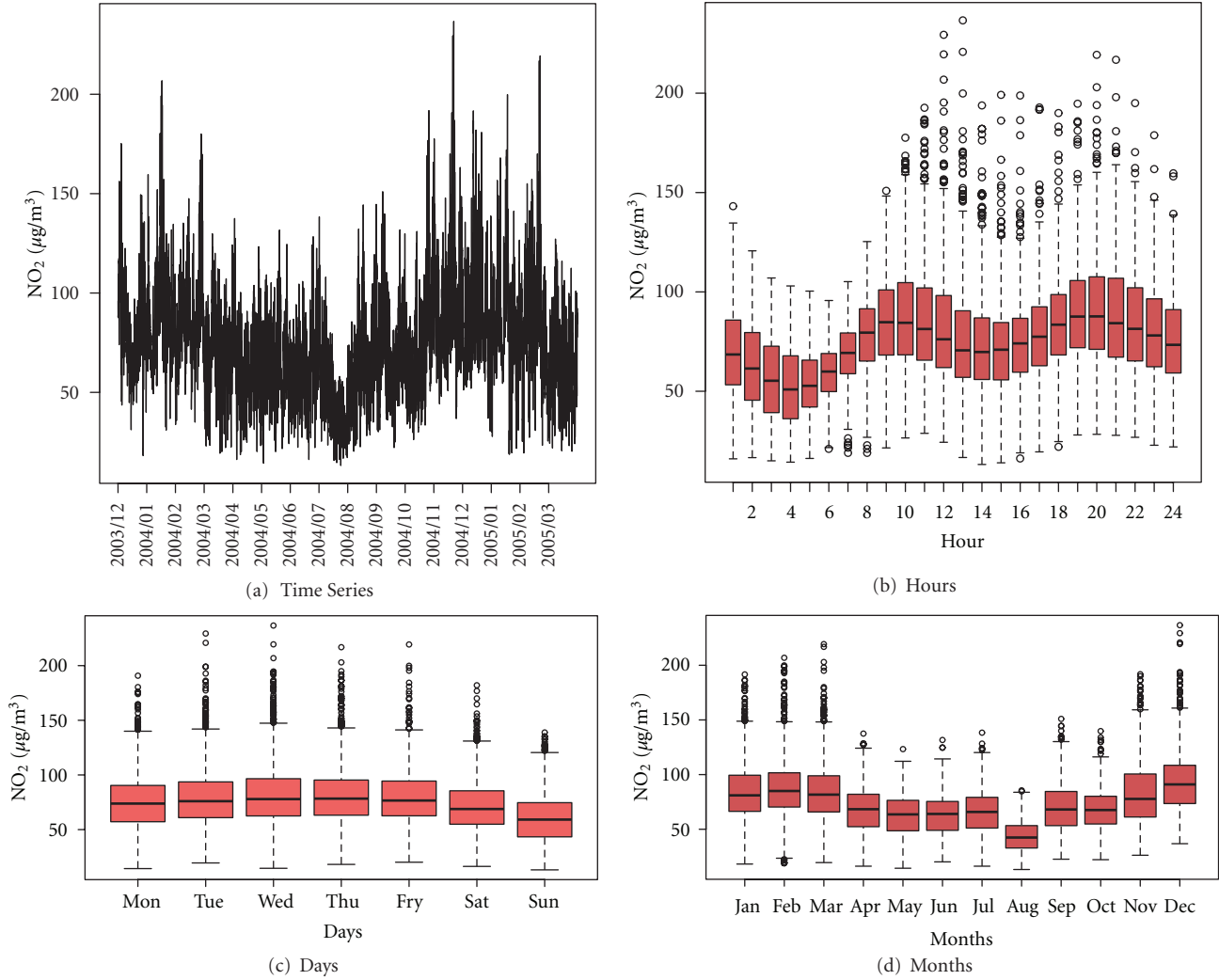


FIGURE 3: Time series and box plots for NO₂ concentration measured at Consolata Station.

limited impact on our results of interest (the sensitivity analysis was examined separately and is not shown in this paper). Moreover, wind direction has been omitted from the model due to the lack of a meaningful single “average” direction for the whole city and the negligible effect observed on the model results (again examined separately and not shown). Finally in our models we also consider the lagged (delayed) effects of some of the crucial meteorological variables, to account for the amount time it takes for certain chemical and physical processes to realize and have an impact.

In Figure 5 we present the time series of the averaged collected meteorological variables. Pressure generally shows variability over time which seems to have a shorter range during the summer. Wind speed is generally low, with some strong events that will turn out to be important in influencing the quality of air. Temperature as well as solar radiation shows the typical seasonal behavior with high values during the summer and low values during the winter.

Relative humidity is generally conditioned by rainfall or wind events.

3. GAM Models for Turin-Wide Pollution

In modeling of air pollution, we will assume that transformed average outcome is additive in predictors and can be appropriately modeled using Generalized Additive Models (GAMs). GAMs have the advantage that they are able to describe nonlinear effects over time and still be easily interpretable due to their additive structure. Moreover, GAMs provide some flexibility via nonlinear or nonparametric terms but do not suffer from the curse of dimensionality like some other nonparametric methods such as kernel smoothing or polynomial modeling. For the outcome (e.g., logarithm of pollutant, $Y = \log(\text{Pollutant})$), we assume that it is additive in its predictors and normally distributed with mean μ_t and variance σ^2 . The systematic part μ_t could include linear and nonlinear components, as well as potential

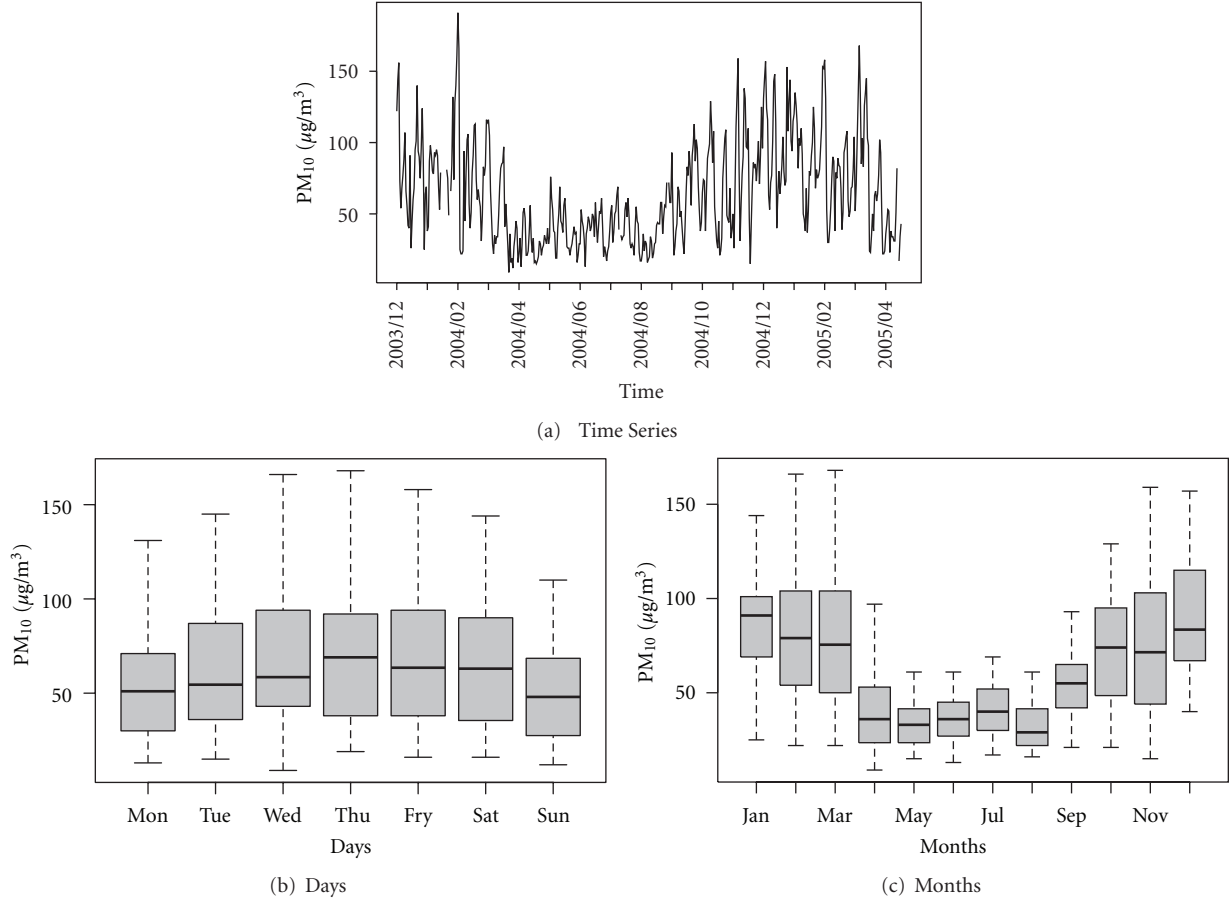


FIGURE 4: Time series and box plots for PM_{10} concentration measured at Consolata Station.

confounders. A general model with additive components would then be

$$\begin{aligned}
 Y_t &\sim \text{Gaussian}(\mu_t, \sigma^2), \\
 \mu_t &= \alpha + \sum_{f=1}^l \beta_f x_{f,t} + \sum_{g=1}^m \sum_{h \in H_g} \eta_{g,h} z_{g,t-h} \\
 &\quad + \sum_{i=1}^p s(k_{i,t}, \lambda_i) + \sum_{j=1}^q \sum_{h \in H_g} s(k_{j,t-h}, \lambda_j),
 \end{aligned} \tag{1}$$

where α is the intercept, \vec{x}_t are the current-time predictors, $\vec{\beta}$ are their (linear) effects, $z_{g,t-h}$ is the value of variable z_g h hours prior to the current time (with lag times taking values in set H_g), with the linear effects $\eta_{g,h}$. Nonlinear effects of covariates k_i (or their lagged version with lag times in H_g) are modeled nonparametrically through smooth functions $s(\cdot, \lambda_i)$, where the smoothness is controlled by the scalar parameter λ_i .

In this study we model the aforementioned pollutants as time series representing the average level of pollution measured hourly or daily, where averaging is done over the available stations (the number of stations at each time changes depending on the pollutant under observation, Table 1). For each pollutant we consider the time series of

the logarithm of the average pollutant concentration over Turin. Given that we wish to estimate the effect on pollution solely due to traffic, we pay special attention to potential confounders, which are related to both the concentration of the pollutant in the atmosphere and to the traffic volume itself. Meteorological variables are the typical confounders and are routinely adjusted for in the pollution analyses. In GAM, we have the added flexibility of considering smooth functions of the meteorological variables, $s(\text{ME}, \lambda_{\text{me}})$. However, there are also potential unmeasured confounders which we have not observed, such as for example health and behavior patterns related to weather (and therefore pollution) and to traffic volume. Though these confounders are unobserved, we can assume that they are varying rather smoothly over time or at least more smoothly than the predictor of interest (in this case traffic). In cases where such assumption is appropriate, we can proxy these unobserved confounders via a smooth function of time.

On the one hand, not adjusting for these unmeasured confounders will result in bias in the estimates of the effect of traffic. On the other, if we adjust too much (using a highly varying function of time), the effect of traffic may be conditioned away. Thus, a sensible model selection criterion which is capable of balancing goodness of fit with penalty due to complexity and high variability of confounder functions is

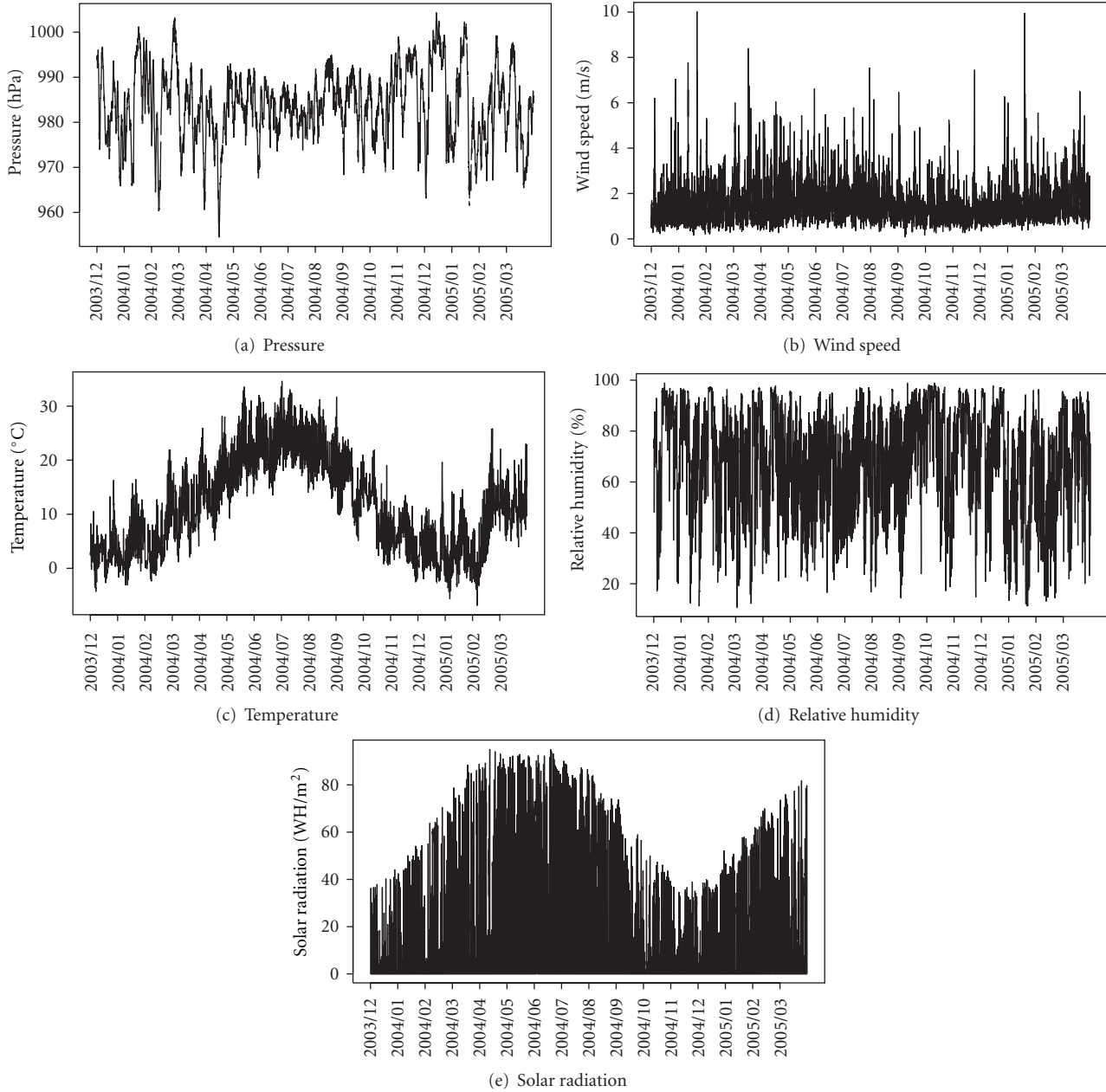


FIGURE 5: Time series of the averaged meteorological variables.

crucial in choosing the optimal GAM model. To that extent, we use the Bayesian information criterion (BIC) [23]. The BIC is like the AIC [24] but with more severe penalization related to the complexity of the model. It takes the form of the penalized log-likelihood where the penalty is equal to the logarithm of the sample size n times the number of estimated parameters θ : $BIC = -2\ell_n(\hat{\theta}) + \log(n)\text{length}(\theta)$.

The main goal of this paper is to assess the effective role of vehicular traffic on two different pollution species. In order to do that thoroughly, we propose two approaches to represent traffic: the first approach is to model the nonlinear effect of traffic using splines, while the second one models a linear effect of simply transformed traffic variables. We select

the most appropriate functional form for each pollutant and the selection of the suitable models is based on the information criterion BIC. We use this criterion to select the most important variables as well as the optimal number of spline basis for each covariate in the model.

Another important issue is related to cross-correlation between pollutants and some meteorological variables. This cross-correlation, when strong, suggests possible use of lagged variables in the model. In fact, this often allows a substantial improvement of fit. Lagged variables have been dealt with in two ways: (a) using a spline of the average of up to twelve previous values (lags 1–12) and (b) using splines only for those individual lagged variables that have

been selected based on the highest correlation with the pollutant. Since the latter procedure always yielded a better BIC score, we will only present results based on it for modeling pollution in our study.

All computation was done in the *R* package `mgcv` [25, 26] that allows to estimate penalized generalized additive models, based on penalized regression splines with automatic smoothness estimation [27].

3.1. Modeling Hourly NO₂. We now describe the global model for the behavior of hourly NO₂ (averaged over the city of Turin), during the period of December 2003 through April 2005. We show how to select the predictors to use in models, which are related to the chemical and physical dynamics of the measured pollutant. This theory-based approach to selecting variables may not necessarily result in a better fit, but it will help incorporate scientific reasoning, physics, and chemistry, behind the behavior of the pollutants.

First, given the hourly scale, lagged values of wind speed and solar radiation are expected to play an important role in the chemistry and physical transport of the pollution throughout the city. Following Carslaw et al. [16], the wind direction was considered in the preliminary phases of this analysis, but no important effects on pollutant concentration have been observed. This result is likely related to the fact that we are working with the average of the variables over the whole city, which may cancel out any directional effects. Moreover, a dummy for rush hour was not found significant when all other variables, including traffic and lagged traffic, were in the model.

Then the proposed model for the average hourly log concentration of NO₂ is given as follows:

$$\begin{aligned}
 M_1: \mu_t = & \alpha + s(t, \lambda_t) + \vec{\beta} \text{DoW} + s(\text{tr}, \lambda_C) + s(\text{lag}(\text{tr}, 1), \lambda_C) \\
 & + s(\text{wsp}, \lambda_C) + s(\text{lag}(\text{wsp}, 1), \lambda_C) \\
 & + s(\text{lag}(\text{wsp}, 2), \lambda_C) + s(\text{sun}, \lambda_C) \\
 & + s(\text{lag}(\text{sun}, 1), \lambda_C) + s(\text{lag}(\text{sun}, 12), \lambda_C) \\
 & + s(\text{rh}, \lambda_C) + s(\text{tmp}, \lambda_C) + s(\text{press}, \lambda_C).
 \end{aligned} \tag{2}$$

Here, social and generally unmeasured confounders are recognized with the smooth function of time $s(t, \lambda_t)$ and to some extent also with the vector of variables indicating the days of the week DoW which turn out to contribute greatly to quality of fit. The other covariates are vehicular traffic (tr) and its lagged version $\text{lag}(\text{tr}, 1)$ that is traffic at the previous hour; wind speed (wsp) and the lagged values at one hour ($\text{lag}(\text{wsp}, 1)$) and two hours ($\text{lag}(\text{wsp}, 2)$); solar radiation (sun) and the lagged values at one hour ($\text{lag}(\text{sun}, 1)$) and twelve hours ($\text{lag}(\text{sun}, 12)$); relative humidity (rh); temperature (tmp) and pressure (press).

To select the best model supported by the available data, we first choose the suitable number of basis for the covariate smooth functions according to the BIC. The actual degrees of freedom (the penalties λ_t and λ_C) are estimated using the generalized cross validation (GCV). Since time has a quite

TABLE 3: Coefficients of the parametric part of the additive model for NO₂ (bold indicates 5% significance).

	Est.	Std. Er.
(Interc.)	4.157781	0.008705
Mon.	0.131553	0.008831
Tue.	0.122523	0.013177
Wed.	0.108691	0.015761
Thu.	0.112780	0.015928
Fri.	0.112615	0.013356
Sat.	0.072378	0.008766

different trend with respect to the other covariates, we fit several models, each with a different number of knots and select the functional form for the time predictor and for the other covariates separately. The resulting smallest BIC is equal to -7085.848 and is obtained in correspondence of 248 and 6 spline basis for time and for meteorological covariates, respectively. Although we do not advocate using the coefficients of determination statistic for assessing goodness of fit, we report for consistency with previous published work that the coefficient of determination in our model is 0.825, in agreement with those reported in Aldrin and Hobæk Haff [17] and Carslaw et al. [16].

Table 3 and Figure 6 summarize the main effects of the predictors under consideration, where linear effects are described with the estimated coefficient values, and the main nonlinear effects are presented graphically as smooth functions.

The estimated function of time and the days of week (DoW) are, as mentioned above, supposed to capture the adjusted effect of unobserved confounders on the pollutant. The first plot shows the estimated spline of time with around 6 knots per week. This relative large number of knots could explain the daily and weekly cyclical social behaviour (i.e., heat during the day or heavy traffic in specific hours of the day or the week) that is related to traffic and pollution. It is reasonable to expect that the number of knots should have some influence on BIC and on the importance we attribute to the unmeasured variables, and that it should have an effect on the other estimates. However, comparing this model with others with smaller number of knots, we observe that this model is still better with respect to the BIC criterion, while the other predictors' estimated spline coefficients change only negligibly.

The smooth effect of time is more pronounced during wintertime (winter 2003-04), see Figure 6(a). Concentrations are generally lower and more stable otherwise, reflecting the usual seasonal behaviour normally associated with the atmospheric boundary layer. Days of week (DOW) always have positive effects with respect to the baseline (Sunday), see Table 3, with Saturdays having the lowest contribution among the six days.

We can observe that *traffic* is, as expected, an important factor (see Figure 6(b) for partial traffic effect with relative standard error), being one of the most important atmospheric nitric oxides generator. Nitric oxides seem to be

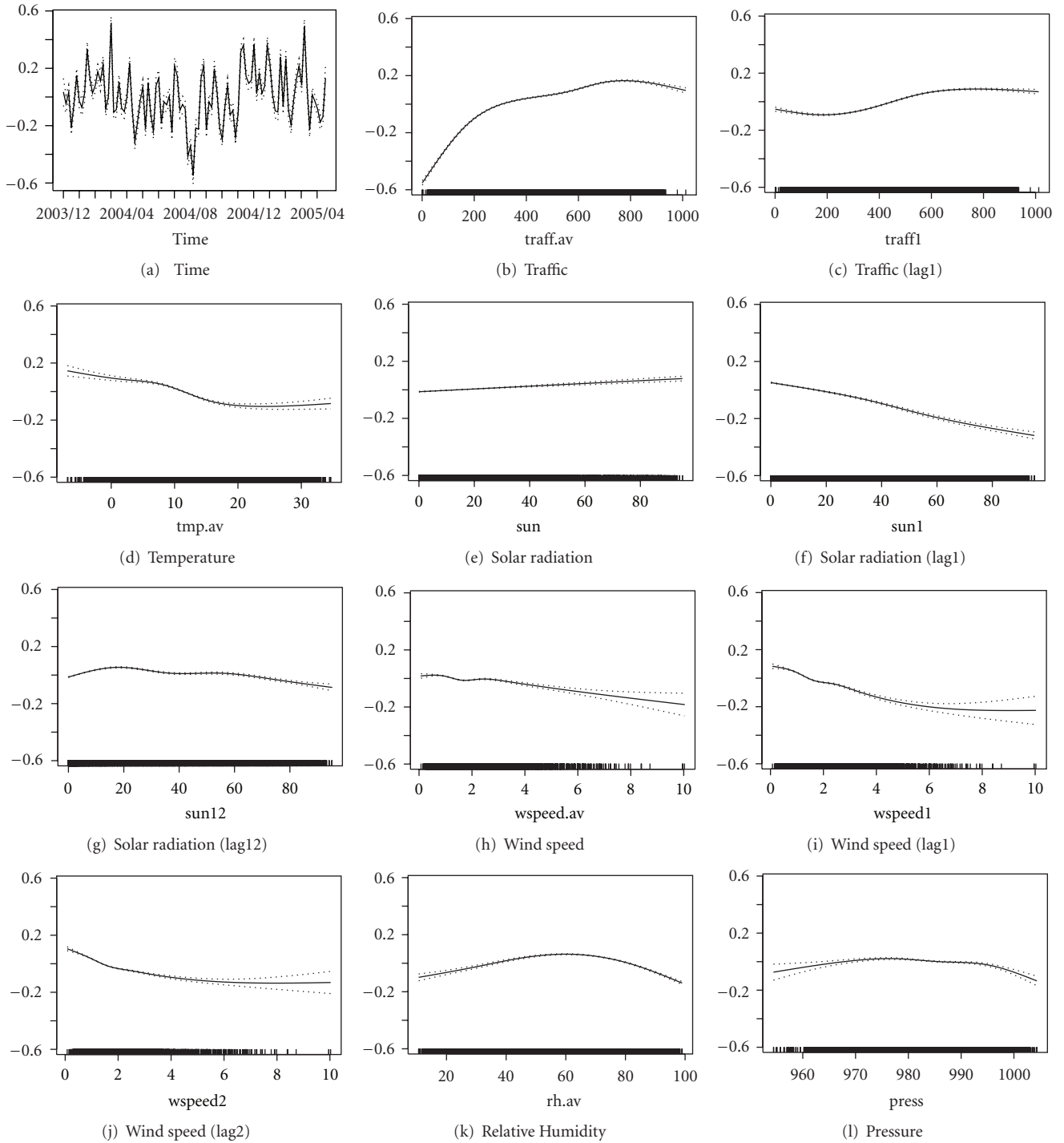


FIGURE 6: Estimated effects of traffic and meteorological variables for NO₂.

especially related to traffic as the average log concentrations keep increasing rapidly with the number of vehicles at lower counts (below the median), ultimately almost leveling off to a saturation level after about 700 vehicles per hour. We can highlight a threshold between 200 and 300 vehicles, corresponding to the night-versus-day time traffic (see Figure 2(a)). Below this threshold the relationship between

the average log concentration and traffic is generally steeper than above it.

On the other hand, the effect of lagged traffic seems close to the zero line, see Figure 6(c). For that reason, we assess the utility of a simpler model for NO₂ with log of traffic with a linear effect and no lagged traffic in the model. All other predictors are kept in the same form. This simpler model

with logarithmic transformation of traffic can be used for policy evaluation and fast prediction. The estimated linear effect of $\log(\text{traffic})$ was 0.26 ($se = 0.003$). The BIC of the simpler model was -6596.97 , while the BIC of the spline model was -7085.85 . This yields support for the model with splines over the model with simpler forms of traffic, but we nonetheless emphasize the potential utility of the simpler model.

Having a model with a linear effect of log-transformed traffic is greatly appealing from the policy evaluation standpoint. The GAM framework allows us to estimate the net effect of traffic, without other confounders, and therefore, having a linear effect facilitates direct estimation of the overall pollutant reduction as a result of a reduction in traffic. For example, our estimated effect of the log of traffic on $\log \text{NO}_2$ was 0.26. From the policy point of view, this means that a 10% decrease in traffic would result in approximately 3% reduction in NO_2 concentration, on average.

At low *temperatures* the average log concentration tends to be higher and almost constant below the 10 degree Celsius (Figure 6(d)). After that it slightly decreases at higher temperatures, levelling off above a temperature around 20 degree Celsius. In fact, the pollutant does not seem to be really conditioned by the temperature and shows an almost linear trend at two different levels. The higher values at low temperatures are apparently related to the seasonal atmospheric situation: generally low temperatures are during the winter, when the solar radiation and boundary layer are reduced too.

The estimated *solar radiation* splines, shown in Figures 6(e)–6(g), suggest that the partial effect of this variable has a generally different behavior in influencing the average concentration depending on the lag of the effect observed: in fact, high values of solar radiation cause a little increasing in the concentration at the same hour, but the lagged variables show negative effects, particularly for the first lag. The persistent effect after many hours is likely explained by the fact that a strong radiation tends to delay a new rise in pollution concentration.

Wind speed has an important effect, given other variables in the model, persistent at different lags, and—as expected—it generally reduces the concentrations considerably as it increases. Lagged variables show that a strong wind may influence NO_2 pollution for many hours (Figures 6(h)–6(j)). The pollutant reduces its concentration for wind speed above 2 m/s suddenly, but lower wind speed could have some effect after one hour or more. The stronger effect of the wind is recognized as a delayed effect, and the lagged covariates have an increase of the effect between 2 and 6 m/s levelling off above that intensity.

Peculiar decrease observed in the partial effect of *relative humidity* (Figure 6(k)) at high values could be associated to rainfall events that usually accompany it. In fact, during rainfall events the humidity that goes to saturation and precipitation is generally effective in pollution reduction. The behaviour at low values could be associated with the increase of wind intensity, when pollution and humidity are normally blown away.

The variation observed in *pressure* (Figure 6(l)) is very small, this is unusual since high pressure is normally related

to atmospheric stability, except in the event of atmospheric inversion, and it could be due to the use of hourly scale for a variable that usually changes more slowly in time.

3.1.1. Modeling NO_2 Separately by Season. We further estimate model M_1 separately by season, to examine whether there are any seasonal differences. The four seasons are defined as follows:

- (i) Winter: 19th December 2003 to 18th March 2004,
- (ii) Spring: 19th March 2004 to 18th June 2004,
- (iii) Summer: 19th June 2004 to 18th September 2004,
- (iv) Fall: 19th September 2004 to 18th December 2004.

As with the global model, the estimated function of time and the days of week (DoW) capture the adjusted effect of unobserved confounders on the pollutant. The day-of-the-week effects appear significant mainly during winter and less so for the other seasons.

Also in separate seasons *traffic* shows important effects on pollution (see Figure 7(a)) but in two very different ways. During springtime and summertime, the traffic partial effect sharply increases for small traffic volumes, till 200–300 vehicles per hours, while it does not vary a lot for higher volumes. For winter and autumn, we observe a traffic partial effect that is almost constant when traffic volume changes and this suggests that the reduction of pollution concentration during wintertime is hard, even through deep traffic regulations. This result is also supported by the traffic role in the conjunction with the industry or domestic heater emissions. In fact, during the cold seasons the effect of typical atmospheric stability on pollutant emissions makes traffic be just one of the agents determining accumulation of pollution (so that high concentrations occur even with low traffic). To the contrary, during warm seasons traffic becomes the most important source of pollution and NO_2 concentration, anyway below limit values, and steeply increases with traffic values until it reaches the saturation condition. The partial effect of the previous hour traffic differs, when comparing cold and warm seasons, only for small traffic volumes (see Figure 7(b)). For volumes higher than 200–300 vehicles per hour, for all seasons the estimated spline is close to the zero line although it is significant.

The seasonal analysis of the meteorological covariates allows us to highlight the sensible differences that characterize the role of a variable in more homogeneous environmental conditions. In fact fitting the model M_1 to any single season allows us to separate the effect of the meteorological variation during the cold seasons or the warm seasons, when pollutants could behave very differently in relation to the meteorological variables. These differences are particularly evident for temperature, the solar radiation, the wind speed (with special attention for the delayed effects), and pressure.

Starting with *temperature* (Figure 7(c)), we can see that during the warm seasons its contribution to NO_2 concentration is low (anyway NO_2 concentration has low values in these seasons). Instead during winter and fall seasons, we can observe that at low temperatures the average log

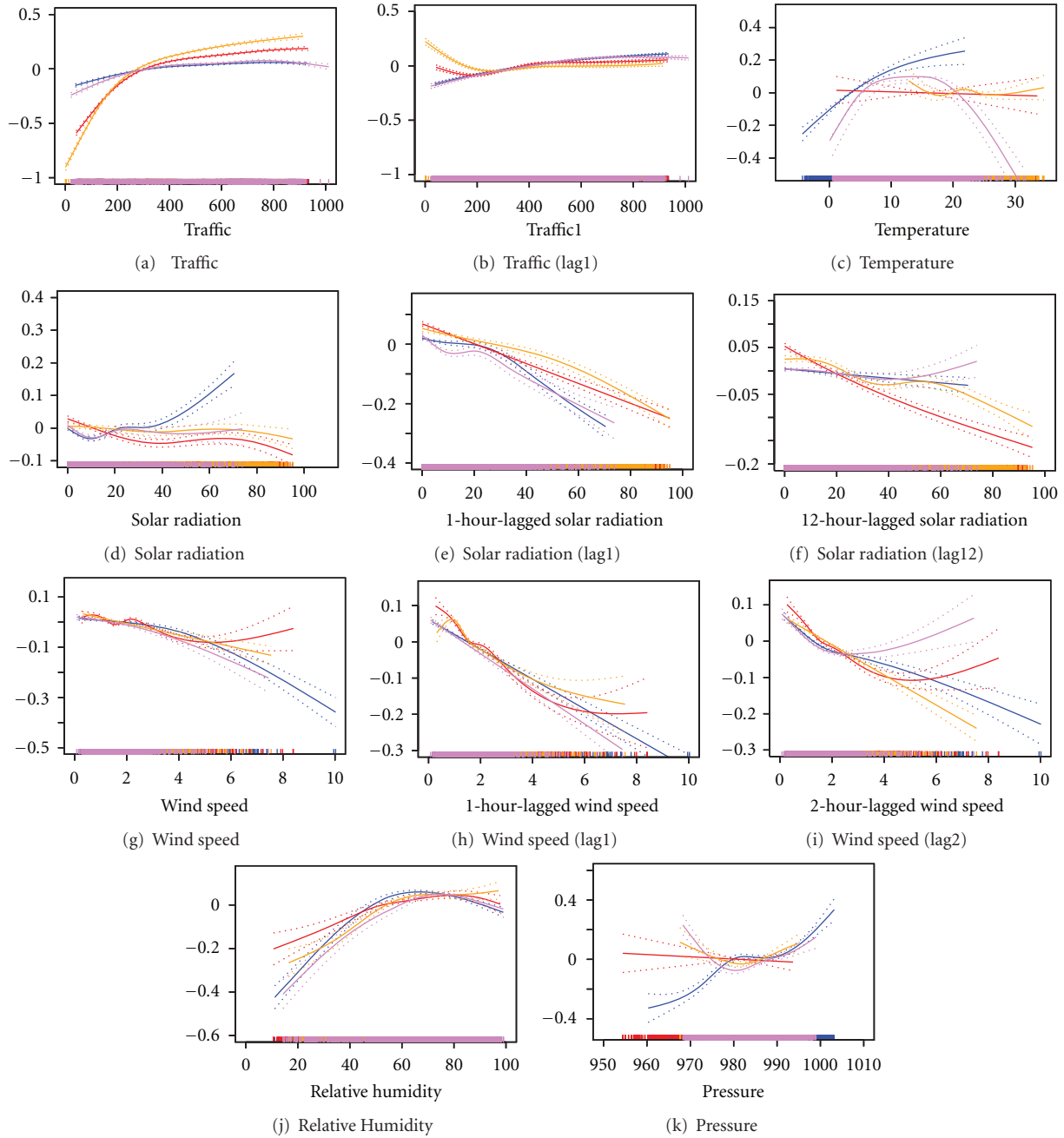


FIGURE 7: Estimated effects of traffic and meteorological variables for NO₂ during different seasons. Blue is Winter, red is Spring, orange is Summer, and violet is Fall.

concentration tends to increase with temperature until 10 degree Celsius. After that value, it slightly decreases at higher temperatures during the autumn, while it keeps to increase during the winter. In this last case, the model shows the same result observed in other studies (e.g., [16, 17]) and it could be explained with the activation of photochemical reactions due to higher radiation (coherently the same situation is presented by the partial effect due to direct solar radiation in Figure 7(d)). Temperature effect during the autumn shows two apparently contrasting behaviours: the concentration

increases for low values of temperature and it decreases for high values. This result can be interpreted by considering that the autumn is a transition season moving from summer to winter, so that for a period the partial effect is similar to the winter one and for another period to the summer one.

The estimated *solar radiation* splines shown in Figures 7(d)–7(f) suggest that the partial effect of this variable has generally a reducing effect on the average log concentration of nitrogen dioxide. The effect is stronger one hour after the exposition and also 12 hours after during the warm

seasons; this persistency is likely explained by the fact that a strong radiation tends to delay a new rise in pollution concentration. The steep increase of the direct radiation effect during wintertime can be connected with the activation of photochemical reactions due to higher radiation that acts on a large amount of pollutant generally present in the winter metropolitan atmosphere such as nitric monoxide.

Observing the estimated *wind speed* splines for different seasons and lags in Figures 7(g)–7(i), we can see that wind speed generally keeps its important effect in reducing NO₂ concentrations, considerably when it increases: a strong wind may influence the pollution for many hours. In particular, during winter and summer the decreasing effect is clear and it starts even at small wind speed intensity; moreover, during the winter we observe the higher wind intensities. In the other two intermediate seasons the wind effect is smaller and for the 2 hours lagged variable seems to have a positive effect that probably needs further analysis.

The partial effect of *relative humidity* (Figure 7(j)) maintains a very similar behaviour during all the seasons that looks like the observed one for the global model. In this case we can highlight that higher values of humidity cause an increase in the average NO₂ log concentration.

As for the *pressure* (Figure 7(k)) we can see that the main effects are visible during the cold season, coherently with the fact that the concentration increases when the pressure increases too. Instead, the positive effect of low pressure values during the fall season needs further study to be explained.

3.2. Modeling Daily PM₁₀. In order to understand the extent to which the behavior of daily PM₁₀ (after the logarithm transformation) depends on traffic intensity, we began with a flexible model that incorporates splines to capture the effects of average daily traffic, as well as the average daily traffic during the previous day, in addition to meteorological predictors. The initial model was thus as follows:

$$\begin{aligned}
 M_2: \mu_t = & \alpha + s(t, \lambda_t) + \vec{\beta}(\text{DoW}) \\
 & + s(\text{tr}, \lambda_C) + s(\text{wsp}, \lambda_C) \\
 & + s(\text{lag}(\text{wsp}, 1), \lambda_C) + s(\text{lag}(\text{wsp}, 2), \lambda_C) \\
 & + s(\text{rh}, \lambda_C) + s(\text{press}, \lambda_C),
 \end{aligned} \tag{3}$$

where μ_t is the average daily log PM₁₀ at day t , and tr is the total traffic during day t in the city of Turin. Furthermore, wsp denotes average daily wind speed, $\text{lag}(\text{wsp}, 1)$ and $\text{lag}(\text{wsp}, 2)$ are the lagged versions of the average daily wind speed from one and two days prior to day t , respectively. These lagged variables have been chosen based on their high pairwise correlation with the pollutant. Similarly, rh and press denote the average daily relative humidity and pressure, respectively. Note that given that PM₁₀ data are daily, we will use daily averages for all the covariates in the model aside from traffic.

However, upon examination of the results from the above model, we see that the estimated effects of traffic appear nearly linear (see Figure 8). In fact, the role of traffic appears

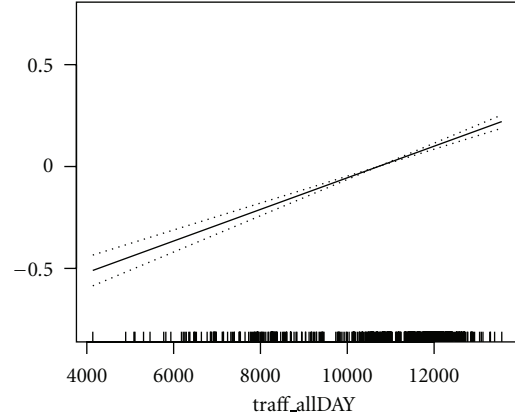


FIGURE 8: Estimated effects of traffic for PM₁₀ (model M_2).

TABLE 4: Estimated coefficients and standard errors of the parametric part of the additive predictors for PM₁₀ (bold indicates 5% significance).

	PM	
	Est.	Std. Er.
(Intercept)	3.05	0.100
Daily traffic	0.00008	0.00001
Monday	-0.01	0.059
Tuesday	0.09	0.062
Wednesday	0.11	0.060
Thursday	0.08	0.060
Friday	0.05	0.066
Saturday	0.06	0.053

to be purely linear, without any saturation effects like those observed in the case of NO₂. This is expected to some degree, since particulate matter can be produced in large quantities through tire ablation and black carbon smoke, implying that increased traffic leads to increased PM₁₀ production. Motivated by this observation, we opted to also fit a simpler model with a simple linear effects of traffic and lagged traffic. Thus, the proposed simpler model is as follows:

$$\begin{aligned}
 M_3: \mu_t = & \alpha + s(t, \lambda_t) + \vec{\beta}(\text{DoW}) \\
 & + \gamma \text{tr} + s(\text{wsp}, \lambda_C) \\
 & + s(\text{lag}(\text{wsp}, 1), \lambda_C) + s(\text{lag}(\text{wsp}, 2), \lambda_C) \\
 & + s(\text{rh}, \lambda_C) + s(\text{press}, \lambda_C).
 \end{aligned} \tag{4}$$

The simpler model's BIC was almost identical to the BIC of the model with the splines, motivating us to present the estimated linear effects of the simpler model only in Table 4. The visual results are shown in Figure 9. We can observe that the coefficient of the traffic variable is positive, indicating a positive linear relationship between traffic and daily PM₁₀ log concentration.

Figure 9(a) shows a strong relative increase of PM₁₀ during wintertime, reflecting confounders like social (e.g., heating) or meteorological (e.g., boundary layer thickness

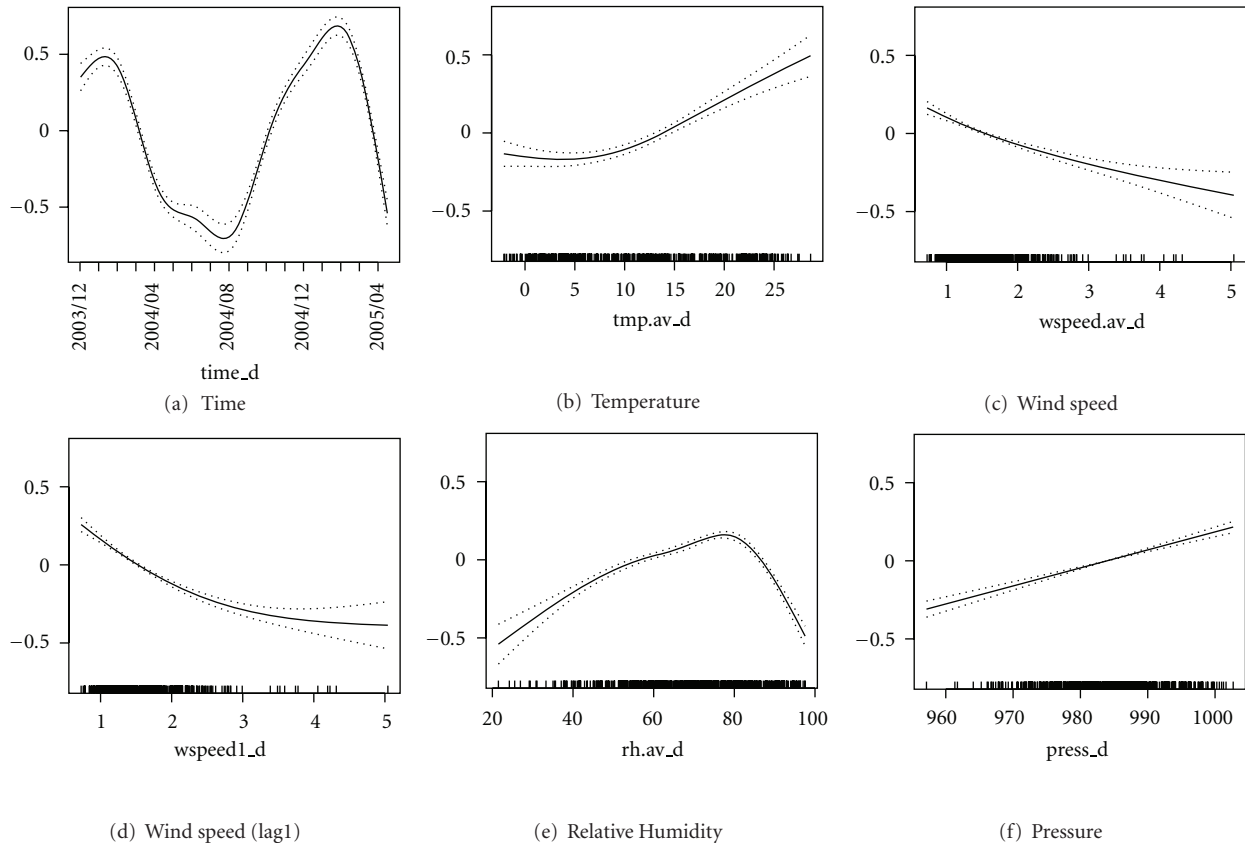


FIGURE 9: Estimated effects of meteorological variables for PM_{10} .

variation) processes. Increase in temperature seems to be associated with an almost linear increase in average PM_{10} log concentration (Figure 9(b)). Increase in wind speed is related to reduced PM_{10} concentration, both for current time (Figure 9(c)) and its one-day-lagged values (Figure 9(d)). Increase in relative humidity is associated with a reduction in average PM_{10} log concentration at high values and with an increase in average PM_{10} log concentration at low values (Figure 9(e)). This could be due to rain (high values) or strong wind (low values), although at low values the data are more sparse. Finally an increase in pressure is related in an almost linear way to the increase in the average PM_{10} log concentration (Figure 9(f)).

The linear effects of traffic are good news from the policy point of view, implying that simpler models with linear effects of traffic could be used to replace the more complex ones. In fact, the estimated linear effect of 0.00008 per day implies that a reduction in traffic of 1,300 cars each day would lead to an approximate reduction in average concentration of Turin’s PM_{10} of about 10%. Note that 1,300 cars are approximately 10% of the average daily traffic in Turin, so effectively a reduction of 10% in traffic intensity would result in the reduction of 10% in Turin’s PM_{10} . This is a remarkable result, which could allow for simple and fast implementation and evaluations of policy decisions.

3.2.1. Modeling PM_{10} Separately by Seasons. The analysis stratified by season for log concentration of PM_{10} shows

similar predictor effects and reveals few difference between seasons, as shown in Figure 10. Most predictors show similar behavior across the four seasons. The only exception is summer, with several notable differences. Traffic seems to have a roughly linear effect in all seasons, except in the summer where a slight saturation effect is observed at very high values. Analogously, relative humidity effects are similar in all seasons except for the summer: in all seasons, PM_{10} log-concentration relationship to relative humidity seems quadratic, rising at first and then declining after a certain threshold is passed. This is expected, as relative humidity would be related to precipitation that tends to happen at high relative humidity values and has suppressing effect on particulate matter in the air. However, in the summer, relative humidity seems to have a purely linear effect on PM_{10} log concentration. This too is expected, as relative humidity in the summer tends not to be related to rain but to “hot and humid” days with little wind.

3.3. Forecasting for Traffic Regulation Assessment. Traffic regulation is one of the most important action to reduce the pollution concentrations. The city of Turin lays in one of the most polluted area of Europe. This condition is basically due to the orographic shape of the plain surrounded by mountains and the high density of industry and population. A very common traffic regulation relies on imposing a general reduction of the number of vehicles selecting them by the European pollution category (Euro stages) or by the numbers of the plate (even or odd for “alternate plates”).

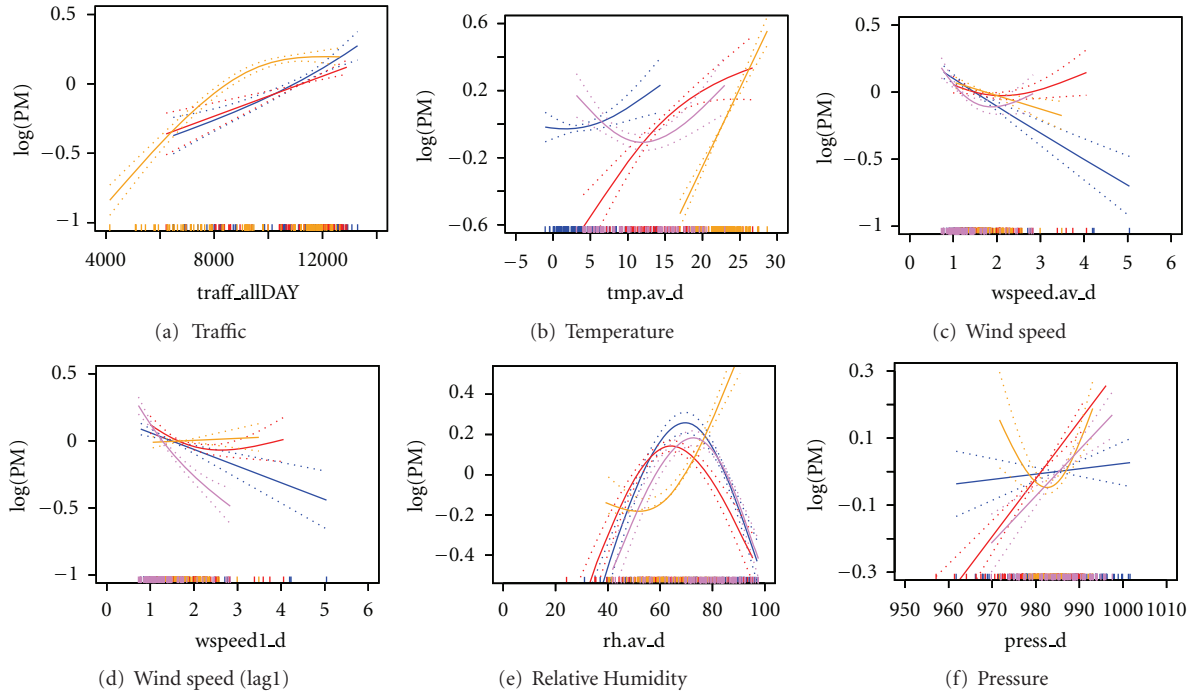


FIGURE 10: Estimated effects of meteorological variables for PM_{10} , by season. Blue is Winter, red is Spring, orange is Summer, and violet is Fall.

In this section we assess the effect of a traffic regulation scenario using GAM prediction. We consider the model M_1 for NO_2 concentration that was fitted on the whole available data (starting on the 19th December 2003 and ending the 27th April 2005 that is about 11904 hours) and was found to generally fit well, with $R^2 = 0.83$ (Section 3.1). To make prediction on a new dataset, we consider a week during the winter time starting on Tuesday 18th January 2005 and ending on Monday 24th January 2005; we choose this part of the week in order to check possible delayed effect on traffic regulation on the next days. To have a new scenario, we choose to evaluate the type of traffic regulation common in Turin, which controls the movement of cars based on whether the last number of their license plate is odd or even. This policy is generally applied during the most polluted days of the week (i.e., Wednesday and Thursday) and is meant to reduce the circulation of around 50% of the vehicles. Figure 11(a) illustrates what a 50% reduction on two days would look like in the week January 18–24, 2005. When we predict NO_2 concentration with the original dataset, we observe in Figure 11(b) that our GAM model is able to describe the variation of the concentration of NO_2 (blue line) with respect of the original data (black line), generally following the hourly variation of the measured concentration. Then we use the “new” traffic values, under the reduction scenario, and it is clearly possible to see the short-term effect of this reduction during the two days in the red line in Figure 11. The numerical impact in reduction of pollution concentration, on a weekly basis, is around the 6% of NO_2 , according to the prediction of the model. During the two regulated days alone, the reduction is around 12%.

4. Conclusions

In this paper we have presented a study of air pollution in the city of Turin through the framework of generalized additive models. We have used the generalized additive models (GAMs) to model the behavior of two species of pollutants (NO_2 and PM_{10}) averaged over the city of Turin as a function of traffic, while controlling for the main meteorological variables as well as an unobserved confounding process. GAMs allow flexible modeling of pollution processes which has traditionally been done in a classical style of differential-equation-based models. In our study, the GAMs have been able to capture the relationship between pollutants and predictors flexibly, using semiparametric components modeled with penalized cubic regression splines, where the penalty (the smoothing parameter) is estimated using generalized cross validation (GCV). One of the main advantages of GAM is perhaps their ability to extend this flexibility to unobserved confounders, by allowing “time” to act as a proxy for them. Including a smoothly varying function of time to capture the behavior of relatively slowly varying unobserved confounders helps address the bias in estimates of the effects of interest, such as traffic.

We have used the Bayesian Information Criterion (BIC) to select the optimal number of knots for the splines and choose among several different models. The results show that for NO_2 , traffic, in its log-transformed form, is adequate for explaining the log-pollution concentration, while for PM_{10} traffic, in its linear form, turns out to be adequate. We also estimate the relationships between other covariates and the pollutants. An increase in traffic volume is clearly associated

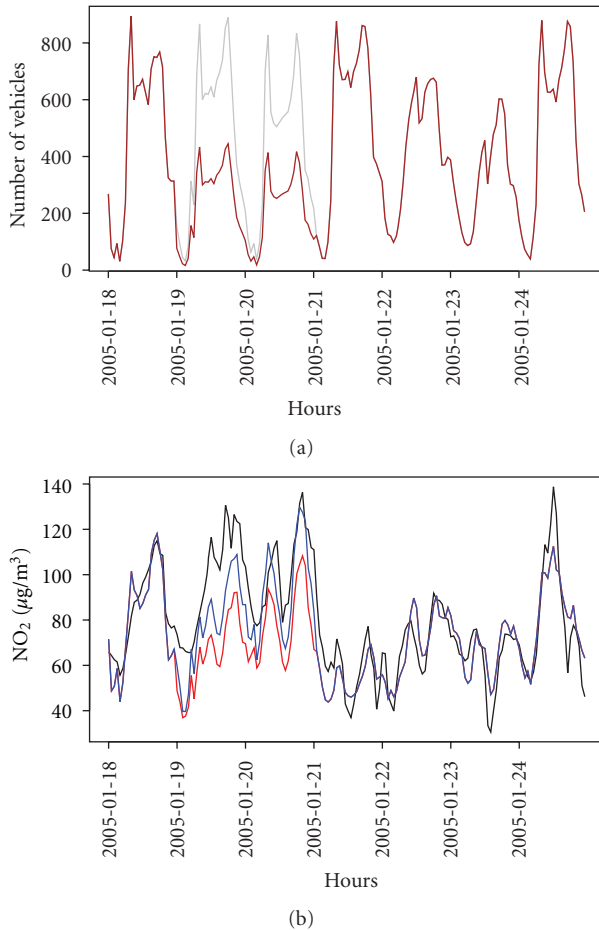


FIGURE 11: (a) Traffic volume in January, 18–24, 2005; original data in grey, policy scenario traffic volume in red. (b) NO₂ concentration in January, 18–24, 2005; measured data in black, predicted values without (blue) and with (red) traffic policy scenario.

with increase in the pollutants adjusted for other factors, while temperature, solar radiation, and wind speed have positive partial effects in the pollution reduction, especially in the winter. The nonlinearities found in other estimated effects confirm that the generalized additive models are a useful framework to estimate and interpret the relations between pollution, traffic, and meteorology.

A seasonal analysis provides a detailed description of the predictors' partial effects, where traffic, temperature, pressure, and solar radiation show the more interesting variations. In particular with respect to traffic that is the covariate that can be controlled, our result shows that the variation of the number of vehicles during the cold seasons (and especially in winter) is less effective than within the warm ones. This behavior can be explained by the general higher presence of pollution during cold seasons and by the presence of other sources of emissions, particularly building heaters that during warm seasons disappear. Hence during the winter, an hypothetical traffic regulation certainly helps to reduce the pollution concentration, but an effective reduction of pollution can be reached only working on all the other sources.

Although forecasting in near future time is possible, we suggest to use our proposed models to evaluate traffic reduction policies by predicting pollutant concentrations with policy-modified traffic data, taking into account the meteorological information.

Moreover, during the last year in Turin a progressive increase of the district heating has been undertaken that should reduce the heating-related pollution problem aforementioned. When new data will be available, the models we propose can be useful to obtain new insights and evaluate the effect of this intervention in the city.

Acknowledgments

The authors would like to thank Regione Piemonte and ARPA Piemonte that provided support and data for Meteorological and Chemical variables. Moreover, the authors thank 5T s.r.l. that provided us support and free access to the traffic database making possible this research. Finally, the authors extend their thanks to ICER and Dr. Enrico Colombatto for providing an environment that helped develop the key ideas for their collaboration. The work was partially supported by Regione Piemonte and ICER.

References

- [1] A. G. Barnett, G. M. Williams, J. Schwartz et al., "Air pollution and child respiratory health: a case-crossover study in Australia and New Zealand," *American Journal of Respiratory and Critical Care Medicine*, vol. 171, no. 11, pp. 1272–1278, 2005.
- [2] M. L. Bell, A. McDermott, S. L. Zeger, J. M. Samet, and F. Dominici, "Ozone and short-term mortality in 95 US urban communities, 1987–2000," *Journal of the American Medical Association*, vol. 292, no. 19, pp. 2372–2378, 2004.
- [3] J. M. Samet, F. Dominici, F. C. Curriero, I. Coursac, and S. L. Zeger, "Fine particulate air pollution and mortality in 20 U.S. cities, 1987–1994," *New England Journal of Medicine*, vol. 343, no. 24, pp. 1742–1749, 2000.
- [4] B. Mlgaard, T. Hussein, J. Corander, and K. Hämeri, "Forecasting size-fractionated particle number concentrations in the urban atmosphere," *Atmospheric Environment*, vol. 46, pp. 155–163, 2012.
- [5] S. Clifford, S. Low Choy, T. Hussein, K. Mengersen, and L. Morawska, "Using the Generalised Additive Model to model the particle number count of ultrafine particles," *Atmospheric Environment*, vol. 45, no. 32, pp. 5934–5945, 2011.
- [6] Dir96/62/EC, "Council directive n. 62 of 27 September 1996 on ambient air quality assessment and management," 1996.
- [7] Dir99/30/EC, "Council directive n. 30 of 22 April 1999 relating to limit values for sulphur dioxide, nitrogen dioxide and oxides of nitrogen, particulate matter and lead in ambient air," 1999.
- [8] Dir00/69/EC, "Council directive n. 69 of 16 November 2000 relating to limit values for benzene and carbon monoxide in ambient air," 2000.
- [9] Dir02/3/EC, "Council directive n. 3 of 12 February 2002 relating to ozone in ambient air," 2002.
- [10] Dir50/08/EC, "Council directive n. 50 of 21 May 2008 on ambient air quality and cleaner air for Europe," 2008.
- [11] P. Bertaccini, M. Cameletti, and A. Fassó, "Urban mobility and atmospheric pollution within the Torino metropolitan area,"

- in *Proceedings of the Atti della Conferenza (SIS '07)*, pp. 607–608, 2007.
- [12] A. Fassó, M. Cameletti, and P. Bertaccini, “Uncertainty decomposition in environmental modelling and mapping,” in *Proceedings of the Summer Computer Simulation Conference (SCSC '07)*, pp. 867–874, 2007.
- [13] Y. Kim and J. M. Guldmann, “Impact of traffic flows and wind directions on air pollution concentrations in Seoul, Korea,” *Atmospheric Environment*, vol. 45, no. 16, pp. 2803–2810, 2011.
- [14] T. J. Hastie and R. Tibshirani, *Generalized Additive Models*, Chapman & Hall, London, UK, 1990.
- [15] J. Schwartz, “Non parametric smoothing in the analysis of air pollution and respiratory illness,” *Canadian Journal of Statistics*, vol. 22, no. 4, pp. 471–488, 1994.
- [16] D. C. Carslaw, S. D. Beevers, and J. E. Tate, “Modelling and assessing trends in traffic-related emissions using a generalised additive modelling approach,” *Atmospheric Environment*, vol. 41, no. 26, pp. 5289–5299, 2007.
- [17] M. Aldrin and I. Hobæk Haff, “Generalised additive modelling of air pollution, traffic volume and meteorology,” *Atmospheric Environment*, vol. 39, no. 11, pp. 2145–2155, 2005.
- [18] M. Aldrin, I. Hobæk Haff, and P. Rosland, “The effect of salting with magnesium chloride on the concentration of particulate matter in a road tunnel,” *Atmospheric Environment*, vol. 42, no. 8, pp. 1762–1776, 2008.
- [19] P. Bertaccini, V. Dukic, and R. Ignaccolo, “Modelling traffic related air pollution in Torino with generalized additive models,” in *Proceedings of the 4th International Workshop on Spatio-Temporal Modelling (METMA '08)*, pp. 123–128, Alghero, Italy, 2008.
- [20] P. Bertaccini, *Methods and models for vehicular traffic-related atmospheric pollution in the turin urban area [Ph.D. thesis]*, Università degli Studi di Torino, 2009.
- [21] P. Kronborg and F. Davidsson, *ImprovementS for a Scandinavian Spoturban Traffic Signal Control SyStem*, TFK—Transport Research Institute, Stockholm, Sweden, 2000.
- [22] K. Wood, *Urban Traffic Control, Systems Review*, PR41, Transport Research Laboratory, Crowthorne, UK, 1993.
- [23] G. Schwartz, “Estimating the dimension of a model,” *The Annals of Statistics*, vol. 6, no. 2, pp. 461–464, 1978.
- [24] H. Akaike, “A new look at the Bayes procedure,” *Biometrika*, vol. 65, no. 1, pp. 53–59, 1978.
- [25] R Development Core Team, *R: A Language And Environment for Statistical Computing*, R Foundation for Statistical Computing, Vienna, Austria, 2012, <http://www.r-project.org/>.
- [26] S. N. Wood, “mgcv: GAMs with GCV/AIC/REML Smoothness Estimation and GAMMs by PQL,” R package version 1.7-13, 2012.
- [27] S. N. Wood, *Generalized Additive Models: An Introduction With R*, Chapman & Hall, London, UK; CRC Press, Boca Raton, Fla, USA, 2006.

Research Article

Temporal Forecasting with a Bayesian Spatial Predictor: Application to Ozone

Yiping Dou,¹ Nhu D. Le,² and James V. Zidek³

¹Finance, eBay Inc., San Jose, CA 95125, USA

²BC Cancer Agency Research Center, Vancouver, BC, Canada V5Z 4E6

³Department of Statistics, University of British Columbia, Vancouver, BC, Canada V6T 1Z2

Correspondence should be addressed to James V. Zidek, jim@stat.ubc.ca

Received 14 January 2012; Revised 24 April 2012; Accepted 27 April 2012

Academic Editor: Tareq Hussein

Copyright © 2012 Yiping Dou et al. This is an open access article distributed under the Creative Commons Attribution License, which permits unrestricted use, distribution, and reproduction in any medium, provided the original work is properly cited.

This paper develops and empirically compares two Bayesian and empirical Bayes space-time approaches for forecasting next-day hourly ground-level ozone concentrations. The comparison involves the Chicago area in the summer of 2000 and measurements from fourteen monitors as reported in the EPA's AQS database. One of these approaches adapts a multivariate method originally designed for spatial prediction. The second is based on a state-space modeling approach originally developed and used in a case study involving one week in Mexico City with ten monitoring sites. The first method proves superior to the second in the Chicago Case Study, judged by several criteria, notably root mean square predictive accuracy, computing times, and calibration of 95% predictive intervals.

1. Introduction

This paper compares two methods for temporally forecasting next-day hourly ground-level ozone concentrations over spatial regions. Software for implementing both methods along with demo files can be downloaded from <http://enviro.stat.ubc.ca/>. The paper focuses on a case study involving Chicago during the summer of 2000. The methods can be used to forecast the maximum eight-hour average ozone concentration, which is reported for many urban areas. For example, on June 27, 2009 the AIRNow website forecasts a maximum for Chicago of between 0 and 50 ppb, rating that as "Good." In contrast, for that day in one part of Los Angeles, the rating was "Unhealthy for sensitive groups," meaning a forecast maximum of between 101 and 150 ppb.

These forecasts are needed to forewarn susceptible groups of high ozone concentrations that are associated with acute health effects. Such effects are well documented in the air quality criterion document (Ozone [1]). See <http://oaspub.epa.gov/eims/eimsapi.dispdetail?deid=149923>, the basis of the recommendations made in 2007 to the US Environment Protection Agency by its Clean Air Scientific Advisory Committee for Ozone, in which the third author served. In fact,

the accumulated body of evidence was so strong that the committee recommended strengthening the air quality standards for this criterion pollutant to meet the requirements of the US Clean Air Act. In particular, the evidence pointed to a strong association between morbidity as well as reduced lung function and high levels of ground-level ozone concentrations. This points to a need for enhanced near-term forecasting methods.

One general method for making such forecasts relies on the fusion of measured hourly ozone concentration values and simulated values obtained from chemical transport models (CTMs) such as CMAQ. Two papers [2, 3] develop methods for doing this, albeit by different approaches unrelated to those in this paper. In future work, all these methods should be compared in domains where CTM data are available. Even without that hypothetical comparison, those in this paper have the advantage of being available in domains where they are not. These Bayes-empirical Bayes methods offer the flexibility needed to characterize environmental space-time processes, while fully representing the various kinds of uncertainty involved in their construction. Both have been developed for and successfully used to model hourly ozone air pollution concentrations in other contexts.

The first method in this paper denoted by M1 adapts a multivariate method developed for modeling space-time fields [4–7]. A univariate version of that method for hourly ozone concentrations is the subject of a companionable paper [8], which compares it with a state space model but for spatial prediction, not temporal forecasting, and it does so in a different geographical region. The goal there is mapping the ozone field for another requirement of the US Clean Air Act of 1970, namely, the protection of human welfare including such things as crop yields. M1 needs some new theory, which is presented in the sequel along with a demonstration on how it may be applied.

The second method denoted by M2 uses a method originally developed for modeling hourly ozone concentrations in Mexico City [9]. That method and the models on which it is based along with the computational algorithms used to implement it seem to have been quite successful in that application. Moreover, even though it was developed for use in Mexico City for one specific week, a strong *prima facie* case can be made for its applicability in other weeks and jurisdictions and that is why we assess the performance of that method here. Much recent work has been done in modeling random space-time pollution fields [10–12]. As one of the photo-oxidants, ozone is produced in the same way in all temporal and spatial domains by a complex interaction of oxides of nitrogen (NO_x) with volatile organic compounds (VOCs) in the presence of heat and sunlight. In most modern urban environments such as Chicago and Mexico City, vehicle emissions are a prime source of the NO_x and VOCs [1]. Furthermore the *prima facie* case is supported by an exploratory data analysis that shows very similar daily cycles in our domain as those observed in the Mexico City application. This led us to match, to the greatest possible extent [8], the method used there in our adaptation of it, and no originality is claimed for it.

The main finding in this paper is that in the case study M1 outperforms M2 in a number of ways. First is its computational efficiency. To run the M2 approach, it often took about a week or so to get the results, while M1 only took about ten to twelve hours at the same Linux server. Thus, M2 would not be suitable for making 24 ahead forecasts, while M1 running on a faster processor could be used for that purpose. We also found that M1 produced more accurate forecasts than M2, as measured by their root-mean-squared-prediction errors. Moreover, M1’s predictive error bands proved to be better calibrated. In other space-time domains, a similar assessment would have to be made to select a forecasting procedure, and M2 may be superior in some. Overall, we believe that the value of this paper lies in the guidance on how that assessment could be made and the source of software that can be used for it.

The layout of this paper will now be described. Section 2 presents both approaches to forecasting hourly ozone concentrations. Section 2.1 introduces M1. Its forecasting (posterior) distribution is developed, and the corresponding pointwise predictive intervals at each gauged site constructed. Section 2.1 also extends the results to forecasting r -step-ahead responses for any $r \in \mathcal{N}$. Section 2.2 reviews M2. Section 3 implements these two methods in a case study

involving Chicago and data from the US EPA’s AQS air quality database. Section 3.1 presents and compares the results for one-day-ahead predictions. Finally, Section 4 summarizes these results and gives our conclusions.

2. Methodology

This section presents our two temporal forecasting approaches. Although both are general and can be used in other contexts, we develop them as methods for forecasting an hourly response tomorrow given data up to today. The measured value of the response is available and serves as a “test value” at each of g monitoring sites for a comparative assessment of the two forecasted methods.

2.1. Method M1

2.1.1. Basic Theory. The general approach [7], on which M1 is based, assumes a multivariate space-time field of p -dimensional random response vectors indexed by their locations, a finite number of sites in a specified geographical domain. These sites need not lie on a lattice.

The general theory involves a geographical region that includes g monitored (i.e., gauged) sites and u unmonitored (i.e., ungauged) sites. Although this paper requires only the part of that theory for those that are monitored, we state it in generalable to link this paper to its companion publication [8]. The p dimensional response vectors at these sites for times $t = 1, \dots, n$ are combined in the response matrix $\mathbf{Y} : n \times (u + g)p$. This matrix can be partitioned as $(\mathbf{Y}^{[u]}, \mathbf{Y}^{[g]})$, where $\mathbf{Y}^{[u]} : n \times up$ contains the response vectors at the ungauged sites and $\mathbf{Y}^{[g]} : n \times gp$, those at the gauged sites. The theory posits ([7], p. 145–146) that

$$\begin{aligned} \mathbf{Y} \mid \beta, \Sigma &\sim N(\mathbf{Z}\beta, \mathbf{I}_n \otimes \Sigma), \\ \beta \mid \Sigma, \beta_0, \mathbf{F} &\sim N(\beta_0, \mathbf{F}^{-1} \otimes \Sigma), \\ \Sigma &\sim \text{GIW}(\Psi, \delta), \end{aligned} \quad (1)$$

where $\mathbf{Z} : n \times l$ denotes the non-site-specific covariates (their site-specific counterparts could be included in the response vectors); $\beta : l \times (u + g)p$ denotes the matrix of site-specific random covariate coefficients; $\Sigma : (u + g)p \times (u + g)p$ denotes the covariance matrix among the responses at any given time point. The hyperparameters for this hierarchical Bayes model are $\beta_0, \mathbf{F}, \delta$, and Ψ , with \mathbf{F} representing the variance component of β between its l rows. Here, GIW denotes the Generalized Inverted Wishart distribution, a conjugate prior for normal matrix distributions. Separability of the hypercovariant matrices for both the response and random coefficient matrices is assumed for computational simplicity. Invoking Box’s celebrated dictum that all models are wrong, we defend this assumption by the good performance of the resulting method as seen in the empirical assessment provided in the sequel.

Validating the modeling assumptions above will usually require a transformation of the random responses, a square root transformation in this paper’s case study. Then systematic components such as the temporal trend over the whole

regions will need to be removed. These can be accurately inferred from the typically large dataset formed by aggregating the data over all sites and times. Finally, something needs to be done to eliminate autocorrelation in the temporal sequence of responses. For example, the temporal series can often be filtered using a regional time series model without site-specific parameters. However, our relative abundance of data leads us here to a different approach described in detail in the next subsection, that splits the transformed, detrended residuals into separate, disjoint subsequences of responses, which are separated widely enough in time as to be uncorrelated and hence independent under our Gaussian sampling model. In our experience, the residuals obtained after these steps have been taken usually satisfy the model assumptions above, and these comprise the response vectors in M1. So the model above can then be applied to each subsequence and type II maximum likelihood estimators found for the hyperparameters. These can subsequently be averaged across the subsequences to get an overall estimate. While this approach would be less efficient than a full-data approach under a correctly specified model, it avoids the risk of model misspecification in complex situations like that of the case study. The forecasting model developed below can then be applied, and the preliminary steps above reversed, to get the forecasts back on the scale of the raw data.

To elaborate on our distributional assumptions, the GIW prior for

$$\Sigma = \begin{pmatrix} \Sigma^{[g,g]} & \Sigma^{[g,u]} \\ \Sigma^{[u,g]} & \Sigma^{[u,u]} \end{pmatrix} : \begin{pmatrix} gp \times gp & gp \times up \\ up \times gp & up \times up \end{pmatrix} \quad (2)$$

can be defined, through the Bartlett decomposition, as follows:

$$\begin{aligned} \Sigma^{[g,g]} &\sim \text{IW}(\Lambda_1, \delta_1), \\ \Gamma^{[u]} &\sim \text{IW}(\Lambda_0, \delta_0), \\ \tau^{[u]} | \Gamma^{[u]} &\sim N(\tau_{00}, \mathbf{H}_0 \otimes \Gamma^{[u]}), \end{aligned} \quad (3)$$

where $\Gamma^{[u]} = \Sigma^{[u,g]} = \Sigma^{[u,u]} - \Sigma^{[u,g]}(\Sigma^{[g,g]})^{-1}\Sigma^{[g,u]}$, and $\tau^{[u]} = (\Sigma^{[g,g]})^{-1}\Sigma^{[g,u]}$. Note that $\Sigma^{[g,g]}$ has an inverted Wishart distribution with hyperparameters (Λ_1, δ_1) ; the matrix τ_{00} is the hypermean of $\tau^{[u]}$, and the matrix \mathbf{H}_0 gives the covariance between the rows of $\tau^{[u]}$. Denote the set of hyperparameters as $\mathcal{H} = \{\mathbf{F}, \beta_0, \Omega, \Lambda_1, \delta_1, \Lambda_0, \delta_0, \tau_{00}, \mathbf{H}_0\}$.

Given the observations at the gauged sites (i.e., $\mathbf{Y}^{[g]}$), the predictive distribution of $\mathbf{Y}^{[u]}$ is completely determined, it is the distribution required in our companionable paper on spatial prediction [8]. Furthermore given partially observed responses at gauged sites, the predictive distribution of the missing responses at gauged sites given these observations can be derived after the hyperparameters have been estimated by an empirical Bayes approach ([7], p. 300–303), and that is how the theory is used in this paper.

Deriving that forecasting model requires a general result that concerns a sequence of n response vectors of which $n-w$ are observed, and w lies in the future. Then with the superscripts “ m ” and “ o ,” respectively, standing for “missing” and “observed,” we may further partition the random response

matrix already partitioned above, as $\mathbf{Y}^{[g]} = (\mathbf{Y}^{[g^m]}, \mathbf{Y}^{[g^o]})' : n \times gp$ with $\mathbf{Y}^{[g^m]} : w \times gp$ and $\mathbf{Y}^{[g^o]} : (n-w) \times gp$. Forecasting requires the predictive posterior distribution of $(\mathbf{Y}^{[g^m]} | \mathbf{Y}^{[g^o]}, \mathcal{H})$ given in the following result ([7], p. 160–161).

Theorem 1. *Let*

$$\begin{aligned} \mathbf{Z}\beta_0^{[g]} &= \begin{pmatrix} \mu_{(1)} \\ \mu_{(2)} \end{pmatrix} : \begin{pmatrix} w \times gp \\ (n-w) \times gp \end{pmatrix}, \\ \mathbf{I}_n + \mathbf{Z}\mathbf{F}^{-1}\mathbf{Z}' &= \begin{pmatrix} \mathbf{A}_{11} & \mathbf{A}_{12} \\ \mathbf{A}_{21} & \mathbf{A}_{22} \end{pmatrix} : \begin{pmatrix} w \times w & w \times (n-w) \\ (n-w) \times w & (n-w) \times (n-w) \end{pmatrix}. \end{aligned} \quad (4)$$

Conditional on the hyperparameters \mathcal{H} , the marginal posterior distribution is a matrix t distribution:

$$\mathbf{Y}^{[g^m]} | \mathbf{Y}^{[g^o]}, \mathcal{H} \sim t_{w \times gp}(\mu_{(u|g)}, \Phi_{(u|g)} \otimes \Psi_{(u|g)}, \delta_{(u|g)}), \quad (5)$$

where

$$\begin{aligned} \mu_{(u|g)} &= \mu_{(1)} + \mathbf{A}_{12}\mathbf{A}_{22}^{-1}(\mathbf{Y}^{[g^o]} - \mu_{(2)}): w \times gp, \\ \Phi_{(u|g)} &= \frac{\delta_1 - gp + 1}{\delta_1 - gp + n - w + 1} \mathbf{A}_{11 \circ 2} : w \times w, \\ \Psi_{(u|g)} &= \frac{1}{\delta_1 - gp + 1} \left\{ \Psi_{gg} + (\mathbf{Y}^{[g^o]} - \mu_{(2)})' \right. \\ &\quad \left. \mathbf{A}_{22}^{-1}(\mathbf{Y}^{[g^o]} - \mu_{(2)}) \right\} : gp \times gp, \end{aligned} \quad (6)$$

$$\delta_{(u|g)} = \delta_1 - gp + n - w + 1,$$

where $\mathbf{A}_{11 \circ 2} = \mathbf{A}_{11} - \mathbf{A}_{12}\mathbf{A}_{22}^{-1}\mathbf{A}_{21}$, and Ψ_{gg} is assumed to be $\Lambda_1 \otimes \Omega$, denoting spatial and between hour correlations, respectively.

Remark 2. This theorem gives the joint predictive distribution for w future response vectors given $(n-w)$ observed responses. As coordinates of those future vector are observed, this distribution yields in turn the conditional predictive distribution for the unobserved coordinate responses, That is how the theorem is applied in the next section.

2.1.2. One-Day-Ahead Forecasts. For expository simplicity, we describe the general method M1 in terms of the goal of forecasting ozone concentrations at a specific hour on Day 121 and each of $g = 14$ monitoring sites based on data collected at those sites during the preceding days, that being the objective in the case study described in the next section. However, we emphasize that M1 is generally applicable to other days and geographical domains with appropriate modifications. In fact, the approach can be adapted for use with other environmental processes. With that caveat, we now describe M1 in this subsection. Note that in our description, hour 1 refers to the period between midnight and 1 AM and so on.

To begin, we follow the standard practice of transforming the hourly data by taking their square roots to achieve a more nearly Gaussian data distribution [13]. Hereafter these transformed values will be our “responses.” M1 then partitions the sequence of responses into blocs of $p = 24$ hours each. For $k < 24$ (hereafter referred to as Case 2), the last bloc spans the 24 hour period from hour $k + 1$ on day 120 to hour k on Day 121, and the first from hour $k + 1$ of Day 1 to hour k of day 2. However $k = 24$ (Case 1) is different, and there the blocs correspond to the days from 1 to 121. In either case, each bloc yields a 24-dimensional multivariate response vector with an unspecified covariance structure. Reformulating our model in this way gives us the advantage of avoiding the challenging task of specifying the complex short-term autocovariance structure, which varies over the day. But it does require the multivariate theory described in the previous subsection.

The next step in developing the forecast model would generally require the removal of any systematic, regional components in the series. In particular, it is necessary to learn which covariates/predictors to include in the design matrix \mathbf{Z} so that in application of the method, site-specific coefficients can be fitted allowing deviations from the regional baselines established for them at the preliminary stage. Note that the EnviRo.stat software (see [14]) referred to in Section 1 automatically estimates the those baseline coefficients as prior hypermeans, using a maximum likelihood-based approach, the key preliminary step here is actually the identification of \mathbf{Z} . Note also that in our application the covariates need to be adapted in form to conform to the temporal span of the response vectors (the so-called “blocs” introduced below), once hour k has been specified.

Finally, we need to address the autocovariance structure. While the responses are primarily an AR(2) time series after removing their diurnal pattern [13], as we do in the case study, we need to allow for a lag 1 autocorrelation in series of the response vectors to capture small but potentially significant longer-term dependence [15]. To eliminate it, we use the approach described in the previous subsection and split the observed response vectors into two groups: those with odd numbers and those with even numbers. For each of the resulting subseries, the model assumptions will hold approximately, and the hyperparameters can be estimated as described in the previous subsection. More detail is given below where we turn to a more precise description of M1.

In Case 2 where $k < 24$, the 24-hour bloc containing hour k includes measured responses for the hours $k + 1, \dots, 24$ on Day 120. Thus we may first apply Theorem 1 with $w = 1$ designating the last bloc in our construction above, to get a joint predictive distribution for its associated “future” response vector. Then we compute the marginal conditional predictive distribution for hour k implied by that joint distribution, given these data from Day 120 to finish the construction.

However, Case 1 is more difficult and the one we treat first. Among options considered by the authors for this case, was changing the bloc length to say $p = 25$ so that the last bloc could reach back to hour k on Day 120, which contains a measured response. That approach was discarded since the sequence of 7 bloc sequences would not synchronize

with weeks. The latter are important structural features of the process that reflect the changing daily traffic patterns and give us the single covariate we have in the case study. Instead we accomplish the same thing, another way, which does preserve the week, namely, we apply Theorem 1 with $w = 2$ to get the initial joint predictive distribution. The required marginal conditional distribution is then obtained by conditioning on all the data from Day 120.

Note that in both cases, the future response or responses in Theorem 1 depend on the bloc immediately preceding them. To avoid the need to model in that dependence, we simply eliminate that data vector. We did explore the result of keeping it in and ignoring that dependence and found virtually no difference in the Case Study. We now turn to a more precise description of M1.

For that we need some notation. Let $Y_{t,i}^{[g_j^m]}$ denote the i th coordinate of the unobserved response vector for blocs t and gauged site j , while $Y_{t',i}^{[g_j^o]}$ denotes the observed response for bloc t' , $t, t' = 1, \dots, n$, $i = 1, \dots, p$, $j = 1, \dots, g$. For bloc t , Sites g_1, \dots, g_{14} , and hours between i and j inclusive, that is, $i : j$, let $Y_{t,i;j}^{[g_l^o]}$, $l = 1, \dots, 14$ denote the random response. Throughout $p = 24$.

The two cases referred to above are as follows.

Case 1 (predict the response for the last hour $k = 24$ day 121). Hyperparameter estimates for its predictive distribution conditional on observed data are found first for the odd blocs $\mathbf{U}_t = (Y_{2t-1,1}^{[g_1^o]}, \dots, Y_{2t-1,p}^{[g_g^o]}) : gp \times 1$, $t = 1, \dots, 60$ as described in the previous subsection, using $\mathbf{Y}^{[g^o]'} = (\mathbf{U}_1, \dots, \mathbf{U}_{60})$. Repeat this procedure for the even blocs, letting $\mathbf{V}_t = (Y_{2t,1}^{[g_1^o]}, \dots, Y_{2t,p}^{[g_g^o]})$, $t = 1, \dots, 59$. Finally average the resulting pairs of hyperparameter estimates to get overall estimates.

Construction of the predictive distribution of the response at hour $k = 24$, begins with the corresponding matrix-variate observed responses, $\mathbf{Y}^{[g^o]}$ made by extracting the corresponding responses from Day 1 to Day 118 according to the above constructed \mathbf{U}_t or \mathbf{V}_t . Now suppose hypothetically that Day 120's responses have not been observed and suppose the corresponding matrix-variate missing responses, $\mathbf{Y}^{[g^m]}$ are constructed as follows:

$$\mathbf{Y}^{[g^m]} = \begin{bmatrix} Y_{121,1}^{[g_1^m]} & \dots & Y_{121,p}^{[g_g^m]} \\ Y_{120,1}^{[g_1^o]} & \dots & Y_{120,p}^{[g_g^o]} \end{bmatrix} = \begin{pmatrix} \mathbf{Y}_{121,1:p}^{[g_{1:g}^m]} \\ \mathbf{Y}_{120,1:p}^{[g_{1:g}^o]} \end{pmatrix} : 2 \times gp, \quad (7)$$

where $\mathbf{Y}_{121,1:p}^{[g_{1:g}^m]} : 1 \times gp$ is the unobserved future response vectors for days 121 and $\mathbf{Y}_{120,1:p}^{[g_{1:g}^o]} : 1 \times gp$, the observed response vector of Day 120. Hence we have $w = 2$ and $n = 121$ in Theorem 1. Thus the predictive posterior distribution of $\mathbf{Y}^{[g^m]}$ can be obtained by applying (6). To obtain that of $\mathbf{Y}_{121,1:p}^{[g_{1:g}^m]}$ given $\mathbf{Y}_{1:120,1:p}^{[g_{1:g}^o]}$, since in reality the latter are observed, one can decompose $\mu_{(u|g)}$ and $\Phi_{(u|g)}$ as follows:

$$\mu_{(u|g)} = \begin{pmatrix} \mu_{1r} \\ \mu_{2r} \end{pmatrix}, \quad \delta_{(u|g)} \Phi_{(u|g)} = \begin{pmatrix} B_{11} & B_{12} \\ B_{21} & B_{22} \end{pmatrix}, \quad (8)$$

where $\mu_{ir} : 1 \times gp$ and $B_{ij} : 1 \times 1$ for $i, j = 1, 2$. Hence, the predictive posterior distribution of $\mathbf{Y}_{121,1:p}^{[g^m]}$ is given by

$$\begin{aligned} & \mathbf{Y}_{121,1:p}^{[g^m]} \mid \mathbf{Y}_{120,1:p}^{[g^o]}, \mathbf{Y}_{1:119,1:p}^{[g^o]}, \mathcal{H} \\ & \sim t_{1 \times gp} \left(\mu_{1r} + B_{12} B_{22}^{-1} \left(\mathbf{Y}_{120,1:p}^{[g^o]} - \mu_{2r} \right), \frac{B_{11 \circ 2}}{\delta_{(u|g)} + 1} \right. \\ & \quad \otimes \boldsymbol{\Psi}_{(u|g)} \left(\mathbf{I}_{gp} + \boldsymbol{\Psi}_{(u|g)}^{-1} \left(\mathbf{Y}_{120}^{[g^o]} - \mu_{2r} \right)' B_{22}^{-1} \right. \\ & \quad \left. \left. \times \left(\mathbf{Y}_{120}^{[g^o]} - \mu_{2r} \right) \right), \delta_{(u|g)} + 1 \right). \end{aligned} \quad (9)$$

To get the joint predictive distribution of responses at these gauged sites for Day 121's last hour, let $\mathbf{e}_k^l : k \times 1$ be such that $e_{kl} = 1$ and $e_{kj} = 0$ for $j \neq l, j = 1, \dots, k$. Let $\mathbf{E}_1 = \text{blocs-diag-matrix} \{ \mathbf{e}_p^l \} : gp \times g$. The joint predictive distribution of the p th unobserved response $\mathbf{Y}_{121,p}^{[g^m]}$, that is, $\mathbf{Y}_{121,1:p}^{[g^m]} \mathbf{E}_1$, is also a multivariate t -distribution:

$$\begin{aligned} & \mathbf{Y}_{121,p}^{[g^m]} \mid \mathbf{Y}_{120,1:p}^{[g^o]}, \mathbf{Y}_{1:119,1:p}^{[g^o]}, \mathcal{H} \\ & \sim t_{1 \times g} \left(\mu^* \mathbf{E}_1, \phi^* \mathbf{E}_1' \boldsymbol{\Psi}^* \mathbf{E}_1, \delta_{(u|g)} + 1 \right), \end{aligned} \quad (10)$$

where $\mu^* = \mu_{1r} + B_{12} B_{22}^{-1} (\mathbf{Y}_{120,1:p}^{[g^o]} - \mu_{2r})$, $\phi^* = B_{11 \circ 2} / (\delta_{(u|g)} + 1)$ and $\boldsymbol{\Psi}^* = \boldsymbol{\Psi}_{(u|g)} (\mathbf{I}_{gp} + \boldsymbol{\Psi}_{(u|g)}^{-1} (\mathbf{Y}_{120,1:p}^{[g^o]} - \mu_{2r})' B_{22}^{-1} (\mathbf{Y}_{120,1:p}^{[g^o]} - \mu_{2r}))$, that completes the description of M1 in this case.

Case 2 (predict the response for hour $k < 24$ on day 121). For bloc t , Sites g_1, \dots, g_{14} , and hours between i and j inclusive, that is, $i : j$, let $\mathbf{Y}_{t,i;j}^{[g^l]}$, $l = 1, \dots, 14$ denote the random response. Now let $\mathbf{Y}^{[g^m]}$ consist of k unobserved responses and $p - k$ observed ones at each of the gauged sites. What we need to do now at each site is to use the hours leading up to the first hour without data on Day 121, that is, hour k for which the forecast is needed. To do this, we can use any data from hours $1 : k$ on Day 121 that may be available, supplemented by the data from the $p - k$ preceding hours on Day 120, $(k + 1) : p = 21 : 24$. Thus we create a $p = 24$ dimensional response vector, $\mathbf{Y}^{[g^m]} = (Y_{120,(k+1):p}^{[g_1]}, Y_{121,1:k}^{[g_1]}, \dots, Y_{120,(k+1):p}^{[g_{14}]}, Y_{121,1:k}^{[g_{14}]})$. The same routine as in Case 1 using odd and even blocs, is then used with the remaining data to obtain parameter estimates, albeit with these shifted 24 dimensional hourly response vectors.

For hour $k < 24$, $\mathbf{Y}^{[g^o]}$ holds the observed responses from Day 1 to the one ending on day 119. To predict the responses one-day-ahead at gauged sites in this field, we have $w = 1$ and $n = 120$ in Theorem 1 with $\mathbf{Y}^{[g^m]}$ rearranged so that all missing responses are at the beginning of the response vector. Specifically, let $\mathbf{e}_1^{i,j} : gp \times 1$, be 1 at the $(pj - i + 1)$ th element and 0 otherwise, for $i = 1, \dots, k$ and $j = 1, \dots, g$; $\mathbf{e}_2^{i,j} : gp \times 1$, be 1 at the $(p(j - 1) + i)$ th element and 0

otherwise, for $i = 1, \dots, p - k$ and $j = 1, \dots, g$. Let $\mathbf{E}_2 : gp \times gp = (\mathbf{e}_1^{1:k,1}, \dots, \mathbf{e}_1^{1:k,g}, \mathbf{e}_2^{1:(p-k),1}, \dots, \mathbf{e}_2^{1:(p-k),g})$. Applying Theorem 1 yields

$$\begin{aligned} & \mathbf{Y}^{[g^m]} \mathbf{E}_2 \mid \mathbf{Y}^{[g^o]}, \mathcal{H} \\ & \sim t_{1 \times gp} \left(\mu_{(u|g)} \mathbf{E}_2, \Phi_{(u|g)} \otimes \mathbf{E}_2' \boldsymbol{\Psi}_{(u|g)} \mathbf{E}_2, \delta_{(u|g)} \right). \end{aligned} \quad (11)$$

Notice that $\mathbf{Y}^{[g^m]} \mathbf{E}_2$ is $(Y_{n,k;1}^{[g_1^1]}, \dots, Y_{n,k;1}^{[g_1^g]}, Y_{n-1,1:(p-k)}^{[g_1^1]}, \dots, Y_{n-1,1:(p-k)}^{[g_1^g]})$. To obtain the predictive distribution for the unobserved responses, we first need to decompose $\mathbf{Y}^{[g^m]} \mathbf{E}_2$, $\mu_{u|g}$ and $\mathbf{E}_2' \boldsymbol{\Psi}_{(u|g)} \mathbf{E}_2$ as follows: $\mathbf{Y}^{[g^m]} \mathbf{E}_2 = (\mathbf{T}_{1c}, \mathbf{T}_{2c}) : (1 \times gk, 1 \times g(p - k))$, where $\mu_{(u|g)} = (\mu_{1c}, \mu_{2c}) : (1 \times gk, 1 \times g(p - k))$, and

$$\begin{aligned} & \mathbf{E}_2' \boldsymbol{\Psi}_{(u|g)} \mathbf{E}_2 \\ & = \begin{pmatrix} \mathbf{C}_{11} & \mathbf{C}_{12} \\ \mathbf{C}_{21} & \mathbf{C}_{22} \end{pmatrix} : \begin{pmatrix} gk \times gk & gk \times g(p - k) \\ g(p - k) \times gk & g(p - k) \times g(p - k) \end{pmatrix}. \end{aligned} \quad (12)$$

Applying standard theory, for the multivariate t distribution yields the predictive distribution of the unobserved response \mathbf{T}_{1c} given data \mathbf{T}_{2c} as a t -distribution given by

$$\begin{aligned} & \mathbf{T}_{1c} \mid \mathbf{T}_{2c}, \mathbf{Y}^{[g^o]}, \mathcal{H} \\ & \sim t_{1 \times gk} \left(\mu_{1c} + (\mathbf{T}_{2c} - \mu_{2c}) \mathbf{C}_{22}^{-1} \mathbf{C}_{21}, \right. \\ & \quad \frac{\delta_{(u|g)}}{\delta_{(u|g)} + g(p - k) + 1} \Phi_{(u|g)} \\ & \quad \times \left\{ 1 + (\delta_{(u|g)} \Phi_{(u|g)})^{-1} (\mathbf{T}_{2c} - \mu_{2c}) \mathbf{C}_{22}^{-1} \right. \\ & \quad \left. \times (\mathbf{T}_{2c} - \mu_{2c})' \right\} \otimes \mathbf{C}_{11 \circ 2}, \\ & \quad \left. \delta_{(u|g)} + g(p - k) + 1 \right). \end{aligned} \quad (13)$$

This completes the description of M1 in this case.

2.1.3. Multi-Day Ahead Forecasts. This subsection generalizes M1 to get a method that provides an r -step-ahead forecast, ($r \in \mathcal{N}$). Let N be the total number of days of observed responses. As before, we consider the multivariate setting, $p = 24$ being the total number of response coordinates and g , the total number of gauged sites. As well, we generalize the forecasting problem in two ways, namely, to forecasting the response on the last hour of the $(N + r)$ th day; hour $k < 24$ on the $(N + r)$ th day.

Case 1 (predict the final response for the last hour on day $N + r$). Here the odd bloc responses are $\mathbf{U}_t^{(1)} = (Y_{2t-1,1}, \dots, Y_{2t-1,p}^{[g^o]})$. Note that $t^O = K$ if $N = 2K$ or $N = 2K - 1$ for some $K \in \mathcal{N}$. The even bloc responses are $\mathbf{V}_t^{(1)} = (Y_{2t,1}^{[g^o]}, \dots, Y_{2t,p}^{[g^o]})$. Note that $t^E = K - 1$ if $N = 2K$ and $t^E = K$ if $N = 2K - 1$ for some $K \in \mathcal{N}$.

Remark 3. Notice that the total number of observations in data submatrices can be different for each N , being an odd or even number. Denote by t^N , the total number of observed responses. Then $t^N = t^O$ for the odd-day-responses and t^E , for the even-day-responses.

As in Section 2.1, we obtain the estimates of hyperparameters by averaging those two sets of estimates given odd or even bloc responses, respectively. Given these final estimates, we now obtain the predictive posterior distributions given all hourly observations up to Day N in Theorem A.1. They are also multivariate t -distributions. The proof and details can be seen in Appendix A.1.

Case 2 (predict the response for hour $k < 24$ on day $N + r$). Here the odds block responses are $\mathbf{U}_t^{(k)} = (Y_{2t-1,k+1}^{[g_i^o]}, \dots, Y_{2t-1,p}^{[g_i^o]}, Y_{2t,1}^{[g_i^o]}, \dots, Y_{2t,k}^{[g_i^o]}, \dots, Y_{2t-1,k+1}^{[g_g^o]}, \dots, Y_{2t-1,p}^{[g_g^o]}, Y_{2t,1}^{[g_g^o]}, \dots, Y_{2t,k}^{[g_g^o]}) : 1 \times gp$. Note that $t^O = K \in \mathcal{N}$ if $N = 2K$ and $t^O = K - 1$ if $N = 2K - 1$ for some $K \in \mathcal{N}$. The even block responses are $\mathbf{V}_t^{(k)} = (Y_{2t,k+1}^{[g_i^e]}, \dots, Y_{2t,p}^{[g_i^e]}, Y_{2t+1,1}^{[g_i^e]}, \dots, Y_{2t+1,k}^{[g_i^e]}, \dots, Y_{2t+1,p}^{[g_i^e]}, \dots, Y_{2t+1,1}^{[g_g^e]}, \dots, Y_{2t+1,k}^{[g_g^e]}) : 1 \times gp$. Note that $t^E = K - 1$ if $N = 2K$ or $N = 2K - 1$ for some $K \in \mathcal{N}$. We do the same thing here to obtain the ‘‘final’’ estimates for hyperparameters. Thus we are able to get the predictive posterior distribution given all observations up to bloc N and estimates for hyperparameters.

Remark 4. We also let t^N be the total number of observed response variables. So t^N is t^O for the odds-day-response blocs and t^E , for the even-day-response blocs.

Given the final estimates in Section 2.1, the predictive posterior distributions given all hourly observations up to N days are also multivariate t -distribution. The proof and details can be seen in Appendix A.2.

Remark 5. From Theorem A.2, the predictive distribution for the unobserved response variables from day $N + 1$ to $N + r$ is the product of a sequence of matrix- t and t distributions. This implies no analytic form can be found for the response variable at the $(k-1)$ th (for $k = 2, \dots, p$) hour of the $(N+r)$ th day at gauged site j ($j = 1, \dots, g$).

2.2. Method M2. An alternative approach to M1, through dynamic linear modeling, can also be used for forecasting and would seem an obvious choice, being an amalgamation of state-space time series models. Let \mathbf{Y}_t be the response vector across all sites at hour t . As in the previous subsections, responses are square root transformed hourly ozone concentrations. Exploratory analysis of these transformed data, found 24- and 12-hour diurnal cycles, pointing to the approach in Huerta et al. [9] for ozone that is based on the same patterns.

Let β_t be the common temporal trend coefficient across the spatial sites at hour t . Furthermore, α_{1t} and α_{2t} denotes the coefficients of the periodic components with respect to 24- and 12-hour diurnal cycles, respectively. These two

components are $S_{jt}(a_j) = \cos(\pi jt/12) + a_1 \sin(\pi jt/12)$ for $j = 1, 2$. Let $\mathbf{x}_t = (\beta_t, \alpha'_{1t}, \alpha'_{2t})' : (2n + 1) \times 1$ be the state vector at hour t and $\mathbf{F}_t : n \times (2n + 1) = [\mathbf{1}'_n, \text{diag}(S_{1t}(a_1)), \text{diag}(S_{2t}(a_2))]$. Furthermore, $\mathbf{V} : n \times n$ denotes the Euclidean intersite distance matrix for all site pairs. In this model, λ is the range parameter, σ^2 , the variance parameter, and a_1, a_2 , the phase parameters. Assume a constant covariance matrix for the state parameter vector \mathbf{x}_t and denote it by \mathbf{W} . That covariance, which accounts for the spatial correlation between sites, is given by $\mathbf{W} = \text{diag}(\tau_y^2, \tau_1^2 \exp(-\mathbf{V}/\lambda_1), \tau_2^2 \exp(-\mathbf{V}/\lambda_2))$. The vector of hyperparameters, $\gamma = (\tau_y^2, \tau_1^2, \lambda_1, \tau_2^2, \lambda_2)$, is identical to that in Huerta et al. [9] based on assessments made for Dou et al. [8].

Thus, the measurement and state equations of the DLM are given by

$$\begin{aligned} \mathbf{Y}_t &= \mathbf{F}'_t \mathbf{x}_t + \nu_t, & \nu_t &\sim N\left(\mathbf{0}, \sigma^2 \exp\left(-\frac{\mathbf{V}}{\lambda}\right)\right), \\ \mathbf{x}_t &= \mathbf{x}_{t-1} + \omega_t, & \omega_t &\sim N(\mathbf{0}, \sigma^2 \mathbf{W}), \end{aligned} \quad (14)$$

with initial information: $\mathbf{x}_0 \mid \mathbf{D}_0 \sim N(\mathbf{m}_0, \sigma_0^2 \mathbf{C}_0)$. The hyperparameters \mathbf{m}_0 , σ_0^2 , and \mathbf{C}_0 are also identical to those in Huerta et al. [9]. One can obtain the posterior distribution of the state parameters at the last known time point, n , that is, $\mathbf{x}_n \mid \mathbf{y}_{1:n}, \theta \sim N(\mathbf{m}_n, \sigma^2 \mathbf{C}_n)$, using the Kalman filter, a smoothing method and the Metropolis-within-Gibbs sampling algorithm [8, 9, 16–18]. We omit details on updating and forecasting the state parameters given the model parameters and observations up to current time point.

Given the distribution of the state parameters at the last time point, n , the observed responses until time n , $\mathbf{y}_{1:n}$, and the model parameters, $\theta = \{\lambda, \sigma^2, a_1, a_2\}$, the r -step-ahead prediction is given by

$$\begin{aligned} &\mathbf{y}_{n+r} \mid \mathbf{y}_{1:n}, \theta \\ &\sim N\left(\mathbf{F}'_{t+r} \mathbf{m}_n, \sigma^2 \left\{ \mathbf{F}'_{t+r} (\mathbf{C}_n + r\mathbf{W}) \mathbf{F}_{t+r} + \exp\left(-\frac{\mathbf{V}}{\lambda}\right) \right\}\right), \end{aligned} \quad (15)$$

for $r \in \mathcal{N}$. Note that \mathbf{F}_{t+r} , \mathbf{m}_n and \mathbf{C}_n can be obtained by application of a standard method [8, 9, 17]. Here $n = 2880$ and $r = 1, \dots, 24$ for the one-day-ahead prediction in the Case Study. For any fixed r , the predictive response, \mathbf{y}_{n+r} , can also be obtained by the MCMC (Markov Chain Monte Carlo) method. More specifically, at iteration j , suppose we have updated the vector of model parameters: $\theta^{(j)} = (\lambda^{(j)}, \sigma^{2(j)}, a_1^{(j)}, a_2^{(j)})$ using the FFBS (forward-filtering-backward-sampling) algorithm [8, 9, 16, 18]. That is, one has

$$\mathbf{x}_n \mid \mathbf{y}_{1:n}, \theta^{(j)} \sim N(\mathbf{m}_n^{(j)}, \sigma^{2(j)} \mathbf{C}_n^{(j)}). \quad (16)$$

Then, the predictive response at iteration j , $\mathbf{y}_{n+r}^{(j)}$ can be drawn from (15), that is,

$$\begin{aligned} \mathbf{y}_{n+r} &| \mathbf{y}_{1:n}, \theta^{(j)} \\ &\sim N\left(\mathbf{F}_{t+r}^{(j)'} \mathbf{m}_n^{(j)}, \sigma^{2(j)} \right. \\ &\quad \left. \left\{ \mathbf{F}_{t+r}^{(j)'} (\mathbf{C}_n^{(j)} + r \mathbf{W}^{(j)}) \mathbf{F}_{t+r}^{(j)} \right. \right. \\ &\quad \left. \left. + \exp\left(-\frac{\mathbf{V}}{\lambda^{(j)}}\right) \right\} \right). \end{aligned} \quad (17)$$

Consequently, the predictive responses are obtained by the sample means of $\{\mathbf{y}_{n+r}^{(j)} : j = 1, \dots, J\}$ ($J = 500$, where J denotes the total number of iteration after burn-in period; $r = 1, \dots, 24$). The empirical predictive intervals at the 95% nominal level can be obtained as the corresponding sample quantiles.

3. Case Study

This section implements the forecasting methods in the last section for one Chicago summer (from May 1 to August 31) using data for that urban area taken from the EPA’s AQS database (2000). These extracted data come from fourteen irregularly distributed monitoring stations measuring hourly ozone concentrations in parts per billion (ppb), which, to assure the validity of our Gaussian model assumptions, are square-root-transformed as noted in the last section. Each has few missing values under the EPA 1997 Standard in 1997 (i.e., 80 parts per billion for the eight-hour ground level ozone concentrations) during the overall time span across all available sites in this region.

To assess the model’s performance for temporal forecasting, 14 sites are selected as “gauged” sites (i.e., $g = 14$) and their observed responses on Day 121 are set aside as test values. Figure 1 shows the geographical locations of these fourteen gauged sites.

To explore these data further, weekday and hourly effects were computed for each site by averaging the transformed hour values over each of the seven weekdays over the whole summer. We found these effects to be very similar from one gauged site to the next. Thus, since “bloc” is the unit of time t , our approach puts the appropriate zero-one elements into the \mathbf{Z} to mark off the progression of blocs as the t progressed. Baseline hourly effects are represented in the hypermean function and are automatically fitted by software, EnviroStat.1.0.1. This then represents the overall diurnal pattern, while allowing site-specific deviations within the model.

3.1. Results and Comparisons. The two methods considered in this paper were applied at all fourteen gauged sites (GSs for short) to predict the twenty-four left out (test) and square-root-transformed hourly observations on Day 121. For all sites, plots showing the observations during the six days leading up to test Day 121, as well as the twenty-four forecasts by both methods for that day, may be seen in Dou et al. [19].

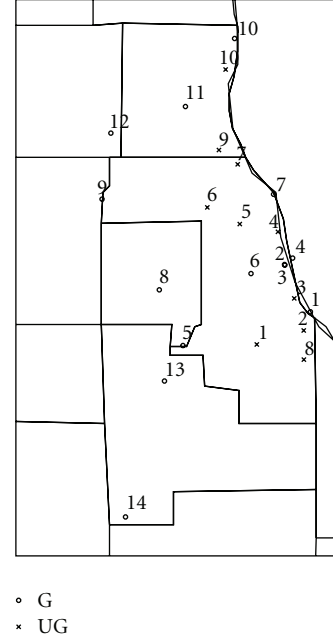


FIGURE 1: Geographical locations for the Chicago AQS database (2000), where the latitude and longitude are measured in degrees. (G: gauged sites; UG: ungauged sites).

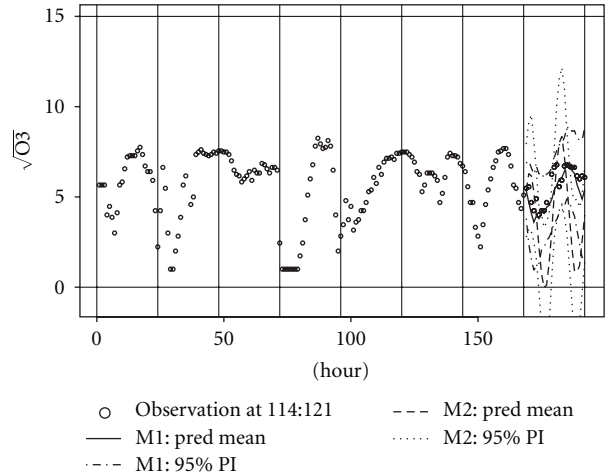


FIGURE 2: The observed square-root of ozone concentrations ($\sqrt{\text{ppb}}$) from Day 114 to Day 121, the predicted values using M1 and M2, and their 95% pointwise predictive intervals at GS 1.

These plots also include the 95% pointwise predictive intervals for that day for M1 and M2. For brevity, we include only figures that present some noteworthy features of these predictors.

To begin, Figure 2 for GS 1 shows a flat ozone field at this location on Day 119 and strongly varying one on Day 120 with two peaks. M1 does better than M2 in following not only the overall trend but tracking the turns quite well. All twenty-four of the test values lie within the 95% predictive credibility band although that for hour 12 overlaps the upper boundary. M2 follows ozone’s peaks fairly well,

but it forecasts valleys that do not turn up—the strong structure provided by the sines and cosines reduces this model’s flexibility and capacity to track the series in this case. Those harmonics point to two twelve-hour cycles despite the general lack of same in the observed series during the days before.

In contrast to the case of spatial prediction [8] where generally four peaks are seen in the sinusoidal curves bounding the DLM’s 95% predictive credibility bands, here there are just two. In fact, four peaks would be expected since the mean model’s components of variation has sines and cosines that are squared when they enter into the posterior variance. Thus their valleys turn into peaks, one every six hours since both twelve- and twenty-four hour cycles are present in the mean. So why only two?

The answer seems to lie in the fact that the random coefficients for the twelve hour components of variance in the forecast at any monitoring site, is not as uncertain in forecasting at that site than they are in spatial prediction at other sites, which may be a substantial distance from the monitoring sites. Consequently these components, although small, would have large posterior variances in the predictor than these components of the forecaster at one of the monitoring sites. In other words, much more information is available in the data leading up to the last day for the forecasts for the test values at that site than is available at a remote and unmonitored sites.

Incidentally, the lower bounds for M2 forecasts can go below zero so in practice would need to be truncated. Moreover, few of the test values lie within the 95% credibility band.

Huerta et al. [9] give similar plots for three stations in their case study for Mexico City using the method that led to our method M2. These plots differ from ours in that their plotted ordinates represent ozone while ours represent square-root-transformed ozone. We elected to keep the latter since that is the scale on which our analysis was done and hence the one that provides maximal diagnostic benefit. Furthermore our square root scale does not risk exaggerating the observed differences between both methods being considered. At the same time, we recognize the practical importance of publishing forecasts on the ozone rather than square-root ozone scale, and hence Table 1 presents comparisons on the former scale.

Huerta et al. [9] focus on just one week, so their forecasts are for their last Day 7, based on the six preceding days (whose observed hourly concentrations are plotted). In contrast, since our forecasts are based on the entire summer, our last day is Day 121 and we plot the observed values for this day (as well as the preceding seven). Although the daily amplitudes of the sinusoids in Huerta et al. [9] vary from day to day, the periodicity is very consistent over those days, with two fairly distinct peaks each day. In contrast, the ozone patterns over the seven days preceding our forecast Day 121, differ markedly from one day to another. Thus while the data series for Day 120 shows two very distinct peaks, that for Day 116 is nearly flat, and that for Day 118 (essentially) shows only one peak, after a monotone increasing trend rising to the end of that day. Finally Day 7 in their plot shows

TABLE 1: The root-mean-square-predictive error (RMSPE) of the one-day-ahead prediction at fourteen gauged sites by using M1 and M2. M1 dominates M2 in all but 1 case.

Gauged site	RMSPE (M1)	RMSPE (M2)
1	0.71	3.06
2	0.63	2.72
3	0.63	2.16
4	0.70	2.06
5	1.73	1.61
6	0.86	1.52
7	0.47	2.05
8	1.00	2.73
9	0.77	2.65
10	0.71	2.35
11	0.70	3.04
12	0.67	1.85
13	0.85	3.50
14	1.04	2.37

good agreement at all three of their stations, between their “predictive median” and the test data values. In contrast, our averages of 500 MCMC generated predicted responses for M2 disagree markedly with many of the hourly test values on Day 121. We would conjecture that these discrepancies occur because the data series on Day 121 tends to be much flatter than on all the preceding days except Day 116. (It may also derive from the additional (temperature) data Huerta et al. [9] had to enhance their forecasts that we did not have).

We do not see in any of the plots in Huerta et al. [9], the four peaks seen in some of our 95% credibility bands, suggesting that the uncertainty in the coefficients of the twelve-hour cyclical components is quite well resolved by the six days of data preceding their test day. The credibility bands for their version of M2 contain all the test values for all three of their sites, as do M2’s bands in Figure 2. (However, that is not the case for all fourteen of our stations as noted below. Moreover, their retrospective 95% credibility bands for all three sites are too narrow and fail to contain a large fraction of the observed values on a number of their days, e.g., on Sep 10 and Sep 12 at the Xalostoc site).

A summary very similar to that above for GS 1 also applies to the omitted figures for GS’s 2–4, 7–13, although for GS 11 M1 forecasts diverge from the test values over the final four hours, and for GS 13 M1 underestimates those test values in the middle of the day.

Figure 3 shows that GS 5 is different. Although M2’s forecast series has two peaks of moderate height, the bounds for the credibility bands have four of them consistent with two twelve-hour cycles. None of the forecast series tracks the series of test values well.

Summaries similar to that for GS 5 applies to GS 6 with the exception that M1 forecasts track the test value series quite well unlike M2 and to GS 14, where both methods underestimate the test values, M1 being closer overall than M2.

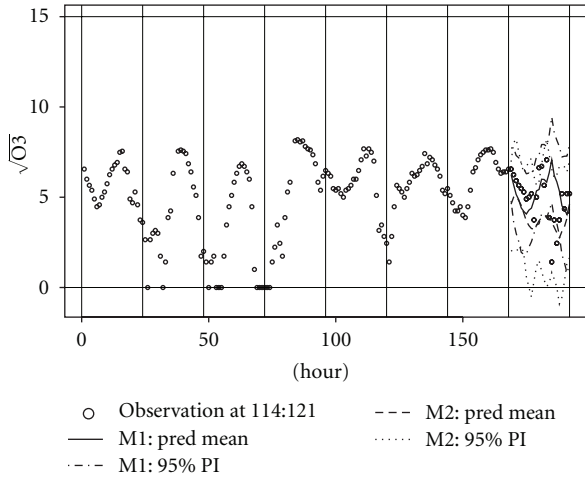


FIGURE 3: The observed square-root of ozone concentrations ($\sqrt{\text{ppb}}$) from Day 114 to Day 121, the predicted values using M1 and M2, and the 95% pointwise predictive intervals using M1 and M2 at GS 5.

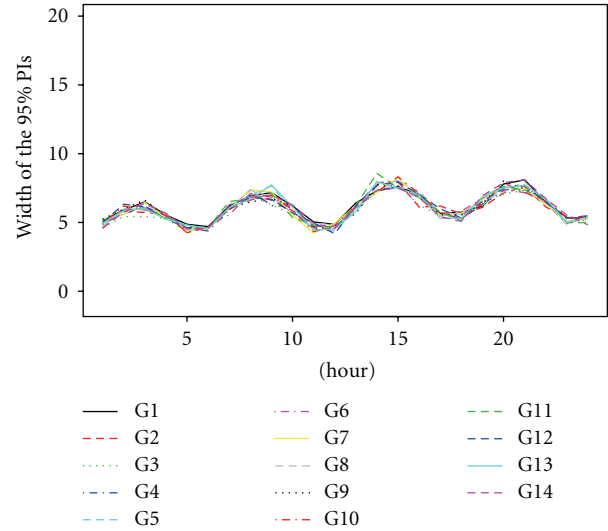


FIGURE 5: The width of the 95% pointwise predictive intervals (PIs) of the one-day-ahead prediction at 14 gauged sites using M2.

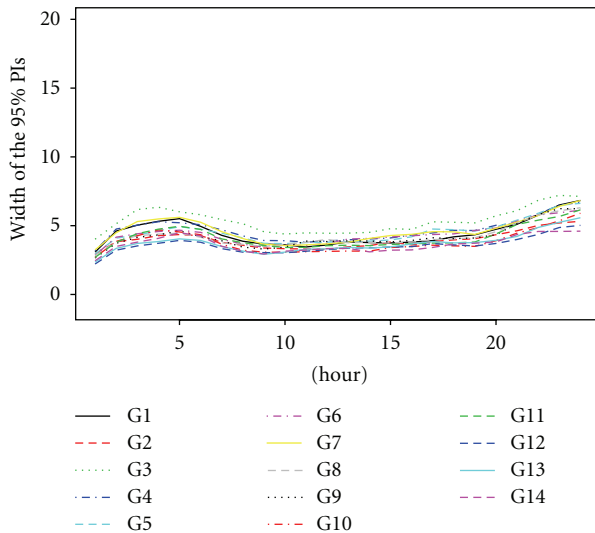


FIGURE 4: The width of the 95% pointwise predictive intervals of the one-day-ahead prediction at 14 gauged sites using M1.

Figure 4 plots the width of the 95% pointwise predictive credibility bands generated by the BSP at each of the twenty-four hours of Day 121. Starting from around 9 AM, these bands tend to increase and continue to do so until the last hour at 11 PM, reflecting the increasing uncertainty about the forecasts since increasingly fewer responses are observed as time increasing.

Figure 5 is a similar plot to that above, but this one for M2 instead of M1. These lengths are close to each other for various sites, exhibiting a wiggly periodic behavior across all gauged sites, a characteristic previously observed in Dou et al. [8, 18]. Although these lengths are very close to each other, M2 actually underestimates the predictive variances at gauged sites as seen in Figure 6, which shows the

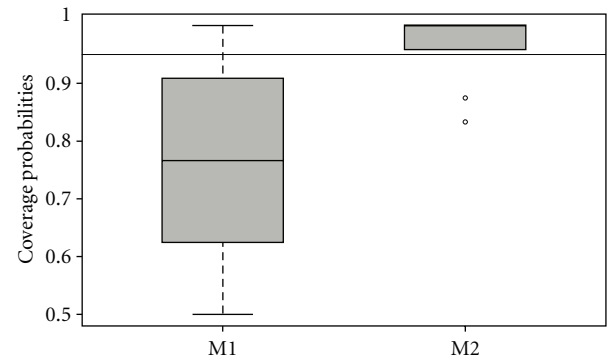


FIGURE 6: Boxplots of the coverage probabilities using M1 and M2 at the 95% nominal level.

coverage probabilities of M1 and M2, and also shows a slightly overestimated predictive variance for M1, at the 95% nominal level.

Table 1 presents the root-mean-square-predictive error (RMSPE) of the predictive responses on the 121st day at each one of fourteen gauged sites using these two approaches. At GS j , the RMSPE of the prediction at hour h can be computed by

$$\text{RMSPE}^j = \sqrt{\frac{1}{24} \sum_{h=1}^{24} (\text{PRED}_h^j - \text{OBS}_h^j)^2}, \quad (18)$$

where PRED_h^j is the predictive response at hour h of Day 121 and OBS_h^j , the corresponding observed response at the same hour, same day, and same site. M2 has a larger RMSPE over all the gauged sites compared with M1. M1 has the smallest RMSPE across most gauged sites.

4. Discussion and Conclusions

For forecasting ground-level hourly ozone concentrations in a Chicago summer, M1 seems better than M2. It seems more accurate, and its 95% predictive credibility interval is better calibrated. However, in any practical application M1 and M2 would need to be assessed in the same manner as in this paper before making a final selection. It should be noted that a new model also based on the dynamic linear approach has been proposed by Sahu et al. [11] for ozone modeling. It would be interesting to compare this new approach with the methods in this paper.

Those methods M1 and M2 are two quite different approaches to modeling space-time process and comparing and contrasting them at a more fundamental level seems worthwhile. To begin, both are quasi-Bayesian models in that they rely on some preliminary data analyses. Thus the diurnal cycles are identified for the M2 mean function, while regional non-site-specific weekday effects are found for M1. Both methods can then incorporate predictors or covariates in their parametric mean functions with random coefficients as well as reflect diurnal patterns of variation. M1 proceeds with this in two steps. First, regional time-dependent covariates or predictors are identified for the construction of the design matrix \mathbf{Z} , in his case day-of-the-week bloc effects. Secondly, it estimates hypermeans for this predictor's coefficients as well as for the multivariate bloc vector's responses, in this case the hourly effects. At the same time, it allows site-specific deviations from these baseline estimates through the random mean coefficients. The case study suggests that these random coefficients capture site-specific hourly effects quite well. In contrast, M2 builds regional features and daily variation into its mean response function through the incorporation of mean trends and periodic components before implementation. Thus, its prescribed mean is fairly structured with Fourier components to describe daily 12- and 24-hour cycles. In contrast, M1 incorporates all general trends and diurnal patterns in the hypermean for its random coefficients and then allows site-specific deviations from this hypermean at all sites. The former is more flexible than the latter, in allowing the coefficients to change over time, but the second is more flexible than the first in allowing an arbitrary shape for the daily pattern of variation and allowing site-specific trends.

Both approaches put spatial covariance structures on their mean models as well as on the residuals. In contrast to M2, M1 does not require a nonstationary spatial covariance structure, and the form of the spatial covariance matrix is completely unspecified at level one of the Bayesian hierarchy. This is not important for the Chicago analysis where the spatial ozone field is quite flat, but we believe it would be an important difference between the models in say Los Angeles or Seattle, where M1 would be favored. M2 prescribes its temporal correlation structure through the structure of its mean function, notably a random walk model for its model coefficient vector. In contrast, M1's 24-hour bloc covariance matrix is unspecified at level one of the hierarchical model, leaving the data a big role in determining its form. However, this feature comes at the price of an assumption that

the 24 autocovariance matrix is separable from the spatial covariance. Moreover, the covariance is constant over time. Both of these assumptions are limitations of M1.

Both M1 and M2 rely on both autocorrelation as well as temporal correlation for forecasting next day ozone levels. We believe responses will be somewhat autocorrelated from day to day and that feature can be exploited to enhance the forecasting performance. As formulated, M2 does borrow that additional strength, where M1 loses in the way we have implemented is parent, the BSP, by dropping a day to avoid having to formulate a multivariate time series model for the vectors of daily bloc responses. However, this is not strictly necessary. The more general version of the BSP approach does allow for that correlation, and in principle we would have estimated the hyperparameters that approach, suffered the consequences of possible misspecification and increased the computational burden of implementing M1. Thus M1 was formulated under the assumption of uncorrelated responses between days, unlike M2 which makes no such assumption, with the goal of ensuring timely 24 ahead ozone forecasts.

M2 has a much more general parent, in the dynamic linear model (DLM) and undoubtedly other implementations of the DLM could be made that retained its positive features while overcoming some of the limitations of M2 noted above. For example, a nonstationary spatial covariance could undoubtedly be used. As well the random walk model which has serious limitations could be replaced by say a more reasonable model like an AR(1), albeit with an added parameter burden. That would in turn further restrict the number of monitoring sites it could realistically handle in an urban area. As it stands, M1 computational efficiency enables it to handle a much larger number of sites than M2 in an urban area such as the greater Los Angeles area, which has 30 sites well beyond the reach of M2.

Although any ozone forecast for hourly concentrations 24 hours in advance cannot be much better than the baseline estimate, we have included Case 1 for completeness. Its Equation (9) is the basis of the forecast for that case. That equation actually gives a predictive distribution for all the hourly concentrations in Day 121 and could be used to forecast them all. However, the forecasts would not be very good compared to those given by the method in Case 2. The reason is that the latter exploits the strong AR(2) structure in any consecutive sequence of 24 hourly responses, unlike the former which assumes the daily vectors of responses are conditionally independent as an approximation made mainly for computational expediency. Thus for all other hours the forecaster in Case 2 should be used when the data in Day 120 are available. Note that within the Bayesian framework, the unconditional distribution of 24 dimensional response vectors are not independent, a feature that Case 1 exploits.

We have not considered the realistic case where only a limited number of hours of Day 120 data are available. That is because this case would be just a formalistic extension of methods M1 and M2.

Finally, we would emphasize that the results in Section 2.1 have been generalized in that section, another way in which M1 and M2 go beyond the limited application

in the Case Study. Moreover, our approach for turning BSP into the temporal forecasting tool in M1 could well be used for any univariate time series. The approach would avoid the need to capture autocorrelation at fine temporal scales, something that can be difficult to do as in the ozone case, where the AR structure varies over the day.

Overall, we have found that for forecasting Chicago's next day ozone concentration levels, M1 would be more practical and more accurate than M2. With its well-calibrated forecast intervals, it seems a promising methodology for practical application.

Appendix

A. Supplementary Results

A.1. Theorem A.1 and Its Proof

Theorem A.1. Let $\mathbf{Y}^{[g^m]} = ((\mathbf{Y}_{N+r,1:p}^{[g_{1:g}^m]})', \dots, (\mathbf{Y}_{N+1,1:p}^{[g_{1:g}^m]})', (\mathbf{Y}_{N,1:p}^{[g_{1:g}^m]})')' : (r+1) \times gp$ and $\mathbf{Y}^{[g^o]} = \mathbf{Y}_{1:(N-1),1:p}^{[g_{1:p}^o]} : (N-1) \times gp$. Then, one has the following predictive distributions:

$$(i) (\mathbf{Y}^{[g^m]} \mid \mathbf{Y}^{[g^o]}, \mathcal{H}) \sim t_{(r+1) \times gp}(\check{\mu}_{(u|g)}, \check{\Phi}_{(u|g)} \otimes \check{\Psi}_{(u|g)}, \check{\delta}_{(u|g)}), \text{ where}$$

$$\begin{aligned} \check{\mu}_{(u|g)} &= \mu_{(1)} + \mathbf{A}_{12} \mathbf{A}_{22}^{-1} (\mathbf{Y}^{[g^o]} - \mu_{(2)}), \\ \check{\Phi}_{(u|g)} &= \frac{\delta_1 - gp + 1}{\delta_1 - gp + N + 1} \mathbf{A}_{11 \circ 2}, \\ \check{\Psi}_{(u|g)} &= \frac{1}{\delta_1 - gp + 1} \\ &\quad \times \left\{ \mathbf{\Lambda}_1 \otimes \mathbf{\Omega} + (\mathbf{Y}^{[g^o]} - \mu_{(2)})' \right. \\ &\quad \left. \times \mathbf{A}_{22}^{-1} (\mathbf{Y}^{[g^o]} - \mu_{(2)}) \right\}, \\ \check{\delta}_{(u|g)} &= \delta_1 - gp + N + 1. \end{aligned} \quad (A.1)$$

(ii) The predictive distribution of $Y_{N+r,p}^{[g_j^m]}$, the p th unobserved response on the $(N+r)$ th day at gauged site j , is t -distributed:

$$Y_{N+r,p}^{[g_j^m]} \mid \mathbf{Y}_{1:N,1:p}^{[g_{1:g}^o]}, \mathcal{H} \sim t_{\check{\delta}} \left(\left(\mathbf{e}_r^j \right)' \check{\mu} \mathbf{e}_g^j, \frac{\check{\delta}}{\check{\delta} - 2} \left(\mathbf{e}_r^j \right)' \check{\Phi} \mathbf{e}_r^j \left(\mathbf{e}_g^j \right)' \check{\Psi} \mathbf{e}_g^j \right), \quad (A.2)$$

where

$$\begin{aligned} \check{\mu} &= \check{\mu}_{1r} + \check{\mathbf{B}}_{12} \check{\mathbf{B}}_{22}^{-1} \left(\mathbf{Y}_{N,1:p}^{[g_{1:g}^o]} - \check{\mu}_{2r} \right), \\ \check{\Phi} &= \frac{1}{\check{\delta}_{(u|g)} + 1} \check{\mathbf{B}}_{11 \circ 2}, \end{aligned}$$

$$\begin{aligned} \check{\Psi} &= \check{\Psi}_{(u|g)} \left[\mathbf{I}_{gp} + \check{\Psi}_{(u|g)}^{-1} \left(\mathbf{Y}_{N,1:p}^{[g_{1:g}^o]} - \check{\mu}_{2r} \right)' \right. \\ &\quad \left. \times \check{\mathbf{B}}_{22}^{-1} \left(\mathbf{Y}_{N,1:p}^{[g_{1:g}^o]} - \check{\mu}_{2r} \right) \right], \end{aligned}$$

$$\check{\delta} = \check{\delta}_{(u|g)} + 1. \quad (A.3)$$

Proof. The result is straightforward by Theorem 1, where $w = r + 1$ and $n = N + r$; decompose $\check{\mu}_{(u|g)}$ and $\delta_{(u|g)} \check{\Phi}_{(u|g)}$ as follows

$$\check{\mu}_{(u|g)} = \begin{pmatrix} \check{\mu}_{1r} \\ \check{\mu}_{2r} \end{pmatrix} : \begin{pmatrix} r \times gp \\ 1 \times gp \end{pmatrix}, \quad (A.4)$$

$$\delta_{(u|g)} \check{\Phi}_{(u|g)} = \begin{pmatrix} \check{\mathbf{B}}_{11} & \check{\mathbf{B}}_{12} \\ \check{\mathbf{B}}_{21} & \check{\mathbf{B}}_{22} \end{pmatrix} : \begin{pmatrix} r \times r & r \times 1 \\ 1 \times r & 1 \times 1 \end{pmatrix}.$$

Hence, we have

$$\mathbf{Y}_{(N+1):(N+r),1:p}^{[g_j^m]} \mid \mathbf{Y}_{N,1:p}^{[g_{1:g}^o]}, \mathbf{Y}_{1:(N-1),1:p}^{[g_{1:g}^o]}, \mathcal{H} \sim t_{r \times gp}(\check{\mu}, \check{\Phi} \otimes \check{\Psi}, \check{\delta}), \quad (A.5)$$

where $\check{\mu}$, $\check{\Phi}$, $\check{\Psi}$, and $\check{\delta}$ are given in Theorem A.1.

We have $(\mathbf{e}_r^j)' \mathbf{Y}_{(N+1):(N+r),1:p}^{[g_j^m]} \mathbf{E}_1 \mathbf{e}_g^j = Y_{N+r,p}^{[g_j^m]}$, that is, the unobserved response of the last hour of the $(N+r)$ th day at Gauged Site j ($j = 1, \dots, g$). Hence, we have

$$Y_{N+r,p}^{[g_j^m]} \sim t_{1 \times 1} \left(\left(\mathbf{e}_r^j \right)' \check{\mu} \mathbf{e}_g^j, \left(\mathbf{e}_r^j \right)' \check{\Phi} \mathbf{e}_r^j \otimes \left(\mathbf{e}_g^j \right)' \check{\Psi} \mathbf{e}_g^j, \check{\delta} \right), \quad (A.6)$$

that is, $t_{\check{\delta}} \left(\left(\mathbf{e}_r^j \right)' \check{\mu} \mathbf{e}_g^j, \left(\check{\delta} / (\check{\delta} - 2) \right) \left(\mathbf{e}_r^j \right)' \check{\Phi} \mathbf{e}_r^j \left(\mathbf{e}_g^j \right)' \check{\Psi} \mathbf{e}_g^j \right)$. \square

A.2. Theorem A.2 and Its Proof

Theorem A.2. Let $\mathbf{Y}^{[g^m]} = ((\mathbf{Y}_{N+r-1}^{[g_{1:g}^m]})', \dots, (\mathbf{Y}_{N+1}^{[g_{1:g}^m]})', (\mathbf{Y}_N^{[g_{1:g}^m]})')' : r \times gp$, where $\mathbf{W}_i^{[g_j^m]} = (Y_{i,k+1}^{[g_j^m]}, \dots, Y_{i,p}^{[g_j^m]}, Y_{i+1,1}^{[g_j^m]}, \dots, Y_{i+1,k}^{[g_j^m]}) : 1 \times gp$, and $\mathbf{Y}_N^{[g_j^m]} = (Y_{N,k+1}^{[g_j^m]}, \dots, Y_{N,p}^{[g_j^m]}, Y_{N+1,1}^{[g_j^m]}, \dots, Y_{N+1,k}^{[g_j^m]}) : 1 \times gp$, for $i = N+1, \dots, N+r-1$ and $j = 1, \dots, g$. We also let $\mathbf{Y}^{[g^o]} = \mathbf{Y}_{1:(N-1)}^{[g_{1:g}^o]} : (N-1) \times gp$, where $\mathbf{Y}_i^{[g_j^o]} = (Y_{i,k+1}^{[g_j^o]}, \dots, Y_{i,p}^{[g_j^o]}, Y_{i+1,1}^{[g_j^o]}, \dots, Y_{i+1,k}^{[g_j^o]}) : 1 \times gp$. One then has the following predictive distributions:

(i)

$$\mathbf{Y}^{[g^m]} \mid \mathbf{Y}^{[g^o]}, \mathcal{H} \sim t_{r \times gp}(\check{\mu}_{(u|g)}, \check{\Phi}_{(u|g)} \otimes \check{\Psi}_{(u|g)}, \check{\delta}_{(u|g)}), \quad (A.7)$$

where

$$\begin{aligned}\tilde{\boldsymbol{\mu}}_{(u|g)} &= \boldsymbol{\mu}_{(1)} + \mathbf{A}_{12}\mathbf{A}_{22}^{-1}\left(\mathbf{Y}^{[g^{\circ 1}]} - \boldsymbol{\mu}_{(2)}\right) : r \times gp, \\ \tilde{\boldsymbol{\Phi}}_{(u|g)} &= \frac{\delta_1 - gp + 1}{\delta_1 - gp + N}(\mathbf{A}_{11} - \mathbf{A}_{12}\mathbf{A}_{22}^{-1}\mathbf{A}_{21}), \\ \tilde{\boldsymbol{\Psi}}_{(u|g)} &= \frac{1}{\delta_1 - gp + 1} \\ &\quad \times \left\{ \mathbf{\Lambda}_1 \otimes \boldsymbol{\Omega} + \left(\mathbf{Y}^{[g^{\circ 1}]} - \boldsymbol{\mu}_{(2)}\right)' \right. \\ &\quad \left. \times \mathbf{A}_{22}^{-1}\left(\mathbf{Y}^{[g^{\circ 1}]} - \boldsymbol{\mu}_{(2)}\right) \right\}, \\ \tilde{\delta}_{(u|g)} &= \delta_1 - gp + N.\end{aligned}\tag{A.8}$$

(ii)

$$\begin{aligned}&\left(\mathbf{Y}_{(N+1):(N+r-1),1:p}^{[g_1^m]}, \mathbf{Y}_{N+r,1:k}^{[g_1^m]} \mid \mathbf{Y}_{1:N,1:p}^{[g_1^{\circ 1}]} \mid \mathcal{H}\right) \\ &\propto \prod_{j=1}^g p\left(\mathbf{T}_{1j}^r \mid \mathbf{Y}_{N+1,1:k}^{[g_j^m]}, \mathbf{Y}_{1:N,1:p}^{[g_j^{\circ 1}]} \mid \mathcal{H}\right) \\ &\quad \times \left(\mathbf{Y}_{N+1,1:k}^{[g_j^m]} \mid \mathbf{Y}_{1:N,1:p}^{[g_j^{\circ 1}]} \mid \mathcal{H}\right) \\ &\sim \prod_{j=1}^g t_{(r-1) \times p}\left(\tilde{\boldsymbol{\mu}}_{1j}^*, \tilde{\boldsymbol{\Phi}}_j^* \otimes \tilde{\boldsymbol{\Psi}}_j^*, \tilde{\delta}_{(u|g)} + 1\right) \\ &\quad \times t_{1 \times k}\left(\tilde{\boldsymbol{\mu}}_{2j}^*, \tilde{\boldsymbol{\Phi}}_{2j}^* \otimes \tilde{\boldsymbol{\Psi}}_{2j}^*, \tilde{\delta}_{(u|g)} + p - k\right),\end{aligned}\tag{A.9}$$

where $\tilde{\boldsymbol{\mu}}_{1j}^*$, $\tilde{\boldsymbol{\Phi}}_j^*$, and $\tilde{\boldsymbol{\Psi}}_j^*$ are given in (A.16) and $\tilde{\boldsymbol{\mu}}_{2j}^*$, $\tilde{\boldsymbol{\Phi}}_{2j}^*$, and $\tilde{\boldsymbol{\Psi}}_{2j}^*$, in (A.19).

Proof. (i) The result is straightforward by Theorem 1 where $w = r$ and $n = N + r - 1$;

(ii) denote $\mathbf{E}_{2j} = (\mathbf{e}_{gp}^{(j-1)p+1}, \dots, \mathbf{e}_{gp}^{jp}) : gp \times p$ for $j = 1, \dots, g$. And let $\mathbf{E}_3 = (\mathbf{e}_p^1, \dots, \mathbf{e}_p^1) : p \times p$. We will have the following results (details can be referred to in [19]):

$$\begin{aligned}&\tilde{\mathbf{Y}}^{[g^m]} \\ &= \mathbf{Y}^{[g^m]}\mathbf{E}_{2j}\mathbf{E}_3 \\ &= \begin{pmatrix} \mathbf{Y}_{N+r,k}^{[g_j^m]} & \dots & \mathbf{Y}_{N+r,1}^{[g_j^m]} & \mathbf{Y}_{N+r-1,1}^{[g_j^m]} & \dots & \mathbf{Y}_{N+r-1,k+1}^{[g_j^m]} \\ \vdots & & \vdots & \vdots & & \vdots \\ \mathbf{Y}_{N+1,k}^{[g_j^m]} & \dots & \mathbf{Y}_{N+1,1}^{[g_j^m]} & \mathbf{Y}_{N,1}^{[g_j^{\circ 1}]} & \dots & \mathbf{Y}_{N,k+1}^{[g_j^{\circ 1}]} \end{pmatrix} : r \times p,\end{aligned}\tag{A.10}$$

for $j = 1, \dots, g$. From (i) in Theorem A.2, we have

$$\tilde{\mathbf{Y}}^{[g^m]} \mid \mathbf{Y}^{[g^{\circ 1}]}, \mathcal{H} \sim t_{r \times p}\left(\tilde{\boldsymbol{\mu}}_j, \tilde{\boldsymbol{\Phi}}_{(u|g)} \otimes \tilde{\boldsymbol{\Psi}}_j, \tilde{\delta}_{(u|g)}\right),\tag{A.11}$$

where

$$\begin{aligned}\tilde{\boldsymbol{\mu}}_j &= \tilde{\boldsymbol{\mu}}_{(u|g)}\mathbf{E}_{2j}\mathbf{E}_3, \\ \tilde{\boldsymbol{\Psi}}_j &= \mathbf{E}_3'\mathbf{E}'_{2j}\tilde{\boldsymbol{\Psi}}_{(u|g)}\mathbf{E}_{2j}\mathbf{E}_3.\end{aligned}\tag{A.12}$$

We first decompose $\tilde{\mathbf{Y}}^{[g^m]}$, $\tilde{\boldsymbol{\mu}}_j$ and $\tilde{\delta}_{(u|g)}\tilde{\boldsymbol{\Phi}}_{(u|g)}$ as follows:

$$\begin{aligned}\tilde{\mathbf{Y}}^{[g^m]} &= \begin{pmatrix} \mathbf{T}_{1j}^r \\ \mathbf{T}_{2j}^r \end{pmatrix} : \begin{pmatrix} (r-1) \times p \\ 1 \times p \end{pmatrix}, \\ \tilde{\boldsymbol{\mu}}_j &= \begin{pmatrix} \tilde{\boldsymbol{\mu}}_{1j} \\ \tilde{\boldsymbol{\mu}}_{2j} \end{pmatrix} : \begin{pmatrix} (r-1) \times p \\ 1 \times p \end{pmatrix}, \\ \tilde{\delta}_{(u|g)}\tilde{\boldsymbol{\Phi}}_{(u|g)} &= \begin{pmatrix} \tilde{\boldsymbol{\Phi}}_{11} & \tilde{\boldsymbol{\Phi}}_{12} \\ \tilde{\boldsymbol{\Phi}}_{21} & \tilde{\boldsymbol{\Phi}}_{22} \end{pmatrix} : \begin{pmatrix} (r-1) \times (r-1) & (r-1) \times 1 \\ 1 \times (r-1) & 1 \times 1 \end{pmatrix}.\end{aligned}\tag{A.13}$$

Consequently, we have

(a)

$$\mathbf{T}_{2j}^r \mid \mathbf{Y}^{[g^{\circ 1}]}, \mathcal{H} \sim t_{1 \times p}\left(\tilde{\boldsymbol{\mu}}_{2j}, \tilde{\boldsymbol{\Phi}}_{22} \otimes \tilde{\boldsymbol{\Psi}}_j, \tilde{\delta}_{(u|g)}\right),\tag{A.14}$$

(b)

$$\mathbf{T}_{1j}^r \mid \mathbf{T}_{2j}^r, \mathbf{Y}^{[g^{\circ 1}]}, \mathcal{H} \sim t_{(r-1) \times p}\left(\tilde{\boldsymbol{\mu}}_{1j}^*, \tilde{\boldsymbol{\Phi}}_j^* \otimes \tilde{\boldsymbol{\Psi}}_j^*, \tilde{\delta}_{(u|g)} + 1\right),\tag{A.15}$$

where

$$\begin{aligned}\tilde{\boldsymbol{\mu}}_{1j}^* &= \tilde{\boldsymbol{\mu}}_{1j} + \tilde{\boldsymbol{\Phi}}_{12}\tilde{\boldsymbol{\Phi}}_{22}^{-1}\left(\mathbf{T}_{2j}^r - \tilde{\boldsymbol{\mu}}_{2j}\right), \\ \tilde{\boldsymbol{\Phi}}_j^* &= \frac{\tilde{\delta}_{(u|g)}}{\tilde{\delta}_{(u|g)} + 1}\left(\tilde{\boldsymbol{\Phi}}_{11} - \tilde{\boldsymbol{\Phi}}_{12}\tilde{\boldsymbol{\Phi}}_{22}^{-1}\tilde{\boldsymbol{\Phi}}_{21}\right),\end{aligned}\tag{A.16}$$

$$\tilde{\boldsymbol{\Psi}}_j^* = \tilde{\boldsymbol{\Psi}}_j\left(\mathbf{I}_p + \tilde{\boldsymbol{\Psi}}_j^{-1}\left(\mathbf{T}_{2j}^r - \tilde{\boldsymbol{\mu}}_{2j}\right)\tilde{\boldsymbol{\Phi}}_{22}^{-1}\left(\mathbf{T}_{2j}^r - \tilde{\boldsymbol{\mu}}_{2j}\right)\right).$$

We then decompose \mathbf{T}_{2j}^r , $\tilde{\boldsymbol{\mu}}_{2j}^r$, and $\tilde{\boldsymbol{\Psi}}_j$ as follows:

$$\begin{aligned}\mathbf{T}_{2j}^r &= \begin{pmatrix} \mathbf{T}_{21}^j & \mathbf{T}_{22}^j \end{pmatrix} : \begin{pmatrix} 1 \times k & 1 \times (p-k) \end{pmatrix}, \\ \tilde{\boldsymbol{\mu}}_{2j}^r &= \begin{pmatrix} \boldsymbol{\mu}_{21}^j & \boldsymbol{\mu}_{22}^j \end{pmatrix} : \begin{pmatrix} 1 \times k & 1 \times (p-k) \end{pmatrix}, \\ \tilde{\boldsymbol{\Psi}}_j &= \begin{pmatrix} \tilde{\boldsymbol{\Psi}}_{11}^j & \tilde{\boldsymbol{\Psi}}_{12}^j \\ \tilde{\boldsymbol{\Psi}}_{21}^j & \tilde{\boldsymbol{\Psi}}_{22}^j \end{pmatrix} : \begin{pmatrix} k \times k & k \times (p-k) \\ (p-k) \times k & (p-k) \times (p-k) \end{pmatrix}.\end{aligned}\tag{A.17}$$

Hence the predictive distribution of \mathbf{T}_{21}^j , that is, $\mathbf{Y}_{N+1,1:k}^{[g_j^m]}$ is given by

$$\mathbf{Y}_{N+1,1:k}^{[g_j^m]} \mid \mathbf{Y}_{1:N,1:p}^{[g^{\circ 1}]}, \mathcal{H} \sim t_{1 \times k}\left(\tilde{\boldsymbol{\mu}}_{2j}^*, \tilde{\boldsymbol{\Phi}}_{2j}^* \otimes \tilde{\boldsymbol{\Psi}}_{2j}^*, \tilde{\delta}_{(u|g)} + p - k\right),\tag{A.18}$$

where

$$\begin{aligned}\tilde{\mu}_{2j}^* &= \mu_{21}^j + (\mathbf{T}_{22}^j - \mu_{22}^j) (\tilde{\Psi}_{22}^j)^{-1} \tilde{\Psi}_{21}^j, \\ \tilde{\Phi}_{2j}^* &= \frac{\tilde{\delta}_{(u|g)}}{\tilde{\delta}_{(u|g)} + p - k} \tilde{\Phi}_{22}^j \\ &\quad \times \left(1 + \left(\tilde{\delta}_{(u|g)} \tilde{\Phi}_{22}^j \right)^{-1} (\mathbf{T}_{22}^j - \mu_{22}^j) \right. \\ &\quad \left. \times \left(\tilde{\Psi}_{22}^j \right)^{-1} (\mathbf{T}_{22}^j - \mu_{22}^j)' \right), \\ \tilde{\Psi}_2^* &= \tilde{\Psi}_{11}^j - \tilde{\Psi}_{12}^j \left(\tilde{\Psi}_{22}^j \right)^{-1} \tilde{\Psi}_{21}^j.\end{aligned}\quad (\text{A.19})$$

Therefore, we have

$$\begin{aligned}p\left(\mathbf{Y}_{(N+1):(N+r-1),1:p}^{[g_{1:g}^m]}, \mathbf{Y}_{N+r,1:k}^{[g_{1:g}^m]} \mid \mathbf{Y}_{1:N,1:p}^{[g_{1:g}^o]}, \mathcal{H}\right) \\ \propto \prod_{j=1}^g p\left(\mathbf{T}_{1j}^r \mid \mathbf{Y}_{N+1,1:k}^{[g_j^m]}, \mathbf{Y}_{1:N,1:p}^{[g_{1:g}^o]}, \mathcal{H}\right) \\ \times p\left(\mathbf{Y}_{N+1,1:k}^{[g_j^m]} \mid \mathbf{Y}_{1:N,1:p}^{[g_{1:g}^o]}, \mathcal{H}\right).\end{aligned}\quad (\text{A.20})$$

The predictive distribution for $\mathbf{Y}_{N+r,k}^{[g_{1:g}^m]}$ has no analytic form. \square

Acknowledgments

This work was partially supported by funding from the Pacific Institute of the Mathematical Sciences as well as the Natural Science and Engineering Research Council of Canada.

References

- [1] Ozone, *Air Quality Criteria for Ozone and Related Photochemical Oxidants*, US Environmental Protection Agency, 2005.
- [2] S. K. Sahu, S. Yip, and D. M. Holland, "A fast Bayesian method for updating and forecasting hourly ozone levels," *Environmental and Ecological Statistics*, vol. 18, no. 1, pp. 185–207, 2011.
- [3] J. V. Zidek, N. D. Le, and Z. Liu, "Combining data and simulated data for space-time fields: application to ozone," *Environmental and Ecological Statistics*, vol. 19, pp. 37–56, 2012.
- [4] N. D. Le and J. V. Zidek, "Interpolation with uncertain spatial covariances: a Bayesian alternative to Kriging," *Journal of Multivariate Analysis*, vol. 43, no. 2, pp. 351–374, 1992.
- [5] N. D. Le, W. Sun, and J. V. Zidek, "Bayesian multivariate spatial interpolation with data missing by design," *Journal of the Royal Statistical Society B*, vol. 59, no. 2, pp. 501–510, 1997.
- [6] J. Zidek, L. Sun, N. Le, and H. Özkaynak, "Contending with space-time interaction in the spatial prediction of pollution: vancouver's hourly ambient PM10 field," *Environmetrics*, vol. 13, no. 5–6, pp. 595–613, 2002.
- [7] N. D. Le and J. V. Zidek, *Statistical Analysis of Environmental Space-Time Processes*, Springer, New York, NY, USA, 2006.
- [8] Y. P. Dou, N. D. Le, and J. V. Zidek, "Modeling hourly ozone concentration fields," *Annals of Applied Statistics*, vol. 4, Article ID 11831213, 2010.
- [9] G. Huerta, B. Sansó, and J. R. Stroud, "A spatiotemporal model for Mexico City ozone levels," *Journal of the Royal Statistical Society C*, vol. 53, no. 2, pp. 231–248, 2004.
- [10] V. J. Berrocal, A. E. Gelfand, and D. M. Holland, "A bivariate space-time downscaler under space and time misalignment," *Annals of Applied Statistics*, vol. 4, pp. 1942–1975, 2010.
- [11] S. K. Sahu, A. E. Gelfand, and D. M. Holland, "High-resolution space-time ozone modeling for assessing trends," *Journal of the American Statistical Association*, vol. 102, no. 480, pp. 1221–1234, 2007.
- [12] D. Wraith, C. Alston, K. Mengersen, and T. Hussein, "Bayesian mixture model estimation of aerosol particle size distributions," *Environmetrics*, vol. 22, no. 1, pp. 23–34, 2011.
- [13] W. Meiring, P. Guttorp, and P. D. Sampson, "Space-time estimation of grid-cell hourly ozone levels for assessment of a deterministic model," *Environmental and Ecological Statistics*, vol. 5, no. 3, pp. 197–222, 1998.
- [14] N. D. Le and J. V. Zidek, *EnviRo.stat. A software for "Statistical Analysis of Environmental Space-Time Processes"*, 2006, <http://enviro.stat.ubc.ca/statisticalanalysis/>.
- [15] C. S. Hirtzel and J. E. Quon, "Statistical analysis of continuous ozone measurements," *Atmospheric Environment A*, vol. 15, no. 6, pp. 1025–1034, 1981.
- [16] C. K. Carter and R. Kohn, "On gibbs sampling for state space models," *Biometrika*, vol. 81, pp. 541–553, 1994.
- [17] W. West and J. Harrison, *Bayesian Forecasting and Dynamic Models*, Springer, 1997.
- [18] Y. P. Dou, N. D. Le, and J. V. Zidek, "A dynamic linear model for hourly ozone concentrations," Tech. Rep. 228, Department of Statistics, University of British Columbia, 2007.
- [19] Y. P. Dou, N. D. Le, and J. V. Zidek, "Temporal prediction with a Bayesian spatial predictor: an application to ozone fields," Tech. Rep. 249, Department of Statistics University of British Columbia, 2009.

Research Article

Application of Multiple Linear Regression Models and Artificial Neural Networks on the Surface Ozone Forecast in the Greater Athens Area, Greece

K. P. Moustris,¹ P. T. Nastos,² I. K. Larissi,³ and A. G. Paliatsos⁴

¹Department of Mechanical Engineering, Technological Education Institute of Piraeus, 250 Thivon and P. Ralli, 12244 Athens, Greece

²Laboratory of Climatology and Atmospheric Environment, Faculty of Geology and Geoenvironment, University of Athens, University Campus, Panepistimiopolis GR 157 84, Athens, Greece

³Laboratory of Environmental Technology, Department of Electronic Computer Systems Engineering, Technological Education Institute of Piraeus, 250 Thivon and P. Ralli, 12244 Athens, Greece

⁴General Department of Mathematics, Technological Education Institute of Piraeus, 250 Thivon and P. Ralli, 12244 Athens, Greece

Correspondence should be addressed to P. T. Nastos, nastos@geol.uoa.gr

Received 15 February 2012; Revised 17 May 2012; Accepted 23 May 2012

Academic Editor: Christer Johansson

Copyright © 2012 K. P. Moustris et al. This is an open access article distributed under the Creative Commons Attribution License, which permits unrestricted use, distribution, and reproduction in any medium, provided the original work is properly cited.

An attempt is made to forecast the daily maximum surface ozone concentration for the next 24 hours, within the greater Athens area (GAA). For this purpose, we applied Multiple Linear Regression (MLR) models against a forecasting model based on Artificial Neural Network (ANN) approach. The availability of basic meteorological parameters is of great importance in order to forecast the ozone's concentration levels. Modelling was based on recorded meteorological and air pollution data from thirteen monitoring sites within the GAA (network of the Hellenic Ministry of the Environment, Energy and Climate Change) over five years from 2001 to 2005. The evaluation of the performance of the constructed models, using appropriate statistical indices, shows clearly that in every aspect, the prognostic model by far is the ANN model. This suggests that the ANN model can be used to issue warnings for the general population and mainly sensitive groups.

1. Introduction

Air quality has emerged as a major factor affecting the quality of living in urban areas, especially in densely populated and industrialized areas. Air pollution control is necessary in order to prevent worsening of air quality in the long run. At the same time, short-term forecasting of air quality is required in order to take preventive and clear action during episodes of atmospheric air pollution [1]. The increasing surface ozone concentrations, in recent decades, have become a major concern worldwide due to the adverse effects on human health [2–6].

Long-term human exposure to ozone causes chest pains, persistent coughing, respiratory irritation, impaired lung function, sense of dry throat, worsening of previous respiratory diseases like asthma, severe inflammation of the lungs, and even irreversible damage to the lungs. All these will result in premature aging and chronic human respiratory

diseases. These concern more certain sensitive groups in the population, such as children, asthmatics, and elderly people [7–11], and therefore, it is clear that ozone's forecast is very important for humans.

In the past, there have been many attempts by scientists to forecast ozone concentrations as well as the concentrations of other pollutants in both urban and nonurban areas [12–24]. Specifically, Ziomas et al. [16] presented analytical models relating maximum ozone concentrations in Athens area with various meteorological variables. For this purpose, 54 pollution periods, during the years 1987–1990, were selected and analysed. The evaluation of the developed relationships showed that their degree of successfulness is rather promising. Spellman [18] developed ANN models so as to be able to forecast surface ozone concentration in five different locations in London, during the warm period of the year. In any case, the evaluation of the results by the developed ANN models, indicate that these models surpassed in

comparison with the regression models. Gómez-Sanchis et al. [19] developed a prognostic model in order to predict tropospheric ozone by using ANN models. For this purpose, ambient ozone concentrations were estimated using surface meteorological variables and vehicle emission variables as predictors. Corani [20] applied feed forward neural networks, pruned neural networks, and lazy learning in order to predict at 9 A.M. the concentration estimated for the current day for ozone and PM₁₀ in Milan, Italy. Heo and Kim [21] in their paper described the method of forecasting daily maximum ozone concentrations at four monitoring sites in Seoul, Korea. The forecasting tools developed were fuzzy expert and neural network systems. The hourly data for air pollutants and meteorological variables, obtained both at the surface and at the high-elevation (500 hPa) stations of Seoul City for the period of 1989–1999, were analyzed. Two types of forecast models were developed. The first model, Part I, uses a fuzzy expert system and forecasts the possibility of high ozone levels (equal to or above 80 ppb) occurring on the next day. The second model, Part II, uses a neural network system to forecast the daily maximum concentration of ozone on the following day. The forecasting system includes a correction function so that the existing model can be updated whenever a new ozone episode appears. The accuracy of the forecasting system has been improved continuously through verification and augmentation.

Furthermore, Elkamel et al. [22], in order to forecast the concentration of surface ozone in Kuwait, developed and trained ANN models by using meteorological parameters along with other pollutants concentrations. Finally the developed ANN models were compared with linear and not linear regression models resulting in the supremacy of ANN models in every case. In addition, Slini et al. [25] by using meteorological parameters, such as air temperature and wind speed along with surface ozone concentration of the previous day, proceeded in forecasting the surface ozone concentration the next 24 hours, applying the method of multiple regression analysis. They reached to the conclusion that cooperation of statisticians and environmentalists, leads to rather significant outcomes in matter of air quality forecasting. Finally, Moustris et al. [23] developed ANN models for predicting air quality in many different areas within GAA, one, two, and three days ahead. They used meteorological data, air pollution data, and air quality indices. The results were encouraging and showed that ANN models could give more reliable predictions concerning the quality of ambient environment in the future.

The objective of this study is to perform and compare the MLR models against a forecasting model based on Artificial Neural Network (ANN) approach, in order to forecast the ozone's concentration levels towards the next 24 hours, within the GAA.

2. Data and Methodology

2.1. Area and Data. Multiple linear regression models and ANN models were used in the present study to forecast the maximum daily surface ozone concentration of the

forthcoming 24 hours, within the GAA. The study was based on maximum daily values of surface ozone concentrations ($\mu\text{g}/\text{m}^3$) that were recorded for a five-year period (2001–2005). Hourly surface ozone concentration data and meteorological variables were acquired by the network of the Hellenic Ministry of Environment, Energy and Climate Change (HMEECC). The meteorological variables of air temperature ($^{\circ}\text{C}$) and wind speed (m/s) were obtained by eight different sites stations of the HMEECC monitoring network. Since surface ozone levels can vary considerably within GAA [16], eight suburban and five urban monitoring stations were selected for the analysis. A detailed description of the HMEECC network is found in relevant publications (e.g., [26]).

In the present study, the data set collection consists of 5-year long daily observations of maximum mean hourly ozone concentrations ($\mu\text{g}/\text{m}^3$), from the thirteen stations of HMEECC monitoring network, maximum hourly air temperature ($^{\circ}\text{C}$), and mean wind speed (m/s), from the eight meteorological observation stations of the HMEECC for the same time period. According to scientific literature [16, 25, 27] the choice of the appropriate meteorological data is based on their availability and their impact on shaping the surface ozone concentrations. Air temperature plays an important role, because an increase in air temperature is linked, with rise of the surface ozone concentration. Additionally, another basic meteorological parameter determining the horizontal transport and dispersion of air pollutants is the mean wind speed.

The final constructed data set, from 2001 to 2005, was divided into two subsets. The first concerns the four-year period, from 2001 to 2004, and the second the one-year period for 2005. The data from the first subset were used for the applied models training. The second data subset was not used for the training of the applied models but only for the evaluation of their predictive ability.

2.2. Methodology. The first step followed in the present analysis was the adjustment of daily observations of maximum mean hourly ozone values to the requirements involved by the application of multiple linear regression analysis. Because of the fact that this method requires the data to be normally distributed, the natural logarithm transformation may be applied in ozone values [28], in order to fulfill this prerequisite assumption. The distribution of original (Figure 1(a)) and transformed (Figure 1(b)) ozone values, indicated by bars, compared to the normal distribution. It is obvious that the transformed ozone values, fit to the normal distribution.

A variety of statistical methods have been utilized in order to develop techniques, which will enable qualitative or quantitative short-term forecasts. The most common alternative is to employ a multivariate statistical approach that is widely used in operational ozone forecasting and research oriented statistical modelling (e.g., [14, 25]). Multiple (multivariate) linear regression analysis is the most popular of these techniques, and it has the general form:

$$y = c + \sum_{i=1}^n a_i x_i + \varepsilon, \quad (1)$$

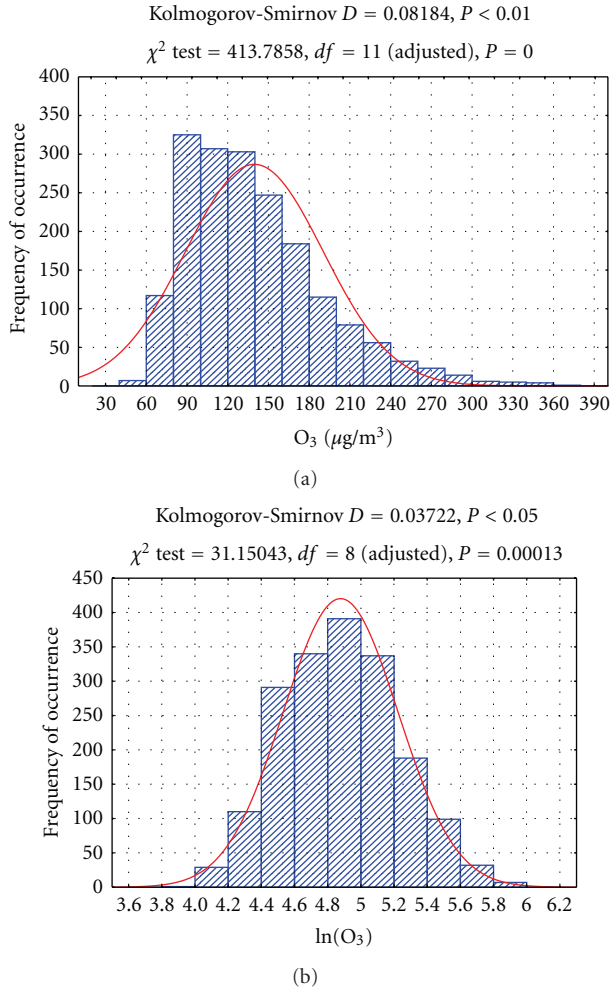


FIGURE 1: Normality test results for ozone (O_3) concentration values (a) and the natural logarithm transformation ($\ln O_3$) of ozone concentrations (b).

where c is the intercept term. a_i , $i = 1, 2, \dots, n$, are the regression coefficients, y is the response variable (surface ozone concentration), x_i , $i = 1, 2, \dots, n$, are the independent predictor variables, and ε is a residual error. When the regression equation is used in predictive mode, e (the difference between actual and predicted values not accounted for by the model) is omitted because its expected value is zero [29].

In multiple regression analysis, an important assumption is that the explanatory variables are independent from each other [30]. However, in some applications of regression, the explanatory variables are related to each other. This problem is called the multicollinearity problem [31]. The non multicollinearity term means that in any case of multiple regression analysis, any correlation between the independent variables should not exist. For this purpose, a multicollinearity index known as variance inflation factor (VIF) is used [30]. The VIF index is calculated by the following equation:

$$\text{VIF} = \frac{1}{1 - R_i^2}, \quad i = 1, 2, 3, \dots, n, \quad (2)$$

where n is the number of predictor variables and R_i^2 is the square of the multiple correlation coefficient of the i th variable with the remaining $(n - 1)$ variables where, according to Hossain et al. [30], if $0 < \text{VIF} < 5$, there is no evidence of multicollinearity problem. If $5 \leq \text{VIF} \leq 10$, there is a moderate multicollinearity problem, and finally if $\text{VIF} > 10$, there is seriously multicollinearity problem of variables.

ANN models are an attempt to imitate and simulate the function of neurons in the human's brain through mathematical functions. In late 1940, Hebb [32, 33] made one of the world's first theories about the mechanism and the ability of human's neurons in the brain, such as their ability to learn. The branch of ANN begins to grow when McCulloch and Pitts [34] create the first ANN model. In 1958, Rosenblatt [35] invented the model of artificial perception-cognition (Perceptron model) which has created more interest in the scientific community for ANN models and their ability to solve at least some simple problems. It is obvious that the simplest ANN model is composed by a single neuron. In this case, of course, the term "network" is unfair because there are no other artificial neurons connected to each other in order to eventually form a network. The only connections are those between inputs $x_1, x_2, x_3, \dots, x_n$ and the artificial neuron. A Perceptron model that is essentially a single artificial neuron is very limited. Such a network, for example, can only represent flat surfaces. This limitation no longer exists when more than one artificial neuron are used. This has led to multilayer perception (MLP). MLP consists of an input layer on which there are the artificial neurons that correspond to the input data (inputs). After the input layer there are one or more hidden layers with one or more artificial neurons. Each artificial neuron on each one of the hidden layers is connected and interchanges information with all the other neurons of both the previous and the next layer. Finally, the output layer, on which there are the "targets" artificial neurons, follows. Since data flow within the artificial neural network from a layer to the next one without any return path, such kind of ANN models are defined as feedforward ANN models. The structure of a feedforward MLP ANN can be found in relevant publications (e.g., [23]).

A weighting factor known as "synaptic weight" corresponds in each connection between neurons. The synaptic weight of an input is a number, which when multiplied with the input gives the weighted input. These weighted inputs are then added together and if they exceed a preset threshold value, the neuron is activated and gives a response-result. When the ANN transfers information from layer to layer the values of these synaptic weights change continuously. After the result reaches the output layer, it is compared with the target value and the error is calculated. In the process, the ANN returns back suitably modifying the values of synaptic weights. When the error is between acceptable limits, the values of synaptic weights are freezing. The ANN model has now been trained properly and is able to replicate and apply its "knowledge" or "experience" on new data and information, which was unknown to it previously. This training ANN process-algorithm is known as the backpropagation error algorithm.

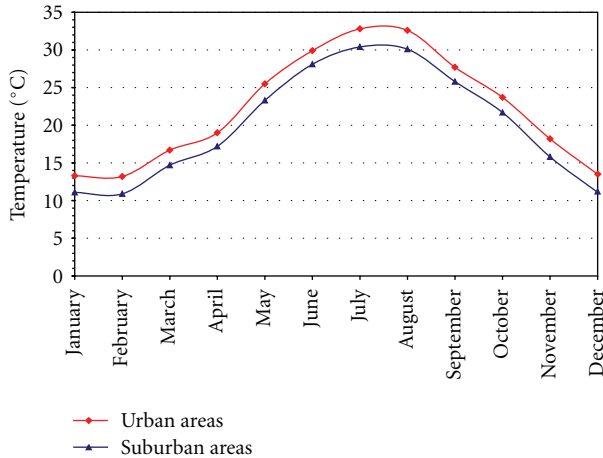


FIGURE 2: Annual variation of mean maximum monthly temperature for the urban and suburban areas within the GAA. Period 2001–2005.

For the evaluation of the results and the predicting performance of the developed model, appropriate statistical indices such as the coefficient of determination (R^2), the mean bias error (MBE), the root mean square error (RMSE) and the index of agreement (IA) were used [29, 36–40]. The RMSE is a commonly used measure of the differences between the predicted values by a predictable model and the real-observed values. The RMSE was used as a single measure that indicates the ability of the model to predict and has the same units as the predicted value. The RMSE is always positive and a zero value is ideal. The MBE provides information on the long-term performance. A low MBE is desirable. Ideally a zero value of MBE should be obtained. A positive value gives the average amount of overestimation in the calculated and negative underestimate. The coefficient of determination is used in cases of statistical models, whose main purpose is the forecast of future outcomes on the basis of other related information. It is the proportion of the variability in a dataset that is accounted for by the statistical model. It provides a measure of how well future outcomes are likely to be predicted by the model. The coefficient values range from zero to one ($0 \leq R^2 \leq 1$). The closer the value is to one, the better and more accurate is the prediction. The index of agreement is a dimensionless measure with values between zero and one ($0 \leq IA \leq 1$). When $IA = 0$, there is no agreement between prediction and observation, while $IA = 1$ denotes a perfect agreement between prediction and observation [37].

3. Results and Discussion

Figure 2 depicts the annual variation of the mean maximum monthly temperature for the urban and suburban examined areas, respectively.

According to Figure 2, there is a permanent difference of about 2°C , between urban and suburban areas. The result is expected and is consistent with the urban heat island (UHI) effect, resulting in higher temperatures within the

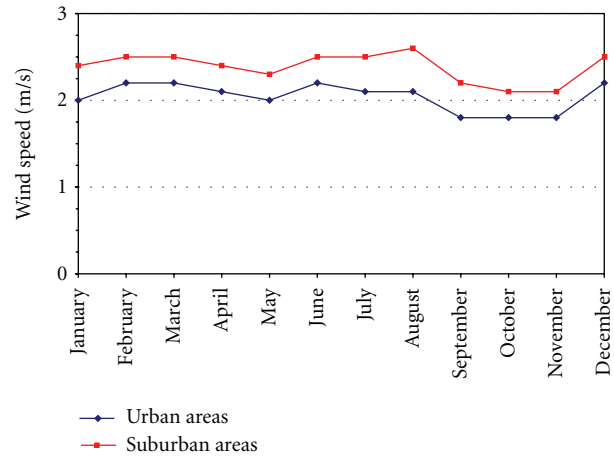


FIGURE 3: Annual variation of mean monthly wind speed for the urban and suburban areas within the GAA. Period 2001–2005.

city's center than the periphery. The mean maximum annual air temperature is about 22.1°C concerning the examined urban areas and 20.1°C for the suburban areas, respectively. During the warm period of the year (May to September), the mean maximum air temperature is about 29.6°C concerning the examined urban areas and 27.5°C for the suburban areas, respectively. Finally, during the cold period of the year (October to April), the mean maximum air temperature is about 16.8°C concerning the examined urban areas and 14.7°C for the suburban areas, respectively.

In a similar way to the above analysis, a brief analysis for the wind speed was done. Figure 3 presents the annual variation of the mean monthly wind speed for the urban and suburban examined areas, respectively.

It is shown that the wind speed for both urban and suburban areas within the GAA is low enough. There is a relatively difference for the wind speed of about 0.3 m/s , between urban and suburban areas. The mean annual wind speed is about 2.0 m/s concerning the examined urban areas and 2.4 m/s for the suburban areas, respectively. During the warm period of the year (May to September) the mean wind speed is about 2.1 m/s concerning the examined urban areas and 2.4 m/s for the suburban areas, respectively. Finally, during the cold period of the year (October to April) the mean wind speed is about 2.0 m/s concerning the examined urban areas and 2.3 m/s for the suburban areas, respectively.

The characteristics and the differences of daily maximum surface ozone concentration in suburban and urban areas were classified and analyzed separately during the examined period 2001 to 2005. Figure 4 shows the annual variation of the mean maximum monthly ozone concentrations. There is a permanent difference of about $15\ \mu\text{g}/\text{m}^3$ between urban and suburban areas. The mean maximum annual ozone concentration is about $89\ \mu\text{g}/\text{m}^3$ for the urban areas and $105\ \mu\text{g}/\text{m}^3$ for the suburban areas, respectively. During the warm period of the year the ozone concentration is about $115\ \mu\text{g}/\text{m}^3$ for the urban areas and $132\ \mu\text{g}/\text{m}^3$ for the suburban areas, respectively. Finally, during the cold period of the year the ozone concentration is about $70\ \mu\text{g}/\text{m}^3$

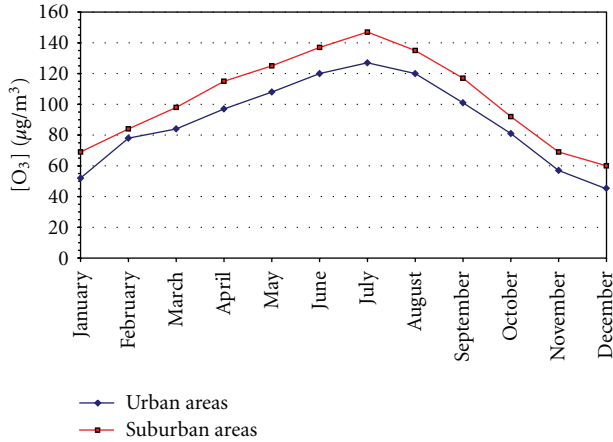


FIGURE 4: Annual variation of mean maximum monthly ozone concentrations for the urban and suburban areas within the GAA. Period 2001–2005.

for the urban areas and $84 \mu\text{g}/\text{m}^3$ for the suburban areas, respectively.

According to the HMEECC, the ozone concentration threshold (maximum hourly values during the day) for the public awareness is $180 \mu\text{g}/\text{m}^3$ and the alert threshold is $240 \mu\text{g}/\text{m}^3$, respectively. For both the urban and suburban examined areas within the GAA, the percentage of days exceeding the above thresholds were analyzed. In an annual base, the results showed that at least in one of the examined urban areas 12.3% of the days exceed the threshold for the public awareness and 95.5% of these days appear during the warm period of the year and only 4.5% during the cold period. During the warm period exceedances days, the mean maximum daily temperature is about 31.9°C and the mean daily wind speed is about 1.7 m/s. Taking into account the suburban areas, 15.8% of the days within the whole year exceed the threshold for the public awareness. From these days, a percentage of 85.5% appears during the warm period of the year and the rest 14.5% during the cold period. Within the warm period exceedances days in suburban areas, the mean maximum daily temperature is 30.0°C and the mean daily wind speed is about 1.9 m/s against 21.5°C and 1.9 m/s, respectively, for the cold period exceedances days.

Concerning the alert threshold in an annual base, 1.6% of the days exceed the threshold at least in one of the examined urban areas. All of these exceedances days (100%) are presented during the warm period of the year. Furthermore, during these days the mean maximum daily temperature is about 33.6°C and the mean daily wind speed is about 1.6 m/s. For the suburban areas, it is found that 4.1% of the days during the whole year exceed the alert threshold. From these days, 86.7% appear during the warm period of the year and the rest 13.3% within the cold period. During the warm period alert exceedances days in suburban areas, the mean maximum daily temperature is 31.3°C and the mean daily wind speed is about 1.7 m/s against 23.7°C 1.5 m/s, respectively, for the cold period. In general, the observed high air temperatures and low wind speeds promote air pollution and especially high ozone concentrations.

For the maximum hourly surface ozone concentration forecast of the next 24 hours within the GAA, prognostic models were developed using multiple linear regression and ANN models. Thus in this work, daily values of the maximum hourly air temperature ($^\circ\text{C}$) and the mean daily wind speed (m/s) within the GAA as well as the daily values of maximum hourly ozone concentrations ($\mu\text{g}/\text{m}^3$) of the previous day were used.

Essentially, three independent variables have been chosen (Table 1) while the dependent variable is the concentration of surface ozone 24 hours ahead (Table 1). Concretely, the independent variable x_1 is the natural logarithm of the maximum observed daily ozone concentration of the previous day, from the thirteen examined areas. The independent variable x_2 is the maximum observed daily air temperature of the previous day, from the eight examined meteorological stations. The independent variable x_3 is the mean daily observed wind speed of the previous day, from the eight examined meteorological stations. Finally, the dependent variable y is the natural logarithm of the maximum daily surface ozone concentration for the next 24 hours, and concerns the maximum ozone concentration from the thirteen examined regions within the GAA one day ahead.

The transformation of ozone concentrations using their natural logarithm was applied, in order to satisfy the linear multiple regression analysis requirement, namely, the values of the independent variable follow the normal distribution. Thus, the dependent variable is now on the natural logarithm of surface ozone concentration 24 hours ahead. The “normality” of both the values of ozone concentrations and the values of the natural logarithm of ozone concentration was checked by the application of the Kolmogorov-Smirnov test (statistic D) and the results are shown in Figure 1. Based on the values of Kolmogorov-Smirnov statistical index D, it is obvious that in the case of the original ozone concentrations ($D = 0.08184$) the residuals do not follow the normal distribution (Figure 1(a)). In the case of the natural logarithm of ozone concentrations ($D = 0.03722$) the residuals seem to follow the normal distribution (Figure 1(b)).

In general terms, we can say that in any case there are three independent variables and one dependent variable. Table 1 presents the variables of all applied forecasting models, which are the same for each developed model as well as their abbreviations.

The nonmulticollinearity between the three independent variables was investigated by the application of the multicollinearity index VIF. Results are presented in Table 2. According to Table 2, the term of nonmulticollinearity between the three independent variables x_1 , x_2 and x_3 is fully fulfilled.

The estimated multiple linear regression (MLR) model was

$$y = 1.4271 + 0.6562x_1 + 0.0101x_2 + 0.0076x_3. \quad (3)$$

As far as the ANN forecasting model is concerned, a multilayer perception neural network with the architecture structure of a time lagged recurrent network (TLRN) was properly developed and trained. Most of the real-world data

TABLE 1: Variables of the developed models.

Independent variables	Description
x_1	The natural logarithm of the maximum daily ozone concentration of the previous day
x_2	The maximum daily air temperature of the previous day
x_3	The mean daily wind speed of the previous day
Dependent variable	Description
y	The natural logarithm of the maximum daily ozone concentration 24 hours ahead

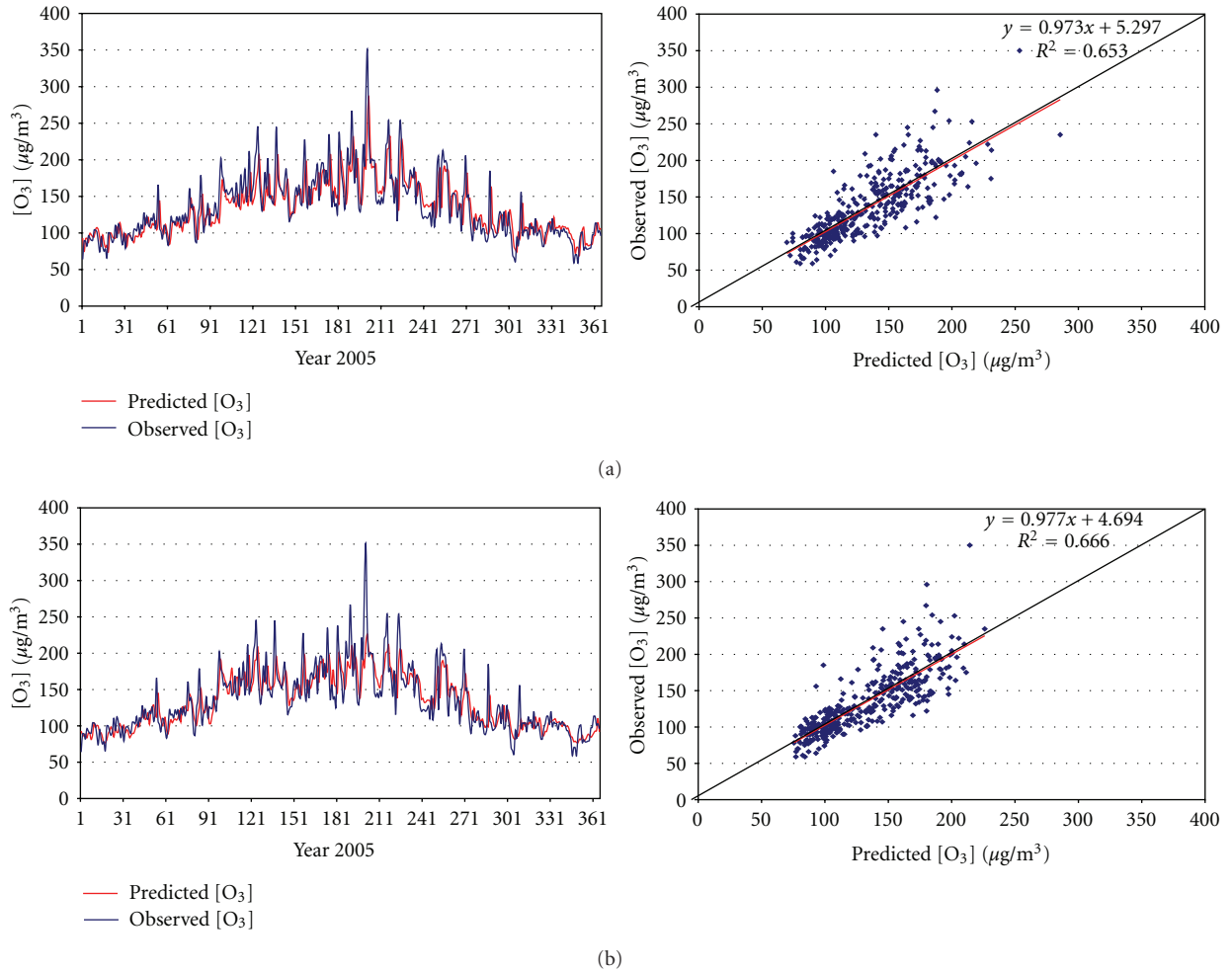


FIGURE 5: Observed (blue line) and predicted (red line) ozone concentration values 24 hours ahead for MLR (a) and ANN (b) model, year 2005.

TABLE 2: Nonmulticollinearity test results between the three independent variables.

Combination of the independent variables	Multiple correlation coefficient	VIF
$x_1 = f(x_2, x_3)$	0.516	2.1
$x_2 = f(x_1, x_3)$	0.509	2.0
$x_3 = f(x_1, x_2)$	0.028	1.0

contain information according the structure of time, that is, how the data changes with time. However, most neural

TABLE 3: Performance statistics for the validation of the developed models.

Forecasting model	R^2	MBE ($\mu\text{g}/\text{m}^3$)	RMSE ($\mu\text{g}/\text{m}^3$)	IA
MLR	0.653	-1.6	25.5	0.887
ANN	0.666	-1.5	25.1	0.892

networks are purely static classifiers. The TLRN neural architecture structure is the evolution of technology in linear time series prediction, system identification, and temporal pattern classification [41, 42].

The developed ANN model consists of one hidden layer with four artificial neurons. The choice of both the type and the architecture of the structure of the developed ANN prognostic model was done by applying the trial-and-error method. In order to train the ANN model, the independent variables x_1 , x_2 , and x_3 (Table 1) were used as input data. The independent variables x_1 , x_2 , and x_3 were chosen as input training data in order that the results of the developed ANN model are comparable with those of the MLR developed model (3). The ANN output is the dependent variable y , the natural logarithm of the maximum daily surface ozone concentration for the next 24 hours, within the GAA. In other words, the input training data are the independent variables x_1 , x_2 , and x_3 of the developed MLR forecasting model, as well as the output of the ANN model is the dependent variable y of the developed MLR forecasting model.

As mentioned before, the used data set was divided into two subsets. The first was included data from the period 2001–2004 and used for the ANN training, and the second subset was the year 2005, which was absolutely unknown to the model and used for the evaluation of the forecasting ability of the developed ANN. The same procedure was followed in the case of all developed MLR models.

Table 3 presents the values of the evaluation statistical indices for both the MLR and the ANN model. At this point, it should be noted that the values of these evaluation statistical indices concern the correlation between the real-observed and the predicted ozone concentrations for the validation year 2005 and they have been emerged after taking back the predicted values of the natural logarithms of surface ozone concentration values of each model.

Figure 5 shows the observed values of maximum daily ozone concentration against the corresponding predicted models values, within GAA for the year 2005. According to Table 3 and Figure 5, it seems that the prediction of all the developed models is in a very satisfactory level ($P < 0.01$). In conclusion, the daily maximum surface ozone concentration forecasting 24 hours ahead is most reliable by using the ANN approach compared to the forecasting by using MLR models. Very close to the ANN prediction is the prediction of the polynomial regression model.

4. Conclusions

The objective of this study was to examine the one-day forecast of the daily maximum surface ozone concentration within GAA, by developing predictive models based on the method of multiple regression analysis against artificial neural network approach. The performed analysis has indicated that the coefficient of determination (MLR: 0.653, ANN: 0.666) and the index of agreement (MLR: 0.887, ANN: 0.892), between the observed and the predicted ozone concentrations for the year 2005, with respect to MLR and ANN models, are statistically significant ($P < 0.01$). Finally, it should be mentioned that ANN models forecasting ability does present a limited precedence against MLR models. Furthermore, the improvement of the predictive ability of the constructed ANN model could be reached

by the use of several others parameters such as nitrogen oxides concentration, the intensity of solar radiation, and the sunlight duration, based on the disposability of those data over space and time.

References

- [1] W. Z. Lu, H. Y. Fan, A. Y. T. Leung, and J. C. K. Wong, "Analysis of pollutant levels in central Hong Kong applying neural network method with particle swarm optimization," *Environmental Monitoring and Assessment*, vol. 79, no. 3, pp. 217–230, 2002.
- [2] M. Lippmann, "Health effects of tropospheric ozone," *Environmental Science and Technology*, vol. 25, no. 12, pp. 1954–1962, 1991.
- [3] M. Brauer and J. R. Brook, "Ozone personal exposures and health effects for selected groups residing in the Fraser Valley," *Atmospheric Environment*, vol. 31, no. 14, pp. 2113–2121, 1997.
- [4] X. Wang, W. Lu, W. Wang, and A. Y. T. Leung, "A study of ozone variation trend within area of affecting human health in Hong Kong," *Chemosphere*, vol. 52, no. 9, pp. 1405–1410, 2003.
- [5] W. Lu, X. Wang, W. Wang, A. Y. T. Leung, and K. Yuen, "A preliminary study of ozone trend and its impact on environment in Hong Kong," *Environment International*, vol. 28, no. 6, pp. 503–512, 2002.
- [6] Y. C. Lee, G. Calori, P. Hills, and G. R. Carmichael, "Ozone episodes in urban Hong Kong 1994–1999," *Atmospheric Environment*, vol. 36, no. 12, pp. 1957–1968, 2002.
- [7] J. Schwartz, "Air pollution and hospital admissions for respiratory disease," *Epidemiology*, vol. 7, no. 1, pp. 20–28, 1996.
- [8] A. G. Paliatsos, K. N. Priftis, I. C. Ziomas et al., "Association between ambient air pollution and childhood asthma in Athens, Greece," *Fresenius Environmental Bulletin*, vol. 15, no. 7, pp. 614–618, 2006.
- [9] P. T. Nastos, A. G. Paliatsos, M. B. Anthracopoulos, E. S. Roma, and K. N. Priftis, "Outdoor particulate matter and childhood asthma admissions in Athens, Greece: a time-series study," *Environmental Health: A Global Access Science Source*, vol. 9, no. 1, article no. 45, 2010.
- [10] E. G. Kalantzi, D. Makris, M. -N. Duquenne, S. Kاكلamani, E. Stapountzis, and K. I. Gourgoulis, "Air pollutants and morbidity of cardiopulmonary diseases in a semi-urban Greek peninsula," *Atmospheric Environment*, vol. 45, pp. 7121–7126, 2011.
- [11] E. Samoli, P. T. Nastos, A. G. Paliatsos, K. Katsouyanni, and K. N. Priftis, "Acute effects of air pollution on pediatric asthma exacerbation: evidence of association and effect modification," *Environmental Research*, vol. 111, no. 3, pp. 418–424, 2011.
- [12] S. M. Robeson and D. G. Steyn, "Evaluation and comparison of statistical forecast models for daily maximum ozone concentrations," *Atmospheric Environment. Part B*, vol. 24, no. 2, pp. 303–312, 1990.
- [13] P. Zannetti, *Air pollution modeling: Theories, Computational Methods and Available Software*, Van Nostrand Reinhold, New York, NY, USA, 1990.
- [14] A. E. Milionis and T. D. Davies, "Regression and stochastic models for air pollution-I. Review, comments and suggestions," *Atmospheric Environment*, vol. 28, no. 17, pp. 2801–2810, 1994.

- [15] R. A. Olea and V. Pawlowsky-Glahn, "Kolmogorov-Smirnov test for spatially correlated data," *Stochastic Environmental Research and Risk Assessment*, vol. 23, no. 6, pp. 749–757, 2009.
- [16] I. C. Ziomas, D. Melas, C. S. Zerefos, and A. F. Bais, "On the relationship between peak ozone levels and meteorological variables," *Fresenius Environmental Bulletin*, vol. 4, no. 1, pp. 53–58, 1995.
- [17] J. Yi and V. R. Prybutok, "A neural network model forecasting for prediction of daily maximum ozone concentration in an industrialized urban area," *Environmental Pollution*, vol. 92, no. 3, pp. 349–357, 1996.
- [18] G. Spellman, "An application of artificial neural networks to the prediction of surface ozone concentrations in the United Kingdom," *Applied Geography*, vol. 19, no. 2, pp. 123–136, 1999.
- [19] J. Gómez-Sanchis, J. D. Martín-Guerrero, E. Soria-Olivas, J. Vila-Francés, J. L. Carrasco, and S. del Valle-Tascón, "Neural networks for analysing the relevance of input variables in the prediction of tropospheric ozone concentration," *Atmospheric Environment*, vol. 40, no. 32, pp. 6173–6180, 2006.
- [20] G. Corani, "Air quality prediction in Milan: feed-forward neural networks, pruned neural networks and lazy learning," *Ecological Modelling*, vol. 185, no. 2–4, pp. 513–529, 2005.
- [21] J. S. Heo and D. S. Kim, "A new method of ozone forecasting using fuzzy expert and neural network systems," *Science of the Total Environment*, vol. 325, no. 1–3, pp. 221–237, 2004.
- [22] A. Elkamel, S. Abdul-Wahab, W. Bouhamra, and E. Alper, "Measurement and prediction of ozone levels around a heavily industrialized area: a neural network approach," *Advances in Environmental Research*, vol. 5, no. 1, pp. 47–59, 2001.
- [23] K. P. Moustris, I. C. Ziomas, and A. G. Paliatsos, "3-day-ahead forecasting of regional pollution index for the pollutants NO₂, CO, SO₂, and O₃ using artificial neural networks in Athens, Greece," *Water, Air, and Soil Pollution*, vol. 209, no. 1–4, pp. 29–43, 2010.
- [24] Y. Feng, W. Zhang, D. Sun, and L. Zhang, "Ozone concentration forecast method based on genetic algorithm optimized back propagation neural networks and support vector machine data classification," *Atmospheric Environment*, vol. 45, no. 11, pp. 1979–1985, 2011.
- [25] Th. Slini, K. Karatzas, and A. Papadopoulos, "Regression analysis and urban air quality forecasting: an application for the city of Athens," *Global Nest*, vol. 4, pp. 153–162, 2002.
- [26] A. G. Paliatsos, J. K. Kaldellis, P. S. Koronakis, and J. E. Garofalakis, "Fifteen year air quality trends associated with the vehicle traffic in Athens, Greece," *Fresenius Environmental Bulletin*, vol. 11, no. 12 B, pp. 1119–1126, 2002.
- [27] M. W. Gardner and S. R. Dorling, "Meteorologically adjusted trends in UK daily maximum surface ozone concentrations," *Atmospheric Environment*, vol. 34, no. 2, pp. 171–176, 2000.
- [28] EPA, *A Guideline for Developing an Ozone Forecasting Programme*, EPA-454/R-99-009, Research Triangle Park, Office of Air Quality Planning and Standards, US Environmental Protection Agency, NC, USA, 1999.
- [29] A. C. Comrie, "Comparing neural networks and regression models for ozone forecasting," *Journal of the Air and Waste Management Association*, vol. 47, no. 6, pp. 653–663, 1997.
- [30] M. G. Hossain, M. Sabiruzzaman, S. Islam, F. Ohtsuki, and P. E. Lestrel, "Effect of craniofacial measures on the cephalic index of Japanese adult female students," *Anthropological Science*, vol. 118, no. 2, pp. 117–121, 2010.
- [31] S. Chatterjee and A. S. Hadi, *Regression Analysis by Example*, Wiley & Sons, New York, 2006.
- [32] D. O. Hebb, "The effects of early and late brain injury upon test scores and the nature of normal adult intelligence," *Proceedings of the American Philosophical Society*, vol. 85, pp. 275–292, 1942.
- [33] D. O. Hebb, *The Organization of Behavior: A Neuropsychological Theory*, Wiley & Sons, New York, NY, USA, 1949.
- [34] W. S. McCulloch and W. Pitts, "A logical calculus of the ideas immanent in nervous activity," *The Bulletin of Mathematical Biophysics*, vol. 5, no. 4, pp. 115–133, 1943.
- [35] F. Rosenblatt, "The perceptron: a probabilistic model for information storage and organization in the brain," *Psychological Review*, vol. 65, no. 6, pp. 386–408, 1958.
- [36] C. J. Willmott, "Some comments on the evaluation of model performance," *Bulletin American Meteorological Society*, vol. 63, no. 11, pp. 1309–1313, 1982.
- [37] C. J. Willmott, S. G. Ackleson, R. E. Davis et al., "Statistics for the evaluation and comparison of models," *Journal of Geophysical Research*, vol. 90, pp. 8995–9005, 1985.
- [38] S. E. Walker, L. H. Slørdal, C. Guerreiro, F. Gram, and K. E. Grønskei, "Air pollution exposure monitoring and estimation Part II. Model evaluation and population exposure," *Journal of Environmental Monitoring*, vol. 1, no. 4, pp. 321–326, 1999.
- [39] M. Kolehmainen, H. Martikainen, and J. Ruuskanen, "Neural networks and periodic components used in air quality forecasting," *Atmospheric Environment*, vol. 35, no. 5, pp. 815–825, 2001.
- [40] A. L. Dutot, J. Rynkiewicz, F. E. Steiner, and J. Rude, "A 24-h forecast of ozone peaks and exceedance levels using neural classifiers and weather predictions," *Environmental Modelling and Software*, vol. 22, no. 9, pp. 1261–1269, 2007.
- [41] S. M. Kelo and S. V. Dudul, "Short-term Maharashtra state electrical power load prediction with special emphasis on seasonal changes using a novel focused time lagged recurrent neural network based on time delay neural network model," *Expert Systems with Applications*, vol. 38, no. 3, pp. 1554–1564, 2011.
- [42] Y. Liang and A. Kelemen, "Time course gene expression classification with time lagged recurrent neural network," *Computational Intelligence in Bioinformatics*, vol. 94, pp. 149–163, 2008.

Research Article

Examining the Impact of Nitrous Acid Chemistry on Ozone and PM over the Pearl River Delta Region

Rui Zhang,¹ Golam Sarwar,² Jimmy C. H. Fung,^{1,3} Alexis K. H. Lau,³ and Yuanhang Zhang⁴

¹Department of Mathematics, The Hong Kong University of Science & Technology, Clear Water Bay, Kowloon, Hong Kong

²Atmospheric Modeling and Analysis Division, National Exposure Research Laboratory, Office of Research and Development, US Environmental Protection Agency, RTP, NC 27711, USA

³Division of Environment, The Hong Kong University of Science & Technology, Clear Water Bay, Kowloon, Hong Kong

⁴College of Environmental Sciences and Engineering, Peking University, Beijing 100871, China

Correspondence should be addressed to Golam Sarwar, sarwar.golam@epa.gov and Jimmy C. H. Fung, majfung@ust.hk

Received 16 February 2012; Accepted 3 April 2012

Academic Editor: Tareq Hussein

Copyright © 2012 Rui Zhang et al. This is an open access article distributed under the Creative Commons Attribution License, which permits unrestricted use, distribution, and reproduction in any medium, provided the original work is properly cited.

The impact of nitrous acid (HONO) chemistry on regional ozone and particulate matter in Pearl River Delta region was investigated using the community multiscale air quality (CMAQ) modeling system and the CB05 mechanism. Model simulations were conducted for a ten-day period in October 2004. Compared with available observed data, the model performance for NO_x, SO₂, PM₁₀, and sulfate is reasonably good; however, predictions of HONO are an order of magnitude lower than observed data. The CB05 mechanism contains several homogenous reactions related to HONO. To improve the model performance for HONO, direct emissions, two heterogeneous reactions, and two surface photolysis reactions were incorporated into the model. The inclusion of the additional formation pathways significantly improved simulated HONO compared with observed data. The addition of HONO sources enhances daily maximum 8-hour ozone by up to 6 ppbV (8%) and daily mean PM_{2.5} by up to 17 ug/m³ (12%). They also affected ozone control strategy in Pearl River Delta region.

1. Introduction

The importance of nitrous acid (HONO) to tropospheric chemistry is well recognized due to its contribution to HO_x (OH + HO₂) budget, which may lead to the enhancement of overall oxidation capacity of the atmosphere [1–10]. Accumulated HONO at night would undergo photolysis after sunrise to become an important source of hydroxyl radical (OH). It is especially important in the early morning when other major OH sources are still small.



Analysis of measured HONO in urban area of Europe suggested that reaction (R1) contributes more than 30% of the integrated photolytic HO_x formation [6, 7]. Some recent studies even suggested its significance through the entire day especially over the remote environment [9, 11–13]. Box model studies by considering the importance of HONO

photolysis to HO_x budget also demonstrated its impact on O₃ buildup [1, 2].

Despite the importance of HONO to tropospheric chemistry, the detail formation mechanisms, especially during daytime, have not been well established yet and incorporated into air quality models. There exist some review papers [14–16] to summarize the current knowledge on HONO formation mechanisms. Normally, four groups of HONO formation pathways were indentified: direct emission, homogeneous reactions, heterogeneous reactions, and surface photolysis reactions.

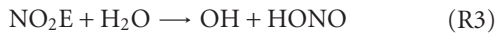
HONO can be directly emitted into the atmosphere via combustion process (e.g., vehicle exhaust) when temperature of produced NO (from nitrogen thermal fixation) is decreased [14]. Measurements of HONO emission from combustion system are mainly focused on motor vehicles, especially diesel vehicles. HONO/NO_x emission ratio from different engines was reported on average to be 0.3~0.8% [19–21]. Direct HONO emission source can possibly play an

important role over heavily polluted areas with high traffic volume.

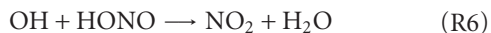
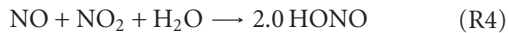
The most important homogeneous reaction that produces HONO is the reverse reaction of (R1) [16]:



This reaction has a greater role during daytime when the mixing ratios of OH and NO are high, and little contribution to the HONO was built up at night. The excited NO_2 (NO_2E) chemistry is another homogenous reaction that can produce HONO in urban areas [22–26]:

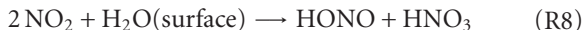


Also, carbon bond 2005 (CB05) chemical mechanism [27] contains the following homogenous reactions which are considered small impacts to HONO formation:

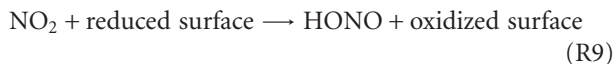


Recently, the photolysis of aromatic compounds containing the *ortho*-nitrophenol was proposed as a new gas-phase source of HONO, which would partially help to explain the high contribution of HONO to oxidation capacity in urban atmosphere environment [28].

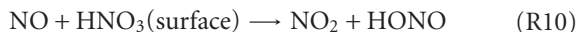
Most chamber studies indicated the importance of HONO production through the heterogeneous conversion of NO_2 absorbed on the available surfaces in the presence of water vapor [14, 29]:



The heterogeneous nature of those reactions was shown by the enhanced conversion frequency with the increase of S/V ratio and the strong dependence on surface properties [30–32]. HONO heterogeneous production can also appear either on soot or on semiorganic surface [33, 34]:



However, the surface deactivation occurs on soot within a few minutes, and consequently, it is not an important pathway for HONO [35, 36]. In regards to the reaction on semiorganic surface, even though the potential to HONO production is relatively high [18], the parameterization method is still open to discuss. Besides those, the renoxification of HNO_3 on surfaces was also believed to be important for HONO formation within the boundary layer of polluted atmosphere [37, 38]:



With the involvement of solar radiation, two surface photolysis reactions are believed to be important for daytime

HONO formation. One is the photosensitized reduction of NO_2 on organic surface [39, 40]:



where A_{red} is the reduced photosensitizer in aromatic hydrocarbons or humid acids. The other one is the photolysis of absorbed nitric acid (HNO_3) deposited on the ground [41, 42]:



Recently, the enhancement of NO_2 to HONO conversion on soot particles with the presence of artificial solar radiation was also proposed as a potential pathway for HONO formation [43].

There are already some modeling attempts to test the impact of different HONO formation pathways to photochemistry using either box model [17, 44] or 3D air quality model [18, 45–47]. For example, Aumont et al. [17] demonstrated the importance of direct emission and heterogeneous reactions to HONO enhancement under polluted condition using two-layer box model. Vogel et al. [44] suggested that reaction (R8) and emission were the most important sources of night time HONO production using a one-dimensional air quality model. Lei et al. [45] reported that reaction (R8) enhanced daytime OH and subsequently increased daytime O_3 by 4–12 ppbV by using a 3D chemical transport model in Houston. Sarwar et al. [46] incorporated reaction (R8), (R12), and direct HONO emission into CMAQ model and reproduced 60% observed HONO value at eastern US. Li et al. [18] pointed out that reaction (R8) and (R9) can significantly improve HO_x simulations during daytime and the partition of NO/NO_2 in the morning in Mexico using WRF-CHEM model. Gonçalves et al. [47] applied the WRF-CMAQ modeling system to quantify the contribution of HONO direct emission and reaction (R8) on predicted O_3 and $\text{PM}_{2.5}$ value. However, most of the studies were carried out over relatively clean area with moderate photochemical precursor level. Evaluating the impact of additional HONO sources to air quality over heavy-polluted areas such as Pearl River Delta region, China has important practical significance.

Measurements in PRD region indicate the presence of elevated ambient HONO levels not only in urban but also in rural areas. For example, early-morning HONO mixing ratio of up to 12 ppbV was measured at Guangzhou (GZ) in June 2000 [48]. Mean noon value of about 4 ppbV at GZ was measured during the first Program of Regional Integrated Experiments on air quality over the PRD in October, 2004 (PRIDE-PRD2004 [49]). A nocturnal peak HONO mixing ratio of over 8 ppbV was reported in PRIDE-PRD2006 campaign [50, 51]. High nighttime HONO levels of up to 4 ppbV [52] occurred even at the rural site Xinken (XK), which is located at the western coast of Pearl River Estuary (PRE) (see Figure 1).

Observation based-model (OBM) also supported the importance of HONO chemistry to the PRD region especially during the episode days. Zhang et al. [8] used the observed HONO data at XK as input to GIT-OBM model

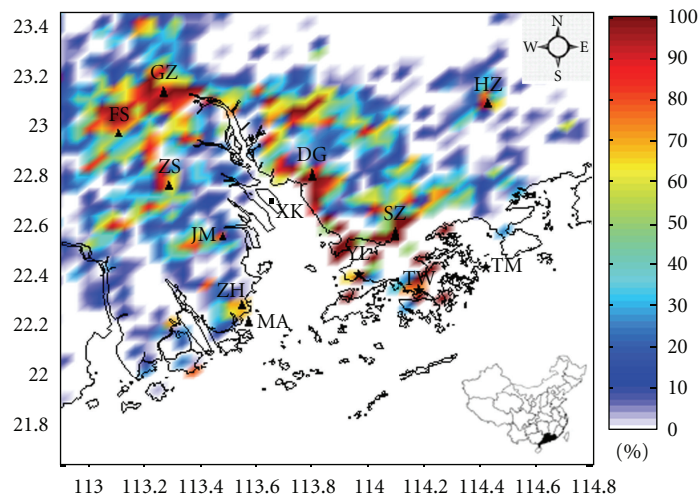


FIGURE 1: The geographic coverage of CMAQ model overlapped with urban density fraction (scaled from 0% to 100%) over Pearl River Delta region, China. \blacktriangle represents the locations of urban cities over this region, in which the star sites Yuen Long (YL), Tsuen Wan (TW) and Tap Mum (TM) are there ambient air quality monitoring stations in Hong Kong with hourly continuous observation data for criteria pollutants. \blacksquare represents the location of Xinken (XK) site.

and compared simulation results to those obtained with gas-phase HONO chemistry only. Two-to-four times increase of OH and ozone production rate were found both at GZ or XK site, which may suggest the importance of heterogeneous reactions of HONO to regional photochemical process. Lu et al. [53] employed the same model to investigate the importance of HONO during the PRIDE_PRD2006 campaign. It was suggested that it is one of the critical species for radical recycling and photochemical O_3 production for the urban areas.

Currently, CMAQ model only considers homogeneous formation pathway for HONO; hence, it may underestimate HONO level by order of magnitude [46]. The additional HONO sources can produce more OH and may improve model performance for O_3 and PM. In this study, direct HONO emissions and four additional HONO formation pathways were incorporated into CMAQ model, and their effects on predicted HONO, O_3 , and PM were investigated over PRD region.

2. Methodology

2.1. Model Description. CMAQ version 4.6 [54] was used for this study. Modeling domain was shown in Figure 1 and consisted of 49×49 grid cells with 4.5 kilometer grid spacing. The boundary conditions of the domain of interest were provided by the outer nesting domains and kept consistent for different case run. Twenty vertical layers were constructed in CMAQ with the first layer around 17 m above the ground and 11 vertical layers below 1 km. The CB05 gas-phase chemical mechanism [27] was used. The calculation of convective cloud mixing in the planetary boundary layer was represented by Asymmetric Convection Model [55]. The aerosol process was represented by fourth-generation CMAQ aerosol module (AERO4), which includes SORGAM [56] as a secondary organic aerosol model, ISORROPIA [57]

as an inorganic aerosol model, and RPM [58] as a regional particulate model. Boundary conditions for the model were generated from the CMAQ results of larger domain covering the southern China. Initial conditions for the model were chosen from default mixing ratio profiles and the first 3-day simulation was used as model spin-up.

The meteorological field for the CMAQ model was simulated by the Fifth-Generation National Center of Atmospheric Research/Pennsylvania State University (NCAR/PSU) Mesoscale Model (MM5) version 3.6.3 [59] with updated land use information and four-dimensional data assimilation (FDDA). Detailed descriptions on model configuration and data preprocessing can be found in Yim et al. [60]. Pervious comprehensive model performance evaluations by comparing the modeled pressure, ground temperature, wind speed, wind direction, and RH with available global telecommunication system observations had demonstrated that this set of MM5 simulation can represent the regional flow pattern reasonably well [60–62] and is suitable for driving chemical transport model for regional air quality study [63, 64].

2.2. Emissions for the Model. PRD local emission inventory developed by “bottom-up” methods was allocated into domain grids by Sparse Matrix Operator Kernel Emissions (SMOKE V2.1) [65] through spatial surrogate file, temporal profiles, and chemical speciation profiles [66]. Due to lack of systematic work on local PM and VOC speciation profiles for different sources in China, the corresponding SPECIATE algorithm [67] was introduced to apportion VOC to CB05 species. Gridded biogenic emission was generated through SMOKE by using the Biogenic Emission Inventory System, version 2 (BEIS2) with emission factors and the land cover information provided by the Hong Kong Planning Department [64].

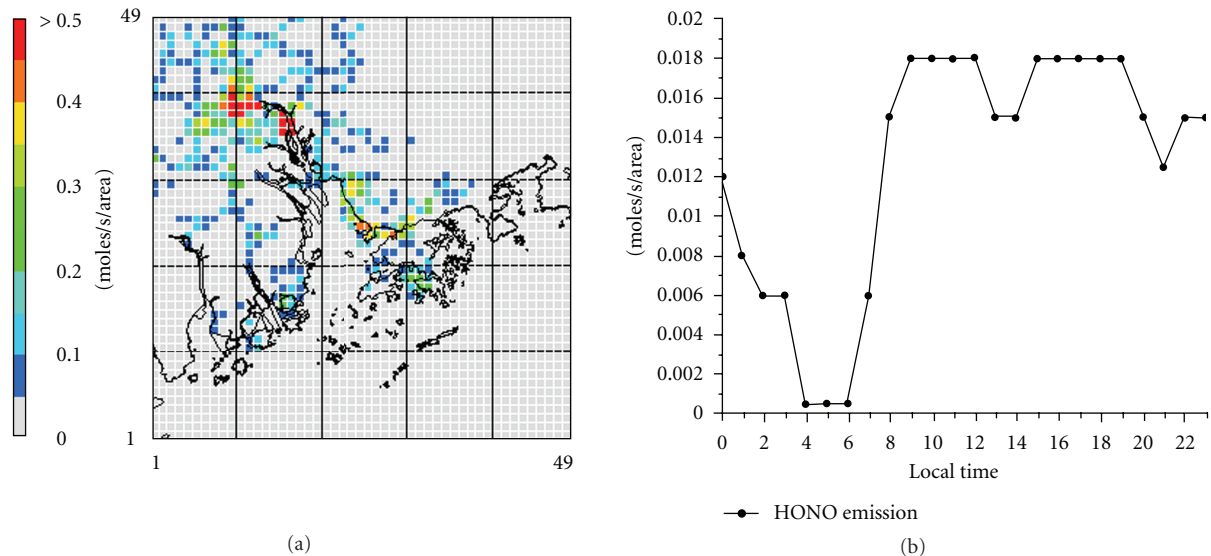


FIGURE 2: (a) Average daily HONO emission rate ($\text{moles s}^{-1} \text{ grid area}^{-1}$) distribution pattern and (b) diurnal profile of HONO emission in the PRD region.

2.3. HONO Formation Pathways. The CB05 gas-phase chemical mechanism in CMAQ model contains known homogeneous reactions involving HONO except the excited NO_2 chemistry and the photolysis of *ortho*-nitrophenols [28]. Reaction (R3) is not included in this study since Sarwar et al. [23] reported that it contributes only a small amount to daytime HONO. CMAQ version 4.6 does not contain any direct HONO emissions from vehicles. In this study, direct HONO emissions are also included. Three groups of additional HONO formation pathways as described earlier were incorporated into CMAQ model. Compared to the similar study of Sarwar et al. [46], reactions (R11) and (R12) are the first time to incorporate into a 3D air quality model for quantifying the HONO impact on air quality modeling results.

Direct HONO emission over PRD region is estimated from on-road and off-road vehicle sources as a fraction of NO_x vehicle emission; HONO/ NO_x emission ratio is set to 0.008 based on the results reported by Kurtenbach et al. [20]. Vehicle NO_x emission was initially speciated into NO by 90% and NO_2 by 10% (by volume). For this study, we modified the speciation of vehicle NO_x emission into NO by 90%, NO_2 by 9.2%, and HONO by 0.8%. Su et al. [52] reported an upper limit of 0.01 for $[\text{HONO}]/[\text{NO}_x]$ ratio in PRD, which is consistent with the value used in this study

$$E_{\text{HONO}} = 0.008 * E_{\text{NO}_x} \quad (\text{R13})$$

Estimates of direct HONO and other emissions were developed using SMOKE [65]. The spatial distribution as well as temporal profile of ground HONO emission rate is demonstrated in Figure 2. The general HONO distribution pattern matches with PRD road network, and the emission rate is scaled by total vehicle volume. Multiple hotspots with the average daily emission rate greater than $0.5 \text{ mol s}^{-1} \text{ area}^{-1}$ (area in this study is $4.5 \text{ km} \times 4.5 \text{ km}$) are found at GZ city and its vicinity area, Dongguan, Shenzhen city cluster,

and Central in Hong Kong. The emission gradient between eastern and the western parts of PRE is noticeable. The diurnal variation of HONO emission rate closely follows the vehicle use pattern. Emission rates are relatively high during daytime (08:00–19:00 LST), then drop after the midnight (00:00 LST), and increase again around 07:00 LST with the start of morning rush hour.

Two heterogeneous reactions (R8) and (R10) were added to the CMAQ model. The first-order reaction constant k_{HONO} is given as

$$k_{\text{HONO}} = \frac{\gamma_{\text{rxn}} \times [S/V] \times \omega}{4}, \quad (1)$$

where γ_{rxn} is dimensionless reactive uptake coefficient. The γ_{rxn} for reaction (R8) is taken as 1.0×10^{-6} [17] and for reaction (R10) is taken as 1.0×10^{-8} [37]; ω is the mean thermal velocity of a given reactant and is calculated following Pleim and Xiu [68].

The estimation of S/V for heterogeneous reactions is a challenging task. Total S/V ratio for reaction (R8) includes model-resolved aerosol surface area and other available surface area at the first model layer:

$$\begin{aligned} \left[\frac{S}{V} \right]_{\text{surface}} &= \left[\frac{S}{V} \right]_{\text{aerosol}} + \left[\frac{S}{V} \right]_{\text{ground}} \\ &= \left[\frac{S}{V} \right]_{\text{aerosol}} \\ &\quad + \left(2 \times \frac{\text{LAI}}{z_s} + \left[\frac{S}{V} \right]_{\text{building}} + \left[\frac{S}{V} \right]_{\text{soil}} \right). \end{aligned} \quad (2)$$

Here, S/V for building is taken to represent surface areas provided by buildings, roads, parking lots, and other structures. Unless during heavily polluted days, the S/V ratio for aerosol is much smaller than corresponding S/V

values for available surface on the ground [46]. S/V ratio for vegetation can be represented by leaf area index (LAI) in the first model layer z_s . The LAI values were multiplied by two to account for both sides of leaves into total reaction interface [69]. The S/V ratio for soil is set to 0.1 m^{-1} . Svensson et al. [29] studied the kinetics of the reaction involving NO_2 and H_2O and suggested an S/V value of 0.2 m^{-1} for typical urban environment. However, Cai [70] used a value of 1.0 m^{-1} to represent the high urban density environment in New York. In this study, the estimated S/V ratio for building at each grid is taken as proportional to the model-resolved urban fraction (PURB, with the range 10% to 100%, see Figure 1) and capped with an empirical upper limit s_{max} . Over the very low urban density place with PURB less than 10%, S/V for building is a fixed value as 10% of s_{max} :

$$\left[\frac{S}{V} \right]_{\text{building}} = \begin{cases} s_{\text{max}} \times \frac{10}{100} = \frac{s_{\text{max}}}{10} & \text{if PURB} < 10\%, \\ s_{\text{max}} \times \frac{\text{PURB}}{100} & \text{if } 10\% < \text{PURB} < 100\%, \end{cases} \quad (3)$$

where $s_{\text{max}} = 0.3 \text{ m}^{-1}$ is used for the base case following Sarwar et al. [46]. Sensitivity study is also conducted to investigate the impact of alternative value of s_{max} on predicted HONO. Values of S/V for building over water were set to zero. In the model, reaction (R8) can produce HONO on aerosol surfaces at all vertical levels, while it can only produce HONO in the first layer on ground surfaces.

For renoxification of nitric acid (reaction (R10)), only the S/V on the ground surface is considered. In the model, production of HONO from reaction (R10) can only occur in the first layer.

Two surface photolysis pathways (reactions (R11) and (R12)) for HONO formation are added into CMAQ to investigate the production of HONO during daytime. As regards to the photosensitized reduction of NO_2 on humic acid coated aerosol (reaction (R11)), HONO production is not linearly increased with the integrated actinic flux F (photons $\cdot\text{m}^{-2} \text{ s}^{-1}$, 300–750 nm) due to the quick deactivation process by reaction with photo-oxidants which are formed simultaneously during the irradiation of humic acid surfaces [39]. In this study, the empirical first-order HONO formation model suggested by Stemmler et al. [40] is parameterized into CMAQ with the uptake coefficient $\gamma_{\text{rxn}}|_{\text{HA}}$:

$$\gamma_{\text{rxn}}|_{\text{HA}} = \frac{4}{\omega} \times \frac{1}{9.3 \times 10^{22} \times [\text{NO}_2] \times [F]^{-1} + 2330}, \quad (4)$$

where mixing ratios of NO_2 is in ppbV. Only the S/V ratio for soil is considered for reaction (R11). In the model, HONO production from reaction (R11) is released in the first layer only.

HONO formation through photolysis of adsorbed HNO_3 on surfaces (reaction (R12)) was incorporated into the model

upon the empirical relationship derived from laboratory measurements [71]

$$\frac{d[\text{HONO}]}{dt} = \frac{\left\{ \alpha \times J_{\text{HNO}_3}^* \times V_d|_{\text{HNO}_3} \times [\text{HNO}_3] \times \Delta t \right\}}{z_s}, \quad (5)$$

where α is the fraction of deposited HNO_3 exposure to full noontime sunlight with the photolysis rate J_{HNO_3} . In this study, α is set as 0.5. $V_d|_{\text{HNO}_3}$ is dry deposition velocity of HNO_3 , $[\text{HNO}_3]$ is the mixing ratio in the first model layer, Δt is accumulated time since the last precipitation event, and z_s is the first layer model height (17 m) in CMAQ configuration. The model assumes that the wet deposition removes all absorbed HNO_3 on the ground and resets it to zero for subsequent simulation. The photolysis rate of adsorbed HNO_3 reported by Zhou et al. [71] is 24 times greater than the photolysis rate of gaseous HNO_3 ; thus, it was taken as $J_{\text{HNO}_3}^* = 24 \times J_{\text{HNO}_3}$ in the model, and HONO production from reaction (R12) is released in the first layer only.

2.4. General Synoptic Condition and Case Selection. The time period for HONO simulation over PRD region is chosen from 23 October, 2004 to 2 November, 2004, when the PRIDE-PRD2004 campaign was carried out. HONO measurements were conducted using rotated wet effluent diffusion denuder (WEDD) methods at two supersites: one at an urban area (GZ: 23.13°N, 113.26°E) and one at a rural area (XK: 22.61°N, 113.59°E) (Figure 1) [49]. During the PRIDE-PRD2004 campaign period, the persistent surface high-pressure system (anticyclone), descent motion outside of hurricane, and frequent sea breeze result in high-level ground mixing ratio for gaseous and particulate pollutants [72]. For instance, at XK supersite, at least two severe episodes were observed on October 25 and October 29 with measured daily peak O_3 mixing ratio reaching over 150 ppbV and $\text{PM}_{2.5}$ peak mixing ratio near or greater than $200 \mu\text{g}/\text{m}^3$ [49]. Observed maximum HONO mixing ratio in XK was reported to be more than 4 ppbV in the nighttime and about 1 ppbV during the daytime [52].

A total of eleven simulation cases were performed to investigate the impact of additional HONO formation pathways on air quality modeling results over PRD region. Sensitivity runs were designed to understand the impacts of uncertainties of selected parameters on air quality. Selected significance test on HONO prediction using the previous proposed parameterization methods was carried out to discuss their robustness over PRD region simulation. The impact of HONO chemistry on O_3 control strategy due to the VOC emission reduction was also evaluated. The case ID, case description, and designed purpose are summarized in Table 1.

3. Results and Discussion

3.1. Model Performance for Base Case CB05. Time series of predicted SO_2 , NO_x , O_3 , and $\text{PM}_{2.5}$, as well as aerosol sulfate and aerosol nitrate (case CB05, see Table 1) are compared

TABLE 1: Design of CMAQ simulation case to evaluate the HONO chemistry.

Case ID	Description	Purpose
CB05	Base case run	
CB05+EM	CB05+HONO emission (R13)	Relative importance of four different formation pathways to simulated HONO
CB05+EM+HT	CB05+EM+HONO heterogeneous reaction ((R6), (R8))	
CB05+EM+HT+SP	CB05+EM+HT+HONO surface photolysis ((R11), (R12))	
HONO_S/V	CB05+EM+HT+SP with $s_{\max} = 1$ in building surface area estimation and soil surface 0.2	Sensitivity study of the uncertainties for selected parameters in HONO formation mechanism
HONO_NOx	CB05+EM+HT+SP with NO _x emission partition NO/NO ₂ /HONO 85%/13.8%/1.2%	
HONO_DV	CB05+EM+HT+SP with deposition velocity of HONO has taken the value as NO ₂	
HONO_G	CB05+EM+SP+HONO heterogeneous reaction on aerosol and ground surfaces follow Aumont et al. [17]	Examine the impacts of other HONO parameterizations published in peer-reviewed articles
HONO_SOA	CB05+HONO heterogeneous reaction with semivolatile organic follows Li et al. [18]	
0.75 VOC	CB05 with the 25% VOC emission reduction over PRD region	Evaluation the possible effect on ozone control strategy due to consideration of additional HONO formation pathway
0.75 VOC w/HONO	CB05+EM+HT+SP with the 25% VOC emission reduction over PRD region	

to the measurements obtained from the Hong Kong Environmental Protection Department (HKEPD) for Yuen Long (YL) monitoring station (Figure 3). Model performance statistics for other locations (CW, TM, TW, TC, and YL) (see Figure 1) are summarized in Table 2. Generally, CMAQ model has skill to reproduce air pollutant mixing ratios, their trends, spatial gradient, and relative abundance. Relatively high indexes of agreement (IOA, [73]) were obtained for all species except aerosol nitrate (ANO₃). Mean normalized bias (MNB) for SO₂, NO_x, O₃, and aerosol sulfate (ASO₄) are less than $\pm 30\%$, which is taken as the acceptable level for model performance [74].

Predicted O₃ mixing ratios agree reasonably well with observed data in terms of diurnal variation however, it sometimes cannot reproduce high observed afternoon O₃ peaks due to the uncertainty of emission precursor (NO_x and VOC) ratio estimation and UV calculation for photochemical reaction (Figure 3). Model tends to underestimate PM_{2.5} mass mixing ratios uniformly by 40~50%. This may be due to the underestimation of related PM emission rates and misrepresentation of particulate species in the model. Current CMAQ aerosol module [58] allocates all unspecified aerosol components into the category “PM_OTHER” and represents them as chemical inert. The modeled PM_{2.5} component has a large portion (25%~40%) of “PM_OTHER,” which may cause the underestimation of specific aerosol component. Modeling results are consistent with the work reported by Kwok et al. [64].

However, the CMAQ model has certain skill to represent sulfate formation pathways via gaseous-phase and aqueous-phase chemical reactions. The second pathway is especially important over PRD region due to high ambient RH and large fraction of cloud cover generally present throughout the year [75]. Simulated ASO₄ is reasonably good with IOA around 0.6 and MNB less than $\pm 25\%$. The grossly underestimation of aerosol nitrate performance (IOA below 0.3 and

MNB greater than -80%) may be due to the underestimation of nitrogen oxide emissions over PRD region and the lack of coarse-mode ANO₃ formation in CMAQ 4.6 either through reaction between HNO₃ and calcium carbonate or between gaseous HNO₃ and NaCl [64]. Ambient observed O₃ and PM_{2.5} outside Hong Kong are not publicly available; thus, predicted mixing ratios cannot be compared with observed data. In summary, model performance statistics simulation is reasonably well, and the model is suitable for evaluating the impact of HONO chemistry over PRD region.

3.2. Model Evaluation at Xinken (XK) and Guangzhou (GZ). During the PRIDE_PRD2004 campaign, HONO was measured at XK and GZ [49]. XK measurement site is located at a rural area, while GZ measurements site is located at an urban area (Figure 1). The model evaluation after incorporation of different HONO chemistry at XK (first column) and GZ (second column) site for NO₂, O₃ and HONO is presented in Figure 4. Daytime (07:00–18:00 LST) as well as nighttime (19:00–06:00 LST) model average values were compared with corresponding observations. The modeled NO₂ mixing ratios for different simulation cases (Table 1) during daytime are underestimated by 26%~28% at XK while during nighttime were overestimated at XK by 21%~26% (no observation for NO₂ available at GZ). On the contrary, the modeled O₃ mixing ratios are consistently underestimated at two sites, and the degree of underestimation was more severe during daytime (-34% at XK and -40% at GZ) than that during nighttime (-28% at XK and -10% at GZ). The reason for the underestimation of O₃ peaks may be associated with the overestimation of NO_x and missing of HONO chemistry in base case CMAQ run. However, the HONO chemistry does not have obvious improvement on the NO₂ and O₃ model performance at XK and GZ sites (pin-pointed with grid area 4.5 km \times 4.5 km) during the campaign.

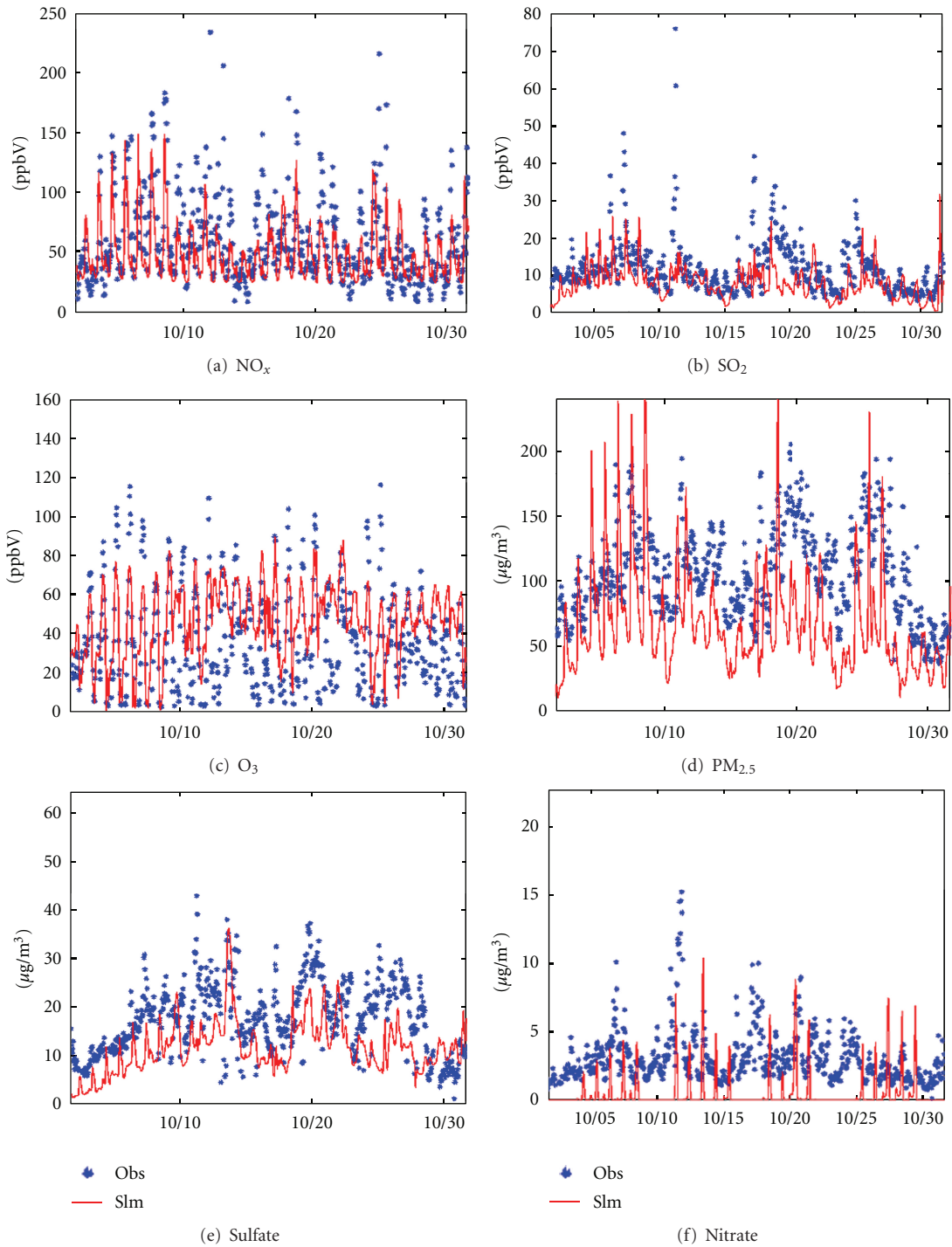


FIGURE 3: Comparison of modeled and observed (a) NO_x , (b) SO_2 , (c) O_3 , (d) $\text{PM}_{2.5}$, (e) aerosol sulfate, and (f) aerosol nitrate concentration at Yuen Long (YL) station in October 2004.

However, in other places over PRD region, the HONO chemistry does have potential to enhance the simulated O_3 peak value, which will be discussed in Section 3.6.

The modeled HONO mixing ratio increases by an order of magnitude after considering different HONO sources from direct emission, heterogeneous reactions

and surface photolysis reactions. The simulation case CB05+EM+HT+SP can predict 40% and 36% of the observation values in XK (1.1 ppbV) and GZ (4.2 ppbV) site, while the values for base case CB05 are only 4% and 2%, respectively. Normalized mean bias (NMB) at XK is lower during nighttime (NMB = -48%) than that during daytime

TABLE 2: Model performance of gaseous pollutant and particulate matter simulation over Hong Kong in October 2004 for case CB05.

		SO ₂ (ppb)	NO _x (ppb)	O ₃ (ppb)	PM _{2.5} (μg m ⁻³)	ASO ₄ (μg m ⁻³)	ANO ₃ (μg m ⁻³)
CW	Obv	18.6	47.3	42.5	76.2	21.6	4.4
	Sim	14.9	50.6	36.4	40.7	17.3	0.2
	IOA*	0.54	0.68	0.73	0.48	0.54	0.30
	RMSE*	4.8	20	14.3	41.3	12.1	4.0
	MNB* (%)	-19.3	7.3	-23.6	-44.6	-16.9	-95.2
	MNE* (%)	39.3	48.6	42.5	45.5	38.9	95.4
TM	Obv	8.6	18.6	63.2	62.5	—	—
	Sim	5.0	9.2	59.3	38.8	—	—
	IOA*	0.44	0.44	0.75	0.51	—	—
	RMSE*	3.6	11	11.1	33.6	—	—
	MNB* (%)	-26.9	-50.2	-3.9	-39.8	—	—
	MNE* (%)	52.1	57.3	25.1	48.2	—	—
TW	Obv	11.0	70.6	53.7	69.3	—	—
	Sim	6.8	62.8	30.2	35.5	—	—
	IOA*	0.43	0.59	0.52	0.50	—	—
	RMSE*	4.5	39	21.6	40.9	—	—
	MNB* (%)	-40.3	-10.6	-47.6	-40.5	—	—
	MNE* (%)	48.3	55.2	79.6	44.6	—	—
TC	Obv	16.9	43.2	80.6	72.6	—	—
	Sim	11.2	36.1	59.1	44.9	—	—
	IOA*	0.58	0.71	0.77	0.43	—	—
	RMSE	6.9	21	18.2	45.1	—	—
	MNB (%)	-26.3	-10.8	-33.2	-40.6	—	—
	MNE (%)	50.3	47.2	54.3	42.5	—	—
YL	Obv	24.9	84.1	89.3	72.6	18.3	6.9
	Sim	18.6	47.6	60.2	45.1	14.3	1.3
	IOA*	0.49	0.65	0.81	0.56	0.56	0.29
	RMSE*	5.2	36	15.3	40.2	10.3	6.1
	MNB* (%)	-22.1	-40.1	-28.1	-45.1	-23.5	-81.7
	MNE* (%)	44.1	54.1	39.9	49.6	39.6	83.7

* IOA: index of agreement, RMSE: root mean square error, MNB: mean normalized bias, MNE: mean normalized error.

(NMB = -71%), while at GZ site, the result is opposite (NMB = -63% during nighttime and (NMB = -57% during daytime). Verification for hourly HONO observations at XK site [52] shows that case CB05+EM+HT+SP can improve the model performance with the statistic metrics NMB from -95% to -54% and IOA from 0.35 to 0.56 compared with case CB05.

Predicted daytime average OH was 2.2×10^6 molec·cm⁻³ at XK for case CB05 (homogeneous reactions only) which increased to 2.3×10^6 molec·cm⁻³, 2.4×10^6 molec·cm⁻³, 2.5×10^6 molec·cm⁻³ for case CB05+EM, CB05+EM+HT, and case CB05+EM+HT+SP, respectively. Predicted daytime average OH was 1.5×10^6 molec·cm⁻³ at GZ for case CB05 (homogeneous reactions only) which increased to 1.7×10^6 molec·cm⁻³, 1.8×10^6 molec·cm⁻³, 1.9×10^6 molec·cm⁻³ for case CB05+EM, CB05+EM+HT, and CB05+EM+HT+SP, respectively. Thus, the additional HONO sources increased daytime OH by 13.6% and 26.7% at XK and GZ, respectively. OH concentration was measured during PRD-PRIDE 2006 campaign at the upper wind of

Guangzhou city [51]; the typical average daytime OH concentration in the similar is above 5×10^6 molec·cm⁻³, which is a factor of two higher than the simulated OH value here in GZ. It may suggest that current MM5-CMAQ modeling system tends to underestimate overall oxidization capacity due to the large uncertainty in VOC emission estimation over PRD region [76].

3.3. Spatial Pattern of HONO Simulation. Spatial patterns of simulated HONO distributions during daytime (Figures 5(a)–5(d)) and nighttime (Figures 5(e)–5(h)) are presented in Figure 5 separately. The HONO fields for different cases in Figure 5 are the daily average of October 28 with the maximum ozone enhancement during the simulation period. The distribution patterns of simulated HONO for daytime and nighttime are generally consistent with the NO_x emission pattern, which is due to the fact that HONO formation pathways are related to NO₂. Remarkable contrast for predicted daytime and nighttime HONO mixing ratio exists in different simulation cases. Mean nighttime HONO

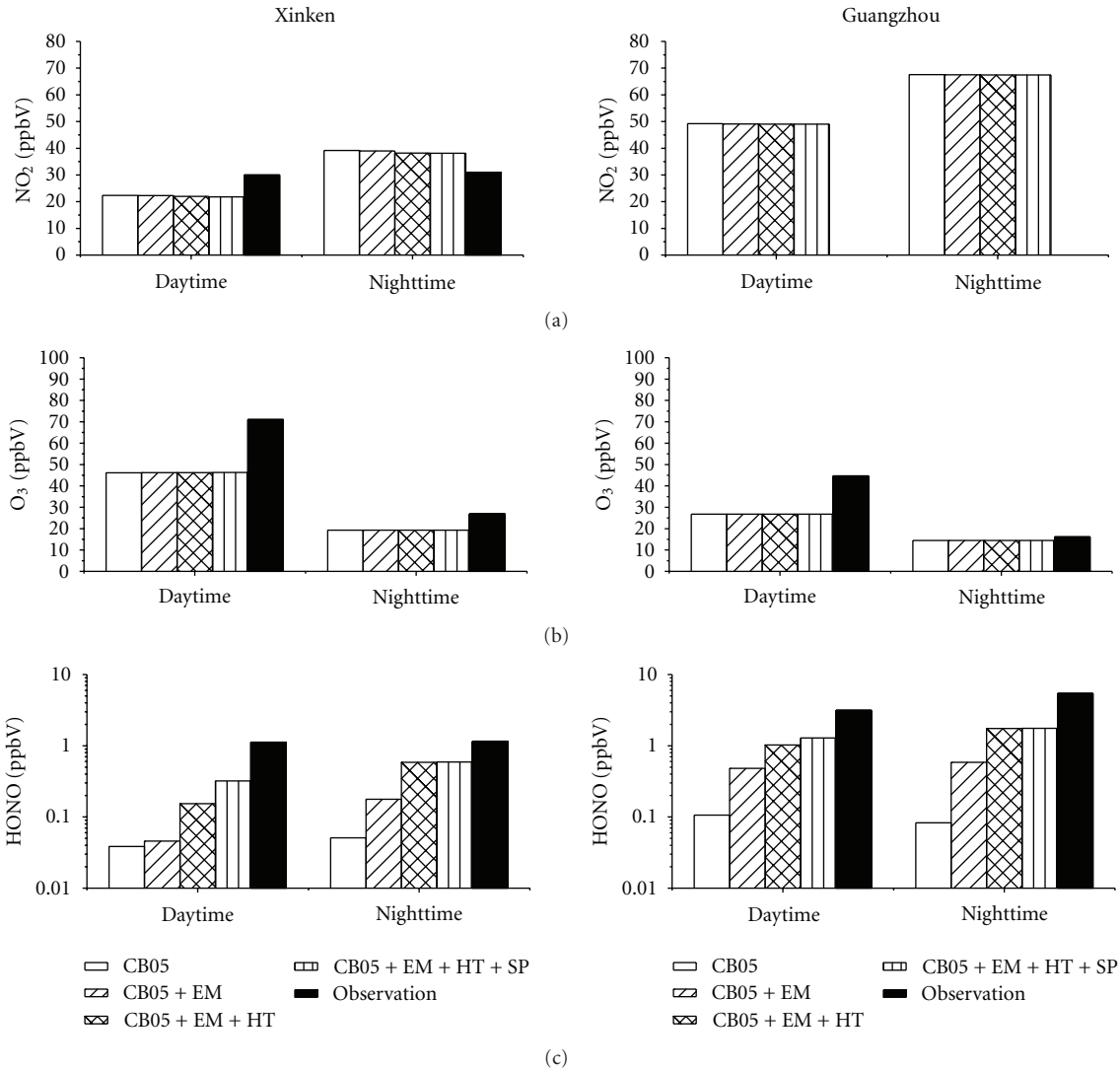


FIGURE 4: Model validations after incorporation of different HONO chemistry at Xinken (XK) and Guangzhou (GZ) site for (a) NO₂, (b) O₃, and (c) HONO simulation.

mixing ratio is about twice that of daytime value. For case CB05+EM+HT, this night-to-day contrast is more pronounced. Over the GZ area, the mean daytime HONO mixing ratio is around 2 ppbV while the predicted nighttime value is above 5 ppbV.

The simulated HONO level from base case (case CB05) is low with the mean daytime value of less than 500 pptV and nighttime value of 800 pptV. The addition of HONO emission (case CB05+EM) increased predicted HONO by 2~3 times. The heterogeneous reactions (case CB05+EM+HT) and surface photolysis (case CB05+EM+HT+SP) further enhanced the modeled HONO level, which resulted in more than 8~10 times greater than homogenous reaction only. Surface photolysis contributes more to the HONO enhancement during daytime due to the available solar radiation (the difference between Figures 5(c) and 5(d)), whereas heterogeneous reactions play a more important role in HONO formation at nighttime (the difference between Figures 5(g)

and 5(f) is as large as 200%). Results are consistent with those reported by Sarwar et al. [46].

3.4. Relative Contribution to HONO from Different Formation Pathways. The average diurnal relative contribution of the four HONO sources to predicted HONO concentration in XK and GZ site is shown in Figure 6. The relative contribution at each site is counted by subtracting the mean predicted value of different formation pathways (emission, heterogeneous reaction, and photolysis) to corresponding base case one at each hour. It can be found that the predicted nighttime HONO concentration is primarily controlled by heterogeneous reaction both at rural and urban sites (up to 89% in XK and 81% in GZ). During daytime, the contribution of surface photolysis increases with the increase of solar radiation. The maximum contribution can reach up to 64% in XK and 31% in GZ at the late afternoon. The relative contribution of direct HONO emission in rural

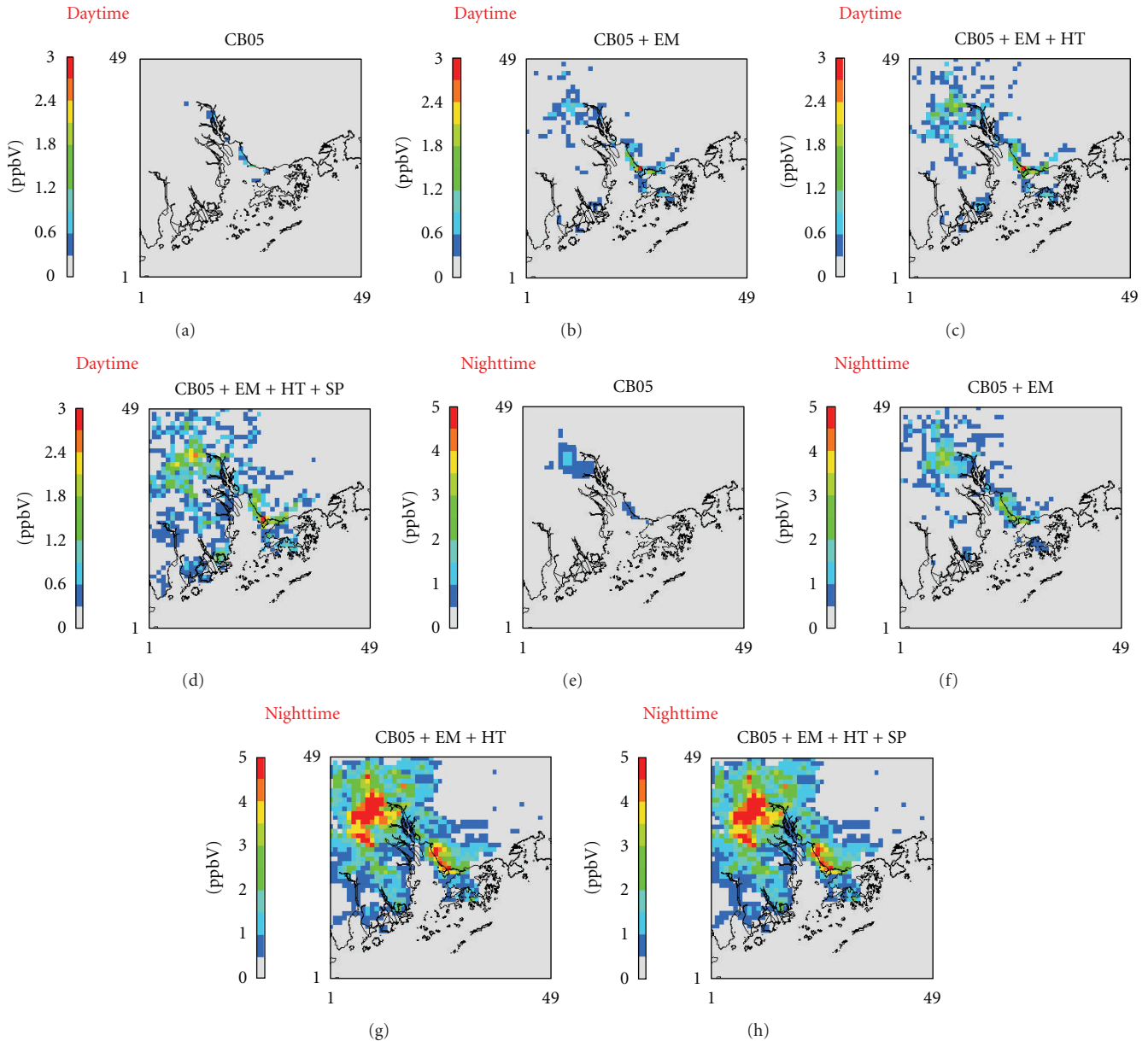


FIGURE 5: Spatial distribution of simulated HONO through homogeneous reactions, direct emission, heterogeneous reaction, and surface photolysis formation pathway at daytime (a–d) and nighttime (e–h).

site is greater at night and nearly negligible during the day due to very low traffic volume. The relative contribution of direct HONO emissions at urban site is relatively high (20–30%) with peak observed during morning and evening rush hour. The relatively high contribution from direct emission at GZ suggests the importance of accurately speciating NO_x emission from vehicles (e.g., reaction (R13)).

3.5. Sensitivity Study of Different HONO Simulation Cases. Three additional model simulations were conducted to investigate the sensitivity of different parameters on simulated HONO. The first parameter investigated is the NO_x emission (from motor vehicle) speciation. For air quality modeling

studies, NO_x emissions are typically speciated into NO and NO_2 by 90% and 10%, respectively (by volume). Long-term observation of NO_2/NO ratio in Hong Kong from vehicle emission suggested that the traditional speciation for NO_x emission may not be suitable for PRD area [77]. Higher NO_2 emission contribution may be due to the unique condition of mobile fleet composition and engine type usage in Hong Kong. Hence, a sensitivity run (case HONO_ NO_x) by using alternative NO_x emissions speciation is designed. For this study, NO_x was speciated into NO, NO_2 , and HONO by 85%, 13.8%, and 1.2%. In this sensitivity run, the impact of increased direct HONO emission on predicted HONO is investigated. The second parameter for the sensitivity

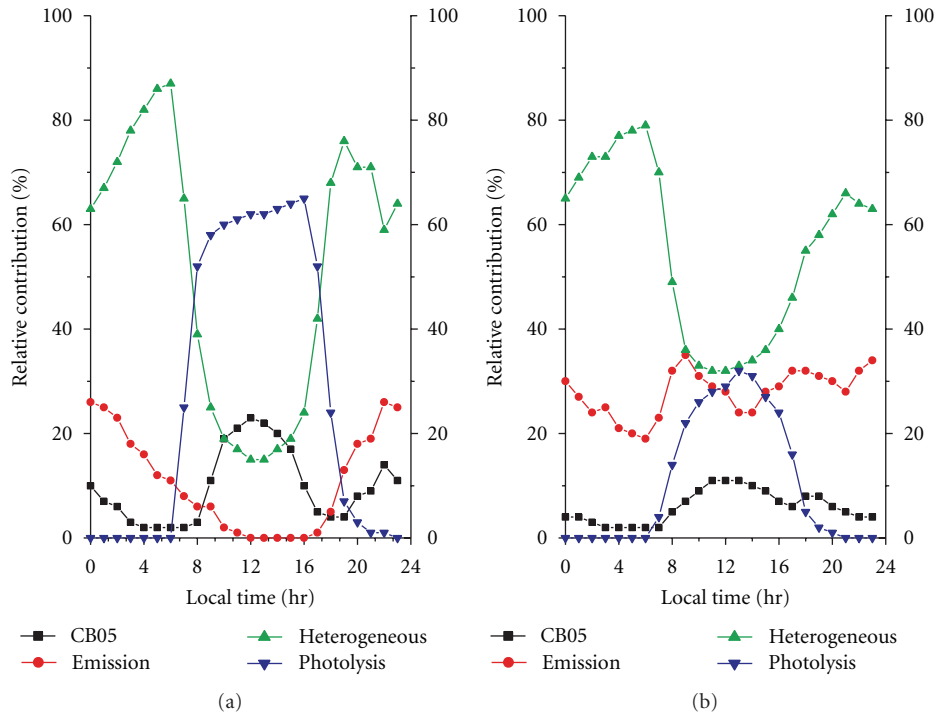


FIGURE 6: Average relative contributions of different HONO sources to predicted ground HONO concentration at (a) Xinken and (b) Guangzhou.

runs is the available surface area for heterogeneous reaction (case HONO_S/V). In case of CB05+EM+HT+SP, $[S/V]$ ratio for soil surface was set at 0.1 m^{-1} , and the $[S/V]$ for building surface in (3) was estimated using an $s_{\text{max}} = 0.3 \text{ m}^{-1}$. For PRD region, especially along the PRE area, the urban density and average building height are much higher than that in US condition [78] and hence may provide more available interface for heterogeneous reaction. For this study, $s_{\text{max}} = 1.0 \text{ m}^{-1}$ and $[S/V]_{\text{soil}} = 0.2 \text{ m}^{-1}$ were used. The third parameter is the HONO deposition velocity (case HONO_DV). An alternative lower deposition velocity taken the value of NO_2 was used as the surrogate in the model to increase the chance for surface HONO accumulation.

Figure 7 gives the diurnal pattern of simulated HONO at XK and GZ with different simulation cases. The mean observation diurnal variation with error bars over PRIDE-PRD2004 campaign is from Figure 3 of Zhang et al. [49]. The diurnal variation of different simulation cases is the mean of each local hour HONO mixing ratio over the simulation window. The characteristic of HONO diurnal profile over PRD region with high peak at night and relatively low during morning is consistent with the observation worldwide [9, 11–13]. The adding of direct emission (case CB05+EM) contributed to the HONO morning peak at the rush hour 0700~0800 local standard time (LST). The adding of heterogeneous reaction (case CB05+EM+HT) mainly contributed to the late afternoon (17:00–22:00 LST) buildup of HONO concentration. The simulation case HONO_S/V nearly followed the observed HONO diurnal variation pattern at GZ, but in XK, it shows that the large overestimation occurred after sunset. However, the current implementation cannot

repeat observed elevated HONO level late at night (02:00~06:00 LST); the model tends to have the steep jump after the peak near the midnight.

Simulated daytime and nighttime mean HONO mixing ratios at XK and GZ for different simulation cases are presented in Figure 8. Mean observed HONO at GZ at daytime is 4.17 ppbV , which is nearly four times greater than that at XK (1.12 ppbV). GZ site is located at an urban area, and NO_2 mixing ratios are much greater than those at the rural XK site. Thus, observed HONO at GZ is much greater than that at XK. Homogenous reactions (case CB05) can only explain 5% or less of the observed HONO, whereas the heterogeneous reactions contribute more than 30% of observed value both in daytime and nighttime.

Compared with simulation case CB05+EM+HT+SP, HONO increases at GZ from sensitivity run HONO_DV, HONO_NO_x, and HONO_S/V are 17%, 13%, and 157%, respectively; while at XK, the values are 37%, 9%, and 207%. The improvement at nighttime is better than that in daytime. Predicted HONO for HONO_S/V case agrees well both at GZ and XK at daytime but overestimates 60% during nighttime at XK. Results of sensitivity runs may suggest the importance of $[S/V]$ value for simulating HONO chemistry. While the PRD region has relatively high urban density and greater building height, the s_{max} value is not currently known. The model with $s_{\text{max}} = 1$ predicts HONO levels closer to the observed data in PRD both in terms of mean and diurnal variation. The details of the HONO chemistry are still unknown. The use of currently known HONO reactions in air quality model does not reproduce observed HONO levels in PRD. Until the details of the HONO chemistry are known,

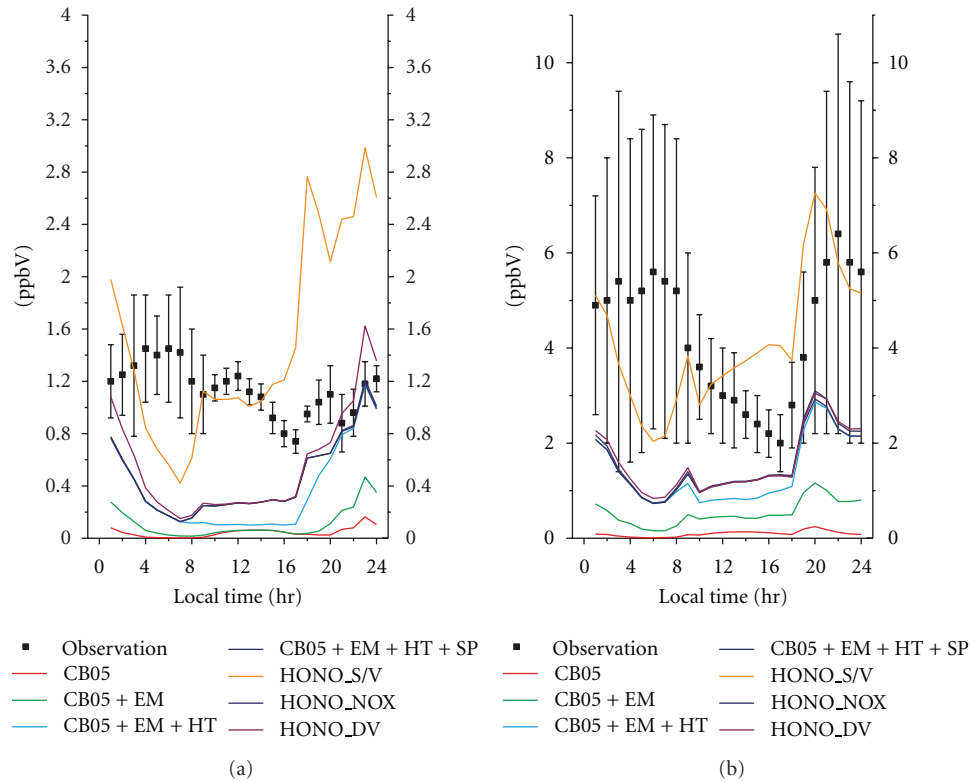


FIGURE 7: Diurnal pattern of simulated HONO at (a) Xinken and (b) Guangzhou with difference simulation cases.

this s_{\max} value can be used in the model for PRD. This is an empirical parameter that produces HONO closer to observed data in PRD and is not intended for other urban areas.

The production of HONO via heterogeneous reaction at ground using procedure described by Aumont et al. [17] (case HONO_G) was also tested. Consistent with the results reported, Sarwar et al. [46] predicted nighttime HONO was 30%–67% lower than the values obtained with CB05+EM+HT+SP and 66%–236% lower than the observed data.

The importance of HONO formation from heterogeneous reaction on semivolatile organics was also examined (case HONO_SOA) using the procedure of Li et al. [18]. HONO production from diesel bound NO_x emission at ground was parameterized as HONO source using the conversion factor of 0.023. The predicted daytime and nighttime mean HONO mixing ratios are 18%–33% higher than that of case CB05+EM+HT+SP but with larger variations (see Figure 8). However, the results were still 43%–57% and 19%–54% lower than corresponding observed data at nighttime and daytime, which suggests that the contribution of the semivolatile organics heterogeneous reaction to HONO formation may subject to high uncertainty and need to parameterize carefully in future.

3.6. Impact of HONO Chemistry on Ozone and PM. The spatial distribution of the largest enhancements of daily maximum 8-hour O_3 and daily mean $\text{PM}_{2.5}$ due to the additional

HONO sources is presented in Figure 9. The largest enhancement occurred on October 28th with northeasterly moderate synoptic wind and relatively steady atmosphere [72]. Daily maximum 8-hour O_3 increased by up to 6 ppbV near the downwind of GZ city with simulated O_3 level of 90 ppbV in base case run (case CB05). The impact on daily mean $\text{PM}_{2.5}$ is relatively significant with the largest increase of nearly $17 \mu\text{g}/\text{m}^3$ or 12% at GZ, the downwind of GZ, Shenzhen area, and northwest of Hong Kong. The impact of additional HONO sources on aerosol sulfate and secondary organic aerosols was small; however, the impact on ammonium and nitrate was relatively large (3.6 and $12.0 \mu\text{g}/\text{m}^3$, resp.) which subsequently enhanced $\text{PM}_{2.5}$. The additional OH from the photolysis of enhanced HONO reacts with NO_2 and produces additional HNO_3 which subsequently generates greater aerosol nitrate and ammonium.

The largest enhancement in morning O_3 (8 am noon), daily maximum 8-hour O_3 , and daily mean $\text{PM}_{2.5}$ in the modeling domain for each day is shown in Table 3. The largest enhancement in daily maximum 8-hour O_3 ranged between 3 and 7 ppbV, while the largest enhancement in morning O_3 ranged between 3 and 9 ppbV. Levels of the morning O_3 increases are generally similar to those of daily maximum 8-hour O_3 . The accumulated HONO at night undergoes photolysis during the day and produces OH which drives the photochemistry and enhances O_3 . The largest enhancement in daily mean $\text{PM}_{2.5}$ ranged between 4 and $17 \mu\text{g}/\text{m}^3$. As mentioned earlier, ambient observed O_3 and $\text{PM}_{2.5}$ data in PRD region outside Hong Kong are not

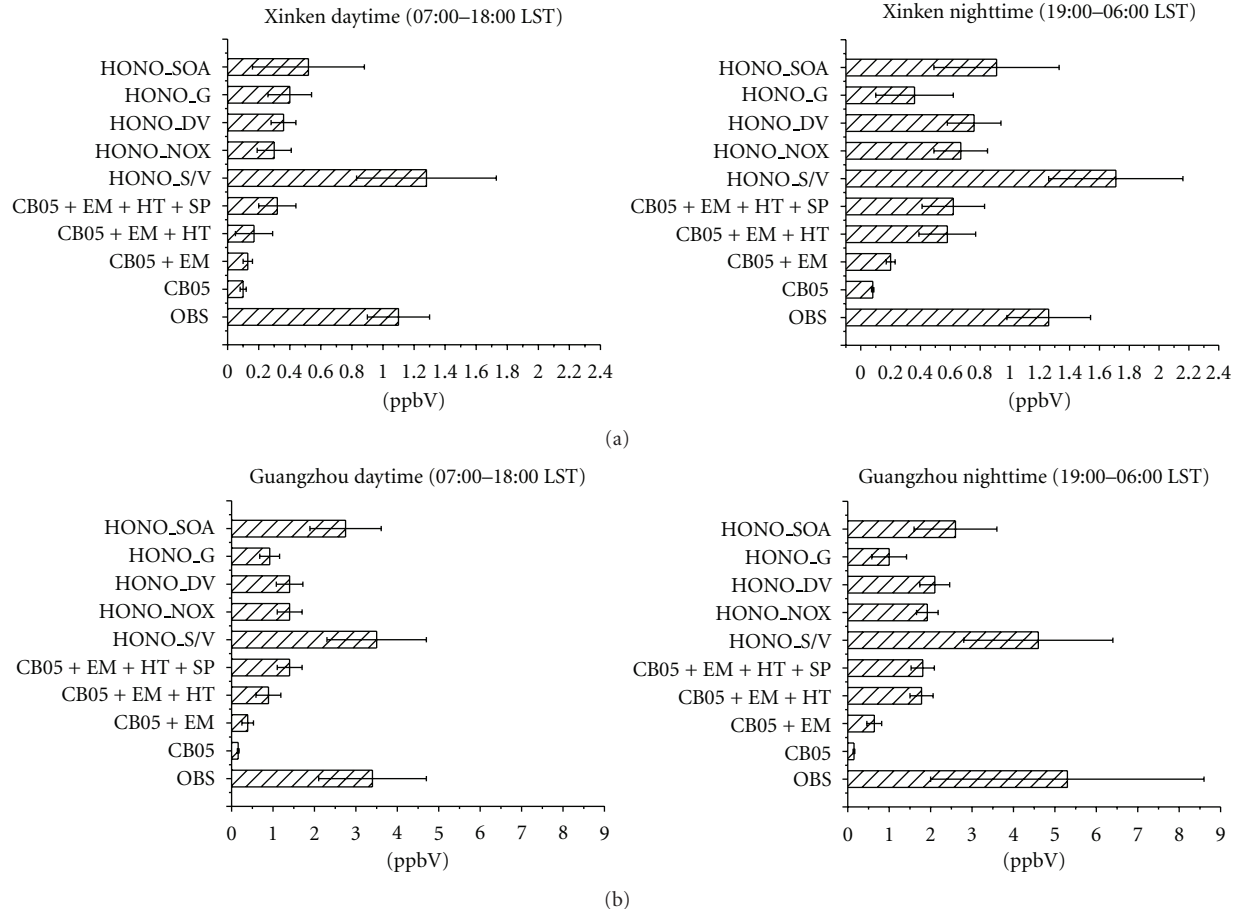


FIGURE 8: Simulated mean daytime and nighttime HONO concentration in (a) Xinken and (b) Guangzhou for different simulation case.

publicly available, and thus, increases in predicted mixing ratios cannot be compared with observed data.

The impact of additional HONO sources on O_3 control strategy is also investigated. Urban areas of PRD are mostly VOC limited for O_3 production [49]; thus, only response of 25% VOC emission reduction was investigated (cases 0.75 VOC and 0.75 VOC w/HONO). The relative response factor (RRF) is calculated to quantify the response of O_3 under different chemical mechanisms. RRF is the average ratio of simulated O_3 mixing ratio with and without reduced emissions. RRF at several cities over PRD with and without additional HONO sources is presented in Figure 10. Relatively high response was obtained in cities where intensive NO_x and VOC emissions are present. The use of additional sources affected the RRF for many cities as shown in the figure. For example, predicted RRF without the additional HONO sources at FS was 0.87 (13% O_3 decrease) due to the 25% VOC emission reduction. The inclusion of additional HONO sources changed the RRF to 0.85 or 15% O_3 decrease due to the same VOC emission reduction (2% increase in O_3 response). Impact on RRF at other cities was also similar. Thus, the use of additional HONO sources in the model affects the O_3 control strategy.

4. Summary

This study investigated the contribution of HONO sources to the photochemistry over PRD using the MM5-SMOKE-CMAQ model system. In addition to the gas-phase reactions, additional heterogeneous and surface photolysis HONO formation pathways and direct emissions were incorporated into the model. 10-day ozone episode in October 2004 was chosen to simulate impact of different HONO sources to HONO formation and ozone and $PM_{2.5}$ yields. The inclusion of additional sources improved HONO predictions significantly with HONO enhancement 8–10 times greater than homogenous reaction. The simulated HONO mean diurnal profiles were compared with observations at rural site XK and urban site GZ. The model can generally produce the daytime variation but cannot maintain the observed elevated HONO late at night. In terms of the relative contribution of different pathway to HONO formation, the weighting from homogenous reaction is no more than 10% both at urban and rural site, while the heterogeneous and daytime surface photolysis reactions can dominate 69%~83% contributions with comparable weightings. Direct emission contribution is more important at urban site than that in rural site.

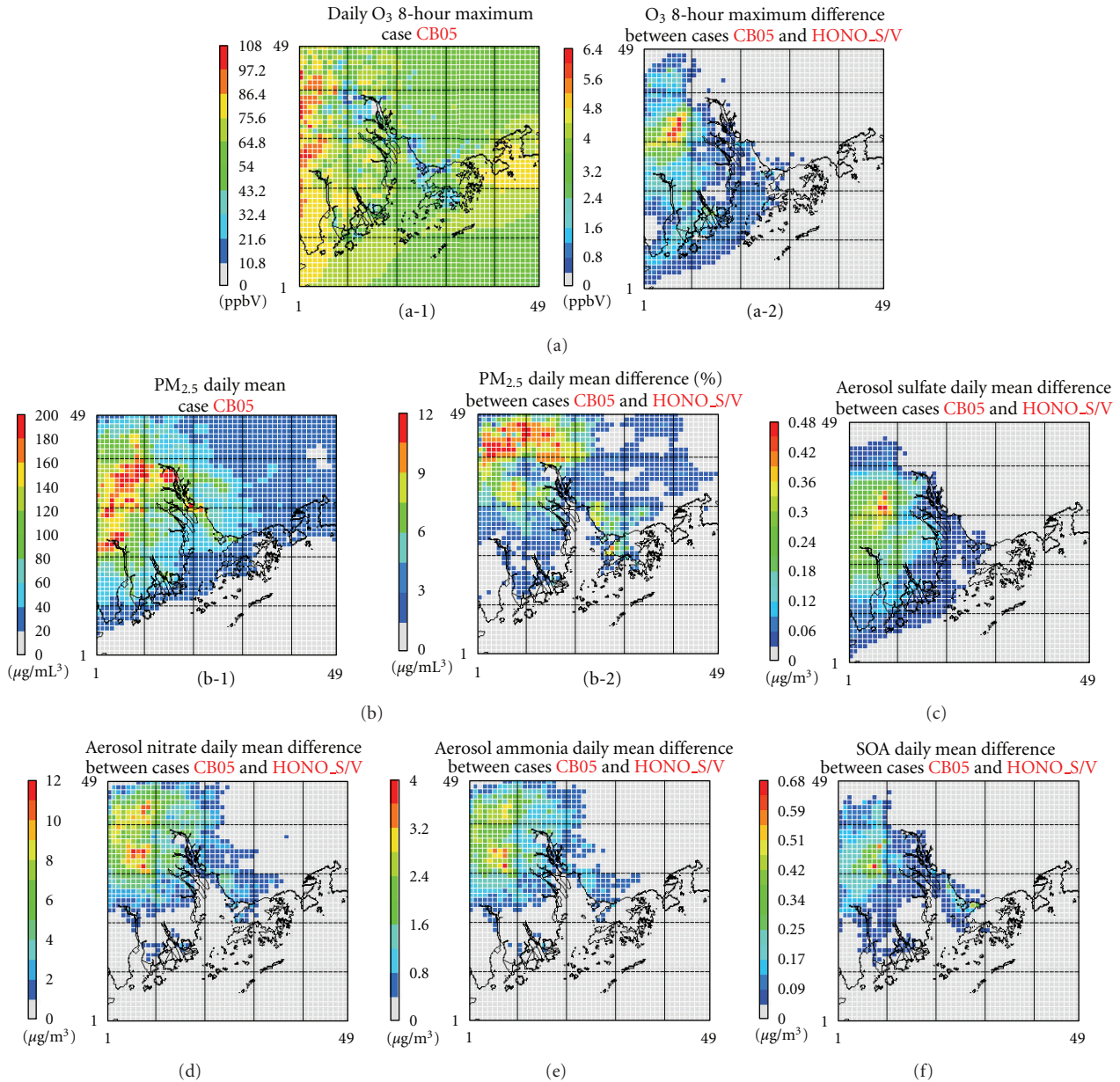


FIGURE 9: Spatial distribution of the maximum enhancement due to the HONO chemistry during the entire simulation period for (a)* daily 8-hour maximum ozone, (b)* daily mean PM_{2.5}, (c) daily mean aerosol sulfate, (d) daily mean aerosol nitrate, (e) daily mean aerosol ammonia, and (f) daily mean SOA. *(a-1) and (b-1) are the spatial distribution of base case simulation CB05, while (a-2) and (b-2) are the spatial distribution of difference between simulation cases HONO_S/V and CB05 (see Table 1).

The inclusion of additional HONO sources enhanced daily maximum 8-hour O₃ by up to 7 ppbV (8%) and daily average PM_{2.5} up to 17 µg/m³ (12%) over the downwind area of GZ. The use of additional HONO sources also affected the O₃ control strategy.

Results of sensitivity studies suggest that the parameterization of surface area for heterogeneous reactions is an important factor that can affect simulated HONO. However, surface area estimates needed for these heterogeneous reactions are not currently available; hence, implementations

of these reactions in air quality models require simplifying assumptions. Thus, the details of these reactions (e.g., their dependence on types of surface, relative humidity, etc.) along with the estimates of available surface areas should be investigated in the future. The atmospheric chemistry community is actively investigating possible HONO sources and it is likely that additional HONO sources, will be identified in the future. When these additional HONO sources are known, the impact of HONO chemistry on air quality in PRD can be reevaluated.

TABLE 3: The largest enhancement in morning (8 am—noon) O₃, daily maximum O₃, and daily mean PM_{2.5} in the modeling domain due the additional HONO sources (case HONO S/V subtract case CB05).

Date	The largest enhancement in morning O ₃ (ppbV)	The largest enhancement in daily maximum 8-hour O ₃ (ppbV)	The largest enhancement in daily PM ₁₀ (μg/m ³)
Oct 22, 2004	4	4	4
Oct 23, 2004	5	4	7
Oct 24, 2004	4	3	6
Oct 25, 2004	5	3	9
Oct 26, 2004	3	3	6
Oct 27, 2004	3	3	8
Oct 28, 2004	4	5	17
Oct 29, 2004	7	7	17
Oct 30, 2004	6	6	7
Oct 31, 2004	9	7	6
Nov 1, 2004	3	5	15

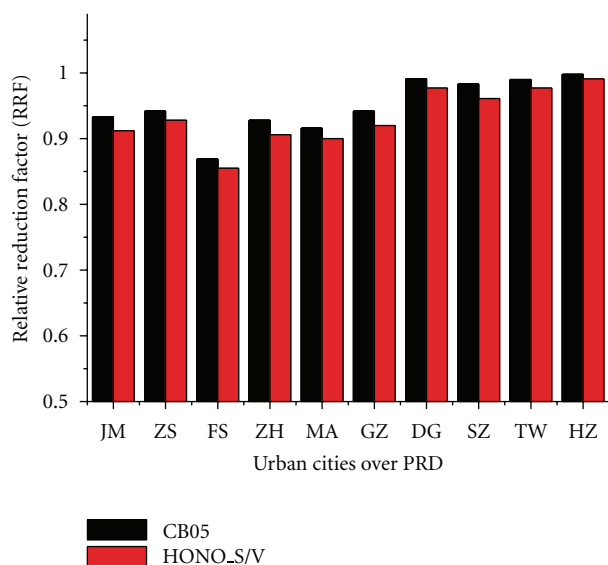


FIGURE 10: Average relative reduction factor (RRF) for ozone is due to 25% VOC emission reduction using simulation cases CB05 and HONO_S/V. The major cities over PRD are ordered by longitude from west to east (see Figure 1): JM: Jiangmen, ZS: Zhongshan, FS: Foshan, ZH: Zhuhai, Ma: Macau, GZ: Guangzhou, DG: Dongguan, SZ: Shenzhen, TW: Tsuen Wan, and HZ: Huizhou.

Acknowledgments

This project was supported by HKUST Oversea Research Grant for PhD student, Grants from the Research Grant Council of Hong Kong (RGC612807, RGC615406), and NSFC/RGC Joint Research Scheme (N_HKUST630/04, N_HKUST631/05). Although this paper has been reviewed by EPA and approved for publication, it does not necessarily reflect EPA's policies or views.

References

- [1] G. W. Harris, W. P. L. Cater, A. M. Winer, J. N. Pitts, U. Platt, and D. Perner, "Observations of nitrous acid in the Los Angeles atmosphere and implications for predictions of ozone-precursor relationships," *Environmental Science Technology*, vol. 16, no. 7, pp. 414–419, 1982.
- [2] M. E. Jenkin, R. A. Cox, and D. J. Williams, "Laboratory studies of the kinetics of formation of nitrous acid from the thermal reaction of nitrogen dioxide and water vapour," *Atmospheric Environment*, vol. 22, no. 3, pp. 487–498, 1988.
- [3] A. M. Winer and H. W. Biermann, "Long pathlength differential optical absorption spectroscopy (Doas) measurements of gaseous HONO, NO₂ and HCNO in the California South Coast Air Basin," *Research on Chemical Intermediates*, vol. 20, no. 3–5, pp. 423–445, 1994.
- [4] T. Staffelbach, A. Neftel, and L. W. Horowitz, "Photochemical oxidant formation over Southern Switzerland 2. Model results," *Journal of Geophysical Research D*, vol. 102, no. 19, pp. 23363–23373, 1997.
- [5] B. Alicke, U. Platt, and J. Stutz, "Impact of nitrous acid photolysis on the total hydroxyl radical budget during the Limitation of Oxidant Production/Pianura Padana Produzione di Ozono study in Milan," *Journal of Geophysical Research D*, vol. 107, no. 22, article 8196, 2002.
- [6] B. Alicke, A. Geyer, A. Hofzumahaus et al., "OH formation by HONO photolysis during the BERLIOZ experiment," *Journal of Geophysical Research D*, vol. 108, article 8247, 17 pages, 2003.
- [7] K. Acker, D. Möller, W. Wieprecht et al., "Strong daytime production of OH from HNO₂ at a rural mountain site," *Geophysical Research Letters*, vol. 33, Article ID L02809, 2006.
- [8] Y. H. Zhang, H. Su, L. J. Zhong et al., "Regional ozone pollution and observation-based approach for analyzing ozone-precursor relationship during the PRIDE-PRD2004 campaign," *Atmospheric Environment*, vol. 42, no. 25, pp. 6203–6218, 2008.
- [9] Y. F. Elshorbany, R. Kurtenbach, P. Wiesen et al., "Oxidation capacity of the city air of Santiago, Chile," *Atmospheric Chemistry and Physics*, vol. 9, no. 6, pp. 2257–2273, 2009.
- [10] K. D. Lu, Y. H. Zhang, H. Su et al., "Regional ozone pollution and key controlling factors of photochemical ozone production in Pearl River Delta during summer time," *Science China Chemistry*, vol. 53, no. 3, pp. 651–663, 2010.
- [11] J. Kleffmann, T. Gavriloaiei, A. Hofzumahaus et al., "Daytime formation of nitrous acid: a major source of OH radicals in a forest," *Geophysical Research Letters*, vol. 32, Article ID L05818, 4 pages, 2005.
- [12] X. Ren, W. H. Brune, A. Oligier et al., "OH, HO₂, and OH reactivity during the PMTACS-NY Whiteface Mountain 2002 campaign: observations and model comparison," *Journal of Geophysical Research D*, vol. 111, Article ID D10S03, 2006.
- [13] J. Mao, X. Ren, S. Chen et al., "Atmospheric oxidation capacity in the summer of Houston 2006: comparison with summer measurements in other metropolitan studies," *Atmospheric Environment*, vol. 44, no. 33, pp. 4107–4115, 2010.
- [14] J. G. Calvert, G. Yarwood, and A. M. Dunker, "An evaluation of the mechanism of nitrous acid formation in the urban atmosphere," *Research on Chemical Intermediates*, vol. 20, no. 3–5, pp. 463–502, 1994.
- [15] G. Lammel and J. N. Cape, "Nitrous acid and nitrate in the atmosphere," *Chemical Society Reviews*, vol. 25, pp. 361–369, 1996.

- [16] J. Kleffmann, "Daytime sources of nitrous acid (HONO) in the atmospheric boundary layer," *ChemPhysChem*, vol. 8, no. 8, pp. 1137–1144, 2007.
- [17] B. Aumont, F. Chervier, and S. Laval, "Contribution of HONO sources to the $\text{NO}_x/\text{HO}_x/\text{O}_3$ chemistry in the polluted boundary layer," *Atmospheric Environment*, vol. 37, no. 4, pp. 487–498, 2003.
- [18] G. Li, W. Lei, M. Zavala et al., "Impacts of HONO sources on the photochemistry in Mexico City during the MCMA-2006/MILAGO Campaign," *Atmospheric Chemistry and Physics*, vol. 10, no. 14, pp. 6551–6567, 2010.
- [19] C. Kessler and U. Platt, "Nitrous acid in polluted air masses—sources and formation pathways," in *Physico-Chemical Behaviour of Atmospheric Pollutants (Proceedings)*, B. Versino and G. Angeletti, Eds., pp. 412–422, Reidel, Dordrecht, The Netherlands, 1984.
- [20] R. Kurtenbach, K. H. Becker, J. A. G. Gomes et al., "Investigations of emissions and heterogeneous formation of HONO in a road traffic tunnel," *Atmospheric Environment*, vol. 35, no. 20, pp. 3385–3394, 2001.
- [21] T. W. Kirchstetter, R. A. Harley, and D. Littlejohn, "Measurement of nitrous acid in motor vehicle exhaust," *Environmental Science & Technology*, vol. 30, no. 9, pp. 2843–2849, 1996.
- [22] S. Li, J. Matthews, and A. Sinha, "Atmospheric hydroxyl radical production from electronically excited NO_2 and H_2O ," *Science*, vol. 319, no. 5870, pp. 1657–1660, 2008.
- [23] G. Sarwar, R. W. Pinder, K. W. Appel, R. Mathur, and A. G. Carlton, "Examination of the impact of photoexcited NO_2 chemistry on regional air quality," *Atmospheric Environment*, vol. 43, no. 40, pp. 6383–6387, 2009.
- [24] J. N. Crowley and S. Carl, "OH formation in the photoexcitation of NO_2 beyond the dissociation threshold in the presence of water vapor," *Journal of Physical Chemistry A*, vol. 101, no. 23, pp. 4178–4184, 1997.
- [25] S. Carr, D. E. Heard, and M. A. Blitz, "Comment on 'atmospheric hydroxyl radical production from electronically excited NO_2 and H_2O '," *Science*, vol. 324, no. 5925, p. 336, 2009.
- [26] S. Li, J. Matthews, and A. Sinha, "Response to comment on 'atmospheric hydroxyl radical production from electronically excited NO_2 and H_2O '," *Science*, vol. 324, no. 5925, p. 336, 2009.
- [27] G. Yarwood, S. Rao, M. Yocke, and G. Whitten, "Updates to the carbon bond chemical mechanism: CB05, final report to the U.S. EPA, RT-0400675," 2005, <http://www.camx.com/>.
- [28] I. Bejan, Y. Abd El Aal, I. Barnes et al., "The photolysis of *ortho*-nitrophenols: a new gas phase source of HONO," *Physical Chemistry Chemical Physics*, vol. 8, no. 17, pp. 2028–2035, 2006.
- [29] R. Svensson, E. Ljungstrom, and O. Lindqvist, "Kinetics of the reaction between nitrogen dioxide and water vapour," *Atmospheric Environment*, vol. 21, no. 7, pp. 1529–1539, 1987.
- [30] R. F. Graham and B. J. Tyler, "Formation of nitrous acid in a gas-phase stirred flow reactor," *Journal of the Chemical Society, Faraday Transactions 1*, vol. 68, pp. 683–688, 1972.
- [31] J. Kleffmann, K. H. Becker, and P. Wiesen, "Heterogeneous NO_2 conversion processes on acid surfaces: possible atmospheric implications," *Atmospheric Environment*, vol. 32, no. 16, pp. 2721–2729, 1998.
- [32] B. J. Finlayson-Pitts, L. M. Wingen, A. L. Sumner, D. Syomin, and K. A. Ramazan, "The heterogeneous hydrolysis of NO_2 in laboratory systems and in outdoor and indoor atmospheres: an integrated mechanism," *Physical Chemistry Chemical Physics*, vol. 5, no. 2, pp. 223–242, 2003.
- [33] M. Ammann, M. Kalberer, D. T. Jost et al., "Heterogeneous production of nitrous acid on soot in polluted air masses," *Nature*, vol. 395, no. 6698, pp. 157–160, 1998.
- [34] L. Gutzwiller, F. Arens, U. Baltensperger, H. W. Gaggeler, and M. Ammann, "Significance of semivolatile diesel exhaust organics for secondary HONO formation," *Environmental Science & Technology*, vol. 36, no. 4, pp. 677–682, 2002.
- [35] J. Kleffmann, K. H. Becker, M. Lackhoff, and P. Wiesen, "Heterogeneous conversion of NO_2 on carbonaceous surfaces," *Physical Chemistry Chemical Physics*, vol. 1, no. 24, pp. 5443–5450, 1999.
- [36] F. Arens, L. Gutzwiller, U. Baltensperger, H. W. Gaggeler, and M. Ammann, "Heterogeneous reaction of NO_2 on diesel soot particles," *Environmental Science & Technology*, vol. 35, no. 11, pp. 2191–2199, 2001.
- [37] A. M. Rivera-Figueroa, A. L. Sumner, and B. J. Finlayson-Pitts, "Laboratory studies of potential mechanisms of renoxification of tropospheric nitric acid," *Environmental Science & Technology*, vol. 37, no. 3, pp. 548–554, 2003.
- [38] E. M. Knipping and D. Dabdub, "Modeling surface-mediated renoxification of the atmosphere via reaction of gaseous nitric oxide with deposited nitric acid," *Atmospheric Environment*, vol. 36, no. 36–37, pp. 5741–5748, 2002.
- [39] K. Stemmler, M. Ammann, C. Donders, J. Kleffmann, and C. George, "Photosensitized reduction of nitrogen dioxide on humic acid as a source of nitrous acid," *Nature*, vol. 440, no. 7081, pp. 195–198, 2006.
- [40] K. Stemmler, M. Ndour, Y. Elshorbany et al., "Light induced conversion of nitrogen dioxide into nitrous acid on submicron humic acid aerosol," *Atmospheric Chemistry and Physics*, vol. 7, no. 16, pp. 4237–4248, 2007.
- [41] X. Zhou, K. Civerolo, H. Dai, G. Huang, J. J. Schwab, and K. L. Demerjian, "Summertime nitrous acid chemistry in the atmospheric boundary layer at a rural site in New York State," *Journal of Geophysical Research D*, vol. 107, no. 21, article 4590, 2002.
- [42] K. A. Ramazan, D. Syomin, and B. J. Finlayson-Pitts, "The photochemical production of HONO during the heterogeneous hydrolysis of NO_2 ," *Physical Chemistry Chemical Physics*, vol. 6, no. 14, pp. 3836–3843, 2004.
- [43] M. E. Monge, B. D'Anna, L. Mazri et al., "Light changes the atmospheric reactivity of soot," *Proceedings of the National Academy of Sciences of the United States of America*, vol. 107, no. 15, pp. 6605–6609, 2010.
- [44] B. Vogel, H. Vogel, J. Kleffmann, and R. Kurtenbach, "Measured and simulated vertical profiles of nitrous acid—Part II. Model simulations and indications for a photolytic source," *Atmospheric Environment*, vol. 37, no. 21, pp. 2957–2966, 2003.
- [45] W. Lei, R. Zhang, X. Tie, and P. Hess, "Chemical characterization of ozone formation in the Houston-Galveston area: a chemical transport model study," *Journal of Geophysical Research D*, vol. 109, Article ID D12301, 15 pages, 2004.
- [46] G. Sarwar, S. J. Roselle, R. Mathur, W. Appel, R. L. Dennis, and B. Vogel, "A comparison of CMAQ HONO predictions with observations from the Northeast Oxidant and Particle Study," *Atmospheric Environment*, vol. 42, no. 23, pp. 5760–5770, 2008.
- [47] M. Gonçalves, D. Dabdub, W. L. Chang, F. Saiz, O. Jorba, and J. M. Baldasano, "The impact of different nitrous acid sources in the air quality levels of the Iberian Peninsula," *Atmospheric Chemistry and Physics Discussion*, vol. 10, pp. 28183–28230, 2010.

- [48] M. Hu, F. M. Zhou, K. S. Shao, Y. H. Zhang, X. Y. Tang, and J. Slanina, "Diurnal variations of aerosol chemical compositions and related gaseous pollutants in Beijing and Guangzhou," *Journal of Environmental Science and Health A*, vol. 37, no. 4, pp. 479–488, 2002.
- [49] Y. H. Zhang, M. Hu, L. J. Zhong et al., "Regional integrated experiments on air quality over Pearl River Delta 2004 (PRIDE-PRD2004): overview," *Atmospheric Environment*, vol. 42, no. 25, pp. 6157–6173, 2008.
- [50] M. Qin, P. H. Xie, H. Su et al., "An observational study of the HONO-NO₂ coupling at an urban site in Guangzhou City, South China," *Atmospheric Environment*, vol. 43, no. 36, pp. 5731–5742, 2009.
- [51] A. Hofzumahaus, F. Rohrer, K. Lu et al., "Amplified trace gas removal in the troposphere," *Science*, vol. 324, no. 5935, pp. 1702–1704, 2009.
- [52] H. Su, Y. F. Cheng, P. Cheng et al., "Observation of nighttime nitrous acid (HONO) formation at a non-urban site during PRIDE-PRD2004 in China," *Atmospheric Environment*, vol. 42, no. 25, pp. 6219–6232, 2008.
- [53] K. D. Lu, Y. H. Zhang, H. Su et al., "Oxidant (O₃+ NO₂) production processes and formation regimes in Beijing," *Journal of Geophysical Research D*, vol. 115, Article ID D07303, 18 pages, 2010.
- [54] D. Byun and K. L. Schere, "Review of the governing equations, computational algorithms, and other components of the models-3 Community Multiscale Air Quality (CMAQ) modeling system," *Applied Mechanics Reviews*, vol. 59, no. 1–6, pp. 51–76, 2006.
- [55] J. E. Pleim and J. S. Chang, "A non-local closure model for vertical mixing in the convective boundary layer," *Atmospheric Environment A*, vol. 26, no. 6, pp. 965–981, 1992.
- [56] B. Schell, I. J. Ackermann, H. Hass, F. S. Binkowski, and A. Ebel, "Modeling the formation of secondary organic aerosol within a comprehensive air quality model system," *Journal of Geophysical Research D*, vol. 106, no. 22, pp. 28275–28293, 2001.
- [57] A. Nenes, C. Pilinis, and S. N. Pandis, "ISORROPIA: a new thermodynamic equilibrium model for multiphase multicomponent inorganic aerosols," *Aquatic Geochemistry*, vol. 4, no. 1, pp. 123–152, 1998.
- [58] F. S. Binkowski and S. J. Roselle, "Models-3 Community Multiscale Air Quality (CMAQ) model aerosol component 1. Model description," *Journal of Geophysical Research D*, vol. 108, no. 4183, 18 pages, 2003.
- [59] G. A. Grell, J. Dudhia, and D. R. Stauffer, "A description of the fifth-generation Penn State/NCAR mesoscale model (MM5)," NCAR Technical Note NCAR/TN-398+STR, National Center for Atmospheric Research, Boulder, Colo, USA, 1994.
- [60] S. H. L. Yim, J. C. H. Fung, A. K. H. Lau, and S. C. Kot, "Developing a high-resolution wind map for a complex terrain with a coupled MM5/CALMET system," *Journal of Geophysical Research D*, vol. 112, no. 5, Article ID D05106, 2007.
- [61] J. C. F. Lo, A. K. H. Lau, J. C. H. Fung, and F. Chen, "Investigation of enhanced cross-city transport and trapping of air pollutants by coastal and urban land-sea breeze circulations," *Journal of Geophysical Research*, vol. 111, Article ID D14104, 2006.
- [62] X. Lu, K. C. Chow, T. Yao, J. C. H. Fung, and A. K. H. Lau, "Seasonal variation of the land-sea breeze circulation in the Pearl River Delta region," *Journal of Geophysical Research D*, vol. 114, no. 17, Article ID D17112, 2009.
- [63] J. P. Huang, J. C. H. Fung, and A. K. H. Lau, "Integrated processes analysis and systematic meteorological classification of ozone episodes in Hong Kong," *Journal of Geophysical Research D*, vol. 111, Article ID D20309, 14 pages, 2006.
- [64] R. H. F. Kwok, J. C. H. Fung, A. K. H. Lau, and J. S. Fu, "Numerical study on seasonal variations of gaseous pollutants and particulate matters in Hong Kong and Pearl River Delta region," *Journal of Geophysical Research D*, vol. 115, Article ID D16308, 2010.
- [65] M. R. Houyoux, J. M. Vukovich, C. J. Coats Jr., N. M. Wheeler, and P. S. Kasibhatla, "Emission inventory development and processing for the seasonal model for regional air quality (SMRAQ) project," *Journal of Geophysical Research D*, vol. 105, no. 7, pp. 9079–9090, 2000.
- [66] CH2M HILL (China) Limited, "Study of air quality in the Pearl River Delta region, technique report (Agreement No. CE 106/98) prepared for the Hong Kong Environmental Protection Department," Hong Kong Administrative Region Government, 2011, <http://www.epd.gov.hk/epd/english/environmentinhk/air/study/rpts/study-pearl.html>.
- [67] USEPA, "SPECIATE data base V3.1," Research Triangle Park, NC, US, 2000, <http://www.epa.gov/ttn/chief/software/speciate/speciate32.html>.
- [68] J. E. Pleim and A. Xiu, "Development and testing of a surface flux and planetary boundary layer model for application in mesoscale models," *Journal of Applied Meteorology*, vol. 34, no. 1, pp. 16–32, 1995.
- [69] M. R. Jones, *Ammonia deposition to semi-natural vegetation [Ph.D. dissertation]*, University of Dundee, Scotland, UK, 2006.
- [70] C. X. Cai, *Implementation and performance evaluation on an air quality forecast modeling system (AQFMS) for northeastern USA [Ph.D. dissertation]*, Department of Earth and Atmospheric Science, University at Albany, State University of New York, Albany, NY, USA, 2005.
- [71] X. L. Zhou, H. L. Gao, Y. He et al., "Nitric acid photolysis on surfaces in low-NO_x environments: significant atmospheric implications," *Geophysical Research Letters*, vol. 30, no. 2217, 4 pages, 2003.
- [72] S. J. Fan, B. M. Wang, M. Tesche et al., "Meteorological conditions and structures of atmospheric boundary layer in October 2004 over Pearl River Delta area," *Atmospheric Environment*, vol. 42, no. 25, pp. 6174–6186, 2008.
- [73] C. J. Willmott, "On the validation of models," *Physical Geography*, vol. 2, no. 2, pp. 184–194, 1981.
- [74] USEPA, "Guidance on the use of models and other analyses in attainment demonstrations for the 8-hour ozone NAAQS," EPA-454/R-99-004, U.S. Environmental Protection Agency, Research Triangle Park, NC, US, 1999.
- [75] J. Z. Yu, X. F. Huang, J. Xu, and M. Hu, "When aerosol sulfate goes up, so does oxalate: implication for the formation mechanisms of oxalate," *Environmental Science & Technology*, vol. 39, no. 1, pp. 128–133, 2005.
- [76] J. Zheng, L. Zhang, W. Che, Z. Zheng, and S. Yin, "A highly resolved temporal and spatial air pollutant emission inventory for the Pearl River Delta region, China and its uncertainty assessment," *Atmospheric Environment*, vol. 43, no. 32, pp. 5112–5122, 2009.
- [77] HKEPD (Hong Kong Environmental Protection Department), "Guideline on modeling vehicle emissions," July 2005, http://www.epd.gov.hk/epd/english/environmentinhk/air/guide_ref/files/EMFAC_HK_Guidelines_on_Modelling_Vehicle_Emissions_July2005.pdf.

- [78] HKPD (Hong Kong Planning Department), "Hong Kong 2030: planning vision and strategy consultancy study to analyze broad land use pattern of the Pearl River Delta Region," 2003, http://www.pland.gov.hk/pland_en/p_study/comp_s/hk2030/eng/consultants/pdf/Tpaper5.pdf.

Research Article

Potential Impacts of the Introduction of Low-Sulfur Fuel on PM_{2.5} Concentrations at Breathing Level in a Subarctic City

Ketsiri Leelasakultum,¹ Nicole Mölders,¹ Huy N. Q. Tran,¹ and Georg A. Grell²

¹Department of Atmospheric Sciences, College of Natural Science and Mathematics and Geophysical Institute, University of Alaska Fairbanks, 903 Koyukuk Drive, Fairbanks, AK 99775, USA

²NOAA/Earth System Research Laboratory, 325 Broadway, Boulder, CO 80305-3337, USA

Correspondence should be addressed to Nicole Mölders, molders@gi.alaska.edu

Received 27 December 2011; Revised 6 March 2012; Accepted 11 April 2012

Academic Editor: Christer Johansson

Copyright © 2012 Ketsiri Leelasakultum et al. This is an open access article distributed under the Creative Commons Attribution License, which permits unrestricted use, distribution, and reproduction in any medium, provided the original work is properly cited.

The effects of using low-sulfur fuel for oil-heating and oil-burning facilities on the PM_{2.5} concentrations at breathing level in an Alaska city surrounded by vast areas were examined with the Weather Research and Forecasting model coupled with chemistry packages that was modified for the subarctic. Simulations were performed in forecast mode for a cold season using the National Emission Inventory 2008 and alternatively emissions that represent the use of low-sulfur fuel for oil-heating and oil-burning facilities while keeping the emissions of other sources the same as in the reference simulation. The simulations suggest that introducing low-sulfur fuel would decrease the monthly mean 24 h-averaged PM_{2.5} concentrations over the city's PM_{2.5} nonattainment area by 4%, 9%, 8%, 6%, 5%, and 7% in October, November, December, January, February, and March, respectively. The quarterly mean relative response factors for PM_{2.5} of 0.96 indicate that with a design value of 44.7 $\mu\text{g}/\text{m}^3$ introducing low-sulfur fuel would lead to a new design value of 42.9 $\mu\text{g}/\text{m}^3$ that still exceeds the US National Ambient Air Quality Standard of 35 $\mu\text{g}/\text{m}^3$. The magnitude of the relation between the relative response of sulfate and nitrate changes differs with temperature. The simulations suggest that, in the city, PM_{2.5} concentrations would decrease stronger on days with low atmospheric boundary layer heights, low hydrometeor mixing ratio, low downward shortwave radiation, and low temperatures.

1. Introduction

In 2009, Fairbanks—a city in Alaska that is the only precursor-source area within a region of hardly any anthropogenic emissions—was designated a PM_{2.5}-nonattainment area (NAA) due to its frequent exceeding of the 24 h-average National Ambient Air Quality Standard (NAAQS) of 35 $\mu\text{g}/\text{m}^3$ for particulate matter of diameter less than 2.5 μm (PM_{2.5}) during past winters [1]. High concentrations of PM_{2.5} suspended in the urban air are health adverse [2] and have led to increased hospital admissions for cerebrovascular and respiratory diseases in Fairbanks [3].

Fairbanks has hills to the North, East, and West (Figure 1) that along with strong inversions from radiative cooling and calm winds (<0.5 m/s at 10 m) limit the horizontal and vertical exchange of air. Extremely low temperatures

($\leq -20^\circ\text{C}$ at 2 m) and the long dark nights cause high emissions from traffic, power generation, and heating during the cold season (October to March) that lead to accumulation of PM and other pollutants under the inversion [1]. Observations combined with trajectory and air-quality modeling studies showed that advection of pollution plays no role for Fairbanks' PM_{2.5} exceedances in winter [4–6]. Fairbanks is the only city within 578 km radius; that is, local emissions are the main contributor to PM_{2.5} concentrations [5, 7].

PM_{2.5} can be emitted directly into the atmosphere or formed in the atmosphere by gas-to-particle conversion [8, 9]. Emitted gases, such as reactive organic gases, can be oxidized at sufficiently low vapor pressure to form secondary organic aerosols. Precursor gases such as NH₃ (ammonia), NO_x (= NO+NO₂ sum of nitric oxide and nitrogen dioxide), and sulfur dioxide (SO₂) are oxidized and form inorganic

aerosols. Fuel combustion releases SO_2 into the atmosphere where it can contribute to sulfate formation. Sulfate besides organic aerosol is the second major component of atmospheric aerosols in the Fairbanks NAA [7].

In the presence of reactive radicals and water vapor, SO_2 oxidation produces sulfuric acid (H_2SO_4). Since H_2SO_4 has a very low vapor pressure, it is assumed to be in the aerosol form under all atmospheric conditions; the sulfate-related aerosol acidity may be further neutralized by NH_3 to form ammonium sulfate aerosol ($(\text{NH}_4)_2\text{SO}_4$) [10, 11]. Ammonia can also neutralize nitric acid (HNO_3), which is the product of oxidized NO_x , and form ammonium nitrate aerosol (NH_4NO_3). The sulfate aerosol scatters radiation, can also be dissolved and act as cloud-condensation nuclei, and consequently may alter cloud albedo [12, 13].

To improve air quality and reduce $\text{PM}_{2.5}$ concentrations, various countries (e.g., Canada and countries of the European Union) introduced regulations and/or incentives to lower fuel-sulfur content in heating oil. Residential heating oil (number 2 fuel oil), which has an average sulfur content of about 2,500 ppm, is normally used for residential and commercial heating and power generation in Fairbanks. Thus, reductions of precursor SO_2 emission can decrease the $\text{PM}_{2.5}$ mass. However, the response to the emission reduction might be nonlinear; in the eastern United States, for instance, a reduction of SO_2 emissions could reduce sulfate concentrations by 50%, but the potential increase of particulate nitrate may decrease the effectiveness of reducing the annual average $\text{PM}_{2.5}$ concentrations by up to 24% [14]. The reduction of SO_2 emissions may increase particulate nitrate, as the replacement of one molecule of ammonium sulfate by two molecules of ammonium nitrate increases the total PM mass; this replacement of sulfate by nitrate can increase at low temperatures [15, 16] such that they occur in the cold season in Fairbanks.

One mitigation strategies discussed for Fairbanks is to reduce the sulfur content in fuel used for oil-fired furnaces and facilities. With a design value for 2008 of $44.7 \mu\text{g}/\text{m}^3$, an emission-control measure to be efficient has to reduce the $\text{PM}_{2.5}$ concentrations by about 22%. Note that a design value describes the air-quality status relative to the NAAQS expressed as a concentration instead of an exceedance.

Fairbanks' low insolation, temperatures, moisture, and wind speeds in winter and the frequent existence of inversions provide quite different environmental conditions for gas-to-particle conversion than found in the eastern US. Since low temperatures favor nitrate formation [15, 16], using low-sulfur fuel may not provide as large reductions as found for the eastern US. The low humidity also hinders particle growth to PM_{10} (PM with diameter $>10 \mu\text{m}$).

This study tests the hypothesis that, under the meteorological conditions during the cold season in Fairbanks, reducing the fuel-sulfur content is not sufficient to achieve the required reduction. In doing so, we turn to numerical modeling as it permits us to assess the response of $\text{PM}_{2.5}$ concentrations at breathing level under the same meteorological conditions. Since Fairbanks is the only major anthropogenic emission source within the area, responses to any local emission-control measures are not diluted by advection of

anthropogenic pollutants. We examined the potential effects of utilizing low-sulfur fuel for power generation and heating on the $\text{PM}_{2.5}$ concentrations at breathing level in Fairbanks by using the Weather Research and Forecasting model [17] inline coupled with chemistry packages (WRF/Chem; [18]) with the modifications for the subarctic introduced by [7]. WRF/Chem had recently been successfully used to assess the response to the emission controls implemented for the 2008 Olympic Games [19, 20].

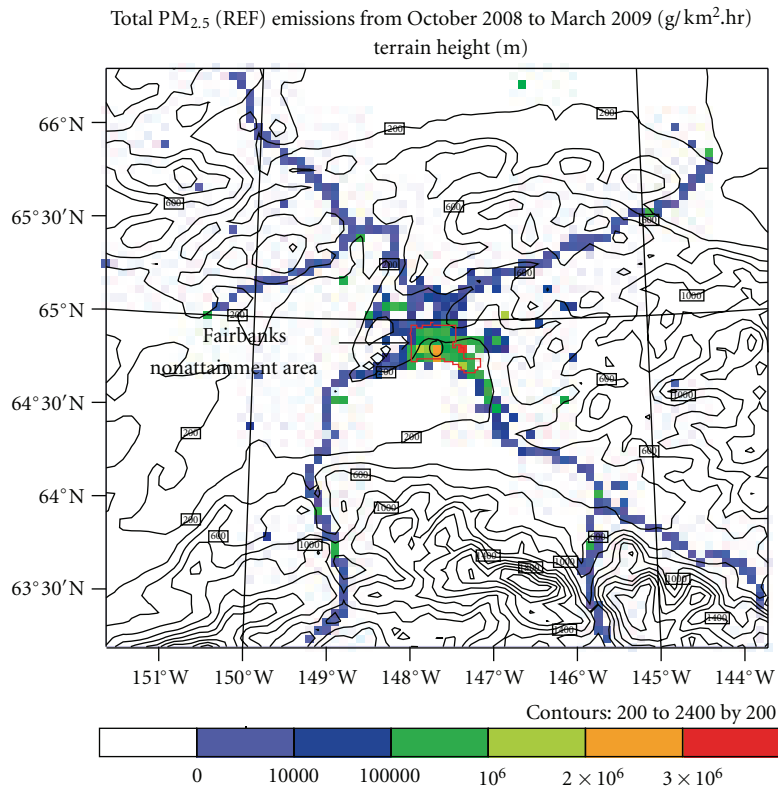
2. Experimental Design

2.1. Model Setup. We used the physical and chemical packages as described in [6]. This model setup includes the six water-class cloud microphysical scheme [21], the further-developed Grell-Dévényi cumulus-ensemble scheme [22] in its 3D version, the Goddard shortwave radiation scheme [23], and the radiative transfer model for long-wave radiation [24]. The processes in the atmospheric boundary layer (ABL) and sublayer were considered following Janjić [25]. The exchange at the surface-atmosphere interface is determined using a modified version of the Rapid Update Cycle land-surface model [26]. The chemistry package considered radiative feedback from aerosols [27]. The gas-phase chemistry by Stockwell et al. [28] with photolysis frequencies calculated following [29] was used. Aerosol dynamics, physics, and chemistry were described by the Modal Aerosol Dynamics Model for Europe (MADE; [30]) and the Secondary Organic Aerosol Model (SORGAM; [9]). For secondary organic formation, WRF/Chem considers the OH-radical, the nitrate-radical, and ozone as oxidants for ROG [9]. For aerosol inorganic chemistry, the model includes sulfate, ammonium, and nitrate for thermodynamic of gas/aerosol equilibrium. Dry deposition of trace gases was determined in accord with Wesely [31], with the modifications by [7].

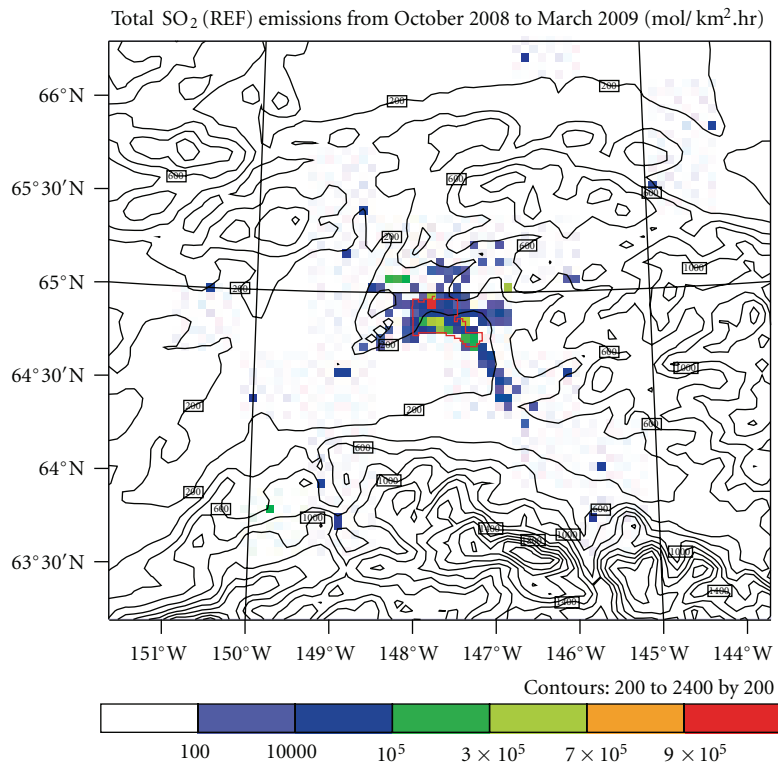
2.2. Simulations. The area for our analysis encompasses 80×70 grid points with a grid increment of 4 km centered over Fairbanks (Figure 1). The vertically stretched grid had 28 layers up to 100 hPa. The initial meteorological conditions, including snow and soil variables, were downscaled from the $1^\circ \times 1^\circ$, 6 h-resolution National Centers for Environmental Prediction global final analyses. This meteorological data was also downscaled as lateral boundary conditions.

The vertical profiles of Alaska-typical background concentrations served to initialize the chemical fields. Since Fairbanks is the only city and major emission source [4–6], Alaska background concentrations served as lateral boundary conditions.

The simulations were performed in forecast mode for October 1, 2008 0000UTC to April 1, 2009 0000UTC, and analyzed for October 1 to March 31 Alaska Standard Time (AST = UTC-9 h). The meteorological fields were initialized every five days. The chemical distributions at the end of each simulation served as the initial contributions for the next simulation.



(a)



(b)

FIGURE 1: Continued.

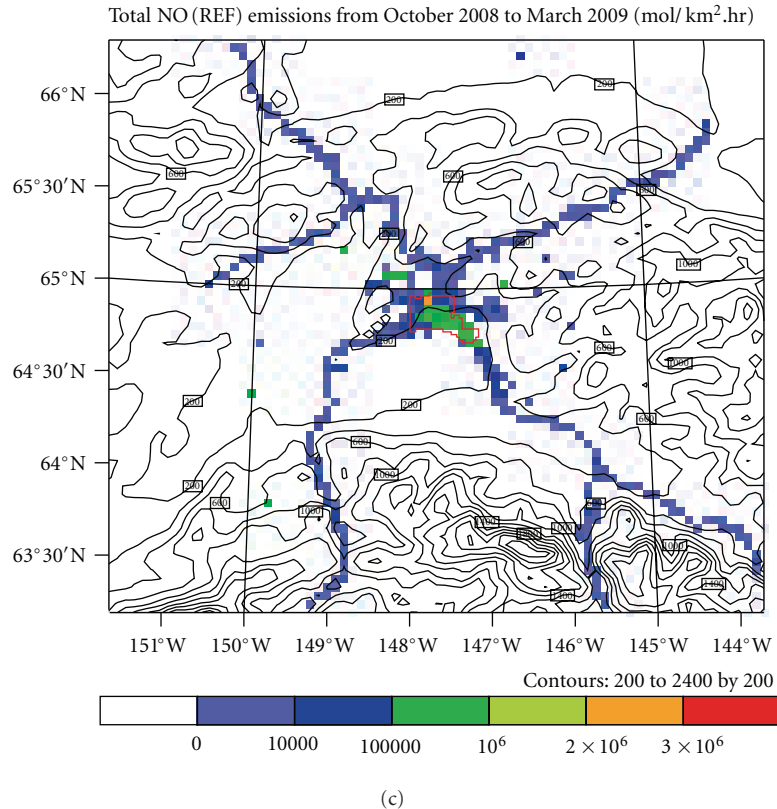


FIGURE 1: Total emission of (a) PM_{2.5}, (b) SO₂, and (c) NO_x from October 1, 2008 to March 31, 2008 (color) from all layers in the analysis domain. Terrain height is superimposed (contour lines). In (a), the red polygon and black circular shape indicate the boundaries of the Fairbanks nonattainment area and the location of the official PM_{2.5}-monitoring site, respectively.

2.3. Emissions. Biogenic emissions were calculated depending on temperature and radiation flux density [32]. Anthropogenic emissions were obtained from the National Emission Inventory of 2008 with updates for point-source and nonpoint source sectors using data from point-source facility operators and local agencies if available. Otherwise, a 1.5% increase per year from the point-source emissions of the previous inventory was assumed. The anthropogenic emissions were allocated according to the source-specific activity in space (e.g., point-source coordinates, population and traffic density) and time (month, day-of-the-week, hour). Empirical functions [6, 33, 34] were used to allocate emissions from power generation, commercial and residential heating, and traffic (cold-starts) temperature dependent. These parameterizations ensured higher (lower) emissions on days with daily mean temperatures below (above) the 1971–2000 average. The temperature-dependency used the downscaled final analysis temperatures to avoid that errors in WRF/Chem-predicted temperatures affect the anthropogenic emissions.

In the reference simulation (REF), emissions from oil-burning facilities and furnaces represent emissions with the current sulfur content. The mitigation simulation (LSF) assumed the use of low-sulfur fuel for these sources. A reduction of sulfur in fuel from 2500 to 500 ppm means emission reductions from oil furnaces, oil-burning facilities, and power generation of 75%, 80%, and 10% for SO₂, PM

and NO_x, respectively; the decrease of NO_x emissions is due to the reduced nitrogen content of low-sulfur fuel [35]. Following [35] we assumed no reduction for the emissions of volatile organic compounds (VOCs) and CO. VOCs include all alkanes, alkenes, aromatics, organic acid, and carbonyl groups [7].

2.4. Analysis. Our analysis focused on the changes in precursor emissions of SO₂, and NO and their effect on the simulated concentrations and composition of PM_{2.5}. We tested the hypothesis that the use of low-sulfur fuel does not affect the PM_{2.5} concentrations using a *t*-test. The word “significant” is used only when data pass this test at the 95% confidence level. To compare the simulation results in a relative rather than absolute sense, we calculated the relative response factors (RRFs) as the ratio of the 24-h-average concentration obtained by LSF to that obtained REF. Multiplication of the RRF with the design value provides the new design value that represents the conditions that would be found if the measure was in place.

The thermodynamic equilibrium between the gas phase and particle-phase shifts toward the gas-phase when temperature increases and vice versa. Water in the atmosphere can change the activity of organic substances [36] and affect the phase transition for inorganic aerosols. As humidity decreases, drops evaporate, and solid particles are formed.

TABLE 1: Total emissions of REF (first value) and LSF (second value) and percent reduction (in brackets) in the nonattainment area, and monthly mean temperatures (T_{mon}) and frequency of days with temperatures lower than the 1971–2000 mean (T_{30}). Bold values indicate significant changes.

	October	November	December	January	February	March	October to March
PM _{2.5} (tons)	4.34 3.86 (−11%)	2.83 2.30 (−19%)	2.92 2.44 (−16%)	3.69 3.21 (−13%)	2.84 2.44 (−14%)	3.05 2.63 (−14%)	23 19.8 (−14%)
PM ₁₀ × 10 ⁴ (mol)	1.48 1.31 (−11%)	1.26 1.04 (−18%)	1.25 1.04 (−17%)	1.38 1.18 (−15%)	1.13 0.97 (−14%)	1.22 1.05 (−13%)	8.99 7.70 (−14%)
SO ₂ × 10 ⁵ (mol)	9.39 6.59 (−30%)	8.13 6.61 (−19%)	7.96 6.33 (−21%)	9.42 7.34 (−22%)	7.13 5.57 (−22%)	7.49 5.87 (−22%)	57.4 44.4 (−23%)
NO × 10 ⁵ (mol)	14.4 14.1 (−3%)	13.9 13.8 (−1%)	13.5 13.2 (−2%)	15.3 15.2 (−1%)	11.7 11.7 (+<1%)	12.4 12.2 (−2%)	94.2 92.8 (−1%)
T_{avg} (°C)	−8.1	−14.7	−17.5	−18.2	−13.7	−13.5	
$T_{30\text{y-average}}$ (°C)	−4.4	−16.7	−21.1	−23.3	−19.9	−23.9	
Frequency of days, with $T_{\text{mon}} < T_{30}$ (%)	61	23	29	42	17	6	

These particles remain solid until the relative humidity increases to the deliquescence [11]. In view of these meteorological effects on particle formation, we examined how differences between REF and LSF change with the meteorological conditions as well.

3. Reference Simulation

3.1. Emissions. In REF, the total monthly PM_{2.5} emissions in the NAA were 4.34, 2.83, 2.92, 3.69, 2.84, and 3.05 tons in October to March (Table 1). Except for October monthly mean temperatures exceeded their 30-year average (1971–2000). Although October was the warmest month of winter 2008/09, it was much colder than the 30-year average and had the highest frequency of daily mean temperatures below that average. Thus, the temperature dependency of the emissions led to higher emissions than they would have occurred in October with normal mean temperatures. Consequently, October had the highest PM_{2.5} emissions in REF and LSF, and the lowest relative PM_{2.5} emission reduction. January had high total emissions as it was the coldest month. In March, recreational use of snow machines as the temperature and daylight hours increased led to an increase in PM_{2.5} emissions.

3.2. Evaluation. The evaluation of REF by data from 23 surface meteorological sites, 9 PM_{2.5} sites, 4 specification sites, and mobile PM_{2.5}-concentration and temperature measurements provides on average over October to March biases of 2 m-temperature, 2 m-dewpoint temperature, sea-level pressure, 10 m-wind-speed and direction of 1.3 K, 2.1 K, −1.9 hPa, 1.55 m/s, and −4°, respectively [6]. The wind errors explain some of the underestimation of the PM_{2.5} concentrations. The overestimation of temperatures led to biases of 0.5 K, 0.8 K, 2 K, 2.6 K, 1.6 K, and 0.3 K and root-mean square errors (RMSEs) of 3.8 K, 4.8 K, 6.1 K, 4.3 K, 5.2 K, and 4.1 K in October to March, respectively; 2 m-dewpoint-temperature RMSEs were less than 5 K except

November (6.2 K). Performance was better on relatively warmer than colder days and in the rural than urban areas [6]. The mobile temperature measurements indicated that, in the NAA, simulated temperatures were about 1.4, 2.4, 1.2, and 2.2 K too high in November, December, January, and February, and 0.9 K too cold in March [6]. No mobile measurement data existed for October.

In Fairbanks during winter, the low-incoming solar radiation yields to radiative cooling, low daily mean temperatures, and inversions [1, 37, 38]. The strength of low level inversions depends on the net radiation loss and marginal to no cloudiness [37]. WRF/Chem well captured this typical behavior of inversion events, low ABL-heights with usually hardly any cloud or ice particles as indicated by low integrated hydrometeor mixing ratio (e.g., Figure 2).

The PM_{2.5} evaluation used the fractional bias $FB = (2/N) \sum_{i=1}^N ((C_s - C_o)/(C_s + C_o)) \times 100\%$, fractional error $FE = (2/N) \sum_{i=1}^N |(C_s - C_o)/(C_s + C_o)| \times 100\%$, normalized mean bias $NMB = (\sum_{i=1}^N (C_s - C_o) / \sum_{i=1}^N C_o) \times 100\%$, and normalized mean error $NME = (\sum_{i=1}^N |C_s - C_o| / \sum_{i=1}^N C_o) \times 100\%$. On average over October to March and all sites, the FB, FE, NMB and NME for 24 h-average PM_{2.5} concentrations were 22%, 67%, 13%, and 71%, respectively, which is slightly weaker than the performance found for various air-quality model applications in midlatitudes [6]. WRF/Chem performed best for PM_{2.5} concentrations between 15 and 50 $\mu\text{g}/\text{m}^3$. Performance was best for organic carbon (OC) followed by sulfate. Ammonium was strongly underestimated. The errors in predicted PM_{2.5} were due to errors in emissions and simulated meteorological conditions (mistiming of fronts, underestimation of inversion strength, overestimation of wind speed), measurement errors and, on some days in March, the chemical boundary conditions [6].

For application in air-quality mitigation studies, a model must perform well around the NAAQS and the design value. Since (1) WRF/Chem achieved the best results for PM_{2.5} concentrations between 15 and 50 $\mu\text{g}/\text{m}^3$, (2) performed acceptable for sulfate species in PM_{2.5}, and (3) LSF and REF

TABLE 2: Monthly mean of 24 h-averaged PM_{2.5}, PM₁₀, sulfate, and nitrate concentrations in the nonattainment area as obtained with REF (first value) and LSF (second value) and percent change (in brackets). Reductions are presented negative. Bold values indicate significant changes.

	October	November	December	January	February	March	October to March
PM _{2.5} ($\mu\text{g}/\text{m}^3$)	13.0 12.5 (−4%)	11.0 10.0 (−9%)	9.2 8.5 (−8%)	11.0 10.4 (−6%)	9.8 9.3 (−5%)	5.7 5.3 (−7%)	9.5 8.9 (−6%)
PM ₁₀ ($\mu\text{g}/\text{m}^3$)	29.4 28.6 (−3%)	28.2 25.9 (−8%)	24.1 22.4 (−7%)	26.6 25.2 (−6%)	24.2 23.0 (−5%)	15.3 14.3 (−7%)	23.6 22.2 (−6%)
Sulfate ($\mu\text{g}/\text{kg}\cdot\text{dryair}$)	2.15 2.07 (−3%)	1.79 1.64 (−8%)	1.49 1.38 (−7%)	1.76 1.67 (−5%)	1.61 1.52 (−6%)	0.98 0.91 (−7%)	1.56 1.47 (−6%)
Nitrate ($\mu\text{g}/\text{kg}\cdot\text{dryair}$)	0.09 0.10 (+3%)	0.12 0.11 (−10%)	0.05 0.04 (−10%)	0.06 0.06 (−8%)	0.06 0.06 (+10%)	0.02 0.02 (−10%)	0.06 0.06 (−4%)
Ammonium \times 10^{-3}	2.64 2.75 (+4%)	2.84 2.83 (0%)	1.71 1.71 (0%)	2.09 2.28 (+9%)	2.50 2.34 (−6%)	1.36 1.35 (+1%)	2.19 2.21 (−1%)
Elemental carbon	0.92 0.89 (−4%)	0.77 0.70 (−9%)	0.62 0.58 (−8%)	0.75 0.71 (−6%)	0.68 0.64 (−6%)	0.40 0.37 (−7%)	0.69 0.65 (−6%)
Organic carbon	4.72 4.55 (−4%)	3.91 3.57 (−9%)	3.19 2.94 (−8%)	3.83 3.61 (−6%)	3.49 3.28 (−6%)	2.02 1.87 (−7%)	3.53 3.31 (−6%)

are affected by errors in the same way; that is, errors may cancel out in the differences, we can expect that WRF/Chem is suitable to assess the impact of low-sulfur fuel on PM_{2.5} concentrations. Furthermore, we discuss the results in a relative sense by means of RRF and relative responses.

3.3. Urban Air Quality and Meteorology. On average over the analysis domain and October to March, the simulated 24 h-average PM_{2.5} concentration was 0.4 $\mu\text{g}/\text{m}^3$ in the lowest layer in REF. In the NAA, PM_{2.5} concentrations were highest. Here, in REF, the monthly averages of 24 h-average PM_{2.5}-concentrations were 13.0, 11.0, 9.2, 11.0, 9.8, and 5.7 $\mu\text{g}/\text{m}^3$ for October to March, respectively.

According to the model, in the NAA, PM_{2.5} strongly depended on temperature, relative humidity, and wind speed (Figure 2). Low temperatures and high emissions led to increased gas-to-particle conversion (e.g., the peak of simulated PM_{2.5} during the cold snaps at the end of October or the beginning of January and March). The highest and second highest sulfate concentrations were simulated for October and January (Table 2). This behavior of WRF/Chem well agrees with regression analysis of observational data [1] that identified low temperatures as one of the main factors for increased 24 h-average PM_{2.5} concentrations in the NAA.

Atmospheric moisture affects aerosol formation, and its impact varies with temperature [37]. WRF/Chem simulated low hourly PM_{2.5} concentrations in the NAA when simulated vapor pressure and relative humidity were high which well reflects the typically observed hygroscopic growth of particles under these conditions [1].

Observations showed that winds with daily average speeds >0.5 m/s dilute the PM_{2.5} concentrations, while calm winds (<0.5 m/s) build up the PM_{2.5} concentrations in the NAA [1]. WRF/Chem showed this behavior during October to March (Figure 2). During these months, the monthly average simulated wind speeds in the NAA were 2.27, 1.93, 2.68, 2.62, 2.18, and 3.74 m/s, respectively. The relatively

stronger wind simulated for March than in other months resulted in the lowest monthly average of 24 h-average simulated PM_{2.5} concentrations, and aerosol compositions including nitrate, ammonium, sulfate, EC, and OC in the NAA (Table 2).

Since Fairbanks is the only major emission source, advection generally brings clean air, except when the aged Fairbanks pollution is advected back into the NAA [6]. Such advection occurred 27 times during winter 2008/09. October, November, and February had the highest frequency of advection of aged Fairbanks urban air (6-7 times/month).

Our analysis showed that the simulated low ABL-heights (<100 m) limited the vertical mixing tremendously, resulting in high PM_{2.5} concentrations. For example, the peak of PM_{2.5} at the beginning of January occurs when the ABL height is lower than 100 m for many days. November had the lowest monthly average simulated ABL-height of winter 2008/09 and the highest simulated monthly nitrate and ammonium concentrations and the second highest simulated monthly concentrations of PM, sulfate, EC, and OC (Table 2).

4. Low Sulfur Fuel

4.1. Emissions. The assumed emission reductions due to low sulfur-fuel usage differ among hours, days, and months as the emissions related to oil-burning furnaces and facilities were prepared temperature dependent for use in WRF/Chem. Compared to REF, assuming that the rates given by [35] for low sulfur fuel reduced the total PM_{2.5} emissions in the NAA by 11%, 19%, 16%, 13%, 14%, and 14% for October to March, respectively, with similar reductions in PM₁₀ emissions. On average over October to March, the PM-emission reduction would be 14%. On average, over these months, the total SO₂ emission would be reduced by $\sim 23\%$ (Table 1). Emissions from all other sources than oil-furnaces and oil-burning facilities were identical to those in REF.

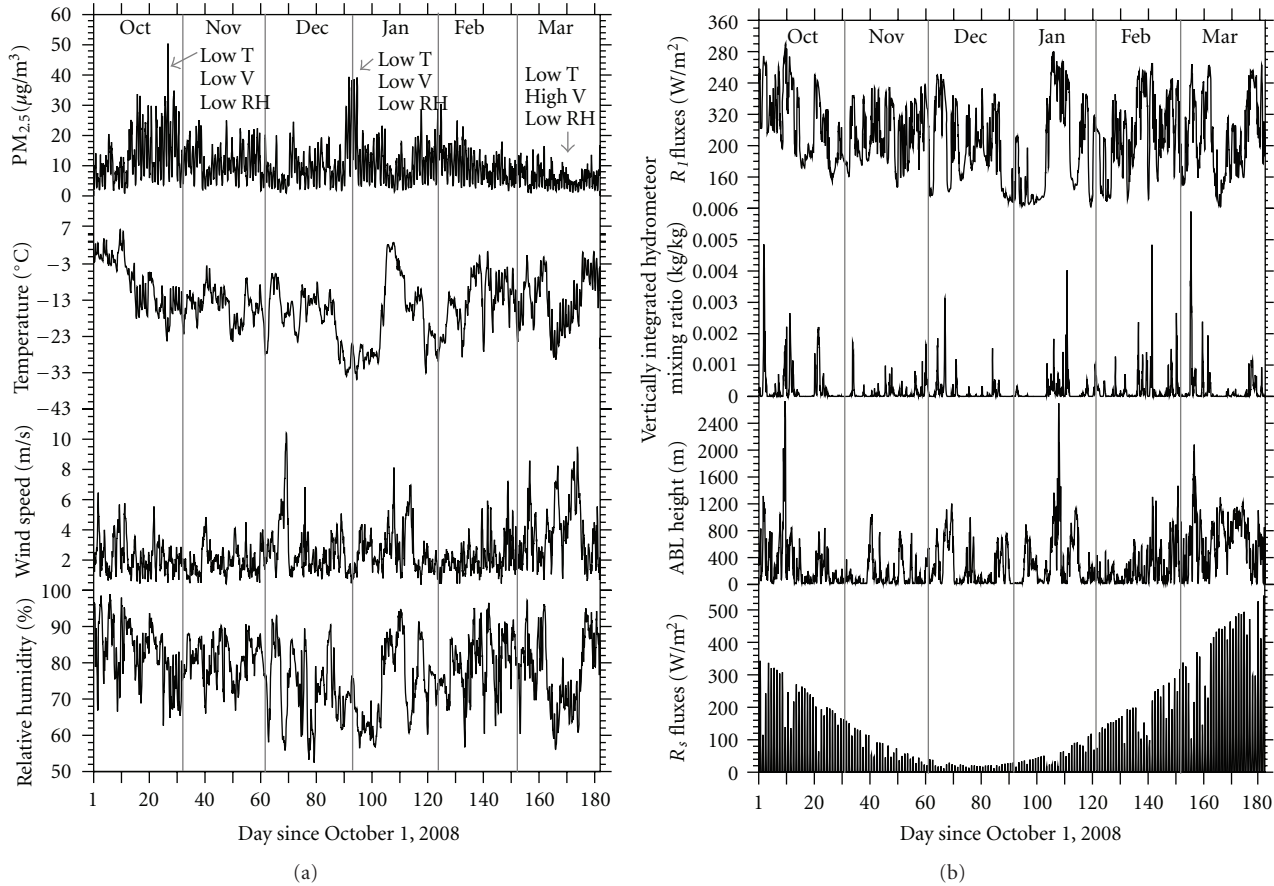


FIGURE 2: Temporal evolution of simulated hourly (a) $PM_{2.5}$ -concentration, temperature, wind-speed, relative humidity, and (b) downward long-wave radiation, hydrometeor mixing ratios, ABL-height and downward shortwave radiation averaged over the Fairbanks nonattainment area for each of the 182 simulation days.

4.2. Impacts on Urban Air Quality. On average over the first layer of the analysis domain and October to March, the assumed usage of low sulfur fuel reduced the simulated $PM_{2.5}$ concentrations by 5%. In LSF, the hourly $PM_{2.5}$ -concentrations significantly decreased in some areas in the first layer as compared to REF (Figure 3). In the NAA, in response to the assumed emission changes, the simulated $PM_{2.5}$ -concentrations decreased by $0.5 \mu\text{g}/\text{m}^3$, $1.0 \mu\text{g}/\text{m}^3$, $0.7 \mu\text{g}/\text{m}^3$, $0.6 \mu\text{g}/\text{m}^3$, $0.5 \mu\text{g}/\text{m}^3$, and $0.4 \mu\text{g}/\text{m}^3$ in October to March, respectively, and by $0.6 \mu\text{g}/\text{m}^3$ on average over these months. These simulated $PM_{2.5}$ -concentration reductions were significant in November, December, and March (Figure 3). The relative monthly mean of 24 h-average $PM_{2.5}$ -concentration reductions would vary between 4% and 9% (Table 2). At the grid cell of the monitoring site, the October to March monthly averaged 24 h-average $PM_{2.5}$ concentrations decreased from 40.2, 30.3, 25.8, 33.9, 27.1, and $17.1 \mu\text{g}/\text{m}^3$ in REF, respectively, to 39.2, 28.6, 24.4, 32.7, 26.0, and $16.2 \mu\text{g}/\text{m}^3$ in LSF, that is $1.2 \mu\text{g}/\text{m}^3$ ($\sim 4\%$) on average.

The simulations suggested that introduction of low sulfur fuel would reduce the number of exceedance days (days with 24 h-average $PM_{2.5}$ -concentrations $>35 \mu\text{g}/\text{m}^3$). The simulated number of exceedance days went down from 20,

10, 5, 15, and 5 days to 19, 8, 4, 14, and 5 days for October to February, respectively. No exceedances were simulated for March. The highest frequency of exceedance days (52 in REF, 47 in LSF) was simulated for the grid-cell that holds the official monitoring site. On most of these days, this grid-cell had the highest 24 h-average $PM_{2.5}$ concentrations in the NAA.

The 24 h-average $PM_{2.5}$ -concentration difference between REF and LSF for each of the 182 simulation days was calculated and sorted from highest to lowest. The investigation of the top 20% (37 days) showed that 14 of the days with the highest concentration differences occurred in November. In November, wind speeds and ABL height, on average, were the lowest of all months (e.g., Figure 2, Table 3). Thus, pollutants accumulated and had enough time for chemical conversion. The changed composition and reduced amount of precursors in LSF as compared to REF, and hence, became most effective due to the relatively long retention of pollutants in the NAA in November. November had the highest monthly average $PM_{2.5}$ -emission reduction and concentration reduction (Tables 1 and 2). Of the 20% days with the lowest concentration differences, 14 days occurred in March. March had the lowest difference between REF- and LSF-simulated $PM_{2.5}$ concentrations. WRF/Chem (correctly)

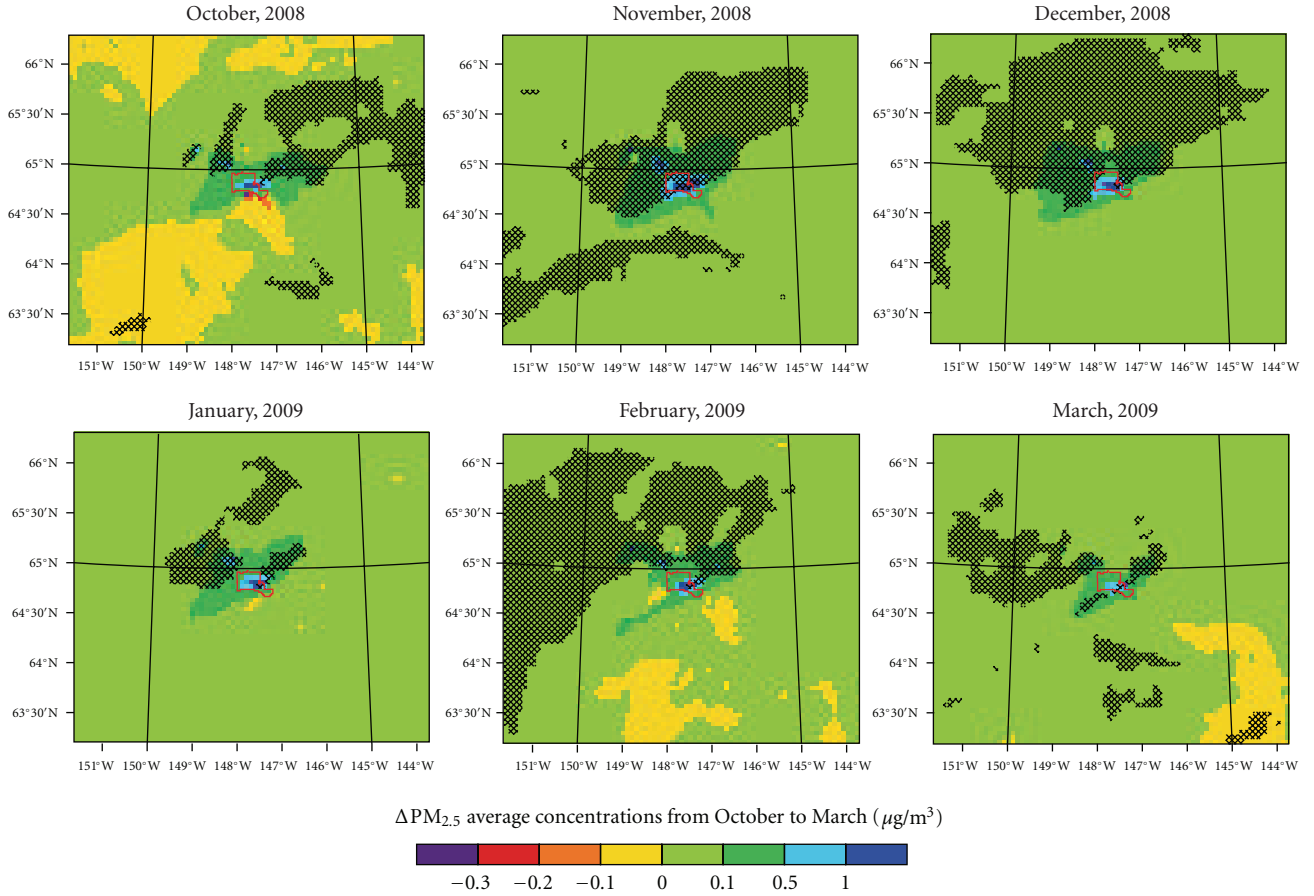


FIGURE 3: Difference REF-LSF of monthly averaged 24 h-average $PM_{2.5}$ concentrations (color) from October to March. The hashed shading indicates significant (95% or higher confidence level) differences. The red polygon indicates the boundaries of the Fairbanks nonattainment area.

TABLE 3: Monthly average of near-surface air temperature (T), dewpoint temperature (T_d), wind speed (v), relative humidity (RH) and downward shortwave radiation (R_s), ABL-height (h) and sea-level pressure (SLP), and precipitation (P) in the nonattainment area as obtained by REF (first value) and LSF (second value). Relative differences are in brackets. The letters L and N represent changes <0.001 and no change, respectively.

	October	November	December	January	February	March
T ($^{\circ}C$)	-8.1 -8.5 (-0.3)	-14.7 -14.7 N	-17.5 -17.5 (-L)	-18.2 -18.2 (-L)	-13.7 -13.9 (-0.2)	-13.5 -13.1 (+0.4)
T_d ($^{\circ}C$)	-10.5 -10.8 (-0.3)	-17.3 -17.3 N	-21.2 -21.2 (-L)	-21.7 -21.7 (-L)	-16.6 -16.8 (-0.2)	-16.6 -16.2 (+0.5)
v (m/s)	2.27 2.23 (-0.04)	1.93 1.93 N	2.68 2.68 (+L)	2.62 2.62 (+L)	2.18 2.17 (-0.01)	3.74 3.74 (-L)
RH (%)	81 81 (+L)	79 79 N	72 72 N	72 72 (-L)	78 78 (+L)	76 76 (+L)
R_s (W/m^2)	50 51 (+1)	12 12 N	2 2 N	8 8 (+L)	38 38 (L)	103 108 (+5)
R_L (W/m^2)	229 227 (+2)	215 215 N	196 196 (-L)	194 194 (-L)	215 215 (+L)	212 212 (-L)
h (m)	306 284 (-21)	157 157 N	258 258 (L)	340 340 (L)	237 233 (-4)	622 630 (+8)
SLP (hPa)	1006.8 1006.9 (+0.1)	1005.9 1005.9 N	1018.6 1018.6 N	1013.0 1013.0 N	1015.2 1015.2 (+0.0)	1012.3 1012.2 (-0.1)
P (mm)	0.5 1.4 (+0.9)	0.4 0.4 N	0.6 0.6 N	0.5 0.5 (+L)	0.7 0.9 (+0.2)	0.6 0.6 (+L)

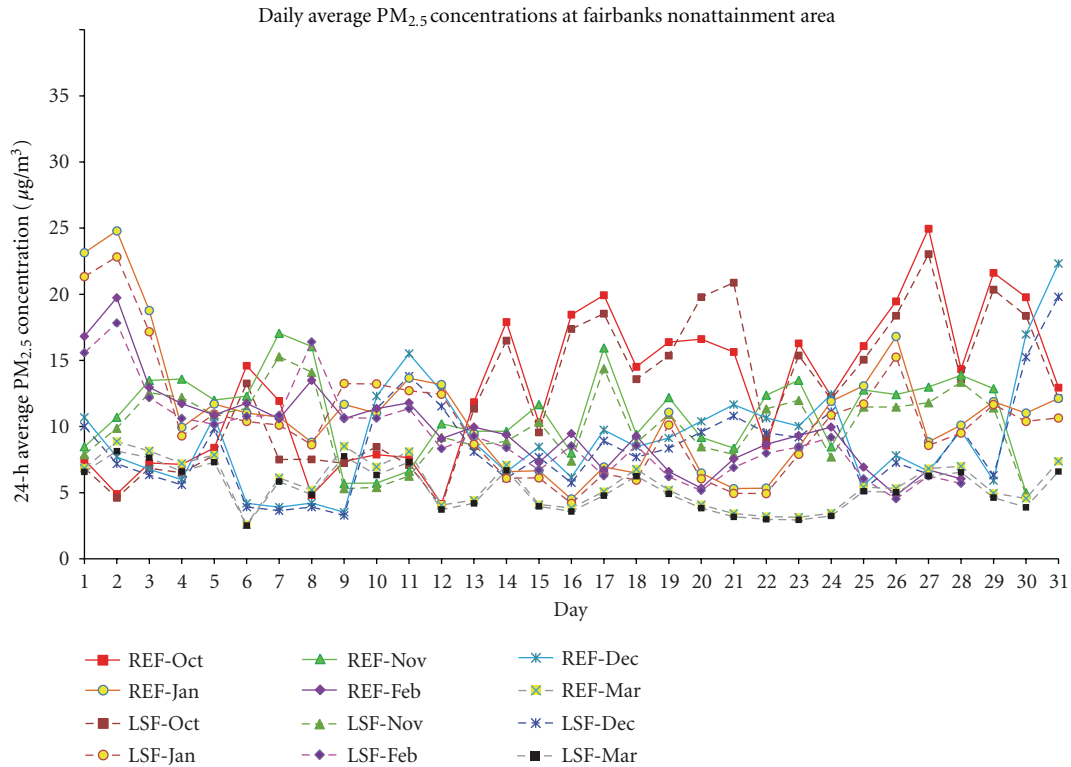


FIGURE 4: Temporal evolution of simulated 24 h-average PM_{2.5} concentrations averaged over the nonattainment area for October to March as obtained by REF and LSF.

simulated the highest wind speeds and ABL heights for March (Figure 2). These relatively stronger wind speeds resulted in quick transport of pollutants out of the NAA and left only short time for aerosol formation from precursor SO₂ than in other months.

On October 8, 10, 20, 21, and 22, December 28, and 29, January 9, and 10, and February 7, 8, and 9, which account for 7% of the 182 days studied, the 24 h-average simulated PM_{2.5} concentrations averaged over the NAA increased in response to the assumed usage of low sulfur fuel (Figure 4). The maximum increases of PM_{2.5} in the NAA and at the grid cell of the monitoring site occurred on October 21 and were 5.2 µg/m³ and 13.3 µg/m³, respectively. The reasons for these increases are discussed in Section 4.4.

The RRFs of the 24 h-average PM_{2.5} concentrations vary only marginally over the NAA in all months (not shown). At the grid cell of the monitoring site, the RRFs were 0.97, 0.94, 0.94, 0.97, 0.96, and 0.95 for October to March, respectively. The quarterly mean RRFs were 0.96 for both the first (January to March) and fourth quarter (October to December). The relatively high RRFs indicate a low sensitivity of simulated PM_{2.5} concentrations to the assumed emission-control measure. Given that the 2008 design value was 44.7 µg/m³, introducing low sulfur fuel would lead to a new design value of 42.9 µg/m³. Thus, the simulations suggest that reducing the sulfur content in fuel alone for the targeted emission sources would not lead to air quality in Fairbanks that is in compliance with the NAAQS.

4.3. Role of Meteorology on the PM_{2.5}-Concentration Reductions. Investigation of the relation between the PM_{2.5}-concentration reductions and the meteorological conditions showed the following. In general, the simulated PM_{2.5}-concentration reductions increased at low near-surface temperatures, low ABL heights, low hydrometeor mixing ratio (cloud, rain, ice, and snow-mixing ratio integrated over all levels), and low downward shortwave radiation (R_s) (Figures 2, 5(a)–5(d)). The highest absolute correlation existed between simulated ABL-height and PM_{2.5}-concentration reductions ($|-0.28|$, significant at the 95% confidence level). For low ABL heights, the atmosphere typically is very stable [1]. Hence, the emitted precursors and PM_{2.5} stay in a relatively thin layer. Consequently, the assumed emission reductions led to relatively high reduction in simulated PM_{2.5} concentrations. The low insolation and relatively strong radiative cooling, low hydrometeor ratio (i.e., marginal cloudiness) also contributed to low ABL-heights. On the contrary, high ABL heights allow mixing of emitted gases and particles over a thicker layer, leading to a seemingly lower impact of the assumed emission reduction on the simulated near-surface PM_{2.5} concentrations.

On some days the simulated meteorological conditions changed slightly in response to the assumed introduction of low-sulfur fuel (Figures 5(e)–5(h)). In the NAA, changes in the simulated meteorological quantities were relatively high in October, February, and March (Table 3). These months have relatively high insolation as compared to November to January (Figure 2) for which the simulated aerosol-radiation

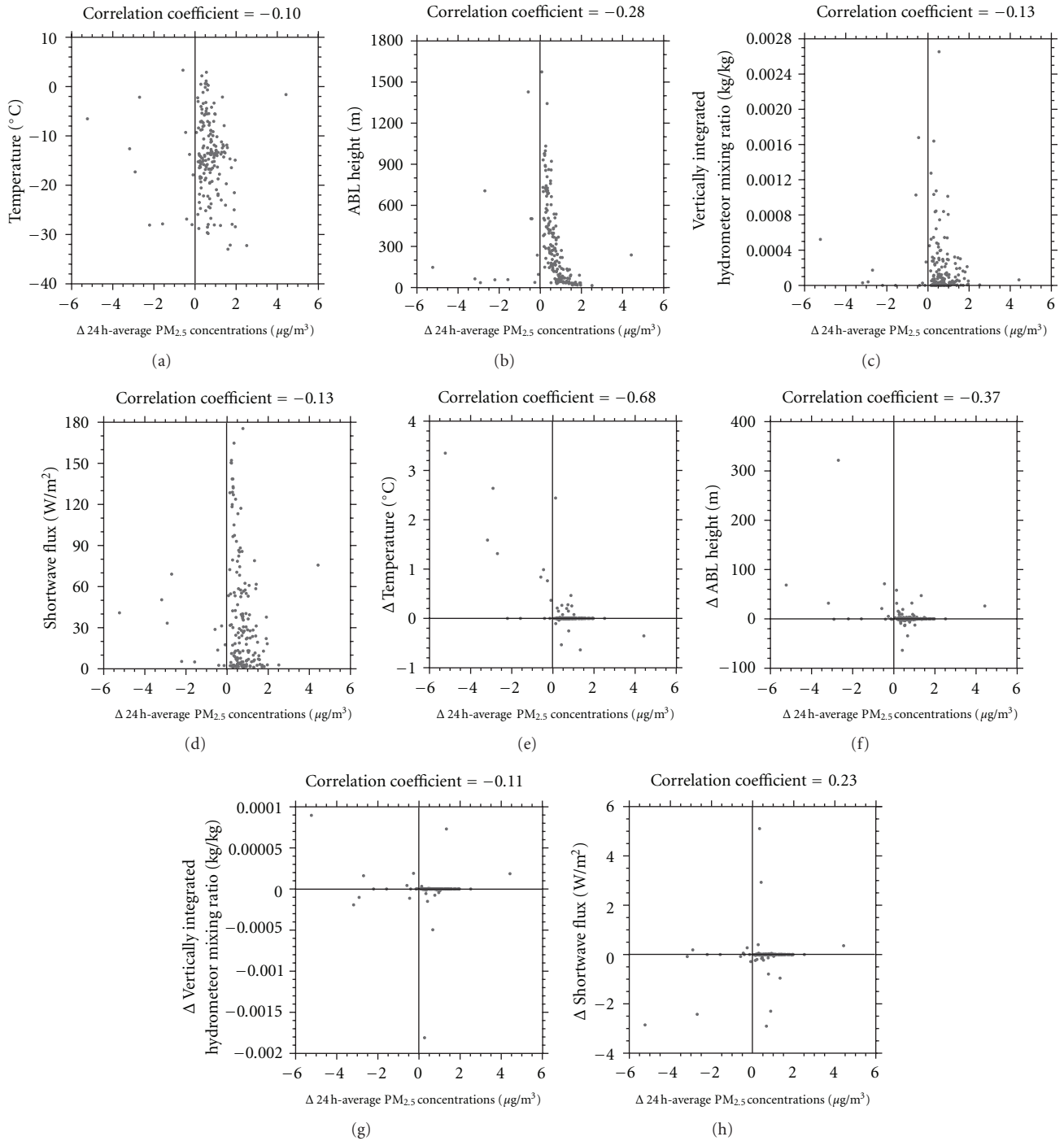


FIGURE 5: Scatter plots of the REF simulation of 24 h-average $\text{PM}_{2.5}$ concentrations versus (a) near-surface temperature, (b) ABL height, (c) vertically integrated hydrometeor mixing ratio, and (d) downward shortwave radiation, and differences REF-LSF of 24 h-average $\text{PM}_{2.5}$ concentrations versus difference (REF-LSF) of daily mean (e) near-surface temperature, (f) ABL height, (g) vertically integrated hydrometeor mixing ratio, and (h) downward shortwave radiation in the nonattainment area for the 182 simulation days. The lines crossing at zero indicate nondifferences with respect to the values at the x and y axis.

feedbacks can become more obvious. The changes in simulated meteorological quantities in October and February led to a more stable atmosphere, that is, reduced vertical and horizontal mixing. In March, the changes enhanced thermal turbulence and hence vertical mixing.

4.4. Speciation. In REF, the speciation of total dry $\text{PM}_{2.5}$ on average over November to March was 1% ammonium, 1.4% nitrate, 11.8% EC, 25.8% sulfate, and 60.1% OC. According to the simulations, introducing low-sulfur fuel would increase the absolute nitrate-aerosol concentrations in the

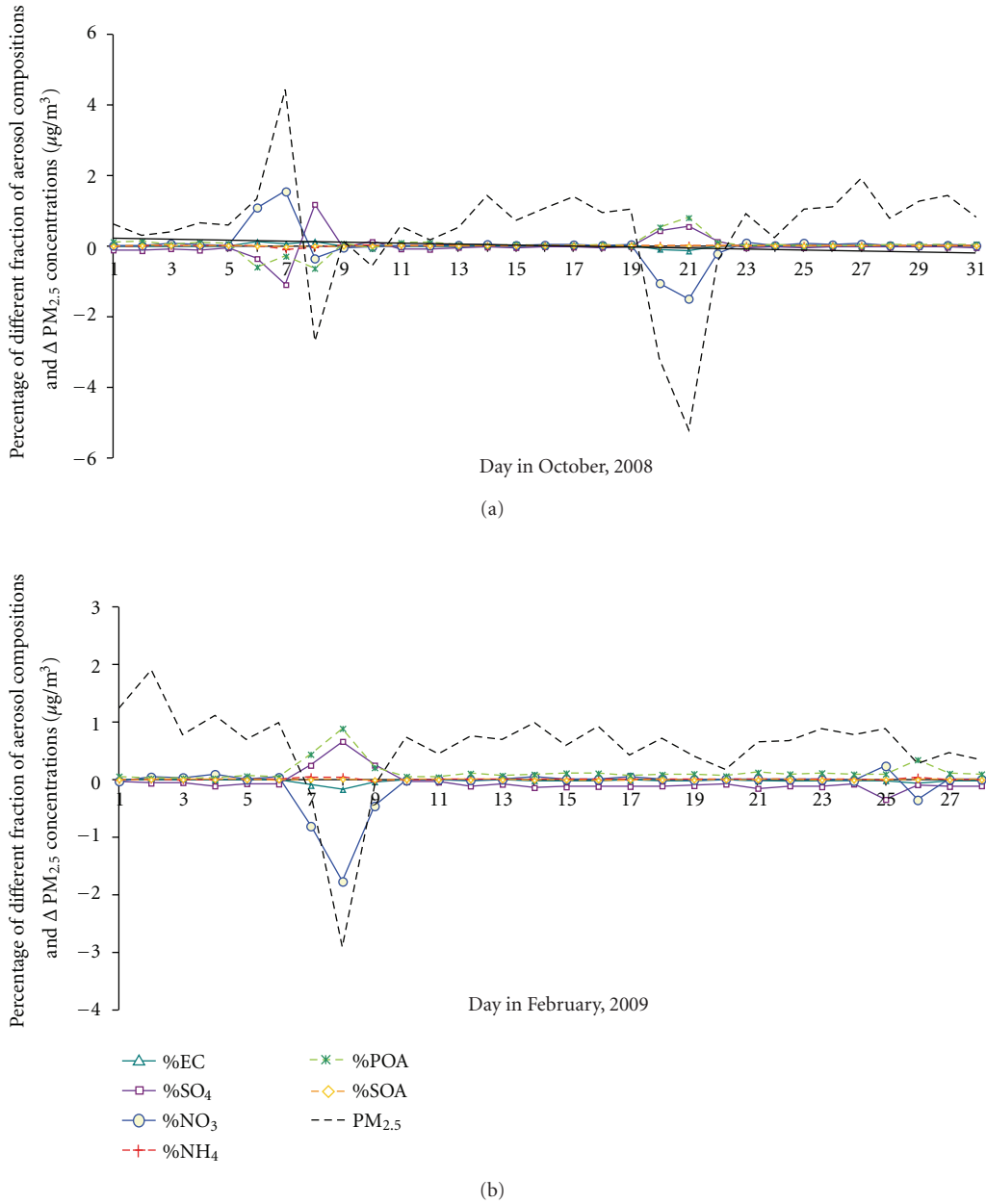
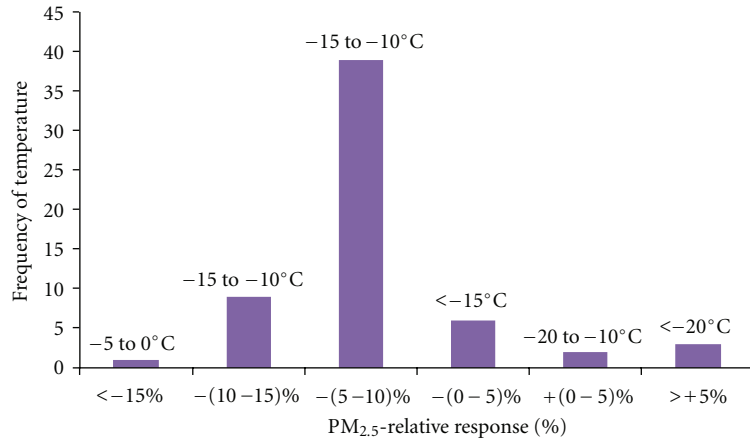


FIGURE 6: Temporal evolution of daily average percent differences in simulated aerosol compositions in the nonattainment area as obtained for October and February.

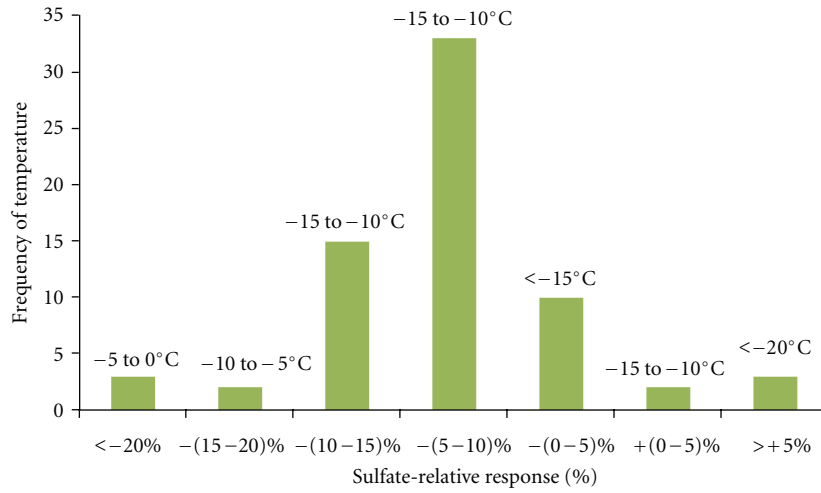
NAA by 3% and 10% in October and February, respectively (Table 2). Though nitrate makes up only a small fraction of the total $PM_{2.5}$, its increasing affected the reduction of $PM_{2.5}$ concentrations in these two months notably (Figure 6). On average over October to March and the NAA, the LSF-simulated OC, sulfate, EC, and emitted $PM_{2.5}$ decreased by 6%, nitrate decreased by 4% and ammonium by 1% as compared to REF. The percent reductions of OC, sulfate, EC, and emitted $PM_{2.5}$ are similar to the percent reduction of $PM_{2.5}$ and PM_{10} in the NAA (Table 2).

To assess how the low Fairbanks temperatures affect the relative responses of the of the total simulated $PM_{2.5}$

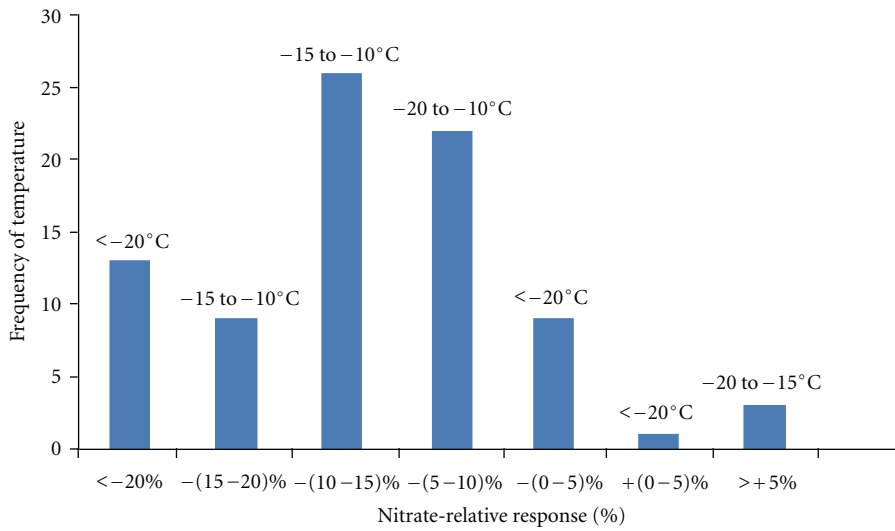
concentrations and its speciation in the NAA, we determined the daily relative response $RR = ((PM_{2.5,LSF} - PM_{2.5,REF})/PM_{2.5,REF}) \times 100\%$ following [15, 16]. Here $PM_{2.5,REF}$ and $PM_{2.5,LSF}$ are the 24 h-average $PM_{2.5}$ concentrations averaged over the NAA for REF and LSF, respectively. The RR of total simulated $PM_{2.5}$ and its speciation were grouped according to their magnitude in classes of 5% increments. We then identified the most frequent occurrence of daily mean temperatures in each group and calculated the frequency of that temperature. According to the simulations, the highest relative reduction of $PM_{2.5}$ (>15%) occurs between -5 and $0^\circ C$ (Figure 7(a)). $PM_{2.5}$ reductions of 5 to



(a)



(b)



(c)

FIGURE 7: Continued.

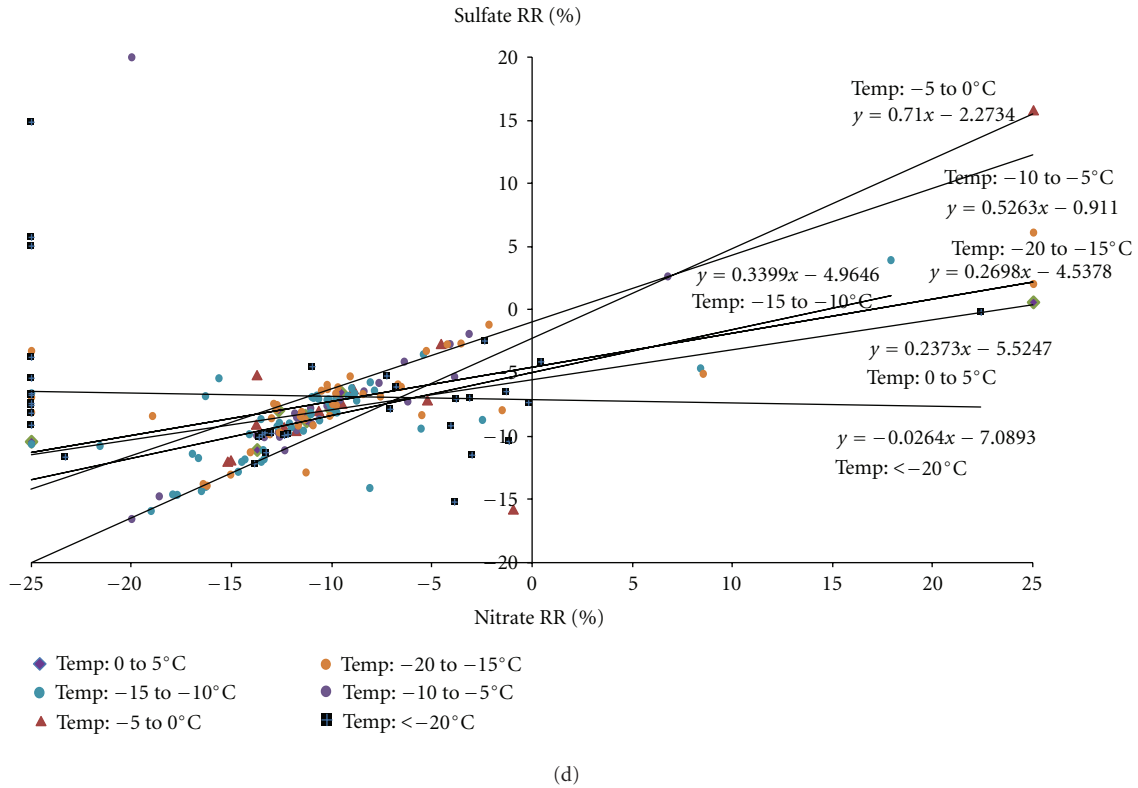


FIGURE 7: Relative responses of (a) total PM_{2.5}, (b) sulfate and (c) nitrate concentrations to the assumed fuel sulfur content reductions and (d) relation of relative responses of sulfate and nitrate at different temperature ranges. The temperature ranges on each bar are the ranges of temperature which has the most frequent occurrence, and the y axis indicates that frequency.

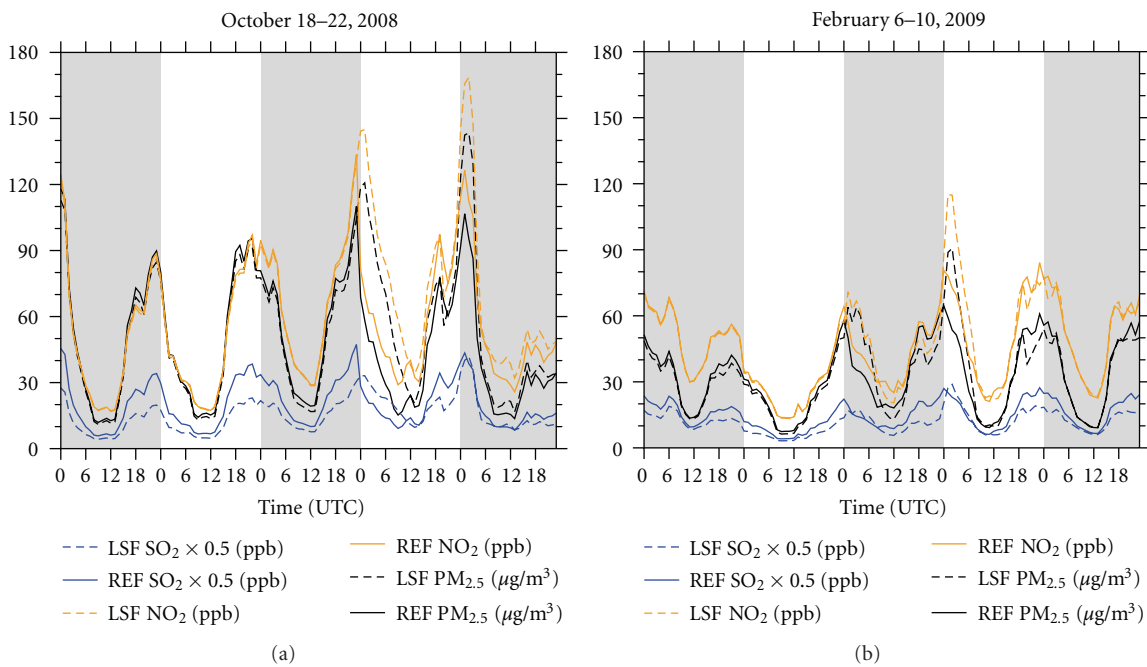


FIGURE 8: Mixing ratios of chemical species and PM_{2.5} concentrations as obtained by REF and LSF for the grid cell that holds the monitoring site for October 18–22, 2008, and February 6–10, 2009 (UTC). The grey color serves to better distinguish among days.

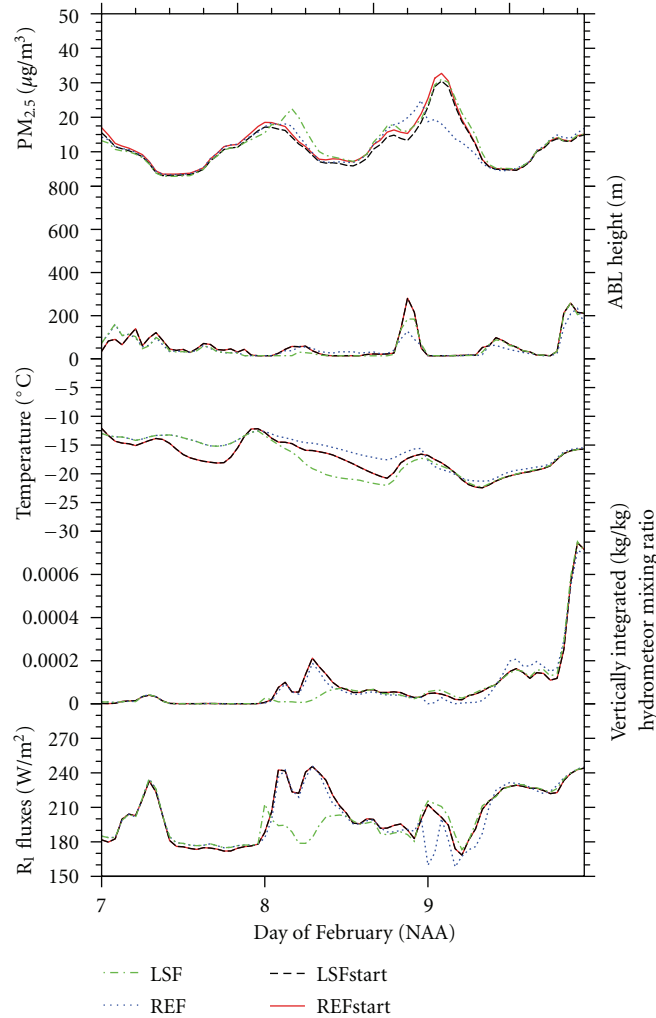


FIGURE 9: Meteorological variables and $PM_{2.5}$ concentrations simulated by REF, LSF, and REFstart and LSFstart averaged over the nonattainment area during February 7–9, 2009 (UTC).

10% would occur most frequently between -15 and -10°C . The same would be true for sulfate (Figure 7(b)). $PM_{2.5}$ and sulfate would decrease 0–5% for temperatures below -15°C (Figures 7(a), 7(b)). At temperatures between -15 and -10°C , nitrate would be reduced most frequently by 10 to 15%. At daily mean temperatures below -20°C , the relative reduction of nitrate would exceed 20% most of the time. However, sometimes at temperatures below -20°C , $PM_{2.5}$, sulfate and nitrate would increase (Figures 7(a), 7(b), and 7(c)). The relative nitrate changes differ from the relative sulfate changes (Figure 7(d)). In the temperature range -15 to -10°C , for instance, nitrate would decrease stronger for a given decrease in sulfate than in the range -20 to -15°C . These findings mean that at low temperatures of Fairbanks' winters, the $PM_{2.5}$ reductions in response to reduced SO_2 -emissions are quite nonlinear. This finding agrees with the response of the particulate nitrate to the SO_2 reductions found in the relative warmer eastern US [14, 15].

The change in simulated meteorological quantities occurred at 1500 AST (0000 UTC) on the days with increased

nitrate and relates to the increase of $PM_{2.5}$ in the NAA. They coincided with changes in various pollutants (e.g., Figure 8). On these days and time, the meteorology was initialized. Note that when running a model in forecast mode for six months, the meteorological conditions have to be initialized on a regular basis as frequent meteorological reinitializations result in improved model skills [39]. However, a reinitialization approach may lead to a discontinuity, which takes a few hours or two days to reach dynamical equilibrium [40, 41]. Discarding the first 6 h after re-initializing the meteorology yields discrepancies between the meteorological fields and the chemical fields initialized from the previous run [7] for which we did not use that approach.

We examined all 37 days with reinitialization of meteorology and found that only 6 days showed increased $PM_{2.5}$ concentrations. On these days also the $PM_{2.5}$ -composition changed. These days were characterized by strong stability ($\gamma = 2.28 \text{ K/1 km}$) over the NAA and averages of simulated ABL heights as low as 107 m and 80 m, in REF and LSF, respectively. Observations showed that on these days a front

came in. At the beginning of a reinitialization, cloud and ice mixing ratios are zero. It takes about 3–6 hours for the clouds and precipitation species to spin up in the model. When on an initialization day a front approaches and fogs and clouds form, downward shortwave radiation can be overestimated during the spinup [7].

To investigate whether the increased PM_{2.5} on these days results from spinup effects, we reinitialized the simulations three days earlier. These simulations and their results are called REFstart and LSFstart. The temporal evolution of hourly average PM_{2.5} concentrations and meteorological quantities hardly differed between REF, REFstart, and LSFstart (Figure 9). Obviously, while the clouds had not yet fully spun up, the radiative feedback with the modified aerosols led to higher long-wave radiation loss in LSF than in REF. Thus, in LSF temperatures decreased, and saturation was reached quicker than in REF. Subsequently gas-to-particle conversion increased, and thermal turbulence and the ABL-height decreased as compared to REF. Thus, PM_{2.5} concentrations increased in LSF. The simulated temperature decrease supported particulate nitrate formation (Figure 7(c)). Later the enhanced cloudiness decreased the long-wave radiation loss as compared to REF (e.g., Figure 9). These findings attribute the increased PM_{2.5} concentrations and changed meteorological quantities to spinup effects.

When excluding six days that had increased PM_{2.5} concentrations due to spinup effects, the RRFs were 0.95, 0.94, 0.93, 0.94, 0.94, and 0.95 for October to March, respectively, at the grid cell of the monitoring site. The quarterly mean RRFs were 0.94 for both quarters. Multiplication of the RRFs with the 2008 design value yielded 42.0 $\mu\text{g}/\text{m}^3$ which is also higher than the NAAQS. These results confirm the findings above that the assumed introduction of low-sulfur fuel alone would not yield compliance.

5. Conclusions

We examined the response of PM_{2.5} concentrations at breathing level to the reduction of sulfur in heating oil and fuel used for oil-burning facilities for a subarctic city surrounded by an area with hardly any anthropogenic emission sources. In doing so, simulations were performed with the subarctic-modified WRF/Chem in forecast mode for October to March (a full-cold season). According to the simulation results, the introduction of low-sulfur fuel would lead to an average decrease of PM_{2.5} concentrations of 0.6 $\mu\text{g}/\text{m}^3$ (6%) and 1.2 $\mu\text{g}/\text{m}^3$ (4.2%) in the nonattainment area and the grid-cell holding the monitoring site, respectively; it also would avoid five exceedance days. According to the simulations, the monthly average relative PM_{2.5}-concentration reductions varied between 4% and 9%. The quarterly average RRFs of 0.96 at the grid cell of the monitoring site indicate a low response of PM_{2.5} concentrations to the assumed emission reductions. Given a design-value of 44.7 $\mu\text{g}/\text{m}^3$ and these RRFs, one has to conclude that introducing low-sulfur fuel without other emission-control measures will not achieve compliance with the NAAQS of 35 $\mu\text{g}/\text{m}^3$.

Investigation of the relationship between the simulated meteorological conditions and the PM_{2.5}-concentration

reduction showed that the measure would be most efficient on very cold days with low ABL heights, low shortwave radiation, and low hydrometeor mixing ratios.

Running WRF/Chem in forecast mode with reinitialization of the meteorology every 5 days for an entire cold season meant 37 initializations. On six of these initialization days simulated PM_{2.5} concentrations increased despite reduced sulfur fuel content. Investigation showed that on these days, the spinup of meteorology, and the aerosol-radiation feedback led to nonlinear processes that favored nitrate-aerosol formation. When removing this artifact, the RRFs decreased to 0.94; that is, the model artifact did not affect the above conclusions.

Acknowledgments

The authors thank G. Kramm, W. R. Simpson, P. Bieniek, T. T. Tran, and the anonymous reviewers for fruitful discussion, the Fairbanks North Star Borough (contract LGFEEQ) for partial financial support of this study, and ARSC for computational support.

References

- [1] H. N. Q. Tran and N. Mölders, "Investigations on meteorological conditions for elevated PM_{2.5} in Fairbanks, Alaska," *Atmospheric Research*, vol. 99, no. 1, pp. 39–49, 2011.
- [2] C. A. Pope, M. Ezzati, and D. W. Dockery, "Fine-particulate air pollution and life expectancy in the United States," *New England Journal of Medicine*, vol. 360, no. 4, pp. 376–386, 2009.
- [3] State of Alaska Epidemiology, "Association between air quality and hospital visits," Bulletin of the Department of Health and Social Services, Anchorage, Alaska, USA, 2010.
- [4] C. F. Cahill, "Asian aerosol transport to Alaska during ACE-Asia," *Journal of Geophysical Research*, vol. 108, no. 23, pp. 1–8, 2003.
- [5] T. T. Tran, G. Newby, and N. Mölders, "Impacts of emission changes on sulfate aerosols in Alaska," *Atmospheric Environment*, vol. 45, no. 18, pp. 3078–3090, 2011.
- [6] N. Mölders, H. N. Q. Tran, C. F. Cahill, K. Leelasakultum, and T. T. Tran, "Assessment of WRF/Chem PM_{2.5}-forecasts using mobile and fixed location data from the Fairbanks, Alaska winter 2008/09 field campaign," *Atmospheric Pollution Research*, vol. 3, pp. 180–191, 2012.
- [7] N. Mölders, H. N. Q. Tran, P. Quinn et al., "Assessment of WRF/Chem to simulate sub-Arctic boundary layer characteristics during low solar irradiation using radiosonde, SODAR, and surface data," *Atmospheric Pollution Research*, vol. 2, pp. 283–299, 2011.
- [8] F. S. Binkowski and U. Shankar, "The regional particulate matter model—1. Model description and preliminary results," *Journal of Geophysical Research D*, vol. 100, no. 12, pp. 26–209, 1995.
- [9] B. Schell, I. J. Ackermann, H. Hass, F. S. Binkowski, and A. Ebel, "Modeling the formation of secondary organic aerosol within a comprehensive air quality model system," *Journal of Geophysical Research D*, vol. 106, no. 22, pp. 28275–28293, 2001.
- [10] E. R. Lovejoy, D. R. Hanson, and L. Gregory Huey, "Kinetics and products of the gas-phase reaction of SO₃ with water," *Journal of Physical Chemistry*, vol. 100, no. 51, pp. 19911–19916, 1996.

- [11] J. H. Seinfeld and S. N. Pandis, *Atmospheric Chemistry and Physics: From Air Pollution to Climate Change*, John Wiley & Sons, 2nd edition, 2006.
- [12] V. Fiedler, R. Nau, S. Ludmann, F. Arnold, H. Schlager, and A. Stohl, "East Asian SO₂ pollution plume over Europe—part I: airborne trace gas measurements and source identification by particle dispersion model simulations," *Atmospheric Chemistry and Physics*, vol. 9, no. 14, pp. 4717–4728, 2009.
- [13] A. J. Alkezweeny, "Trend analyses of sulfur dioxide emissions and sulfate concentrations and their application to global cooling," *Atmosfera*, vol. 8, no. 2, pp. 91–97, 1995.
- [14] J. J. West, A. S. Ansari, and S. N. Pandis, "Marginal PM_{2.5}: nonlinear aerosol mass response to sulfate reductions in the Eastern United States," *Journal of the Air and Waste Management Association*, vol. 49, no. 12, pp. 1415–1424, 1999.
- [15] R. W. Pinder, R. L. Dennis, and P. V. Bhave, "Observable indicators of the sensitivity of PM_{2.5} nitrate to emission reductions—part I: derivation of the adjusted gas ratio and applicability at regulatory-relevant time scales," *Atmospheric Environment*, vol. 42, no. 6, pp. 1275–1286, 2008.
- [16] R. L. Dennis, P. V. Bhave, and R. W. Pinder, "Observable indicators of the sensitivity of PM_{2.5} nitrate to emission reductions—part II: sensitivity to errors in total ammonia and total nitrate of the CMAQ-predicted non-linear effect of SO₂ emission reductions," *Atmospheric Environment*, vol. 42, no. 6, pp. 1287–1300, 2008.
- [17] W. C. Skamarock, J. B. Klemp, J. Dudhia et al., "A description of the advanced research WRF version 3," Tech. Rep. NCAR/TN-475+STR, NCAR, 2008.
- [18] G. A. Grell, S. E. Peckham, R. Schmitz et al., "Fully coupled "online" chemistry within the WRF model," *Atmospheric Environment*, vol. 39, no. 37, pp. 6957–6975, 2005.
- [19] Y. Zhou, Y. Wu, L. Yang et al., "The impact of transportation control measures on emission reductions during the 2008 Olympic Games in Beijing, China," *Atmospheric Environment*, vol. 44, no. 3, pp. 285–293, 2010.
- [20] Y. Gao, X. Liu, C. Zhao, M. Zhang, and Y. Wang, "Emission controls versus meteorological conditions in determining aerosol concentrations in Beijing during the 2008 Olympic Games," *Atmospheric Chemistry and Physics*, vol. 11, no. 6, pp. 16655–16691, 2011.
- [21] S.-Y. Hong and J.-O. Lim, "The WRF single-moment 6-class microphysics scheme (WSM6)," *Journal of The Korean Meteorological Society*, vol. 42, no. 2, pp. 129–151, 2006.
- [22] G. A. Grell and D. Dévényi, "A generalized approach to parameterizing convection combining ensemble and data assimilation techniques," *Geophysical Research Letters*, vol. 29, no. 14, pp. 38–1, 2002.
- [23] M.-D. Chou and M. J. Suarez, "An efficient thermal infrared radiation parameterization for use in general circulation models," NASA Center for Aerospace Information, 1994.
- [24] E. J. Mlawer, S. J. Taubman, P. D. Brown, M. J. Iacono, and S. A. Clough, "Radiative transfer for inhomogeneous atmospheres: RRTM, a validated correlated-k model for the longwave," *Journal of Geophysical Research D*, vol. 102, no. 14, pp. 16663–16682, 1997.
- [25] Z. I. Janjić, "The step-mountain eta coordinate model: further developments of the convection, viscous sublayer, and turbulence closure schemes," *Monthly Weather Review*, vol. 122, no. 5, pp. 927–945, 1994.
- [26] T. G. Smirnova, J. M. Brown, S. G. Benjamin, and D. Kim, "Parameterization of cold-season processes in the MAPS land-surface scheme," *Journal of Geophysical Research D*, vol. 105, no. 3, pp. 4077–4086, 2000.
- [27] J. C. Barnard, J. D. Fast, G. Paredes-Miranda, W. P. Arnott, and A. Laskin, "Technical note: evaluation of the WRF-chem "aerosol chemical to aerosol optical properties" module using data from the MILAGRO campaign," *Atmospheric Chemistry and Physics*, vol. 10, no. 15, pp. 7325–7340, 2010.
- [28] W. R. Stockwell, P. Middleton, J. S. Chang, and Xiaoyan Tang, "The second generation regional acid deposition model chemical mechanism for regional air quality modeling," *Journal of Geophysical Research*, vol. 95, no. 10, pp. 16343–16367, 1990.
- [29] S. Madronich, "Photodissociation in the atmosphere—1. Actinic flux and the effects of ground reflections and clouds," *Journal of Geophysical Research*, vol. 92, no. 8, pp. 9740–9752, 1987.
- [30] I. J. Ackermann, H. Hass, M. Memmesheimer, A. Ebel, F. S. Binkowski, and U. Shankar, "Modal aerosol dynamics model for Europe: development and first applications," *Atmospheric Environment*, vol. 32, no. 17, pp. 2981–2999, 1998.
- [31] M. L. Wesely, "Parameterization of surface resistances to gaseous dry deposition in regional-scale numerical models," *Atmospheric Environment*, vol. 23, no. 6, pp. 1293–1304, 1989.
- [32] D. Simpson, A. Guenther, C. N. Hewitt, and R. Steinbrecher, "Biogenic emissions in Europe 1. Estimates and uncertainties," *Journal of Geophysical Research*, vol. 100, no. 11, pp. 22875–22890, 1995.
- [33] M. Weilenmann, J. Y. Favez, and R. Alvarez, "Cold-start emissions of modern passenger cars at different low ambient temperatures and their evolution over vehicle legislation categories," *Atmospheric Environment*, vol. 43, no. 15, pp. 2419–2429, 2009.
- [34] M. Hart and R. De Dear, "Weather sensitivity in household appliance energy end-use," *Energy and Buildings*, vol. 36, no. 2, pp. 161–174, 2004.
- [35] NESCAUM, "Low sulfur heating oil in the Northeast States: An overview of benefits, costs and implementation issues," Boston, Mass, USA, 2005.
- [36] D. R. Cocker, S. L. Clegg, R. C. Flagan, and J. H. Seinfeld, "The effect of water on gas-particle partitioning of secondary organic aerosol—part I: α -pinene/ozone system," *Atmospheric Environment*, vol. 35, no. 35, pp. 6049–6072, 2001.
- [37] G. Wendler and P. Nicpon, "Low-level temperature inversions in Fairbanks, Central Alaska," *Monthly Weather Review*, vol. 103, pp. 34–44, 1974.
- [38] N. Mölders and G. Kramm, "A case study on wintertime inversions in Interior Alaska with WRF," *Atmospheric Research*, vol. 95, no. 2–3, pp. 314–332, 2010.
- [39] J. C. F. Lo, Z. L. Yang, and R. A. Pielke, "Assessment of three dynamical climate downscaling methods using the Weather Research and Forecasting (WRF) model," *Journal of Geophysical Research D*, vol. 113, no. 9, Article ID D09112, 2008.
- [40] K. S. Yap, "Impact of a newtonian assimilation and physical initialization on the initialization and prediction by a tropical mesoscale model," *Monthly Weather Review*, vol. 123, no. 3, pp. 833–861, 1995.
- [41] Z. T. Pan, E. Takle, W. Gutowski, and R. Turner, "Long simulation of regional climate as a sequence of short segments," *Monthly Weather Review*, vol. 127, no. 2–3, pp. 308–321, 1999.

Research Article

An Air Quality Management System for Policy Support in Cyprus

**Nicolas Moussiopoulos,¹ Ioannis Douros,¹ George Tsegas,¹
Savvas Kleanthous,² and Eleftherios Chourdakis¹**

¹Laboratory of Heat Transfer and Environmental Engineering, Aristotle University, University Campus, P.O. Box 483, 54124 Thessaloniki, Greece

²Department of Labour Inspection, Ministry of Labour and Social Insurance, Apelli 12, 1480 Nicosia, Cyprus, Greece

Correspondence should be addressed to Ioannis Douros, jdouros@aix.meng.auth.gr

Received 13 February 2012; Accepted 22 March 2012

Academic Editor: Tareq Hussein

Copyright © 2012 Nicolas Moussiopoulos et al. This is an open access article distributed under the Creative Commons Attribution License, which permits unrestricted use, distribution, and reproduction in any medium, provided the original work is properly cited.

The recent air quality directive (2008/50/EC) encourages the introduction of modelling as a necessary tool for air quality assessment and management. Towards this aim, an air quality management system (AQMS) has been developed and installed in the Department of Labour Inspection (DLI) of the Republic of Cyprus. The AQMS comprises of two operational modules, providing hourly nowcasting and daily forecasting of the air quality status, implemented as an integrated model system that performs nested grid meteorological and photochemical simulations. A third operational module provides the capability of an interactive configuration of custom emission scenarios and corresponding model runs covering user-defined domains of interest. Statistical indicators are calculated at the end of each day for the measurement locations of DLI's air quality monitoring network. Besides, the system provides an advanced user interface, which is realised as a web-based application providing access to model results from any computer with an internet connection and a web browser.

1. Introduction

The new air quality directive (2008/50/EC) introduces additional requirements for air quality assessment and management. As a result, along with air quality measurements, modelling tools should also be used by authorities and policy makers in order to assess pollutant concentrations in ambient air. It also requires that up-to-date information on concentrations of all regulated pollutants in ambient air should be readily available to the public.

Towards this aim, an operational web-based system for air quality management developed by the Laboratory of Heat Transfer and Environmental Engineering (LHTEE) has been installed in the Department of Labour Inspection of the Ministry of Labour and Social Insurance in the Republic of Cyprus. The system offers a range of features for nowcasting, forecasting, and performing scenario calculation for air quality in Cyprus. Besides, a number of statistical indices [1] and validation maps are calculated at the end of each day at various points coinciding with the locations of DLI's air

quality monitoring stations [2] in order to assess the system's accuracy.

The main goals of the system lie in providing useful up-to-date information to the public on pollutant concentrations in ambient air, as well as supporting local authorities and decision makers in air quality assessment and management.

2. Methodology

The core of the system handles the compilation of an emissions inventory that includes data from all major activity sectors and functions on the basis of a continuous update of the emissions database. This part of the software dealing with emissions provides functionality for setting up emission scenarios based both on the application of measures as well as targeted modifications. Emission data are prepared as an emissions grid that is subsequently fed into the air quality modelling system [3].

TABLE 1: Description of MEMO and MARS-aero nested grids.

	Depth of nesting	Number of nested grids	Grid size	Grid resolution	Type of nesting
Coarse	2	1	60 × 60	25 km ²	1-way
Fine		5	50 × 50	1 km ²	

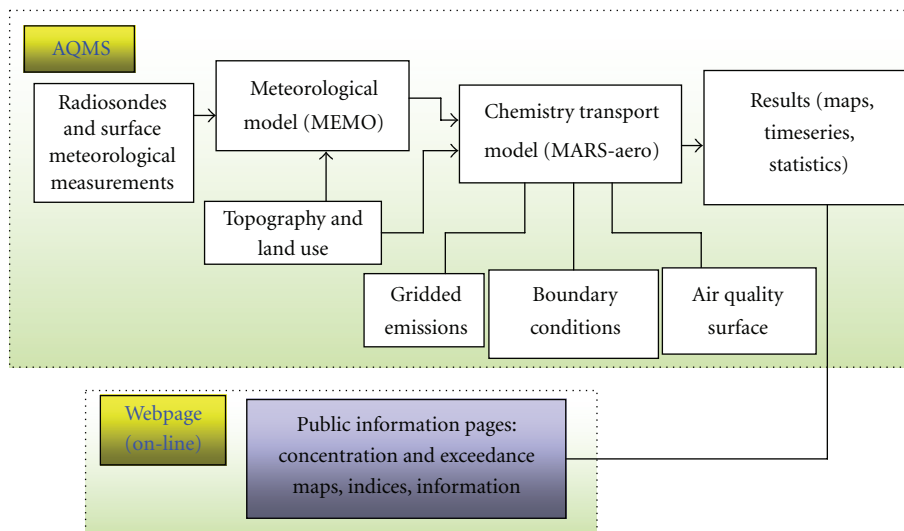


FIGURE 1: The structure of the air quality management system.

The part of the AQMS dealing with the calculation of ambient concentrations has a functional structure similar to that followed by most AQMSs operating on an around-the-clock basis (see Figure 1). The AQMS comprises of two operation modes, nowcasting and forecasting, which are implemented based on an automated scheme that performs nested grid meteorological and photochemical model simulations. The mesoscale meteorological model MEMO and the chemistry-transport model MARS-aero are used for this purpose, both parts of the EZM (European Zooming Model) system [4]. MEMO [5] is a three-dimensional, non-hydrostatic, prognostic mesoscale model which simulates mesoscale air motion and inert pollutant dispersion at the local-to-regional scale, over complex terrain, allowing multiple nesting. MARS-aero [6] is an Eulerian chemistry-transport model for reactive species operating at similar scales. The modular structure of MARS-aero allows any of four chemical reaction mechanisms for the gaseous phase to be used, while the calculation of secondary aerosols, organic and inorganic, can be enabled at will [7, 8]. Meteorological data such as wind speed, temperature, TKE, surface roughness, Monin-Obukhov length, and friction velocity are required input for the dispersion calculations and are provided by MEMO. Both MEMO and MARS-aero are used in a nested configuration (see Table 1).

For the initialisation of MEMO, a number of vertical profiles of the key meteorological variables originating from the Global Forecast System (GFS) are used [9]. Such profiles are also assimilated into the model calculations on a 3-hour basis. The downloader module of the automated system

undertakes the downloading of the GFS data, processes them, and stores them in a data pool which is kept updated at all times. The scheduler selects only the most recent dataset for input to the MEMO model. Each of these processes keeps a separate event log and diagnostic files accessible to the operator of the system.

The MARS-aero model runs back-to-back with the MEMO model, featuring real time integration of ambient pollutant concentration data that are provided both from valid measurement data, as well as from larger scale models results and are used both as initial and lateral conditions in the model calculations as well as for data assimilation purposes. An upgraded methodology has been developed and incorporated in the system's core for providing increased flexibility in the coupling of the nested domains. Additionally, a dynamic dust concentration component is included in the PM₁₀ and PM_{2.5} boundary conditions that are fed in the model core, so as to improve the accuracy of calculated PM concentrations during Saharan dust episodes. These upgrades significantly enhance the operational prognostic skills of the AQMS in the cases of elevated concentration levels that are associated with transboundary transport of air pollutants.

In nowcasting mode the system computes, on an hourly basis, the pollutant concentration fields in Cyprus and, at higher resolution, in the five largest cities. Model results are automatically processed and a range of maps, timeseries graphs, and statistical indices are produced for five major pollutants, namely, PM₁₀, PM_{2.5}, NO₂, O₃, and benzene. These results become available to the public via DLI's web

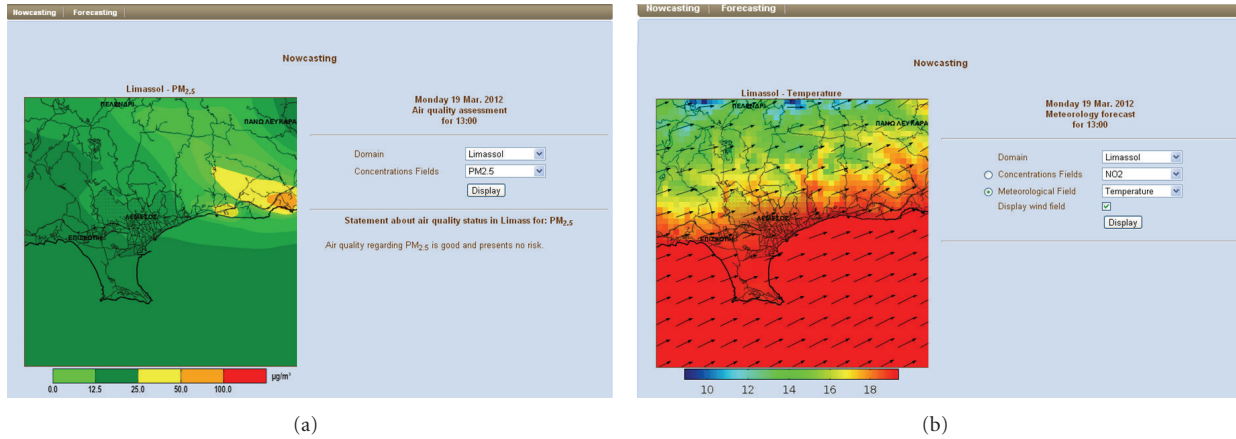


FIGURE 2: Snapshots of nowcasting for pollutant concentrations (a) and meteorological parameters (b).

page and are also accessible in even greater detail to the staff of the department. In forecasting mode 24-hour photochemical model simulations are driven by corresponding prognostic meteorological simulations of GFS, in order to produce daily air quality forecast maps and graphs for the domains of interest and the prescribed pollutants. Daily forecasts become available to the department and the public through a set of web pages accessible through a similar interface.

The system's user interface is realised as a web-based application which is accessible from any computer having internet access. Through this interface, the authorized DLI users are provided with numerous possibilities for reviewing both the process and the results of the calculations as well as for configuring the information that becomes available in the public web page. The informational public pages represent a very important aspect of the system's structure as, in addition to the concentration levels, the public is also informed on the expected health impacts of the forecasted air quality situation, thus allowing them to manage their activities accordingly.

In order to evaluate the system's performance, suitable statistical indicators are calculated at the end of each day regarding the sites where DLI's air quality measurements take place. An automated procedure operating on an around-the-clock basis undertakes the downloading of the available observation data from DLI's server, processes them, and keeps them in a data base, where historical monitoring data are stored. In addition, model results for the measurement locations of DLI's air quality monitoring network are also kept in appropriate data pool. At the end of each day, a wide range of statistical indices are calculated regarding the stations and pollutants of interest and numerous charts are produced, which demonstrate the system's performance in both nowcasting and forecasting mode. In order to have a better overview of the system's efficiency, validation charts are also produced. These charts present comparisons between the calculated and the observed timeseries concerning air pollutant concentration, wind speed, and wind direction.

The AQMS can also be operated by DLI to support air-quality-related assessment and decision making, by allowing

interactive configuration of custom emission scenarios and corresponding model runs. This operational module provides the capability to study emission scenarios and assess their effect on air quality in the five major urban areas of Cyprus or over user-defined domains. The meteorology used for assessment calculations is based on a number of representative meteorological situations which are analysed and duly weighted according to the frequency of their occurrence during a full calendar year.

3. Results

Through the system's interface the public and the authorized DLI users can view the model results, both for nowcasting and forecasting. In the nowcasting section, hourly meteorological and air quality maps are available to any computer with an internet connection through interactive web pages (see Figures 2 and 3). The public is also informed on the expected health impacts of the forecasted air quality situation by messages that are automatically produced and constitute a statement about the expected exposure to air pollution levels on an hourly basis.

Figure 3 demonstrates the gradual dust transport over the Cyprus domain during a typical Saharan dust episode. The system performs reasonably well in predicting the occurrence of Saharan dust episodes. Besides, the model results presented in Figure 3 indicate the high ability of the system in producing the spatial distribution of PM during these episodes.

In the forecasting section of the web interface, a wide range of maps, timeseries graphs, and statistical indices are made accessible to the public, providing information both on forecast pollutant concentrations as well as on meteorological parameters, such as temperature, relative humidity, and wind speed (see Figure 4).

Furthermore, through this interface, the authorized DLI users are provided with geospatial tools for setting up emission scenarios, as well as reviewing the results of the corresponding model runs (see Figure 5). In the scenarios results

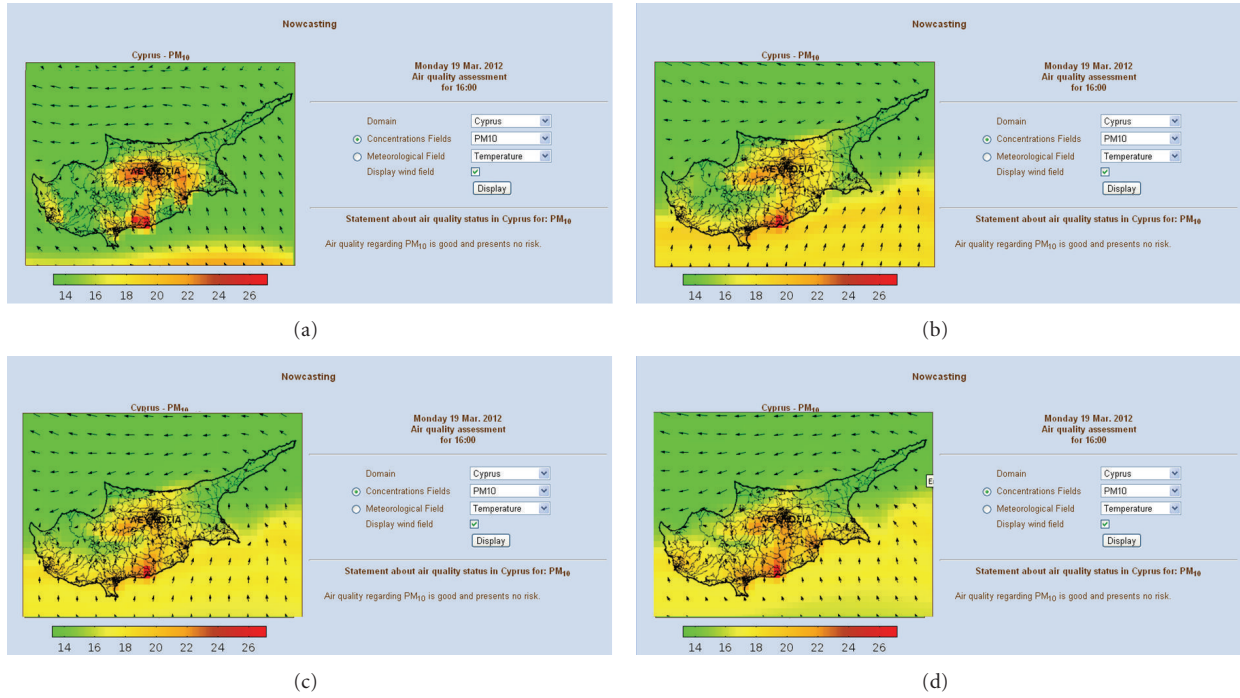


FIGURE 3: Snapshots of nowcasting results for PM₁₀ during a Saharan dust episode.

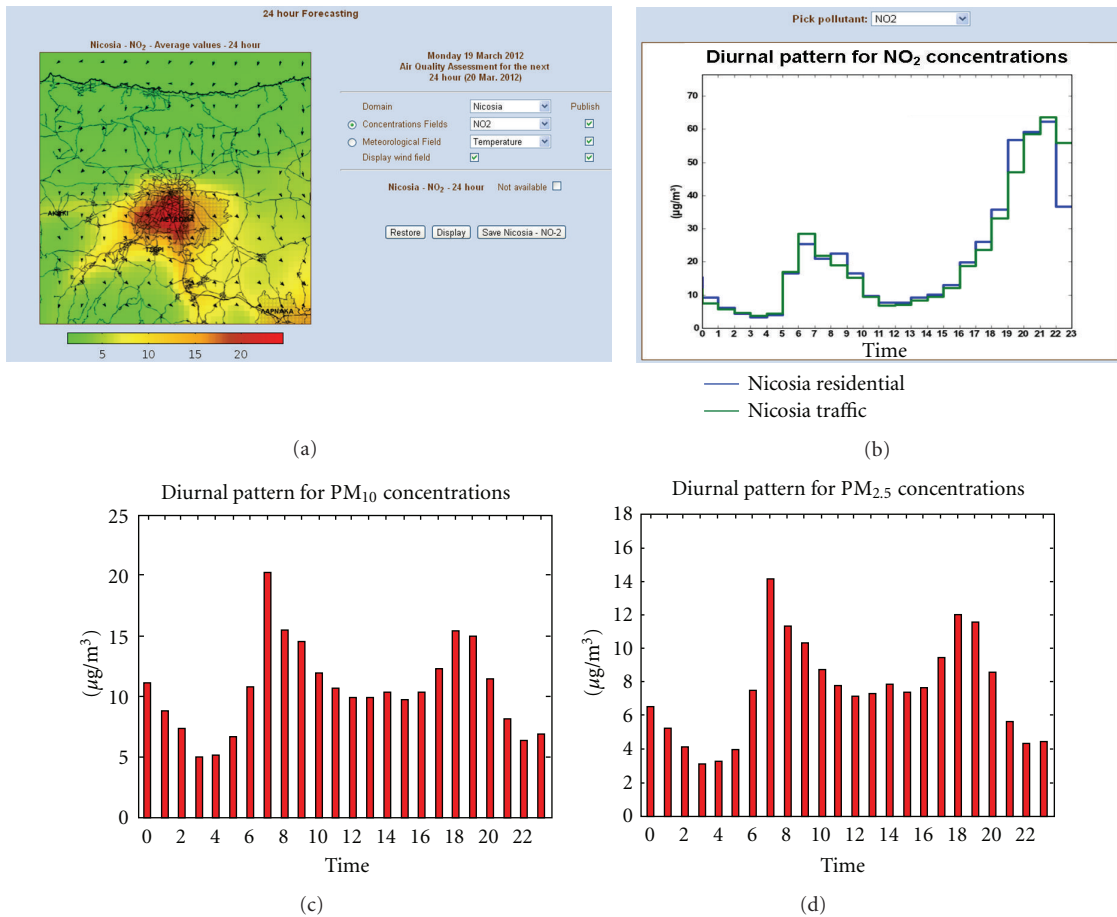
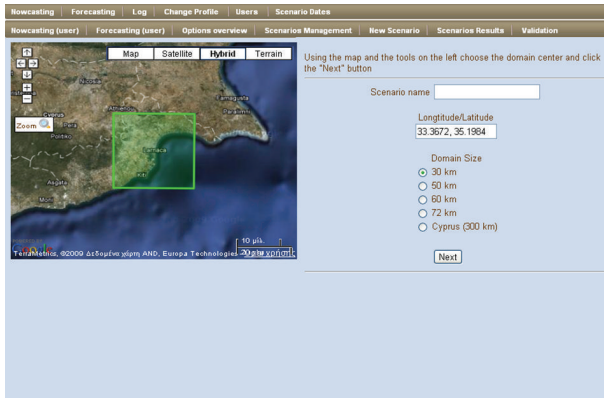
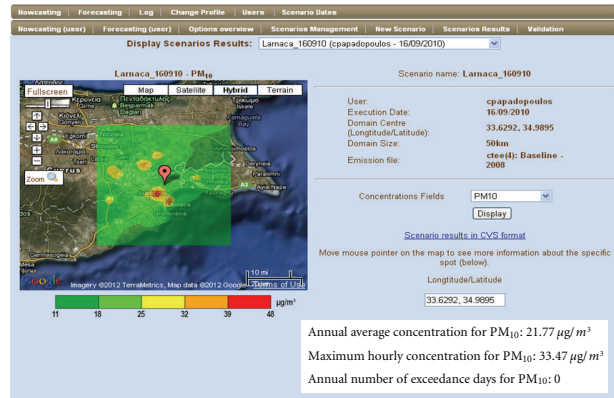


FIGURE 4: Snapshots of forecasting results for pollutant concentrations.

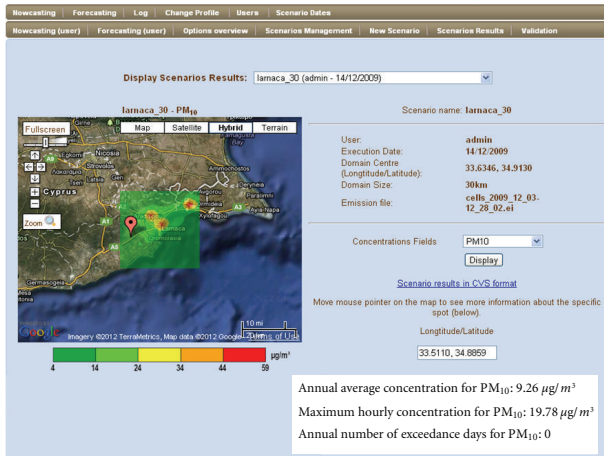


(a)

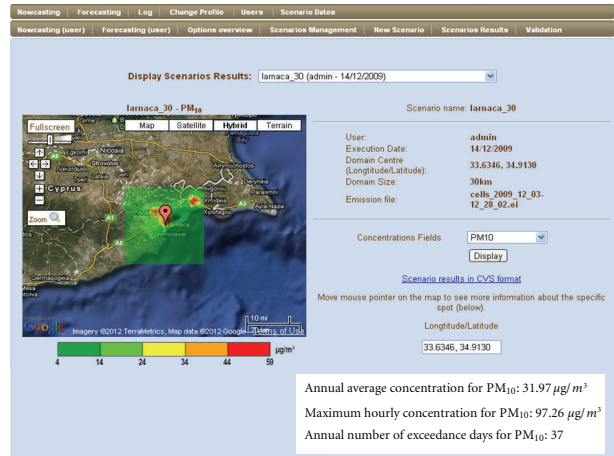


(b)

FIGURE 5: Emission scenario set up (a) and scenarios results (b).

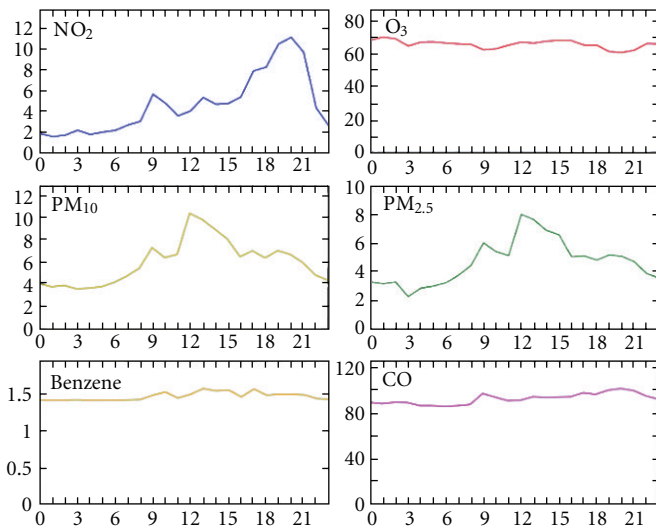


(a)



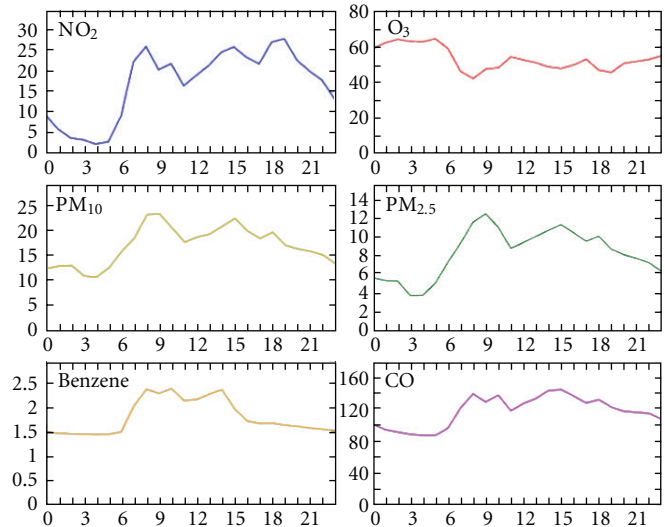
(b)

Concentration diurnal patterns ($\mu\text{g}/\text{m}^3$)



(c)

Concentration diurnal patterns ($\mu\text{g}/\text{m}^3$)



(d)

FIGURE 6: Statistical indices and graphs produced for two different locations inside the computational domain of a particular emission scenario.

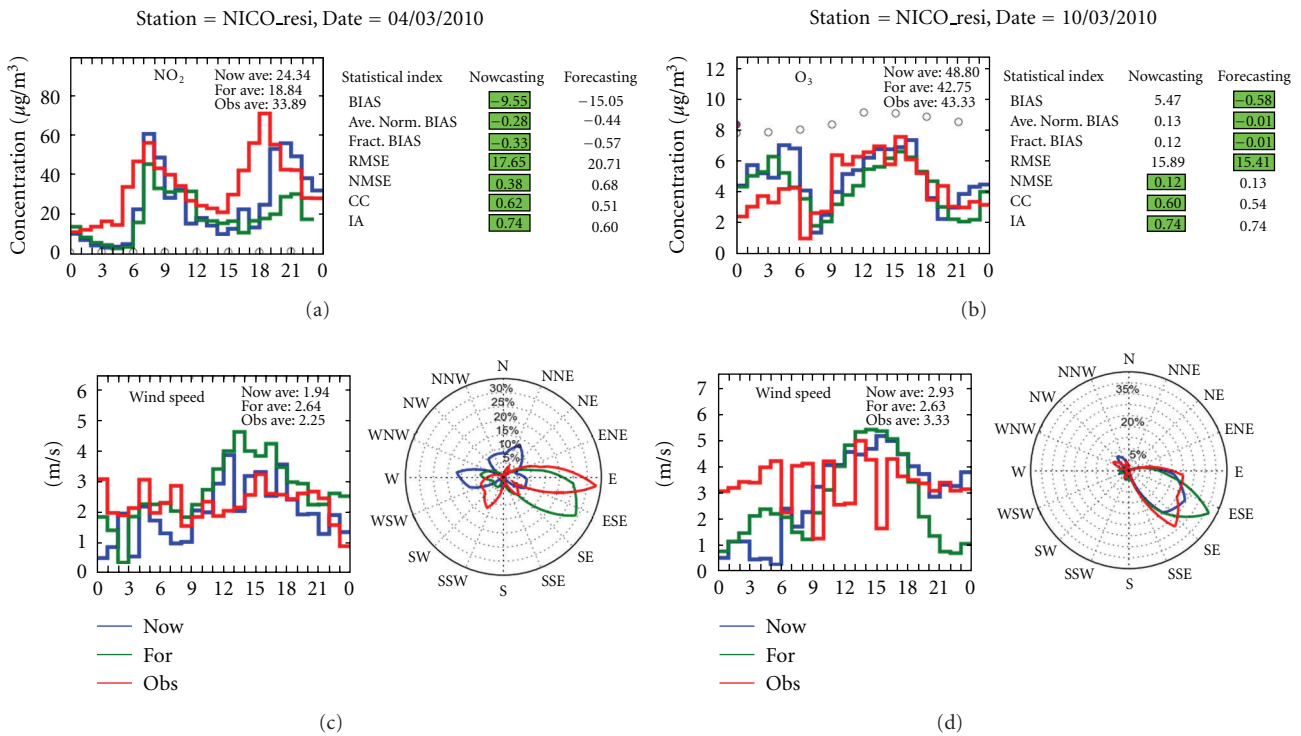


FIGURE 7: Air quality and meteorological validation graphs as regards the residential station of Nicosia for the 4th and 10th of March 2010 concerning NO₂ and O₃, respectively.

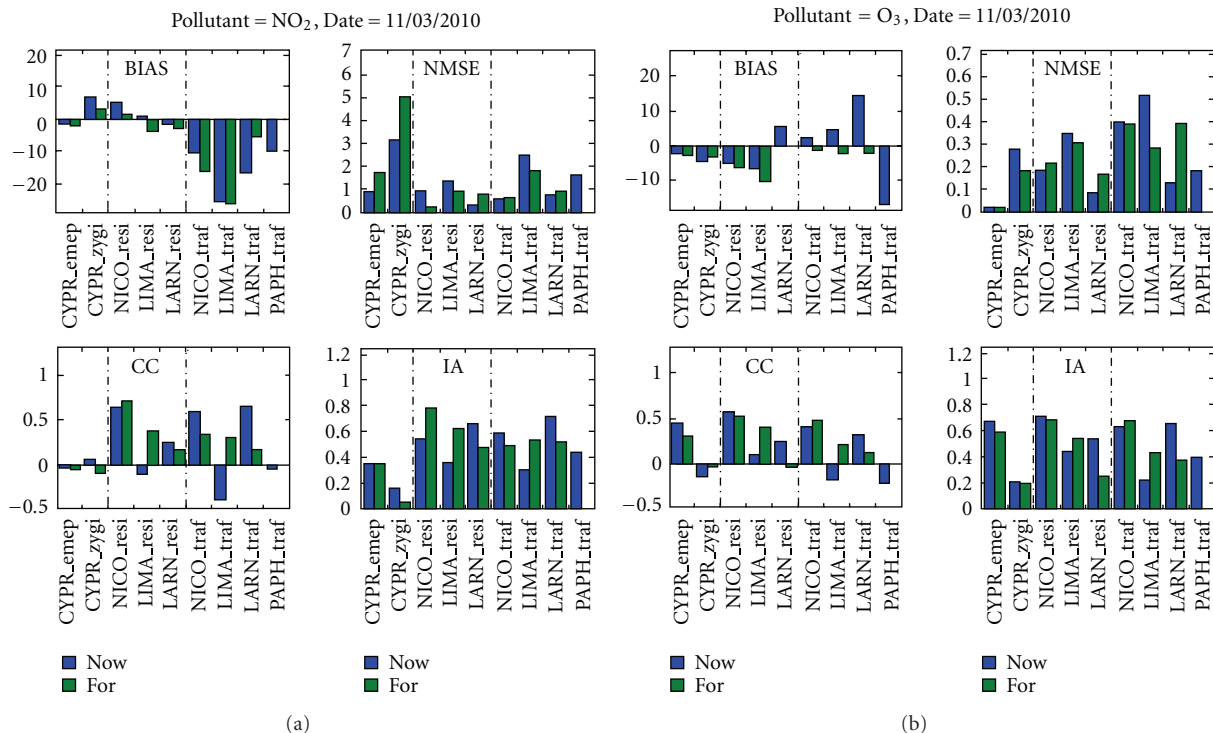


FIGURE 8: Statistical indices calculated for the 11th of March 2010 as regards NO₂ (a) and O₃ (b).

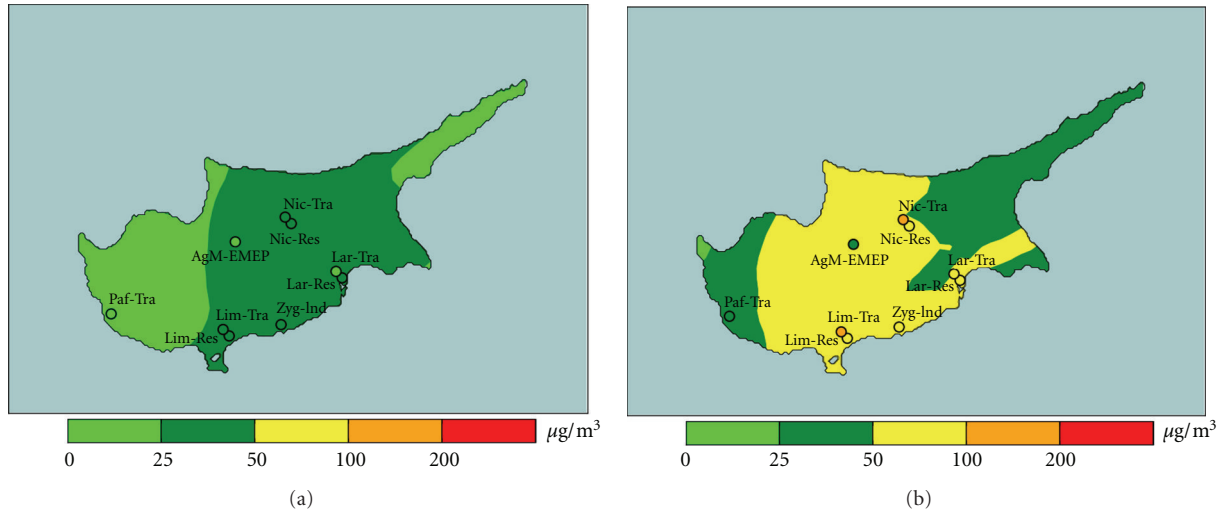


FIGURE 9: Validation maps as regards PM_{10} for a typical winter day (a) and a day in which a slight Saharan dust episode occurs (b).

section, the DLI user can not only access pollutant concentration maps produced by the automatic process of the respective model runs but also to manually produce statistical indices and timeseries graphs for any location inside the calculation domain, using a suitable interactive feature (see Figure 6).

In Figure 7 air quality and meteorological validation graphs as they are operationally produced by the system are presented. Each graph shows comparisons between model simulations and the respective observation data regarding air pollutant concentrations, as well as wind speed and direction. Additional information about the model accuracy is also provided in the form of statistical indices, namely, “BIAS”, “Average Normalised BIAS” (ANB), “Fractional Bias” (FB), “Root Mean Square Error” (RMSE), “Normalised Mean Square Error” (NMSE), “Correlation Coefficient”, and “Index of Agreement”. In this field of the graphs, green colour indicates which mode between nowcasting and forecasting operates better according to each statistical index.

As depicted from Figure 7, the system’s performance as regards the suburban areas is good in the case of O_3 , where concentration levels are determined by the transboundary transport which enters the model as initial and lateral boundary conditions from the results of larger scale models. On the other hand, the supplementary use of air quality measurements in the formation of the boundary conditions leads to increased model efficiency in the cases of air pollutants which are related to human activities, such as NO_2 . This fact occurs because most of DLI’s measurement stations are located close to areas which contain a wide range of human activities, including transport and industry, and as a result, the obtained concentration values are affected by the aforementioned activities. Thus, the exploitation of observation data as boundary conditions of the model simulations improves the system’s computational performance in assessing air pollutant levels mostly influenced by human activities.

Figure 8 presents a subset of the calculated statistical indicators, namely, “BIAS”, “Normalised Mean Square

Error”, “Correlation Coefficient”, and “Index of Agreement”, for three typical days regarding nitrogen dioxide (NO_2) and ozone (O_3). As evidenced from the indicators shown in Figure 8, the results of the model are in fairly good agreement with the observed concentrations, the only exceptions being the industrial and traffic stations. This is more or less expected for these hotspots that are highly affected by local and street scale activities.

Figure 9 shows validation maps as regards PM_{10} for a typical winter day and a day in which a slight Saharan dust episode occurs. In these maps the calculated model concentration maps are compared to the concentrations observed at the measurement locations at the same time.

4. Conclusions

The AQMS developed and installed in the Department of Labour Inspection of the Republic of Cyprus is an integrated operational state-of-the-art air quality management system for meteorological and photochemical model simulations which offers a range of features for nowcasting, forecasting, and performing scenario calculations for air quality in areas of interest. Results of the calculations can be reviewed in detail by the DLI, while they can also be accessed in a condensed form by the general public via a user friendly web page. In order to evaluate the system’s performance, suitable statistical indicators are calculated at the end of each day for the measurement locations of DLI’s air quality monitoring network. Besides, validation charts are also produced, presenting comparisons between the calculated and the observed timeseries concerning air pollutant concentration, wind speed, and wind direction. The AQMS can also be operated by authorised DLI users to support air-quality-related assessment and decision making by performing air quality calculations based on custom emission scenarios. The capabilities offered by this AQMS for producing high-quality assessments of the air quality situation are expected to be

a valuable aid to the authorities of Cyprus towards compliance with the relevant EU standards.

Acknowledgments

This work was cofinanced by the EU in the framework of the transition facility 2005 for Cyprus. The authors would also like to thank the director of DLI Leandros Nicolaides and the DLI team involved in the project.

References

- [1] COST728, *Overview of Tools and Methods for Meteorological and Air Pollution Mesoscale Model Evaluation and User Training*, 2008.
- [2] <http://www.airquality.dli.mlsi.gov.cy/>.
- [3] S. Kleanthous, G. Tsegas, I. Douros, and N. Moussiopoulos, "An air quality management system for Cyprus," in *Proceedings of the 7th International Conference on Air Quality-Science and Application (Air Quality '09)*, R.-M. Hu, Ed., pp. 405–408, CD-ROM edition, Istanbul, Turkey, March 2009.
- [4] N. Moussiopoulos, "The EUMAC Zooming Model, a tool for local-to-regional air quality studies," *Meteorology and Atmospheric Physics*, vol. 57, no. 1–4, pp. 115–133, 1995.
- [5] N. Moussiopoulos, T. Flassak, P. Sahm, and D. Berlowitz, "Simulations of the wind field in Athens with the nonhydrostatic mesoscale model MEMO," *Environmental Software*, vol. 8, no. 1, pp. 29–42, 1993.
- [6] N. Moussiopoulos, P. Sahm, and C. Kessler, "Numerical simulation of photochemical smog formation in Athens, Greece—a case study," *Atmospheric Environment*, vol. 29, no. 24, pp. 3619–3632, 1995.
- [7] A. Arvanitis, N. Moussiopoulos, and S. Kephelopoulos, "Development and testing of an aerosol module for regional/urban scales," in *Proceedings of the 2nd Conference on Air Pollution Modelling and Simulation (APMS '01)*, pp. 277–288, Champs-sur-Marne, April 2001.
- [8] B. Schell, I. J. Ackermann, H. Hass, F. S. Binkowski, and A. Ebel, "Modeling the formation of secondary organic aerosol within a comprehensive air quality model system," *Journal of Geophysical Research D*, vol. 106, no. 22, pp. 28275–28293, 2001.
- [9] <http://www.emc.ncep.noaa.gov/gmb/moorthi/gam.html>.

Research Article

Wood-Burning Device Changeout: Modeling the Impact on PM_{2.5} Concentrations in a Remote Subarctic Urban Nonattainment Area

Huy N. Q. Tran and Nicole Mölders

*Department of Atmospheric Sciences, Geophysical Institute and College of Natural Science and Mathematics,
University of Alaska Fairbanks, 903 Koyukuk Drive, Fairbanks, AK 99775-7230, USA*

Correspondence should be addressed to Nicole Mölders, molders@gi.alaska.edu

Received 4 January 2012; Accepted 14 February 2012

Academic Editor: Lidia Morawska

Copyright © 2012 H. N. Q. Tran and N. Mölders. This is an open access article distributed under the Creative Commons Attribution License, which permits unrestricted use, distribution, and reproduction in any medium, provided the original work is properly cited.

The effects of exchanging noncertified with certified wood-burning devices on the 24h-average PM_{2.5} concentrations in the nonattainment area of Fairbanks, Alaska, in a cold season (October to March) were investigated using the Weather Research and Forecasting model inline coupled with a chemistry package. Even changing out only 2930 uncertified woodstoves and 90 outdoor wood boilers reduced the 24 h-average PM_{2.5} concentrations on average by 0.6 $\mu\text{g}\cdot\text{m}^{-3}$ (6%) and avoided seven out of 55 simulated exceedance days during this half-a-year. The highest reductions on any exceedance day ranged between 1.7 and 2.8 $\mu\text{g}\cdot\text{m}^{-3}$. The relative response factors obtained were consistently relatively low (~ 0.95) for all PM_{2.5} species and all months. Sensitivity studies suggest that the assessment of the benefits of a wood-burning device changeout program in avoiding exceedances heavily relies on the accuracy of the estimates on how many wood-burning devices exist that can be exchanged.

1. Introduction

In 2006, the Environmental Protection Agency (EPA) has tightened the 24 h National Ambient Air Quality Standards (NAAQS) to 35 $\mu\text{g}\cdot\text{m}^{-3}$ for fine particulate matter having diameters equal to or less than 2.5 μm (PM_{2.5}). From October to March the PM_{2.5} data collected in prior years indicated that PM_{2.5} concentrations exceeded the NAAQS frequently at the official monitoring site in Fairbanks [1]—a remote urban area in the subarctic of Alaska. Therefore, Fairbanks was designated a PM_{2.5} nonattainment area in 2009.

In Fairbanks, wood-burning devices are major contributors to the PM_{2.5} emissions in residential areas [2]. An estimated 9240 wood-burning devices exist in Fairbanks, of which 7980 devices are woodstoves [2]. Due to the increasing price of heating fuel, many Fairbankisan households added wood-burning devices or shifted to a higher percentage of heating with wood as is evident from the threefold increase of wood-cutting permits from 2007 to 2009 (Conner, pers. com. 2010).

The emissions from wood-burning devices vary with fuel type, fuel moisture, burning practice, and control techniques

of the devices [3]. In general, EPA-certified woodstoves emit up to 87% less PM_{2.5} than uncertified ones [3]. EPA [4] estimated that 10 million woodstoves are being used in the United States, about 80% of which are uncertified devices. Exchanging uncertified woodstoves with certified ones has been a successful tool to mitigate PM_{2.5} concentrations in many places [5].

The effects of woodstove changeout programs on reducing ambient PM_{2.5} concentrations have been evaluated mainly based on observations. For example, the PM_{2.5} sampling campaign related to the changeout of 1200 uncertified woodstoves in Libby, Montana, showed that 24 h-average PM_{2.5} concentrations decreased by 20% during the changeout period [6]. Indoor PM_{2.5} concentration measured in 16 homes prior and after the woodstove changeout in a Rocky Mountain valley community [7] indicated reduction of average and maximum PM_{2.5} concentrations of 71% and 76%, respectively. A similar study performed in 15 homes in British Columbia, Canada, found no consistent relationship between the indoor PM_{2.5} reductions and the woodstove changeout [8].

Of the 8610 inserts and woodstoves in Fairbanks, about 2930 devices are uncertified ones [2]. An assessment of the benefits of a wood-burning device changeout for any high latitude urban community based on observational studies in midlatitudes is difficult. Fairbanks' subarctic meteorological conditions differ strongly from those in the mid-latitude places where wood-burning device changeout programs have been applied successfully to mitigate air pollution. In Fairbanks, the often stagnant air and strong radiative cooling during the long nights lead to low temperatures and strong inversions. Inversions exist on 78–97 days between October and March and often last for more than ten consecutive days. The 1971–2000 monthly mean temperatures in October, November, December, January, February, and March were -9 , -18 , -22 , -23 , -18 , and -14°C , respectively. Such extremely low temperatures result in high heating demands. The calm winds (0.5–2.5 m on monthly average between October and March) and inversions mean low mixing of the polluted air with the unpolluted environment.

Whereas the observational approach applied in mid-latitudes requires an extensive measurement campaign over the changeout program lifetime, numerical modeling can provide a quick and low-cost assessment of the benefits of a wood-burning device changeout program. Furthermore, modeling permits assessment of the potential benefits of a changeout program prior to its implementation/completion and hence permits implementation of additional measures in case the changeout program alone may not be sufficient enough to achieve compliance.

To this aspect, the Weather Research and Forecasting model inline coupled with a chemistry model commonly known as WRF/Chem [9, 10] has been widely used to investigate pollution sensitivity to changes in emissions. For example, WRF/Chem served to investigate the effects of changing emission of nitrogen oxides (NO_x) from power plants on ozone concentrations in the eastern United States [11]. The simulations elucidated complex relationships between ozone concentrations and NO_x emission strength, the proximity of other NO_x sources, the availability of volatile organic carbon (VOC), and sunlight. WRF/Chem simulations to study the impacts of urban expansion on the formation of secondary organic aerosol over the Pearl River Delta, China, showed that urban expansion can alter the meteorological conditions and therefore induce increases of secondary organic aerosol between 3 and 9% [12]. WRF/Chem investigations showed that the emission changes between 1990 and 2000 in the North Pacific region caused the increasing trends of sulfate aerosols observed at coastal Alaska sites [13]. These simulations also showed that at coastal sites in southern Alaska, sulfate aerosol was not governed by the local emission changes but by the increased ship emissions and Canadian emissions.

Among many efforts in seeking effective pollution controls to comply with the NAAQS, Fairbanks started conducting a “woodstove replacement” program. Given that Fairbanks' 2008 design value is $44.7 \mu\text{g}\cdot\text{m}^{-3}$, any emission-control strategy requires a relative response factor (RRF) lower than 0.78 to reach compliance with the NAAQS. In this study, we used WRF/Chem with its modifications for Alaska

TABLE 1: Parameterizations used in this study.

Process	Scheme and reference
Cloud microphysics	Six water-class cloud microphysical scheme [16]
Subgrid-scale convection	Further developed 3D version of the Grell-Dévényi cumulus-ensemble scheme [17]
Radiation	Goddard shortwave radiation scheme [18], Radiative Transfer Model for long-wave radiation [19], radiative feedback from aerosols [20]
Atmospheric boundary layer and sublayer processes	[21]
Land-surface processes	Modified Rapid Update Cycle land-surface model [22]
Gas-phase chemistry	[23]
Photolysis frequencies	[24]
Aerosol physics, chemistry and dynamics	Modal Aerosol Dynamics Model for Europe [25] and Secondary ORGanic Aerosol Model [26]
Dry deposition	[27] with the modifications by [14]
Biogenic emissions	calculated inline depending on meteorological conditions [28]

[14, 15] to assess the benefits of exchanging uncertified with certified wood-burning devices on the $\text{PM}_{2.5}$ concentrations at breathing level in the Fairbanks nonattainment area.

2. Experimental Design

2.1. Simulations. Simulations were performed for October 1, 2008 0000 UTC, to April 2, 2009 0000 UTC, with the Alaska modified WRF/Chem in forecast mode. The physical and chemical schemes selected for the simulations are listed in Table 1 and were described in detail in [15].

The model domain encompasses most of Interior Alaska centered over the Fairbanks nonattainment with 4 km horizontal grid-increment from the surface to 100 hPa with 28 stretched vertical layers (Figure 1). The top of the first layer (breathing level) is at 8 m height. The initial conditions for the meteorological fields and meteorological lateral boundary conditions were downscaled from the $1^{\circ} \times 1^{\circ}$, 6 h-resolution National Centers for Environmental Prediction global final analyses. The chemical fields were initialized with vertical profiles of Alaska typical background concentrations. Since Fairbanks is the only major emission source and urban area within 578 km radius and observational and modeling studies showed hardly any advection of pollutants [13, 15], Alaska background concentrations served as lateral boundary conditions.

We performed simulations without (REF) and with “woodstove replacement” (WSR). In WSR, the numbers of wood-burning devices to be changed out were based on [2]. These authors estimated, there are in total 9240 wood-burning devices of which 2930 and 90 are uncertified woodstoves and outdoor wood boilers, respectively. Since an

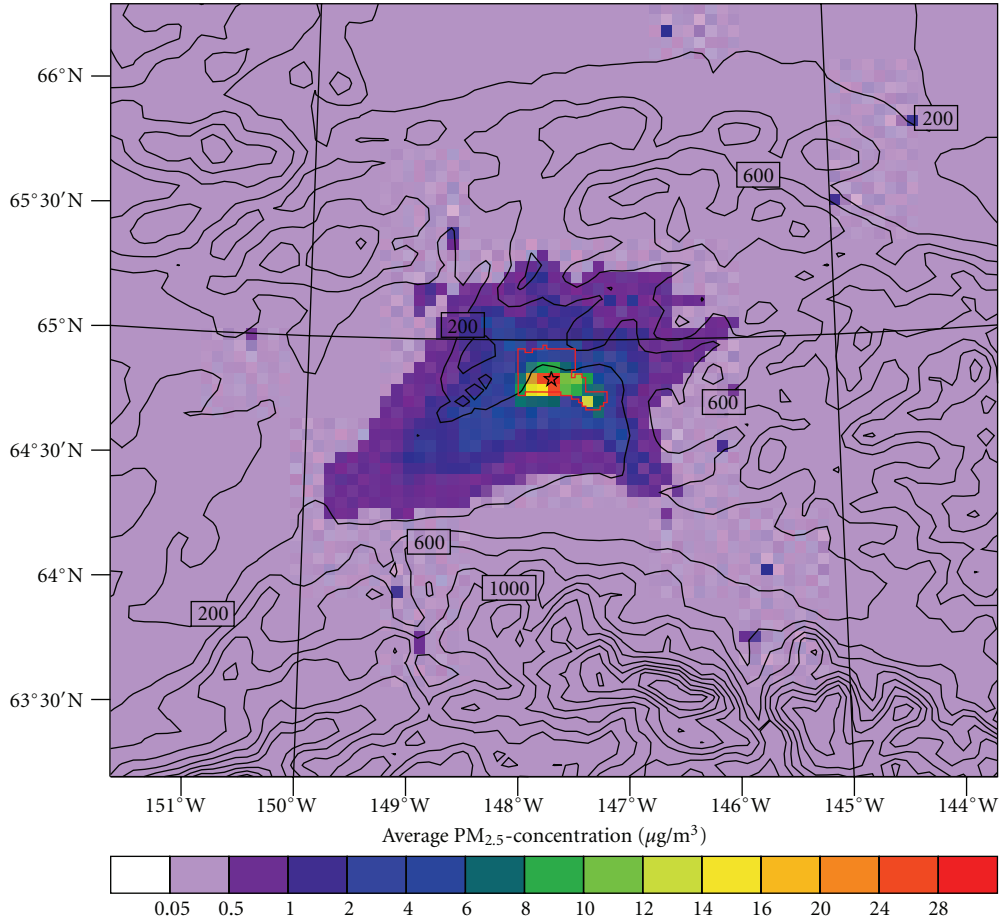


FIGURE 1: Average $PM_{2.5}$ concentration in the domain of interest in October to March as obtained in REF with terrain contours overlain. The star and red polygon indicate the grid cell holding the official monitoring site and the outline of the nonattainment area.

earlier study [29] estimated that there exist 13829 wood-burning devices of which 5042 and 1500 are uncertified woodstoves and outdoor wood boilers, respectively, we performed a sensitive simulation (WSS1) assuming a changeout based on these numbers. A second sensitivity simulation (WSS2) was based on unpublished data by Carlson and collaborators (2009; pers. comm.) that marginally differed in the numbers of total wood-burning devices (9241) and uncertified woodstoves (2934) from the numbers published in [2] and used in WSR, but did not consider pellet stoves (0 versus 370 devices). The sensitivity studies were run for 14 days to assess the sensitivity to the number of wood-burning devices (WSS1) and type of devices (WSS2).

2.2. Emission Inventories. We developed the annual anthropogenic emission inventory based on the National Emission Inventory (NEI) of 2008 available by October 2010. As no point-source emissions were available at that time, we used point-source emission data from facility operators (if provided) and assumed a 1.5%/y increase from the previous NEI otherwise. For some industrial/commercial/institutional sectors that were not available in the NEI2008, we assumed they remained as in the NEI2005 as there was just marginal

change in these sectors over 2005–2008. Emission estimates for residential wood combustion were obtained from [29]. The annual emissions for 2009 were assessed with a 1.5% increase from the 2008 base-year.

We considered changes in emission of $PM_{2.5}$, particulate matter having diameters equal to or less than $10\ \mu m$ (PM_{10}), sulfur dioxides (SO_2), carbon monoxide (CO), carbon dioxides (CO_2), ammonia (NH_3), methane (CH_4), and VOC per wood-burning device exchanged. We calculated the emission of the i th species from wood-burning devices in WSR as follows:

$$E_{WSR,i} = E_{REF,i} + N_{exch}E_{cert,i} - \sum N_j E_{j,i}, \quad (1)$$

where $N_{exch} = \sum N_j$ and $E_{cert,i}$ are the number of certified wood-burning devices installed and their emission rates for the i th species; N_j and E_j are the numbers of noncertified wood-burning devices of type j and their emission rates for the i th species per device j ; $E_{REF,i}$ and $E_{WSR,i}$ are the total emission rates of the i th species from wood-burning devices in REF and WSR, respectively. The emission rates from wood-burning devices for all species were derived from [29, 30]. Analogously, we calculated the emissions for the assumed changeout of WSS1 and WSS2 with the

corresponding numbers N_{exch} and N_j for each sensitive study. The emissions of all other sectors than wood-burning remained the same in WSR, WSS1, and WSS2 as they were in REF.

This annual emission data was allocated in space and time based on source-specific activity data (land use, population density, traffic counts, point-source coordinates, hour, day of the week, month, etc.) (e.g., Figure 2). In addition, temperature was considered for emissions from traffic, residential, and commercial heating and power generation leading to higher (lower) emissions for daily mean temperatures below (above) the monthly mean temperature [15].

2.3. Analysis Methods. We analyzed the simulations over an area of 80×70 grid points (Figure 1) from October 1 0000 Alaska Standard Time (AST) to April 1 0000 AST (which is UTC+8 h) as the 24 h-average is to be evaluated with respect to AST. We determined the differences of $\text{PM}_{2.5}$ and its components in REF in comparison with WSR, WSS1 and WSS2. The $\text{PM}_{2.5}$ concentration differences (REF-WSR, REF-WSS1, REF-WSS2) were tested for their significance at the 95% confidence level by using a t -test with the null hypothesis that $\text{PM}_{2.5}$ concentrations in REF and in each of WSR, WSS1, and WSS2 do not differ.

We evaluated the benefit of the wood-burning device changeout by examining how many “exceedances” and “exceedance days” were avoided. In doing so, we considered 24 h-average $\text{PM}_{2.5}$ concentrations at any grid-cell greater than the NAAQS on any day as an “exceedance” and any day that had at least one “exceedance” anywhere as an “exceedance day”.

We calculated the relative response factors in response to the emission changes YYY by dividing the concentrations in YYY by those of REF (YYY/REF) where YYY stands for WSR, WSS1, and WSS2, respectively. The RRFs were calculated for total $\text{PM}_{2.5}$ and its major components namely sulfates (SO_4), nitrates (NO_3), ammonium (NH_4), organic carbon (OC), elemental carbon (EC), and other primary inorganic particulate matter (others). The RRFs were calculated for all grid cells in the nonattainment area including the grid cell that holds the official monitoring site to assess the effects of the wood-burning device changeout over the nonattainment area.

3. Result

3.1. Model Performance. The evaluation of the baseline simulation (REF) [15] can be summarized as follows. WRF/Chem overestimated temperatures measured at 3, 11 and 22 m at the meteorological tower in downtown Fairbanks by 0.6 K, 0.7 K, and 1.1 K, respectively. It overestimated wind speeds measured at 11 m (22 m) by 1.15 m.s^{-1} (2.39 m.s^{-1}) and overestimated relative humidity by 16%. It well captured the temporal evolution of the meteorological quantities observed at the 23 meteorological surface stations in the domain. In the domain, the overall biases of temperature, dew point temperature, relative humidity, sea-level pressure, wind

speed and direction over October to March were 1.3 K, 2.1 K, 5%, -1.9 hPa , 1.55 m.s^{-1} , and 4° , respectively. WRF/Chem slightly overestimated the 24 h-average $\text{PM}_{2.5}$ concentration on polluted days ($\text{PM}_{2.5}$ concentration $>35 \mu\text{g.m}^{-3}$) but failed to capture the extremes to their full extent. The occurrence frequency was acceptably captured for $\text{PM}_{2.5}$ concentrations between 15 and $50 \mu\text{g.m}^{-3}$. WRF/Chem simulated 52 exceedances at the grid cell holding the monitoring site where only 26 exceedances were observed.

The failure to capture the $\text{PM}_{2.5}$ maxima (minima) to their full extent on extremely polluted (clean) days does not affect the number of simulated exceedance days and exceedances. During these events, $\text{PM}_{2.5}$ concentrations namely were much higher (lower) than the $35 \mu\text{g.m}^{-3}$ threshold for exceedances. Thus, we can use the REF and WSR simulations to assess the impact of a wood-burning device changeout on the $\text{PM}_{2.5}$ concentration in the nonattainment area.

3.2. Emission Reduction. On annual average, $\text{PM}_{2.5}$ emissions from residential heating devices made up about 21% of the total $\text{PM}_{2.5}$ emissions from all source categories. Wood-burning devices contributed 66.6, 1.4, 14.7, 59.9, 96.5 and 95.8% of the emitted $\text{PM}_{2.5}$, SO_2 , NO_x , NH_3 , VOC, and CO from residential heating.

On average over the nonattainment area, $\text{PM}_{2.5}$ emissions in October, November, December, January, February, and March were 941.7, 632.9, 632.5, 799.8, 680.5, and $661.0 \text{ g.km}^{-2} \text{ h}^{-1}$, respectively. Temperatures were appreciably below the 1971–2000 30-year average in October and above in November, December, January, and February. Consequently, $\text{PM}_{2.5}$ emissions were higher in October and lower in November, December, and January than on average.

Over October to March, WSR reduced the total $\text{PM}_{2.5}$ emissions by 3.7% compared to REF. The monthly average $\text{PM}_{2.5}$ emission reductions were 4.0, 3.2, 2.7, 3.0, 3.9, and 5.6% in October, November, December, January, February, and March, respectively. The magnitude of emission reductions differed among pollutants. On average over the nonattainment area, SO_2 emission reductions were 19.5, 8.16, 9.1, 11.7, 11.0, and 15.8% in October to March, respectively. The respective NO_x (VOC) emission reductions were 16.0 (20.3), 5.5 (8.1), 6.8 (6.6), 8.9 (10.7), 7.3 (11.0), and 11.4 (11.2)%, respectively.

3.3. Reference Simulation. The diurnal courses of $\text{PM}_{2.5}$ concentrations were similar in REF and WSR, that is, changes in emissions from wood burning do not affect the general diurnal course of $\text{PM}_{2.5}$ concentration. The diurnal course of $\text{PM}_{2.5}$ concentration rather reflects the temporal variation of the emissions from all sources. The diurnal course of hourly $\text{PM}_{2.5}$ concentrations on days having 24 h-average $\text{PM}_{2.5}$ concentrations less than $25 \mu\text{g.m}^{-3}$ showed a peak at 1000 AST followed by a slightly stronger peak at 1900 AST. On days having 24 h-average $\text{PM}_{2.5}$ concentration greater than $25 \mu\text{g.m}^{-3}$, the second peak often dominated the first one and had its maximum between 1500 to 1700 AST. Typically, the hourly $\text{PM}_{2.5}$ concentrations sharply increased

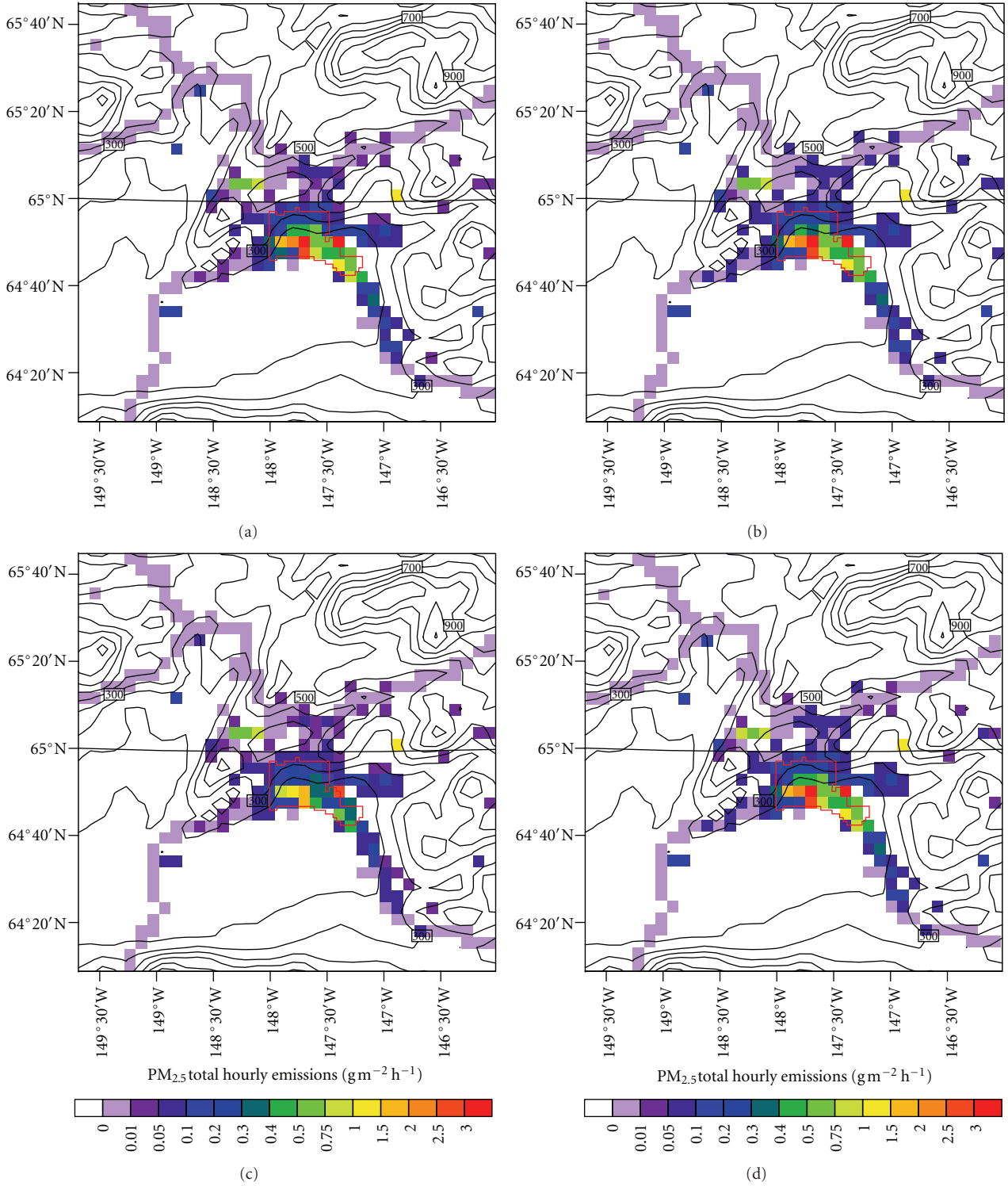


FIGURE 2: Zoom-in on PM_{2.5} emissions in (a) REF, (b) WSR, (c) WSS1, and (d) WSS2 on average over October to March for REF and WSR and October 01–14, 2008, for WSS1 and WSS2.

after 600 AST and quickly decreased after reaching the second peak. From October to March, nighttime (2200–0600 AST) hourly PM_{2.5} concentrations were typically lower and fluctuated less ($\mu = 15.7 \mu\text{g}\cdot\text{m}^{-3}$, $\sigma = 9.9 \mu\text{g}\cdot\text{m}^{-3}$) than

during the remaining hours of the day ($\mu = 37.2 \mu\text{g}\cdot\text{m}^{-3}$, $\sigma = 22.0 \mu\text{g}\cdot\text{m}^{-3}$).

Over the nonattainment area, REF monthly average PM_{2.5} concentrations were 12.9, 11.0, 9.2, 11.0, 9.8, and

$5.7 \mu\text{g}\cdot\text{m}^{-3}$ in October, November, December, January, February, and March, respectively. In the nonattainment area, $\text{PM}_{2.5}$ concentrations were governed by the emission strength and meteorological conditions. At the grid cell holding the monitoring site, the correlations of 24 h-average $\text{PM}_{2.5}$ concentration with 2 m air temperature (T), 10 m wind speed (v), atmospheric boundary layer height (ABL-height), downward shortwave radiation, relative humidity, and sea level pressure were -0.404 , -0.626 , -0.613 , -0.298 , 0.043 , and -0.001 , respectively (all significant at the 95% confidence level). Here, the 24 h-average $\text{PM}_{2.5}$ concentrations were strongly driven by emission strength ($R = 0.668$, significant). The average compositions of the 24 h-average $\text{PM}_{2.5}$ concentration in all grid cells in the nonattainment area were 21.3–25.0, 0.6–0.8, <0.1 , 8.9–9.3, 45.4–47.7, 19.8–20.7% SO_4 , NO_3 , NH_4 , EC, OC, and others, respectively. This finding indicates no notable differences in local $\text{PM}_{2.5}$ composition in the nonattainment area.

The on-average high $\text{PM}_{2.5}$ emissions ($188.3 \text{ g}\cdot\text{km}^{-2}\text{ h}^{-1}$) and relative low wind speeds ($1.9 \text{ m}\cdot\text{s}^{-1}$) over the nonattainment area in October led to the highest monthly average $\text{PM}_{2.5}$ concentrations of October to March. On monthly average, wind speed and ABL-height were lowest ($0.9 \text{ m}\cdot\text{s}^{-1}$ and 122.7 m at the grid cell holding the monitoring site, respectively) in November, which explains the high monthly average $\text{PM}_{2.5}$ concentrations despite of the on-monthly-average second lowest $\text{PM}_{2.5}$ emissions of October to March. In March, the on-average relatively high wind speed and ABL height ($2.6 \text{ m}\cdot\text{s}^{-1}$ and 567.2 m at the grid-cell of the monitoring site) provided good dilution and transported polluted air out of the nonattainment area, which yielded low $\text{PM}_{2.5}$ concentration over the nonattainment area.

In REF, all maximum 24 h-average $\text{PM}_{2.5}$ concentrations obtained on any day during October to March occurred in the nonattainment area. Of the 182 days, the highest 24 h-average $\text{PM}_{2.5}$ concentrations occurred at the grid-cell holding the monitoring site and/or the grid cells adjacent to it to the south and west (these three grid cells are called site group hereafter) on 86, 64, and 32 days, respectively. This fact is due to relative strong $\text{PM}_{2.5}$ emissions in these grid cells in comparison with other grid cells in the nonattainment area. The site group $\text{PM}_{2.5}$ emissions made up 34.3% of the total emissions in the nonattainment area that encompasses 31 grid cells.

In REF, 55 exceedance days and 131 exceedances were simulated during October to March, of which 52 exceedances occurred at the grid cell of the monitoring site. The number of exceedance days (exceedances) in October, November, January, February, and March was 20 (57), 10 (13), 5 (13), 15 (37), 5 (11), and 0 (0), respectively. All exceedances typically occurred in the site group. The highest and lowest 24 h-average $\text{PM}_{2.5}$ concentrations on any exceedance day were 72.2 and $35.1 \mu\text{g}\cdot\text{m}^{-3}$ and occurred on October 27, 2008, and January 4, 2009, respectively.

Exceedances typically occurred when at least any two of the following conditions coexisted: strong emission rate ($>3600 \text{ g}\cdot\text{km}^{-2}\text{ h}^{-1}$), low wind speed ($v < 1 \text{ m}\cdot\text{s}^{-1}$), low temperature ($<-20^\circ\text{C}$) and low ABL height ($<20 \text{ m}$). These four critical conditions occurred on 23.1, 15.4, 20.3

and 20.3% of the 182 days. Days with high exceedances ($>60 \mu\text{g}\cdot\text{m}^{-3}$) occurred when all four above mentioned critical conditions occurred concurrently. No exceedances occurred on days with wind speeds greater than $2 \text{ m}\cdot\text{s}^{-1}$ and ABL-heights greater than 100 m. On days with wind speeds greater than $1 \text{ m}\cdot\text{s}^{-1}$ and ABL heights greater than 100 m anywhere in the nonattainment area but not at the site group, exceedances were simulated at the grid cell of the monitoring site and/or its adjacent grid cells while the 24 h-average $\text{PM}_{2.5}$ concentrations at the other grid cells in the nonattainment area remained low ($<15 \mu\text{g}\cdot\text{m}^{-3}$). Large concentration gradients always existed between the grid cells of the site group and the other grid cells in the nonattainment area.

On days with calm wind ($<0.5 \text{ m}\cdot\text{s}^{-1}$), high 24 h-average $\text{PM}_{2.5}$ concentrations and often exceedances occurred in the nonattainment area and its surrounding area (Figure 3(a)). During October to March, no exceedance occurred when the prevalent northeast wind or the occasional northwest wind advected clean and relatively warm air into the nonattainment area and flushed the polluted air toward the southwest or southeast (Figure 3(b)). Exceedances typically occurred when (1) in the nonattainment area, weak northeast winds were not able to remove the cold and stable air mass (Figure 3(c)), (2) in the nonattainment area, wind came from different directions and hindered the transport of polluted air out of the nonattainment area (Figure 3(d)), (3) northeast or southwest winds transported polluted air out of the nonattainment area that then was advected back into the nonattainment area as aged polluted air (Figure 3(e)), and (4) southeast winds advected polluted air from the community of North Pole (2226 inhabitants, located in the nonattainment area 22 km southeast of downtown Fairbanks) towards the grid-cell of the monitoring site and slowly drained toward the southwest.

3.4. Wood-Burning Device Changeout. On all except eight days, the highest 24 h-average $\text{PM}_{2.5}$ concentrations occurred at the same grid cells in WSR and REF. On those eight days, the 24 h-average $\text{PM}_{2.5}$ concentration maxima in WSR, however, still occurred within the site group like in REF. The slight shifts in position of the local maxima were due to marginal (in the order of measurement accuracy) changes in meteorological conditions due to indirect and direct feedback between the aerosol concentrations and radiation.

In WSR, the monthly average $\text{PM}_{2.5}$ concentrations in the nonattainment area were 12.2, 10.3, 8.6, 10.3, 9.2, and $5.3 \mu\text{g}\cdot\text{m}^{-3}$ in October, November, December, January, February, and March, respectively. The values led to monthly average $\text{PM}_{2.5}$ differences (REF-WSR) of 0.7, 0.7, 0.6, 0.7, 0.6, and $0.3 \mu\text{g}\cdot\text{m}^{-3}$ for October to March, respectively. The $\text{PM}_{2.5}$ differences were higher in months with on-average relatively higher than relatively lower $\text{PM}_{2.5}$ concentration.

The highest 24 h-average $\text{PM}_{2.5}$ difference obtained anywhere in the domain was $5.7 \mu\text{g}\cdot\text{m}^{-3}$ (October 27 2008). The highest ($2.1 \mu\text{g}\cdot\text{m}^{-3}$) and the second highest ($2.0 \mu\text{g}\cdot\text{m}^{-3}$) 24 h-average $\text{PM}_{2.5}$ differences over the nonattainment area were obtained for October 27 2008 and January 1 2009,

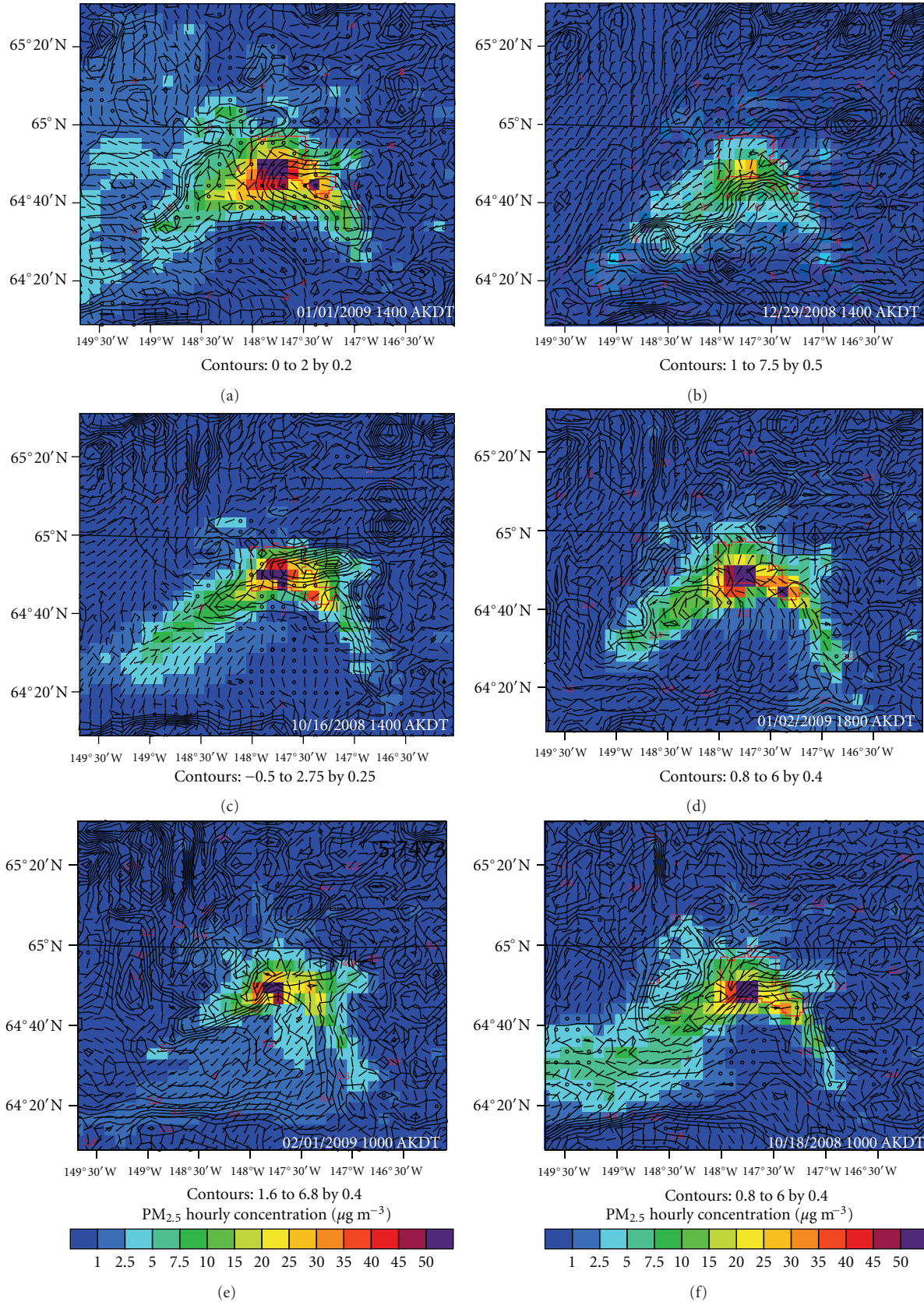


FIGURE 3: Zoom-in on typical wind circulation patterns at breathing level associated with high and low PM_{2.5} concentrations in the nonattainment area in October to March. The contour lines represent the potential temperature gradient ($\Delta\theta/\Delta z$) ($\text{K}\cdot 100\text{ m}^{-1}$) between the surface and 150 m above the ground; the red polygon indicates the nonattainment area. The community of North Pole is located in the lower right region of the nonattainment area.

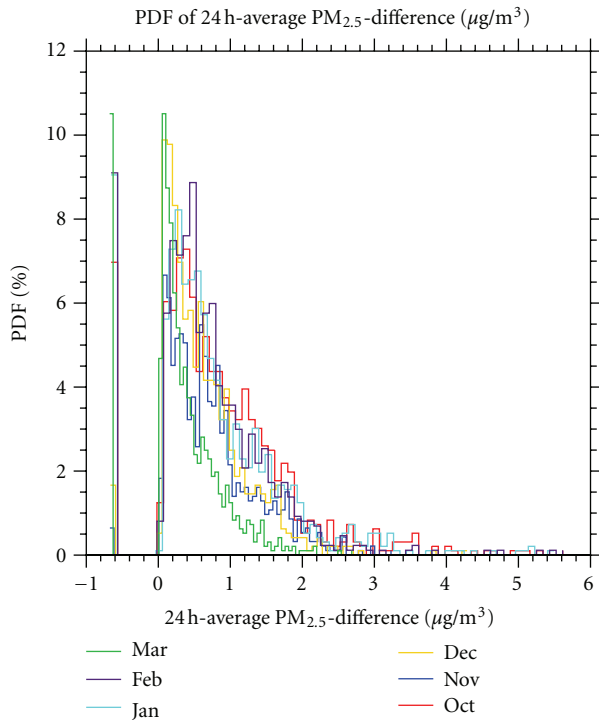


FIGURE 4: Population distribution of 24 h-average $PM_{2.5}$ difference in the nonattainment area as obtained for WSR in each month. The occurrences of all 24 h-average $PM_{2.5}$ differences $< 0.0 \mu\text{g}\cdot\text{m}^{-3}$ were summed up and their distribution is shown on the left most of the x-axis.

respectively. On average over the nonattainment area and October to March, the $PM_{2.5}$ difference was $0.6 \mu\text{g}\cdot\text{m}^{-3}$. This value equals to 8% (6%) of the highest (average) $PM_{2.5}$ concentration reductions over the nonattainment area.

In the nonattainment area over October to March, about 45% and 33% of the 24 h-average $PM_{2.5}$ differences fell between $0.5\text{--}1 \mu\text{g}\cdot\text{m}^{-3}$ and $0\text{--}0.5 \mu\text{g}\cdot\text{m}^{-3}$, respectively. However, for the nonattainment area the frequency distribution of the 24 h-average $PM_{2.5}$ differences varied strongly among months (Figure 4). High 24 h-average $PM_{2.5}$ differences ($> 3 \mu\text{g}\cdot\text{m}^{-3}$) only occurred 3, 2.4, and 1.2% of the time in October, January and February, respectively. In November, December, and March, more than 75% of the 24 h-average $PM_{2.5}$ differences ranged between 0 and $1 \mu\text{g}\cdot\text{m}^{-3}$. In October, more than 40% of the 24 h-average $PM_{2.5}$ differences in the nonattainment area exceeded $1 \mu\text{g}\cdot\text{m}^{-3}$.

On the nine days when the maximum 24 h-average $PM_{2.5}$ concentrations exceeded $60 \mu\text{g}\cdot\text{m}^{-3}$, the average 24 h-average $PM_{2.5}$ difference in the nonattainment area was $1.5\text{--}2.1 \mu\text{g}\cdot\text{m}^{-3}$ and the maximum 24 h-average $PM_{2.5}$ difference in the nonattainment area was $3.4\text{--}5.7 \mu\text{g}\cdot\text{m}^{-3}$. On these days, 60–87% (16–32%) of all grid-cells in the nonattainment area experienced 24 h-average $PM_{2.5}$ differences greater than $1 \mu\text{g}\cdot\text{m}^{-3}$ ($2 \mu\text{g}\cdot\text{m}^{-3}$). On the 46 days when the maximum 24 h-average $PM_{2.5}$ concentrations ranged between $35 \mu\text{g}\cdot\text{m}^{-3}$ and $60 \mu\text{g}\cdot\text{m}^{-3}$, the average 24 h-average $PM_{2.5}$ differences were $0.7\text{--}1.5 \mu\text{g}\cdot\text{m}^{-3}$ and the maximum

24 h-average $PM_{2.5}$ differences were $1.9\text{--}4.0 \mu\text{g}\cdot\text{m}^{-3}$. About 52% of the 24 h-average $PM_{2.5}$ differences were less than $1.0 \mu\text{g}\cdot\text{m}^{-3}$ and 8% of all grid-cells in the nonattainment area had 24 h-average $PM_{2.5}$ differences greater than $2 \mu\text{g}\cdot\text{m}^{-3}$. On days with maximum 24 h-average $PM_{2.5}$ concentration lower than $35 \mu\text{g}\cdot\text{m}^{-3}$, the 24 h-average $PM_{2.5}$ differences were about $0.5 \mu\text{g}\cdot\text{m}^{-3}$ on average, and 77% of them were less than $1.0 \mu\text{g}\cdot\text{m}^{-3}$. On these days, only 1% of the 24 h-average $PM_{2.5}$ differences exceeded $2 \mu\text{g}\cdot\text{m}^{-3}$ and typically occurred in the site group.

On 111 out of the 182 days, the maximum 24 h-average $PM_{2.5}$ difference occurred within the site group. The maximum 24 h-average $PM_{2.5}$ differences typically occurred in the site group on days with calm winds ($v < 0.5 \text{m}\cdot\text{s}^{-1}$) or on days with winds ($v > 2 \text{m}\cdot\text{s}^{-1}$) and uniform wind direction over the nonattainment area. When the maximum difference occurred at another place in the nonattainment area, winds ranged between 0.7 and $1.2 \text{m}\cdot\text{s}^{-1}$ from various directions and advected pollutants from relatively strong polluted areas within the nonattainment area.

In the nonattainment area at grid-cells with strong $PM_{2.5}$ emissions ($> 1400 \text{g}\cdot\text{km}^{-2}\cdot\text{h}^{-1}$), the 24 h-average $PM_{2.5}$ differences strongly depended on the $PM_{2.5}$ emission reduction ($R = 0.617$ to 0.894 , significant). At grid-cells with low $PM_{2.5}$ emissions ($\leq 1400 \text{g}\cdot\text{km}^{-2}\cdot\text{h}^{-1}$), the 24 h-average $PM_{2.5}$ difference was less sensitive to the $PM_{2.5}$ emission reduction ($R = 0.161$ to 0.556) than at those with high emission rates. Instead, the meteorological conditions gained importance for the magnitude of the concentration reduction.

$PM_{2.5}$ speciation in REF hardly differed from that in WSR ($< 0.1\%$). The low changes in the partitioning among SO_4 , NO_3 , and other $PM_{2.5}$ species was partly due to the low emission reductions, the low availability of NH_3 and low shortwave radiation in Fairbanks during October to March.

In WSR, 1 (8), 3 (5), 2 (3), 1 (8), 0 (0), and 0 (0) exceedance days (exceedances) were avoided in October, November, December, January, February, and March, respectively, as compared to REF. Out of them eight exceedances were avoided at the grid cell holding the monitoring site. On all exceedance-days except February 8, 2009, the locations of exceedances were identical in WSR and REF. On February 8, 2009, more grid-cells experienced exceedances in WSR than REF (three versus two grid-cells) due to the close to $35 \mu\text{g}\cdot\text{m}^{-3}$ concentrations and slight changes in meteorological conditions due to radiation-aerosol feedbacks.

At exceedance locations, about 18.3, 9.9, 42.0, 22.1, 10.7, and 6.1% of the 24 h-average $PM_{2.5}$ differences varied between < 2 , $2\text{--}3$, $3\text{--}4$, $4\text{--}5$, and $> 5 \mu\text{g}\cdot\text{m}^{-3}$, and the maximum 24 h-average $PM_{2.5}$ difference obtained on any exceedance-day was $5.7 \mu\text{g}\cdot\text{m}^{-3}$ (October 27, 2008). The maximum 24 h-average $PM_{2.5}$ differences on any avoided exceedance-days were between 1.7 and $2.8 \mu\text{g}\cdot\text{m}^{-3}$. This finding means the changeout of wood-burning devices avoided exceedance-days only on days with 24 h-average $PM_{2.5}$ concentrations slightly above $35 \mu\text{g}\cdot\text{m}^{-3}$.

At the grid-cell of the monitoring site the RRFs of 24 h-average $PM_{2.5}$ concentrations were 0.951, 0.950, 0.952, 0.956, 0.941, and 0.940 in October, November, December, January, February, and March, respectively. At this grid-cell,

the daily RRFs of 24 h-average $\text{PM}_{2.5}$ concentration were 0.938, 0.949, and 0.965 at the 50th, 75th, and 90th percentile, respectively. These findings suggest that the RRFs of total $\text{PM}_{2.5}$ concentrations at the grid-cell of the monitoring site were relatively consistent throughout October to March. The overall RRFs for NO_3 were 0.835, 0.893, 0.913, 0.868, 1.035, and 0.873 in October to March, and 0.866, 0.897 and 0.960 at the 50th, 75th, and 90th percentile, respectively. The RRF of NO_3 greater than 1 may be an artifact related to the very low NO_3 concentrations ($<1 \mu\text{g}\cdot\text{m}^{-3}$). At low concentrations, the RRF becomes highly sensitive to even small concentration changes. The RRFs of NH_4 were relative consistent (~ 1) throughout October to March.

Similar RRFs as obtained for the grid-cell of the monitoring site were also obtained for the other grid-cells of the site group. At the other grid-cells in the nonattainment area, the RRFs of all $\text{PM}_{2.5}$ species were slightly decreased (increased) as compared to that of the grid-cell with the monitoring site when those grid-cells were located in the upwind (downwind) of the site group. For all species, the RRFs obtained at these other grid-cells in the nonattainment area varied about ± 0.1 of the RRFs obtained at the grid-cell of the monitoring site. The grid-cells with the lowest RRFs, that is, lowest reduction, were typically located along the boundary of the nonattainment area and in the upwind of grid-cells with high pollution. The grid-cells along the boundary of the nonattainment area namely experienced frequently clean air advection from outside the nonattainment area. Therefore, the emission reductions related to the changeout of wood-burning devices hardly affected them. The grid-cells with the highest RRFs typically occurred inside the nonattainment area and had low 24 h-average $\text{PM}_{2.5}$ concentrations ($<4 \mu\text{g}\cdot\text{m}^{-3}$) because the RRF tends to be more sensitive to low than to high $\text{PM}_{2.5}$ concentrations.

The benefits of the changeout of wood-burning devices on the 24 h-average $\text{PM}_{2.5}$ concentrations drastically decreased outside and downwind of the nonattainment area. At radii of 4 km, 8 km, 12 km, and 16 km downwind of the nonattainment area, the 24 h-average $\text{PM}_{2.5}$ differences were about 27.5, 13.1, 7.3, and 4.6% of the 24 h-average $\text{PM}_{2.5}$ differences obtained on average over the nonattainment area. A *t*-test showed that the 24 h-average $\text{PM}_{2.5}$ differences were significant nowhere in the domain except within the nonattainment area and some adjacent grid-cells (Figure 5).

3.5. Sensitivity Studies. WSS1 represents a large emission reduction (Figure 2) due to the high number of wood-burning devices being changed out. On average over the nonattainment area and the 14 days, the total $\text{PM}_{2.5}$ emission was 39.8% less in WSS1 than in REF for the same time. WSS2 examined the impact of pellet-stove replacement. Over the 14-day period, WSR and WSS2 yielded total $\text{PM}_{2.5}$ emission reductions of 5.6% and 6.6%, respectively.

The maximum 24 h-average $\text{PM}_{2.5}$ concentrations obtained in REF, WSR, WSS1, and WSS2 on any day of the 14d sensitivity study were 51.1, 47.6, 26.9, and 47.5 $\mu\text{g}\cdot\text{m}^{-3}$ on October 14, 2008. The 24 h-average $\text{PM}_{2.5}$ differences of REF-WSS1 were appreciably higher than those of REF-WSR

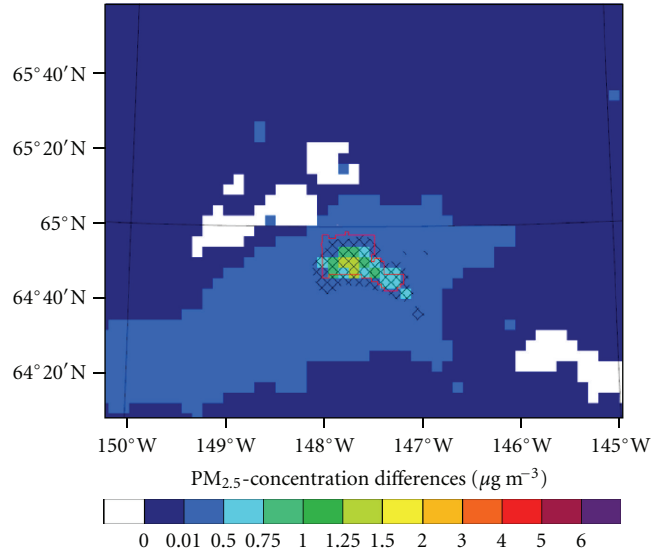


FIGURE 5: Zoom-in on the average differences of $\text{PM}_{2.5}$ concentration between REF and WSR for October to March. Hashed shading indicates grid cells with significant differences at the 95% or higher level of confidence.

or REF-WSS2 because the emission reduction was the highest in WSS1 (Figures 2 and 6). The maximum 24 h-average $\text{PM}_{2.5}$ differences obtained on any day in WSS1 was 24.9 $\mu\text{g}\cdot\text{m}^{-3}$. On the contrary, the maximum 24 h-average $\text{PM}_{2.5}$ difference obtained on any of the 14 days in WSS2 was 3.6 $\mu\text{g}\cdot\text{m}^{-3}$, which was only marginally higher than that obtained in WSR (3.5 $\mu\text{g}\cdot\text{m}^{-3}$) for the same timeframe. About 16.7, 25.3, 18.2, 8.8, 13.1, 13.4, and 5.5% of the 24 h-average $\text{PM}_{2.5}$ differences REF-WSS1 fall within <1 , 1-2, 2-3, 3-4, 4-6, 6-10, and $>10 \mu\text{g}\cdot\text{m}^{-3}$, respectively. During the same 14d period, about 77.0 (80.2), 18.4 (17.1), 3.5 (2.3), 1.2 (0.5), and 0 (0)% of 24 h-average $\text{PM}_{2.5}$ differences of REF-WSS1 (REF-WSR) fell between <1 , 1-2, 2-3, 3-4, and $>4 \mu\text{g}\cdot\text{m}^{-3}$, respectively.

The average RRFs of the 24 h-average $\text{PM}_{2.5}$ concentrations obtained at the grid-cell of the monitoring site for WSS1, WSS2, and WSR were 0.543, 0.913, and 0.930, respectively, for the 14d episode. The RRFs of NH_4 were about 1 in all sensitivity simulations. The RRFs of NO_3 were 0.471, 0.815, and 0.818 in WSS1, WSS2 and WSR, respectively, while those of SO_4 , OC, EC, and others were similar to those for $\text{PM}_{2.5}$.

The spatial variations of RRFs were within ± 0.1 of the RRF at the grid-cell of the monitoring site for any species at any grid-cell in the nonattainment area for both WSS2 and WSR. On the contrary, in WSS1, the spatial variations of RRFs reached from no difference to 0.4 greater RRF values than the RRF-value at the grid-cell of the monitoring site. On six and five out of the 14 days of the sensitivity study, the highest response, that is, highest reduction in the nonattainment area, occurred at the grid-cell of the monitoring site and other grid-cells of the site group. The highest response (RRF = 0.821) occurred at the grid-cell of

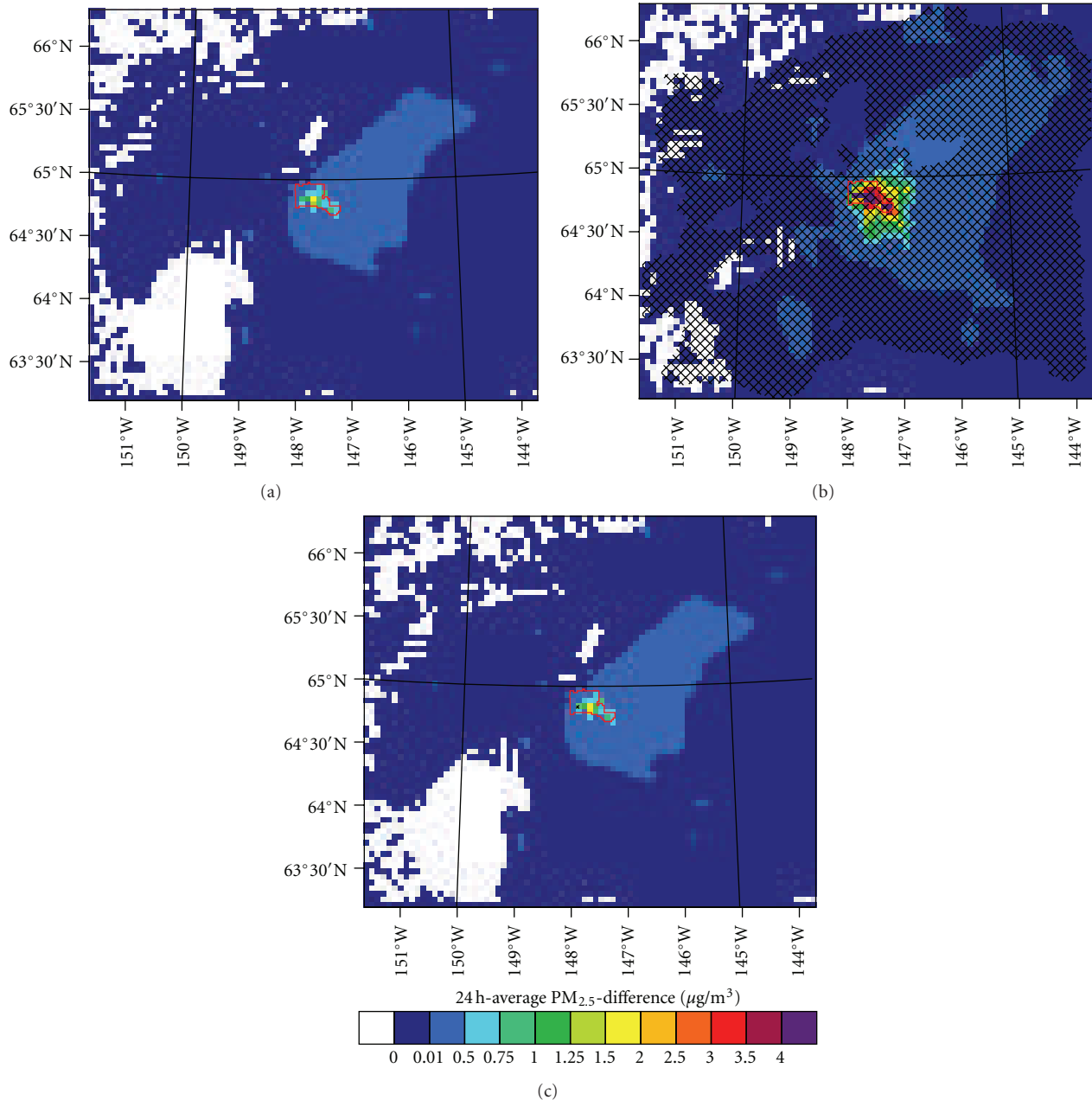


FIGURE 6: Like Figure 5, but for 24 h-average $PM_{2.5}$ differences (a) REF-WSR, (b) REF-WSS1, and (c) REF-WSS2 from October 1 to October 14 2008 AST.

the monitoring site on one day in WSS2. However, on no day the strongest response occurred at the grid-cell of the monitoring site in WSR.

The high number of wood-burning devices changed out in WSS1 led to avoidance of all 4 (6) exceedance days (exceedances) that occurred in REF during the same time. No exceedances were avoided in both WSS2 and WSR during these 14 days. The highest (lowest) 24 h-average $PM_{2.5}$ difference obtained at any exceedance location in WSS1 was 24.9 (16.8) $\mu\text{g}\cdot\text{m}^{-3}$. The locations of exceedances were the same in REF, WSS2, and WSR and all occurred in the nonattainment area.

4. Conclusions

The effects of exchanging noncertified wood-burning devices with certified woodstoves on reducing the 24 h-average $PM_{2.5}$ concentrations at breathing level in the Fairbanks nonattainment area were investigated for October 1, 2008, to March 31, 2009, using results from WRF/Chem simulations. The results indicated that the assumed wood-burning device changeouts helped to reduce the 24 h-average $PM_{2.5}$ concentrations at breathing level in the nonattainment area. However, the reduction effectiveness depends on the number of wood-burning devices changed out and what kinds of devices

are changed out. The wood-burning device changeout scenario based on data reported by [2] yielded only a 3.7% $\text{PM}_{2.5}$ emission reduction from the reference scenario and consequently a low decrease of 24 h-average $\text{PM}_{2.5}$ concentrations. On average over the nonattainment area and October to March, the 24 h-average $\text{PM}_{2.5}$ differences (REF-WSR) were $0.6 \mu\text{g}\cdot\text{m}^{-3}$, which equals a 6% $\text{PM}_{2.5}$ concentration reduction. About 79% of the 24 h-average $\text{PM}_{2.5}$ differences were less than $1 \mu\text{g}\cdot\text{m}^{-3}$. This means given a design value of $44.7 \mu\text{g}\cdot\text{m}^{-3}$ the assumed changeout does not lead to compliance and may only reduce the number of exceedances on days with concentrations slightly higher than the NAAQS.

The magnitude of the 24 h-average $\text{PM}_{2.5}$ differences REF-WSR differed strongly among days and locations. High 24 h-average $\text{PM}_{2.5}$ differences ($>3 \mu\text{g}\cdot\text{m}^{-3}$) often occurred in October, January, and February. Wind speed and wind direction were the key factors that governed the distribution of the maximum 24 h-average $\text{PM}_{2.5}$ difference. The magnitude of the 24 h-average $\text{PM}_{2.5}$ difference depended more on the $\text{PM}_{2.5}$ emission reduction at grid-cells having relative strong than relative low $\text{PM}_{2.5}$ emissions. The maximum 24 h-average $\text{PM}_{2.5}$ differences typically occurred in the grid-cells of the site group on days having calm wind ($v < 0.5 \text{m}\cdot\text{s}^{-1}$) or wind speeds exceeding $2 \text{m}\cdot\text{s}^{-1}$. Under other wind conditions, the maximum 24 h-average $\text{PM}_{2.5}$ differences typically occurred at grid-cells in the downwind of the site group. Based on these findings one has to conclude that mitigation is spatially heterogeneous and local emission conditions together with the meteorological conditions strongly govern the magnitude of mitigation.

The wood-burning device changeout assumed in WSR only effectively helped to avoid 7 out of 55 exceedance days that occurred in REF. Moreover, this avoidance occurred only on days with 24 h-average $\text{PM}_{2.5}$ concentration slightly above $35 \mu\text{g}\cdot\text{m}^{-3}$. The RRFs of $\text{PM}_{2.5}$ concentration and its major components typically varied between 0.950–0.965 and were relatively consistent throughout October to March. The lowest RRFs, that is, highest reductions, were not obtained at the grid-cell of the monitoring site but at other grid-cells in the nonattainment area. These findings support the above conclusion that the assumed changeout is not sufficient to achieve compliance. Thus, one has to conclude that the changeout of wood-burning devices may improve the air quality locally in large parts of the nonattainment area without becoming obvious at the monitoring site. Based on the relative consistency of RRF one has to conclude that wood-burning changeout provides a relative reliable reduction.

The 14d sensitive simulations assuming the number of wood-burning devices reported by [29] (WSS1) yielded up to a 39.8% $\text{PM}_{2.5}$ emission reduction as compared to the baseline simulation (REF) and a much higher 24 h-average $\text{PM}_{2.5}$ concentration reduction over the nonattainment area than WSR and WSS2. In total four of the exceedance days that were simulated in REF during these 14 days were avoided in WSS1 and the maximum 24 h-average $\text{PM}_{2.5}$ difference (REF-WSS1) at any exceedance location was $24.9 \mu\text{g}\cdot\text{m}^{-3}$. The relative response factors of $\text{PM}_{2.5}$

concentrations obtained at the grid-cell of the monitoring site were as high as 0.543 on average and the highest RRFs were frequently obtained at the grid-cell of the monitoring site and other grid-cells of the site group. The results of the sensitivity study WSS2 only marginally differed from those of WSR. Based on the 14d sensitivity study WSS1, one has to conclude that if the number of uncertified wood-burning devices assumed in WSS1 could be changed out, the number of exceedances in the nonattainment area could effectively be reduced. On the contrary, changing out wood-burning devices at the comparatively low numbers assumed in WSR and WSS2 seems not to be sufficient to achieve compliance with the NAAQS. Together the results of the sensitivity studies suggest that accurate knowledge on the number of noncertified devices that have to be or can be changed out is of greatest importance to assess the potential benefits of a changeout program on the 24 h-average $\text{PM}_{2.5}$ concentrations.

Acknowledgments

The authors thank C. F. Cahill, G. Kramm, W. R. Simpson, G. A. Grell, K. Leelasakultum, T. T. Tran, and the anonymous reviewers for fruitful discussion. This research was in part supported by the Fairbanks North Star Borough under contract LGFEEQ. Computational resources were provided by the Arctic Region Supercomputing Center.

References

- [1] H. N. Q. Tran and N. Mölders, "Investigations on meteorological conditions for elevated $\text{PM}_{2.5}$ in Fairbanks, Alaska," *Atmospheric Research*, vol. 99, no. 1, pp. 39–49, 2011.
- [2] T. R. Carlson, S. H. Yoon, and R. G. Dulla, "Fairbanks home heating survey," Tech. Rep., Sierra Research, Sacramento, Calif, USA, 2010.
- [3] J. E. Houck and D. R. Broderick, "PM_{2.5} emission reduction benefits of replacing conventional uncertified cordwood stoves with certified cordwood stoves or modern pellet stoves," Tech. Rep., Arlington, Va, USA, 2005.
- [4] United State Environmental Protection Agency (EPA), "Agencies-changeout guide," 2011, <http://www.epa.gov/burnwise/how-to-guide.html>.
- [5] United State Environmental Protection Agency (EPA), "Agencies—case studies," 2011, <http://www.epa.gov/burnwise/casestudies.html>.
- [6] M. A. Bergauff, T. J. Ward, C. W. Noonan, and C. P. Palmer, "The effect of a woodstove changeout on ambient levels of $\text{PM}_{2.5}$ and chemical tracers for woodsmoke in Libby, Montana," *Atmospheric Environment*, vol. 43, no. 18, pp. 2938–2943, 2009.
- [7] T. Ward and C. Noonan, "Results of a residential indoor $\text{PM}_{2.5}$ sampling program before and after a woodstove changeout," *Indoor Air*, vol. 18, no. 5, pp. 408–415, 2008.
- [8] R. W. Allen, S. Leckie, G. Millar, and M. Brauer, "The impact of wood stove technology upgrades on indoor residential air quality," *Atmospheric Environment*, vol. 43, no. 37, pp. 5908–5915, 2009.
- [9] G. A. Grell, S. E. Peckham, R. Schmitz et al., "Fully coupled "online" chemistry within the WRF model," *Atmospheric Environment*, vol. 39, no. 37, pp. 6957–6975, 2005.

- [10] S. E. Peckham, J. D. Fast, R. Schmitz et al., “WRF/Chem version 3.1 user’s guide,” pp. 78, 2009.
- [11] G. J. Frost, S. A. McKeen, M. Trainer et al., “Effects of changing power plant NO_x emissions on ozone in the eastern United States: Proof of concept,” *Journal of Geophysical Research, D*, vol. 111, no. 12, Article ID D12306, 2006.
- [12] X. Wang, Z. Wu, and G. Liang, “WRF/CHEM modeling of impacts of weather conditions modified by urban expansion on secondary organic aerosol formation over Pearl River Delta,” *Particuology*, vol. 7, no. 5, pp. 384–391, 2009.
- [13] T. T. Tran, G. Newby, and N. Mölders, “Impacts of emission changes on sulfate aerosols in Alaska,” *Atmospheric Environment*, vol. 45, no. 18, pp. 3078–3090, 2011.
- [14] N. Mölders, H. N. Q. Tran, P. Quinn, K. Sassen, G. Shaw, and G. Kramm, “Assessment of WRF/Chem to simulate sub-Arctic boundary layer characteristics during low solar irradiation using radiosonde, sodar, and surface data,” *Atmospheric Pollution Research*, vol. 2, no. 3, pp. 283–299, 2011.
- [15] N. Mölders, H. N. Q. Tran, C. F. Cahill, K. Leelasakultum, and T. T. Tran, “Assessment of WRF/Chem PM_{2.5}-forecasts using mobile and fixed location data from the Fairbanks, Alaska winter 2008/09 field campaign,” *Atmospheric Pollution Research*, vol. 3, no. 2, pp. 180–191, 2012.
- [16] S. Y. Hong and J. O. J. Lim, “The WRF single-moment 6-class microphysics scheme,” *Journal of The Korean Meteorological Society*, vol. 42, no. 1, pp. 129–151, 2006.
- [17] G. A. Grell and D. Dévényi, “A generalized approach to parameterizing convection combining ensemble and data assimilation techniques,” *Geophysical Research Letters*, vol. 29, no. 14, 2002.
- [18] M. D. Chou and M. J. Suarez, “An efficient thermal infrared radiation parameterization for use in general circulation models,” Tech. Rep., NASA Center for Aerospace Information, 1994.
- [19] E. J. Mlawer, S. J. Taubman, P. D. Brown, M. J. Iacono, and S. A. Clough, “Radiative transfer for inhomogeneous atmospheres: RRTM, a validated correlated-k model for the longwave,” *Journal of Geophysical Research D: Atmospheres*, vol. 102, no. 14, pp. 16663–16682, 1997.
- [20] J. C. Barnard, J. D. Fast, G. Paredes-Miranda, W. P. Arnott, and A. Laskin, “Technical note: evaluation of the WRF-chem ”aerosol chemical to aerosol optical properties” module using data from the milagro campaign,” *Atmospheric Chemistry and Physics*, vol. 10, no. 15, pp. 7325–7340, 2010.
- [21] Z. I. Janjic, “The step-mountain eta coordinate model: further developments of the convection, viscous sublayer, and turbulence closure schemes,” *Monthly Weather Review*, vol. 122, no. 5, pp. 927–945, 1994.
- [22] T. G. Smirnova, J. M. Brown, S. G. Benjamin, and D. Kim, “Parameterization of cold-season processes in the maps land-surface scheme,” *Journal of Geophysical Research D: Atmospheres*, vol. 105, no. 3, pp. 4077–4086, 2000.
- [23] W. R. Stockwell, P. Middleton, J. S. Chang, and X. Tang, “The second generation regional acid deposition model chemical mechanism for regional air quality modeling,” *Journal of Geophysical Research*, vol. 95, no. 10, pp. 16343–16367, 1990.
- [24] S. Madronich, “Photodissociation in the atmosphere. 1. Actinic flux and the effects of ground reflections and clouds,” *Journal of Geophysical Research*, vol. 92, no. 8, pp. 9740–9752, 1987.
- [25] I. J. Ackermann, H. Hass, M. Memmesheimer, A. Ebel, F. S. Binkowski, and U. Shankar, “Modal Aerosol Dynamics model for Europe: development and first applications,” *Atmospheric Environment*, vol. 32, no. 17, pp. 2981–2999, 1998.
- [26] B. Schell, I. J. Ackermann, H. Hass, F. S. Binkowski, and A. Ebel, “Modeling the formation of secondary organic aerosol within a comprehensive air quality model system,” *Journal of Geophysical Research D*, vol. 106, no. 22, pp. 28275–28293, 2001.
- [27] M. L. Wesely, “Parameterization of surface resistances to gaseous dry deposition in regional-scale numerical models,” *Atmospheric Environment*, vol. 23, no. 6, pp. 1293–1304, 1989.
- [28] D. Simpson, A. Guenther, C. N. Hewitt, and R. Steinbrecher, “Biogenic emissions in Europe 1. estimates and uncertainties,” *Journal of Geophysical Research*, vol. 100, no. 11, pp. 22875–22890, 1995.
- [29] J. Davies, D. Misiuk, R. Colgan, and N. Wiltse, “Reducing PM_{2.5} emissions from residential heating sources in the Fairbanks North Star Borough: emission estimates, policy options, and recommendations,” Tech. Rep., Fairbanks, Alaska, USA, 2009.
- [30] United State Environmental Protection Agency (EPA), “AP 42, Fifth Edition, Vol. I - Chapter 1: External combustion sources,” 2011, <http://www.epa.gov/ttn/chief/ap42/ch01/index.html>.